TURBULENCE MEASUREMENTS IN TRAILING VORTICES FOR B.W.I. NOISE PREDICTION

Report to NASA Langley under grant NAG-1-1119

by

William J Devenport[1], Stewart A L Glegg[2]
and Gautam Sharma[3]

June 1992

Also published as:
Report VPI-AOE-192, Department of Aerospace and Ocean Engineering,
Virginia Polytechnic Institute and State University, Blacksburg, Virginia, 24061

---

[1]Assistant Professor, Department of Aerospace and Ocean Engineering, Virginia Polytechnic Institute and State University

[2]Professor, Department of Ocean Engineering, Florida Atlantic University

[3]Graduate Student, Department of Aerospace and Ocean Engineering, Virginia Polytechnic Institute and State University

Overall these data reveal two fairly typical adverse-pressure gradient turbulent boundary layers back to back. On a semi-logarithmic scale the mean profiles (figures 3.1c and d) show a large outer region and almost no log-law region. The turbulence stress profiles (figure 3.1b) show a broad peak where $\sqrt{\overline{u^2}}/U_e$ reaches a maximum of about 10%. The U spectra show a clear inertial subrange at all z positions where G_{uu} varies as $f^{-5/3}$. No distinct peaks are visible in the spectra suggesting no coherent vortex shedding from the trailing edge of the wing.

Close comparison between those parts of the profiles measured on opposite sides of the wake shows some small but significant asymmetries at y/c=3.6, especially in the normal stress (figure 3.1b). This asymmetry can also be seen in the 'boundary-layer', displacement and momentum thicknesses presented in table 3.3. Note that these were calculated separately for the two sides of the wake. At y/c=3.6 the displacement and momentum thicknesses are as much as 12% higher on the positive z side. Differences between the two sides at the other y locations are less than 3%. After re-examining the wing we believe this asymmetry was due to local unevenness in the trip. It is worth noting, however, that the rest of measurements show the trip to be fairly uniform. The profiles shapes, especially those of mean velocity (figures 3.1b and c), vary little along the trailing edge. y variations in the total momentum and displacement thicknesses of the wake (the sum of contributions from its two sides) are also small.

Figures 3.2 and 3.5a-d and table 3.3 show the effects of angle of attack α, at 0, 2.5, 5.0 and 7.5°, on the near wake at y/c=1.2, Re_c=400000. Increase in angle of attack causes a thinning of the boundary layer leaving the pressure (positive z) side of the wing because of a reduction in the adverse pressure gradient it experiences. This thinning is accompanied by an increase in the mean-velocity gradients and a decrease in turbulence levels in the outer part of the layer (figures 3.2a and b). The boundary layer remains turbulent, however, since even at 7.5° power spectra of U (figure 3.5d) show a clear inertial subrange. In contrast, the boundary layer leaving the suction side thickens with angle of attack. The thickening produces a reduction in mean velocity gradients and in overall increase in turbulence levels. These changes are particularly rapid between α = 5 and 7.5°. Spectra

measured on this side of the wake again show a clear inertial subrange at all angles. It is worth noting that, while the details of the wake structure change substantially with angle of attack the total wake momentum thickness does not, being only a few percent higher at α = 7.5° than at zero angle of attack.

Figures 3.3 and 3.5c,e,f and g show the effects of Reynolds number on the near wake at y/c=1.2 with the wing at 5° angle of attack. Reynolds numbers Re_c of 130000, 260000, 400000 and 530000 are represented. Re_c has no substantial influence on the overall boundary-layer thicknesses (table 3.3) or mean velocity profiles (figure 3.3a) over this range. Between 260000 and 530000, Re_c also has only minor effects on the turbulence stresses (figure 3.3b) and power spectra (figure 3.5c, f and g). Turbulence stress levels increase slightly between 530000 and 260000 but the profile shape remains the same. At the same time the inertial subrange in the spectra shrinks as dissipation effects become more important. Significant Reynolds number effects do occur between Re_c = 260000 and 130000. The peak turbulence stress rises from 0.012 to 0.019 and the stress profiles become much more peaked (figure 3.3b). The spectra cease to show any inertial subrange. It would appear then that at Re_c=130000 the boundary layers leaving the wing are not fully turbulent.

Figures 3.4 and 3.5g and h show the effects on the wake of removing the boundary layer trip at Re_c=530000 and y/c=1.2 with the wing at 5° angle of attack. Those effects are fairly dramatic. The boundary layer momentum thickness decreases by a factor of about 2 on both sides (table 3.3). The turbulence stress profiles become much narrower (figure 3.4(b)) and, on the pressure side (positive z), the peak value of $\overline{u^2}/U_e^2$ increases by a factor of 3.8, from .009 with the trip to .034 with it. The reason for this dramatic increase is apparent in spectra measured without the trip (figure 3.5(h)). These show peaks at frequencies of $f\delta/U_e$ = .4 and its harmonics and sub-harmonics that are very strong on the pressure side. These peaks are presumably a consequence of organized vortex shedding from the pressure-side boundary layer, implying that this boundary layer is laminar at the trailing edge. In contrast, the suction side boundary layer appears to be fully turbulent. The spectra measured here showing an inertial subrange.

ABSTRACT

Blade wake interaction (BWI) noise is the broadband noise generated by the ingestion of turbulent tip vortices into helicopter rotors. Prediction of BWI noise requires knowledge of the turbulence structure of the tip vortex. This report describes a joint investigation to measure that structure and incorporate the results into a noise prediction scheme.

Measurements were performed on the tip vortex shed by a single rectangular NACA 0012 half wing placed in a wind tunnel test section. The properties of the vortex were studied for a range of angles of attack (2.5° to 7.5°) and chord Reynolds numbers (130000 to 530000). Initially the vortex was examined for stability and probe interference effects through flow visualization. Then detailed three-component velocity, turbulence and spectral measurements were made using multiple hot wires between 20 and 30 chordlengths downstream of the wing. These measurements show the flow to consist of a small axisymmetric core surrounded by a large non-axisymmetric region in which the wing wake forms a spiral around the core. In contrast to the results of previous workers, most of whom studied vortices generated by split wing configurations, there appeared to be little axisymmetric region of merged turbulent flow. Turbulence levels in the spiral wake decay with downstream distance. They also fall as the core is approached, presumably because of the effects of the increased straining and curvature on the turbulent structures here. Turbulence spectra measured in the wake are very similar in form, regardless of conditions and exact location, and bear a strong resemblance to a von Karman spectrum. At most conditions true turbulence levels in and immediately adjacent to the core are very low. Velocity fluctuations, however, are intense as a consequence of coherent lateral motions of the core and possible wave motions and instabilities travelling along it. Velocity autospectra in the core show the lateral motions to be anisotropic at very low frequencies and isotropic and mid frequencies. A large part of these motions may well be self induced. Circulation profiles in this region show Hoffman and Joubert's semi-logarithmic region, and in one case reveal the core to be fully developed.

From the point of view of BWI noise prediction the flow measurements identify three

sources of velocity fluctuations; low-frequency anisotropic core motions, mid-frequency isotropic core motions, and turbulence in the surrounding spiral wake. Estimates of the noise produced by these different frequency regimes show that it is the mid-frequency isotropic motions which is the most important mechanism for noise production, but the spectral shape and the predicted directionality for this mechanism are not in agreement with the measurements of BWI noise. The original noise-prediction scheme, based on the concept of a more turbulent vortex, has been shown to be the wrong basis for the correct description of the flow, but in spite of this the results are significantly better than those presented here. This suggests that the flow measured in the wind tunnel does not have the same turbulence upwash spectrum as that encountered by the helicopter rotor. One of the features of a real helicopter rotor which was not considered is the effect of a downstream blade upon the tip vortex. This may cause vortex bursting or alter the flow structure in the rotor disc plane in other ways. Measurements to evaluate this concept are planned for the future.

TABLE OF CONTENTS

PART II: THEORY AND NOISE PREDICTIONS

OVERVIEW

Blade wake interaction (BWI) noise has been identified (Brooks and Martin (1987)) as the most important contributor to helicopter noise during level flight and mild climb conditions. This noise source mechanism has been shown (Brooks and Marcolini (1987), Glegg (1989)) to be the result of interaction of the rotor blades with turbulence associated with the tip vortices in the rotor disk plane. A prediction method based on this concept has been developed (Glegg (1989)), which estimates the levels of BWI noise quite well, but fails to predict the spectral shape correctly. This has been attributed to insufficient information on the turbulence structure in the vortex. The overall objectives of the work presented in this report were,

(i) to measure the turbulence structure of tip vortices over a range of conditions, and,
(ii) to use this information to improve the BWI noise prediction method.

The results of the experimental work, carried out at Virginia Tech by Dr. William Devenport and Mr Gautam Sharma, are described in part I of this report. Theoretical work and BWI noise predictions, performed at Florida Atlantic University by Dr Stewart Glegg, are then presented in part II.

REFERENCES

Brooks T F and Martin R M, 1987, "Results of the 1986 NASA/FAA/DFVLR Main Rotor Test Entry in the German-Dutch Wind Tunnel (DNW)", NASA TM 100507.

Brooks T F, Marcolini M A and Pope D S, 1987, "Main rotor noise study in the DNW", presented to the AMS Specialist Meeting on Aerodynamics and Aeroacoustics, Arlington, Texas.

Glegg S, 1989, "The prediction of Blade Wake Interaction noise based on a turbulent vortex model", AIAA Paper 89-1134, 12th Aeroacoustics Conference, San Antonio, Texas.

ACKNOWLEDGEMENTS

The authors would like to thank NASA Langley, in particular Tom Brooks and Mike Marcolini, for their support under grant NAG-1-1119. The assistance of Mike Rife and Jeff Zsoldos in taking many of the measurements presented here is also gratefully acknowledged.

PART I: MEASUREMENTS

1. INTRODUCTION

The far-field behavior of wing-tip vortices has been the subject of many previous experimental investigations. However, almost all of these (for example Mason and Marchman (1972)), have considered only the mean velocity distribution. Thus very little is known about the turbulence structure of such flows. The lack of turbulence measurements is a result of the fact that tip vortices generated in wind tunnels tend to meander (i.e. their core location is a function of time) and be sensitive to probe interference. Meandering causes a fixed probe to greatly overestimate turbulence stresses in regions where there are significant mean velocity gradients across the vortex. In severe cases meandering also smooths mean velocity profiles significantly. Baker et al. (1974) conducted experiments on a trailing vortex generated by a rectangular wing in a water tunnel using laser Doppler velocimetry. They found that vortex meandering decreased the maximum tangential velocities by 30% and increased the measured core radius by a factor of 2.2. Baker attributed the meandering to freestream turbulence. Chigier and Corsiglia (1972) and Corsiglia et al. (1973) conducted triple hot-wire measurements on a trailing vortex in the NASA Ames 40x60 wind tunnel. They observed a spanwise meandering of about ± 2 chordlengths. As a result mean-velocity measurements made with a fixed hot-wire probe underestimated the peak tangential velocity by as much as 50%.

Probe interference problems in wing-tip vortices have been reported by Orloff (1971), Gasparek (1960) and Mason and Marchman (1972). Orloff and Gasparek found that the trajectory of the vortex moved when a small diameter probe was inserted into the core. Mason and Marchman also found that a probe changed the vortex trajectory but only if it was pitched or yawed relative to the free stream direction. Stifle and Panton (1991) examined the effects of passing a wire through the core of a tip vortex produced by a delta wing. The found that disturbances introduced into the vortex core propagated both upstream and downstream with smaller disturbances produced by a slower moving wire.

Despite these problems there have been a few investigations of the turbulence structure of single-wing vortices. Singh and Uberoi (1976) measured the vortex generated by a laminar flow half wing with fixed hot-wire probes. They observed relatively high frequency unsteadiness in the core due to laminar flow instabilities but little or no low-frequency meandering. They inferred that the laminar flow instabilities had symmetric and helical modes with wavelengths of the same order as the core diameter. Helical, axisymmetric and other core instabilities in vortical flows have also observed been in flow visualizations by Sarpkaya (1992) and Maxworthy et al. (1985) and studied theoretically by a number of authors (see for example Kelvin (1880), Lundren and Ashurst (1989), Marshall (1991)). In addition, instantaneous velocity distributions have been examined by Corsiglia at al. (1973), using a flying hot wire, and by Green and Acosta (1991) using double-pulsed holography of small bubbles.

In an attempt to generate stable trailing vortices, some workers have used a split wing configuration. Here the vortex is generated not at a tip but at the junction of two wings placed at equal and opposite angles of attack. A small nacelle is often placed between the two wings and used to join the wings together. Although the split wing vortex is supposed to be more stable, its lacks the same initial turbulence or mean flow structure as a tip vortex. Hoffman and Joubert (1963) were among the first to use the split wing concept to generate a trailing vortex. They analyzed the circulation distribution of the vortex and found a region where the circulation is proportional to the logarithmic radius for various conditions. In addition they developed a circulation defect law in the inner region of the vortex analogous to a turbulent boundary layer. Leuchter and Solignac (1983) used a split wing to examine the effect of wind tunnel adverse pressure gradients on the decay of a vortex. Using laser doppler velocimeter, they obtained mean and turbulence quantities and found that with increased pressure gradients, vortex breakdown occurred much more rapidly. Bandyopadhyay et al.(1990) also made turbulence measurements using a split wing in various amounts of freestream turbulence. Using smoke flow visualizations and hot-wires, they observed that momentum transfer takes place between the core and outer region. They

also discovered that turbulent fluid inside the core relaminarizes due to the rotational motion of the core. The most complete set of turbulence measurements for a split wing vortex to date is due to Phillips and Graham (1984). Using slant hot-wires they obtained mean velocities and Reynolds stresses for all three directions. Ways to increase the decay rate were also examined by introducing jets and wakes into the core.

The objective of the present experimental investigation was to make detailed measurements of the turbulence structure and spectral properties of a true tip vortex over a range of conditions. The investigation was split into two parts;

(i) helium bubble flow visualizations, to examine the stability of the vortex and its sensitivity to probe interference,

(ii) detailed hot-wire measurements of mean velocity, turbulence stresses and spectra.

The results of the helium bubble visualizations were reported by Devenport and Sharma (1990). They concluded that at all conditions studied the vortex was insensitive to the interference of a hot-wire probe at the measurement point. They also showed the vortex to be relatively stable, wandering by less than $\pm 5\%$ of the wing chord as far as 30 chordlengths downstream of the wing. Note that these results were, to a certain extent, expected. In this study we used the same wing and wind tunnel used to generate the tip vortex studied by Mason and Marchman (1972). While Mason and Marchman made only mean velocity measurements their results strongly suggested that they had a stable tip vortex largely unaffected by the presence of a probe alligned with the free stream.

The purpose of part I of this report is to present and discuss the velocity measurements.

2. EXPERIMENTAL APPARATUS AND TECHNIQUES

2.1 Wind Tunnel

Experiments were performed in the Virginia Tech Stability Wind Tunnel (figure 2.1). This closed circuit facility is powered by a 600 h.p. axial fan. It has a test section 7.33m long and with a square cross section 1.83m on edge. Upstream of the test section is a settling chamber, containing 7 anti-turbulence screens, and a 9:1 contraction. Downstream is a diffuser with a 3° half angle. Vortex generators are used to prevent separation in the diffuser. Flow speed in the test section can be continuously varied from 0 to 56 m/s.

The quality of the flow through the empty test section has been the subject of a number of previous investigations. For a speed of 47 m/s Lee (1979) showed the flow velocity to be uniform to within 0.5% across the section. For speeds between 6 and 30 m/s Reynolds (1979) observed a slight favorable pressure gradient along the test section $\partial C_p/\partial x = -0.003/m$ as a consequence of the growth of the side-wall boundary layers. This acceleration causes some convergence of the streamlines. Choi and Simpson (1987) showed the convergence, illustrated in figure 2.2, to be centered roughly in the middle of the test section at speeds of 15 and 37.5 m/s. Flow angles produced by the convergence are small near the middle of the test section but increase to about 2° near the walls. Choi and Simpson (1987) also observed free stream turbulence levels of 0.04% at 15 m/s and 0.07% at 37.5 m/s increasing slightly as the walls are approached. Reynolds (1979) reported somewhat lower values, from .02% at 9m/s to 0.045% at 30 m/s.

During operation of the wind tunnel the free stream dynamic pressure and flow temperature are monitored continuously. The former is measured using a pitot-static probe located at the upstream end of the test section (figure 2.3) connected to a Barocell electronic manometer. The latter is sensed using an Omega thermocouple located within the test section boundary layer, there being no significant temperature gradient across the boundary layer.

2.2 Wing

Mason and Marchman's (1972) wing model was used. This model has a rectangular planform, a NACA 0012 section and a blunt wing tip. Its chord and span are .203m and 1.219m respectively. It is made from solid brass.

The wing was mounted vertically at the mid span of the test section (figure 2.3). In this position the small variations in flow direction across the test section shown in figure 2.2 were expected to have minimal influence on the local angle of attack of the wing. The wing root was bolted to a turntable assembly flushed into the upper wall of the wind tunnel (figure 2.4). The turntable allowed the wing to be rotated to any angle of attack about its quarter chord location. At zero angle of attack the wing leading edge was 0.33m downstream of the test-section entrance.

To eliminate flow-induced vibration the wing was braced at its mid span with two pairs of 2.4mm-diameter steel cables stretched horizontally between the wing and the two side walls of the wind tunnel (figures 2.3 and 2.4). These cables were covered with a 4.8-mm thick shroud of airfoil cross section to minimize and stabilize their wakes. The cables were attached to the walls on the outside of the test section using a turnbuckle arrangement that allowed them to be placed under tension. The cables were attached to the wing via a pin centered on its axis of rotation (i.e. the quarter-chord location). The cables thus did not prevent the wing from being rotated to angle of attack.

The boundary layer on the wing surface was tripped using distributed roughness to avoid any unsteadiness or non-uniformity resulting from natural transition and to better simulate higher Reynolds number flows. The roughness consisted of a band of 0.5mm diameter glass beads were glued with an average density of 200 beads per cm^2 along a spanwise strip from the 20% to 40% chord locations.

The orientation of the wing corresponding to zero angle of attack was found using a removable aluminum tip containing 48 static pressure taps (figure 2.5). Other angles of attack were measured relative to this location. The tip had a rectangular planform and had the same NACA 0012 section and chordlength as the main wing. The taps were arranged on both sides of the tip in 3 rows located 19mm, 44mm and 70mm from its outer edge. Zero

angle of attack was found, to an accuracy of about $\pm 0.1°$, by equalizing the pressures on the two sides. Pressures were measured using SETRA model 239 pressure transducer interfaced to an IBM/AT computer through a data translation DT2801-A A/D converter. The transducer was connected to the taps through a Scanivalve system and lengths of 2mm diameter Tygon tubing.

2.3 Traverse Gear

A traverse gear (figures 2.3 and 2.6) was used to position probes in the test section. Three Compumotor stepper motors were used to control vertical and horizontal motions under commands from a Compumotor IF1 controller interfaced to an IBM AT compatible computer. Thus the traverse gear could be automatically controlled from data acquisition programs. The accuracy of the horizontal and the vertical traverse positions was estimated to be ± 0.05mm.

2.4 Hot wire Anemometry

Velocity measurements were made using hot wire anemometry. Single, cross, triple, and quad hot wire probes were used in conjunction with a Dantec anemometer system. This consisted of four Dantec 56C17 bridges and four 56C01 constant temperature anemometer units mounted in a Dantec 56B12 main frame. The output voltages from the anemometer bridges were recorded by the IBM AT compatible computer using an Analogic 12 bit HSDAS-12 A/D converter having an input voltage range of 0-2.5 volts and 12 bit resolution. The HSDAS-12 can sample up to four of its sixteen channels simultaneously at a maximum rate of 100 kHz per channel. In addition to those channels used for hot wire signals, two other channels of HSDAS-12 were used to measure flow temperature and free-stream pitot-static pressure. Raw hot wire signals were linearized and processed in the computer using an 18-8 laboratories PL1250 array processor. Optical disc cartridges were used to store the raw and processed data.

All probes were operated at an overheat of 1.7. They were calibrated frequently by placing them in the free stream and comparing their output voltages (E) with cooling velocities (U_{eff}) determined from the velocity sensed by the pitot-static probe located at the test-section entrance. King's law

$$E^2 = A + BU_{eff}^n \tag{1}$$

was used. The exponent n was taken as 0.45 the constants A and B were determined via linear regression from 10 to 20 calibration points. Root mean square errors between the points and the King's-law fit were typically less than 0.5% in velocity. Flow temperature in the stability wind tunnel was found to drift by typically 1 to 2°C per hour. Hot wire signals were corrected for temperature changes using the method of Bearman (1970). For all probes the anemometer bridges were balanced to give a frequency response of better that 20kHz.

A probe holder, shown in figure 2.7a was used to attach hot-wire probes to the traverse gear. The holder was designed to position the measurement point of the probes 0.84m upstream of the leading edge of the traverse. It consisted of a 23.6mm diameter steel tube aligned with the free stream and two 6.2mm diameter rods normal to it. The purpose of the rods was to offset the axis of the probe from that of the tube by 114mm. Thus the tube did not have to be placed in or near the vortex core for measurements to be made there. For all measurements the axis of the probe and tube were held parallel to the test section axis and thus free-stream flow direction. Probes were not pitched or yawed to face the local mean flow direction since, as demonstrated by Mason and Marchman (1972), this can seriously disrupt a trailing vortex flow.

2.4.1 Single Hot Wire Probe

A standard single hot wire probe (TSI type 1210T1.5) was used to measure profiles of mean velocity and turbulence intensity as well as spectra of velocity fluctuations in the wing wake immediately downstream of the trailing edge. This probe has a tungsten wire sensor 4μm in diameter and 1.5mm in length. During these measurements the sensor was aligned parallel to the trailing edge, i.e. normal to the mean-velocity gradient. It was thus

sensitive primarily to the streamwise component of mean velocity and velocity fluctuations in that direction.

This probe was calibrated in the freestream with its sensor normal to the flow direction. For measurements of mean velocity and turbulence intensity the anemometer output was sampled at a rate of 2kHz. 30 records of 1024 points were collected over a total period of about 30 seconds. For spectral measurements, 50 records of 30,000 samples were taken at a rate of 30kHz over a total sampling time of about 1 minute.

2.4.2 Cross Hot Wire Probe

A cross-hot wire probe (Dantec 55P51) was used to measure profiles of mean velocities and Reynolds stresses, as well as auto and cross spectra of velocity components, in the vortex. The Dantec 55P51 X-wire probe consists of two gold plated tungsten wire sensors 1.25mm in length and 5μm in diameter, with a nominal spacing of 1mm between the sensors.

To obtain all mean velocities and Reynolds stresses components, it was necessary to rotate the probe about its axis in steps of 45°. These rotations were accomplished using computer controlled stepper motor located at the downstream end of the probe holder (figure 2.7b). Rotary motion was transferred to the probe through a shaft, gears and timing belt. The probe itself was mounted on teflon bearings and carefully adjusted to ensure that the axis of rotation passed through the center of the measurement volume. For the present measurements the X-array probe was rotated to roll angles of -45°, 0°, 45° and 90° within an accuracy of $\pm 0.5°$.

Relationships for the statistical velocity measurements made with the X wire probe may be deduced from its geometry shown in figure 2.8. Here the probe is shown at a roll angle ψ in a flow with velocity components U, V and W, where U is aligned with the probe axis. Consider one of the wires lying at an angle ϕ to the U direction. The effective velocity U_{eff} sensed by this wire is given by the equation

$$U_{eff}^2 = U_s^2 + k^2V_s^2 + h^2W_s^2 \tag{2}$$

(see Jorgensen, 1971) where U_s, V_s and W_s are velocity components fixed in the wire; V_s being measured along the wire, U_s normal to it and in the plane of the prongs and W_s normal to the plane of the prongs. 'k' and 'h' are empirical constants referred as the pitch and yaw factors respectively. Expressing these components in terms of U, V and W we obtain,

$$U_{eff}^2 = AU^2 + BV^2 + CW^2 + DUV + EUW + FVW \tag{3}$$

where

$$\begin{aligned} A &= \sin^2\phi + k^2\cos^2\phi \\ B &= \cos^2\psi\cos^2\phi + k^2\cos^2\psi\sin^2\phi + h^2\sin^2\psi \\ C &= \sin^2\psi\cos^2\phi + k^2\sin^2\psi\sin^2\phi + h^2\cos^2\psi \\ D &= 2(1-k^2)\cos\psi\cos\phi\sin\phi \\ E &= 2(1-k^2)\sin\psi\cos\phi\sin\phi \\ F &= 2\cos\psi\sin\psi(\cos^2\phi + k^2\sin^2\phi - h^2) \end{aligned} \tag{4}$$

Note that changing the coordinate directions of U, V and W alters the expressions for these coefficients but not the form of equation 3. The following thus applies regardless of coordinate system. Separating the velocity components into their mean and fluctuating parts, i.e. letting U = U + u, V = V + v and W = W + w, equation 3 may be written as,

$$U_{eff}^2 = AU^2\left[1+\frac{2u}{U}+\frac{u^2}{U^2}+\frac{B}{A}\left(\frac{V^2}{U^2}+\frac{2Vv}{U^2}+\frac{v^2}{U^2}\right)+\right.$$
$$\frac{C}{A}\left(\frac{W^2}{U^2}+\frac{2Ww}{U^2}+\frac{w^2}{U^2}\right)+\frac{D}{A}\left(\frac{V}{U}+\frac{v}{U}+\frac{Vu}{U^2}+\frac{uv}{U^2}\right)+ \quad (5)$$
$$\left.\frac{E}{A}\left(\frac{W}{U}+\frac{w}{U}+\frac{Wu}{U^2}+\frac{uw}{U^2}\right)+\frac{F}{A}\left(\frac{VW}{U^2}+\frac{Vw}{U^2}+\frac{Wv}{U^2}+\frac{vw}{U^2}\right)\right]$$

Assuming u, v, w, V and W are small compared to U gives

$$U_{eff} = \sqrt{A}U\sqrt{1+\frac{2u}{U}+\frac{D}{A}\left(\frac{V}{U}+\frac{v}{U}\right)+\frac{E}{A}\left(\frac{W}{U}+\frac{w}{U}\right)} \quad (6)$$

Separate expressions for the mean and fluctuating cooling velocities are obtained from equation (6) by expanding the square root. Neglecting higher order terms this gives

$$U_{eff} = \sqrt{A}U + \frac{D}{2\sqrt{A}}V + \frac{E}{2\sqrt{A}}W \quad (7)$$

$$u_{eff} = \sqrt{A}u + \frac{D}{2\sqrt{A}}v + \frac{E}{2\sqrt{A}}w \quad (8)$$

Using subscripts a and b to distinguish the two sensors of the X-array hot wire probe, equation (7) and (8) can be written as

$$U_{eff_a} = \sqrt{A_a}U + \frac{D_a}{2\sqrt{A_a}}V + \frac{E_a}{2\sqrt{A_a}}W \tag{9}$$

$$U_{eff_b} = \sqrt{A_b}U + \frac{D_b}{2\sqrt{A_b}}V + \frac{E_b}{2\sqrt{A_b}}W \tag{10}$$

$$\overline{u_{eff_a}^2} = A_a\overline{u^2} + \frac{D_a^2}{4A_a}\overline{v^2} + \frac{E_a^2}{4A_a}\overline{w^2} + D_a\overline{uv} + E_a\overline{uw} + \frac{D_aE_a}{2A_a}\overline{vw} \tag{11}$$

$$\overline{u_{eff_b}^2} = A_b\overline{u^2} + \frac{D_b^2}{4A_b}\overline{v^2} + \frac{E_b^2}{4A_b}\overline{w^2} + D_b\overline{uv} + E_b\overline{uw} + \frac{D_bE_b}{2A_b}\overline{vw} \tag{12}$$

$$\overline{u_{eff_a}u_{eff_b}} = \sqrt{A_aA_b}\overline{u^2} + \frac{D_aD_b}{4\sqrt{A_aA_b}}\overline{v^2} + \frac{E_aE_b}{4\sqrt{A_aA_b}}\overline{w^2} + \left(\frac{D_a}{2}\sqrt{\frac{A_a}{A_b}} + \frac{D_b}{2}\sqrt{\frac{A_b}{A_a}}\right)\overline{uv} + \left(\frac{E_b}{2}\sqrt{\frac{A_a}{A_b}} + \frac{E_a}{2}\sqrt{\frac{A_b}{A_a}}\right)\overline{uw} + \left(\frac{D_aE_b}{4\sqrt{A_aA_b}} + \frac{D_bE_a}{4\sqrt{A_aA_b}}\right)\overline{vw} \tag{13}$$

In principle measuring $\overline{U_{eff_a}}$, $\overline{U_{eff_b}}$, $\overline{u^2_{eff_a}}$, $\overline{u^2_{eff_b}}$, $\overline{u_{eff_a}u_{eff_b}}$ at more than three angles enables equation 9 through 13 to be solved (with some redundancy), for all the mean velocity components and all Reynolds stresses.

In applying this procedure the choice of the coordinate system from which to measure U, V and W can affect accuracy since in some systems the mean velocities V and W will not be negligibly small. To avoid problems with large V or W the following procedure was applied to reduce the present measurements;

(1) Reduction using a coordinate system aligned with the test section to determine approximately the mean flow direction.

(2) Re-reduction using a coordinate system aligned in that direction.

(3) Rotation of the mean-velocity vector and Reynolds stress tensor back into test-section coordinates.

Iteration of this procedure was found to be unnecessary.

Relationships for spectral measurements made with the cross-wire probe may be obtained through a similar analysis beginning with equation 8 expressed for the two wires. Taking the Fourier transform of these equations, combining those transforms and averaging leads to the following expressions,

$$G_{Ueff_aUeff_a} = A_a G_{UU} + \frac{D_a^2}{4A_a} G_{VV} + \frac{E_a^2}{4A_a} G_{WW} + \frac{D_a}{2} Re\{C_{UV}\} + \frac{E_a}{2} Re\{C_{UW}\} + \frac{D_a E_a}{4} A_a Re\{C_{VW}\} \quad (14)$$

$$G_{Ueff_bUeff_b} = A_b G_{UU} + \frac{D_b^2}{4A_b} G_{VV} + \frac{E_b^2}{4A_b} G_{WW} + \frac{D_b}{2} Re\{C_{UV}\} + \frac{E_b}{2} Re\{C_{UW}\} + \frac{D_b E_b}{4} A_b Re\{C_{VW}\} \quad (15)$$

$$C_{Ueff_aUeff_b} = \sqrt{A_a A_b} G_{UU} + \frac{D_a D_b}{4\sqrt{A_a A_b}} G_{VV} + \frac{E_a E_b}{4\sqrt{A_a A_b}} G_{WW} + \frac{D_b}{2}\sqrt{\frac{A_a}{A_b}} C_{UV} + \frac{D_a}{2}\sqrt{\frac{A_b}{A_a}} C_{VU} + \frac{E_b}{2}\sqrt{\frac{A_a}{A_b}} C_{UW} + \frac{E_a}{2}\sqrt{\frac{A_b}{A_a}} C_{WU} + \frac{D_a E_b}{2\sqrt{A_a A_b}} Re\{C_{VW}\} \quad (16)$$

where, for example, G_{UU} and C_{UV} refer to the average auto spectrum of U and averaged cross spectrum of U and V respectively and, $Re\{\}$ identifies the real part. Note that these equations contain no term for the imaginary part of the VW cross spectrum, which consequently cannot be determined. All other spectra may be obtained by solving equations (14) through (16) after making measurements at more than 3 angles of roll.

Unlike the statistical measurements spectra were reduced only once, into coordinates aligned with the test section. This was because, without the imaginary part of the VW cross spectrum, a coordinate system rotation of the spectra could not be performed. It is possible that this introduced some error into spectral measurements made in regions where the rotational velocity of the vortex was large, though none was observed.

The pitch factors k, yaw factors h and wire angles, required by the above equations, were determined experimentally for each sensor by pitching and yawing the probe in a uniform flow of known velocity and direction, produced by a small calibration wind tunnel.

Within their uncertainty, values of k and h were found to be the same for all sensors used, having values of 0.18 and 1.05 respectively in a uniform flow of 20m/s.

The sensors of the X-array probe were calibrated for velocity in the wind tunnel freestream with the probe axis parallel to the flow direction. The effective velocities experienced by the sensors during calibration were deduced from the free stream velocity using the measured wire angles and pitch factors.

For statistical measurements between 30,000 and 90,000 velocity samples (depending on local turbulence level) were taken at each probe position and orientation over total sampling time of about 50 seconds. For spectral measurements, 150 blocks of 10,000 samples were taken at sampling rate of between 20 and 40 kHz depending on free-stream speed.

2.4.3 Triple Hot-Wire Probe

A triple hot-wire probe (Dantec 55P91) was also used to make statistical and spectral velocity measurements in the vortex. This probe has three gold plated tungsten wire sensors of 1.25mm length and 5μm diameter. The geometry of the probe is shown in figure 2.9. The sensors are arranged in an orthogonal system and lie within a sphere of 3mm diameter. Each sensor makes the same angle with the probe axis.

One of the advantages of the triple wire is that the three cooling velocities it experiences can be used instantaneously to determine the three velocity components. Following Jorgensen (1971), the relationship between the cooling velocities U_{eff1}, U_{eff2}, U_{eff3} and the velocity components U_s, V_s and W_s in a coordinate system aligned with the sensors (see figure 2.9) is

$$\begin{pmatrix} U_{eff_1}^2 \\ U_{eff_2}^2 \\ U_{eff_3}^2 \end{pmatrix} = \begin{pmatrix} k_1^2 & 1 & h_1^2 \\ h_2^2 & k_2^2 & 1 \\ 1 & k_3^2 & h_3^2 \end{pmatrix} \begin{pmatrix} U_s^2 \\ V_s^2 \\ W_s^2 \end{pmatrix} \quad (17)$$

Velocity components in any other coordinate system may be obtained simply by rotation, e.g. components in a system aligned with the triple wire probe stem are given by

$$\begin{pmatrix} U \\ V \\ W \end{pmatrix} = \begin{pmatrix} \frac{1}{\sqrt{3}} & \frac{1}{\sqrt{3}} & \frac{1}{\sqrt{3}} \\ -\frac{1}{\sqrt{2}} & \frac{1}{\sqrt{2}} & 0 \\ \frac{1}{\sqrt{6}} & \frac{1}{\sqrt{6}} & -\sqrt{\frac{2}{3}} \end{pmatrix} \begin{pmatrix} U_s \\ V_s \\ W_s \end{pmatrix} \quad (18)$$

Once the instantaneous velocity components have been found in this way, determining the mean velocities, Reynolds stresses and spectra is simply a matter of applying their definitions.

The pitch and yaw factors k and h required by equation (17) were estimated separately for each sensor by making measurements of its output over a range of yaw and pitch angles in a uniform flow of known velocity generated by the calibration tunnel. Within their uncertainty, values of pitch and yaw factor were found to be same for all sensors, having values of 0.15 and 1.03 respectively in a uniform flow of 20m/s.

The sensors of the triple-wire probe were calibrated for velocity in the wind tunnel freestream with the probe axis parallel to the flow direction. The effective velocities experienced by the sensors during calibration were deduced from the free stream velocity using the measured wire angles and pitch factors.

For statistical velocity measurements between 30,000 and 100,000 velocity samples (depending on local turbulence level) were taken at each probe position over a total sampling time of about 50 seconds. For most spectral measurements, 150 blocks of 10,000 samples were taken at a rate of 20-40kHz (depending on freestream velocity). For some low-frequency-range spectra, 80 blocks of 10,000 samples were also taken at a sampling rate of 1 kHz.

2.4.4 Quad hot-wire probe

At one condition measurements in the vortex were also made using the 4-sensor hot-wire probe shown in figure 2.10. This probe, manufactured by Auspex Corporation (Model AVOP-4-100), consists of two orthogonal arrays of X wires within a sensing volume approximately 1mm in diameter. Like the triple-wire probe it is capable of instantaneous measurements of all three velocity components. The procedure used to obtain those components from the quad-wire outputs is only briefly summarized here, for more details see Zsoldos (1992).

The outputs of the quad-wire sensors may be related to the velocity components through equations similar to (7) and (8). However, these equations are less accurate than for a simple X-wire probe because of greater variations in wire angles and greater prong interference effects. Accuracy may be restored by calibration. The quad-wire probe is placed in a uniform flow of known velocity and direction at a series of known pitch and yaw angles. At each angle the velocity components given by the equations are compared with their actual values and a table of errors is constructed. This table is then used to correct instantaneous velocity measurements made in the vortex.

The sensors of the quad-wire probe were calibrated for velocity in the wind tunnel freestream with the probe axis parallel to the flow direction, the relationship between the effective velocities experienced by the sensors and the freestream velocity being taken into

account. Both spectral and statistical velocity measurements were made by sampling the quad-wire outputs at a rate of 30kHz. 150 blocks of 6000 velocity samples were taken over a total sampling time of about 3 minutes.

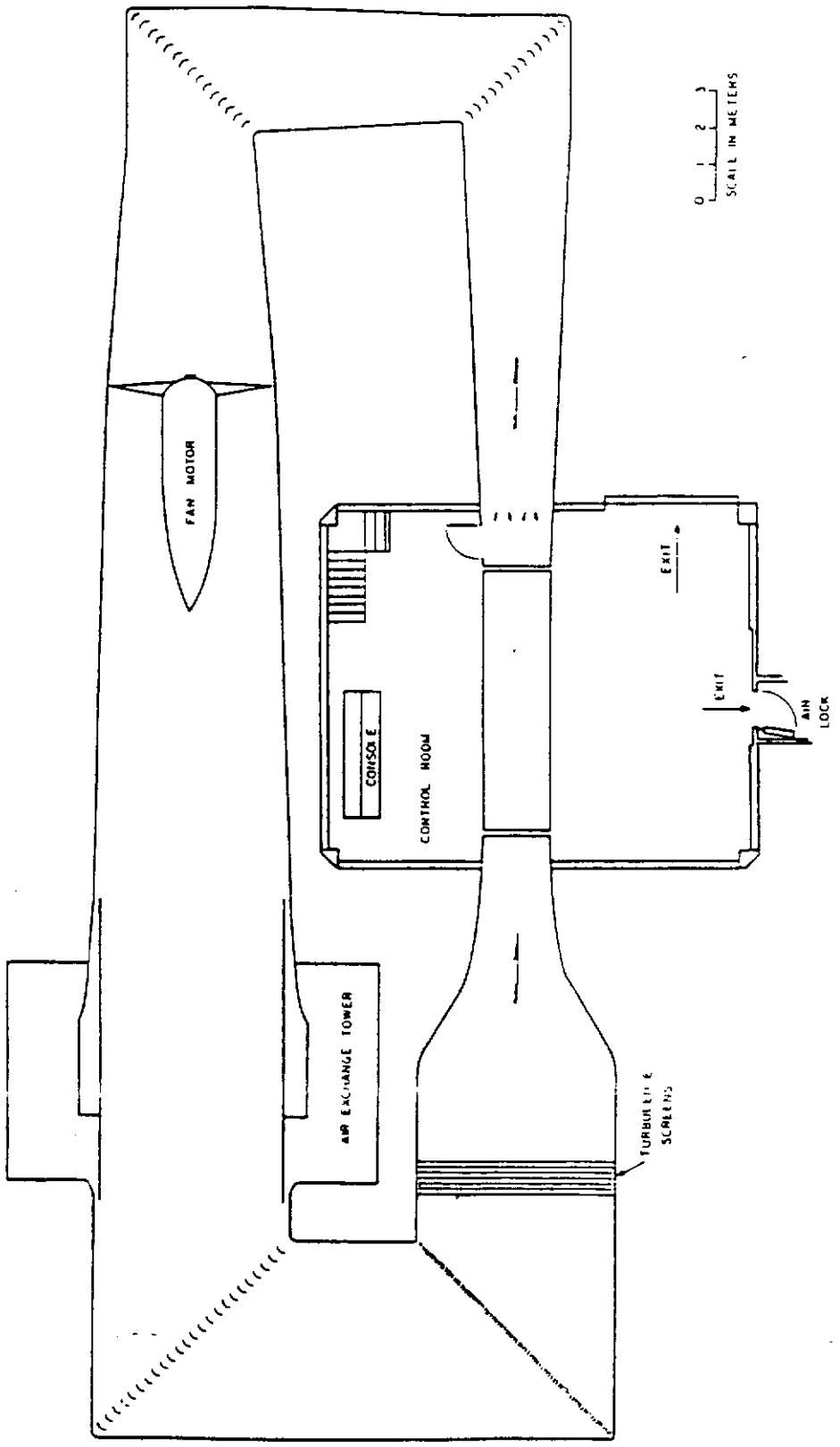

Figure 2-1. Schematic of the stability wind tunnel.

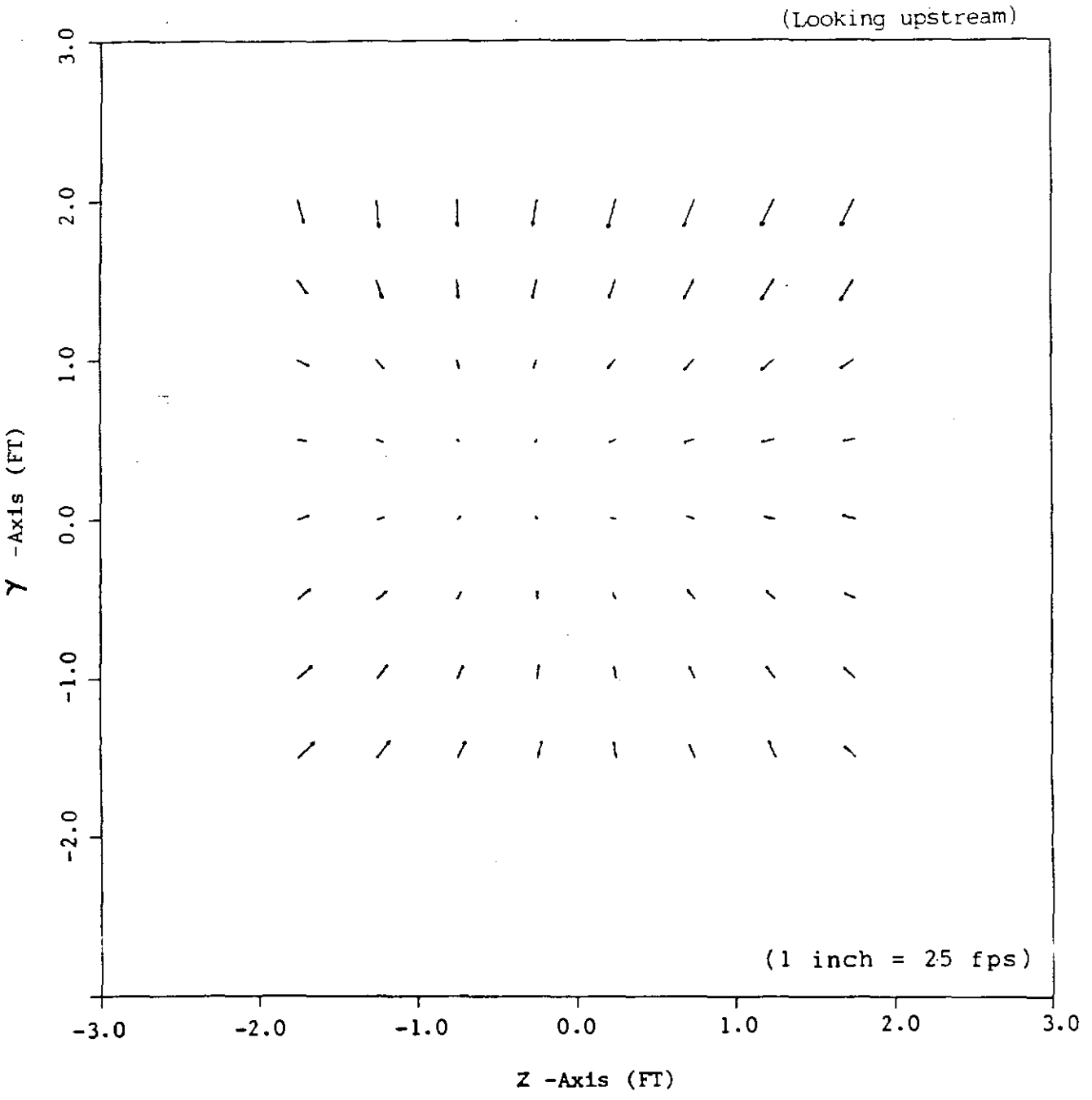

Figure 2-2. Convergence of flow through the empty test section at 37.5 m/s (125fps). From Choi and Simpson (1987).

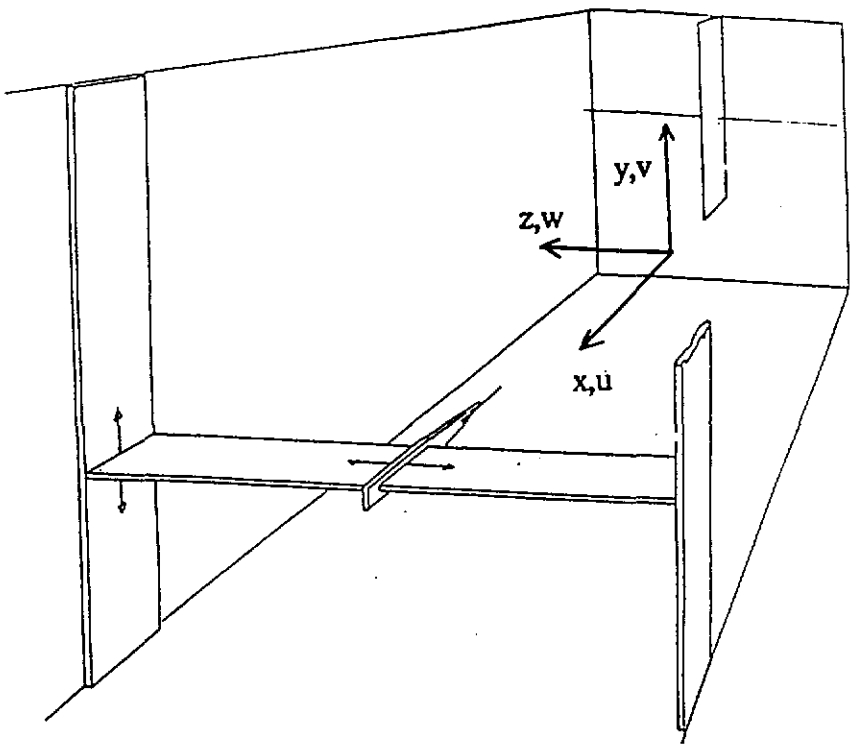

Figure 2-3. Schematic of the Stability Wind Tunnel test section showing the location of the wing, its bracing and the traverse gear. Also note the coordinate system.

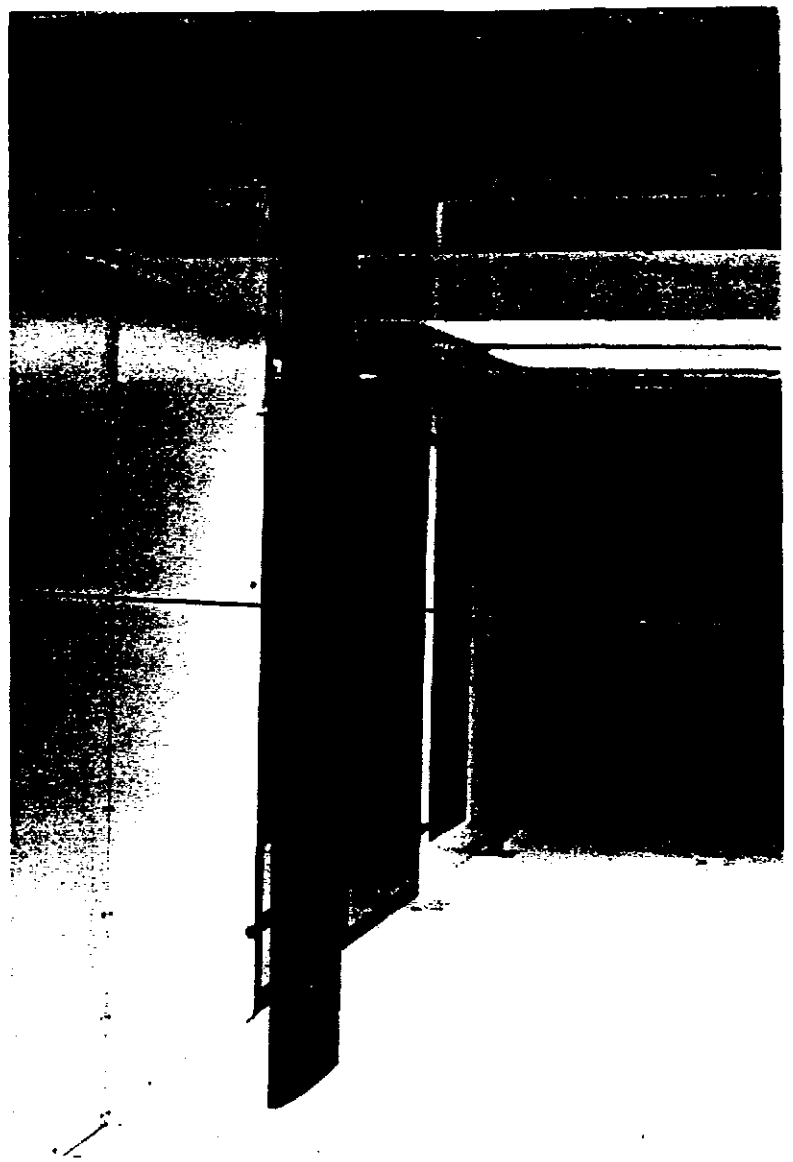

Figure 2-4. Photograph of the wing mounted in the test section, view from upstream. Note the turntable to which the wing is mounted and the wire braces.

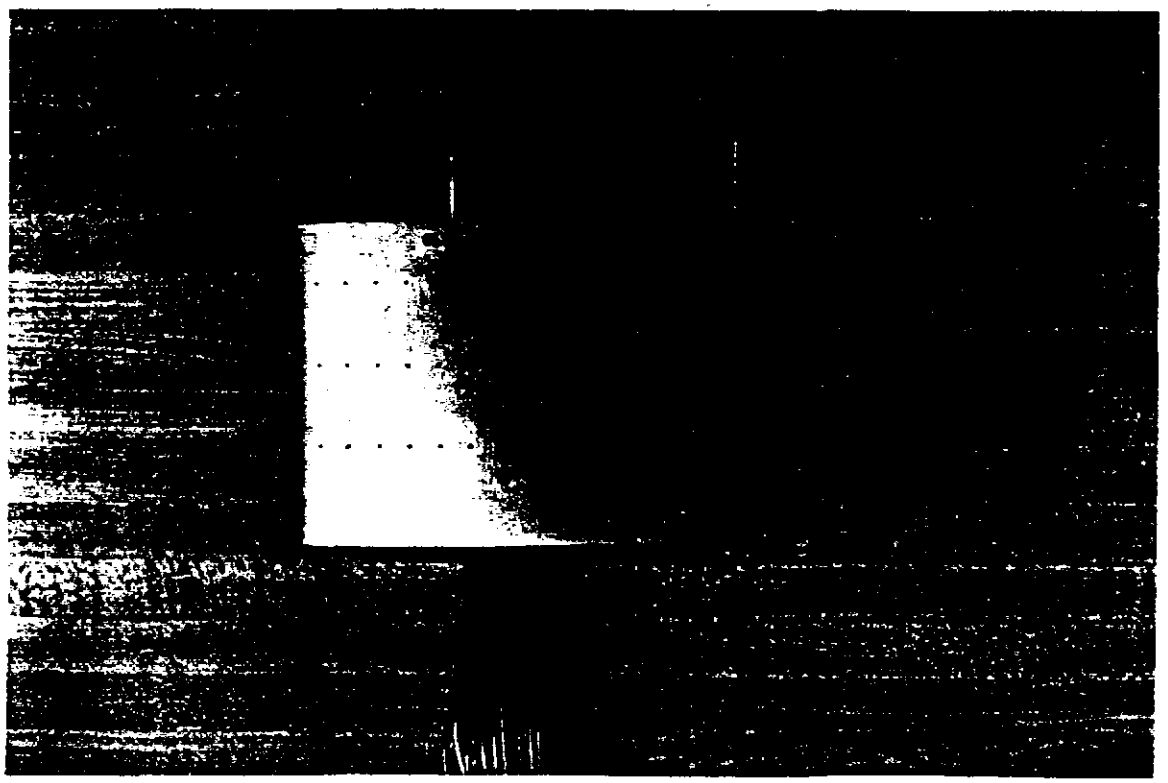

Figure 2-5. Photograph of the removable wing tip used to zero angle of attack.

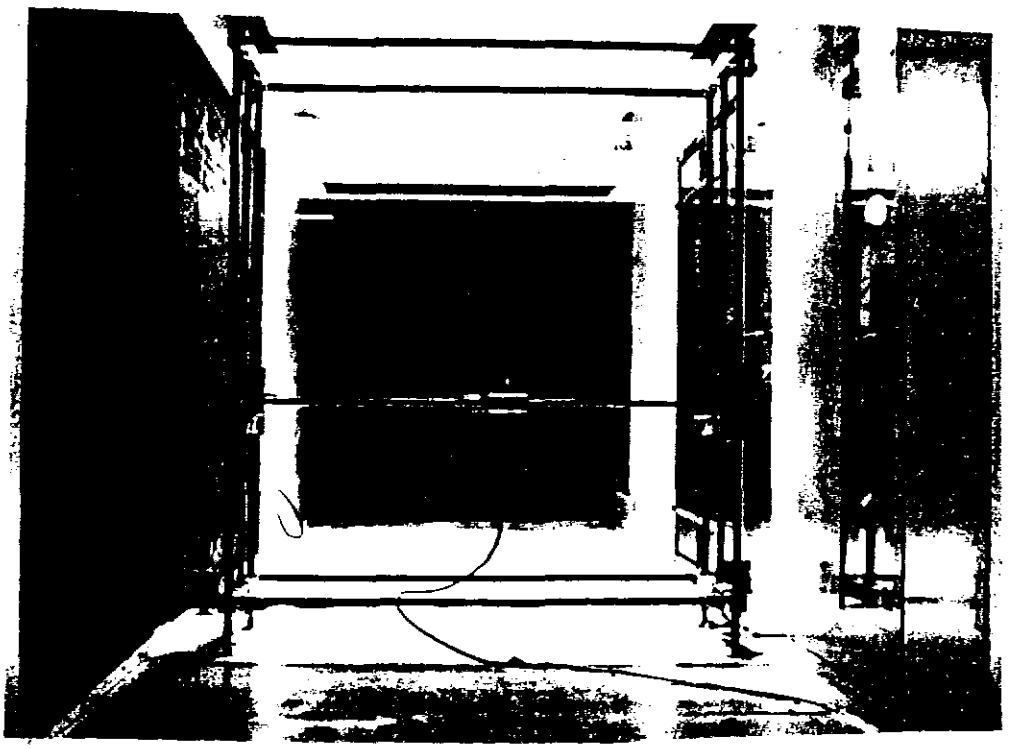

Figure 2-6. View of the traverse gear from downstream.

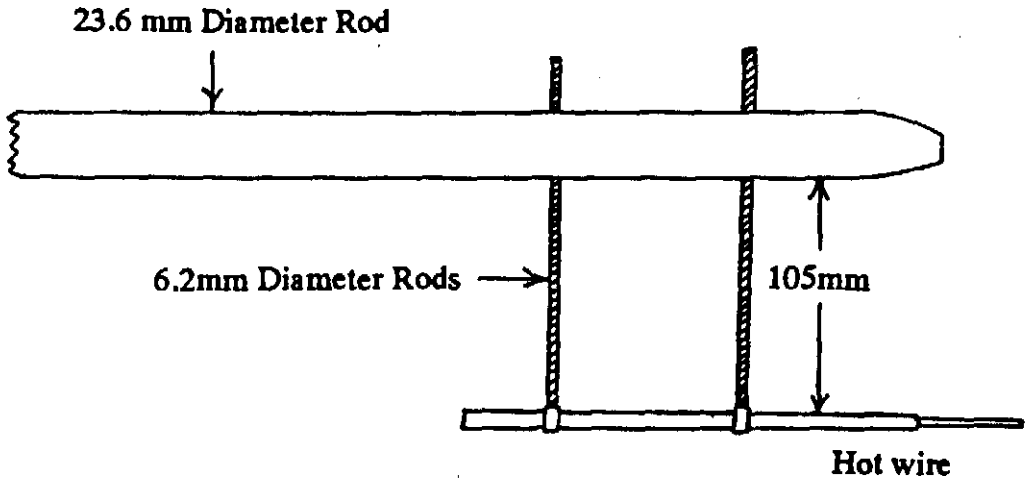

Figure 2-7a. Schematic of the hot-wire probe holder.

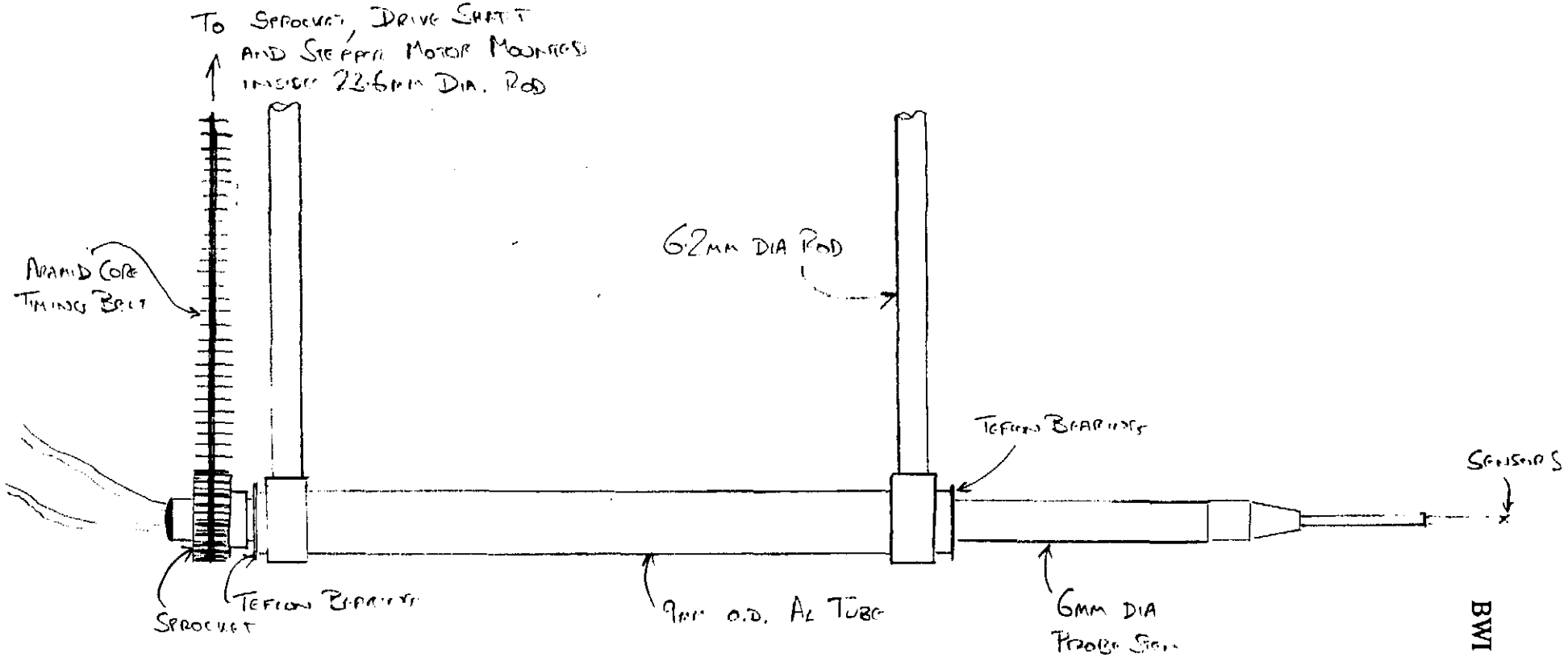

Figure 2-7b. Detail showing the assembly used to rotate the cross-wire probe.

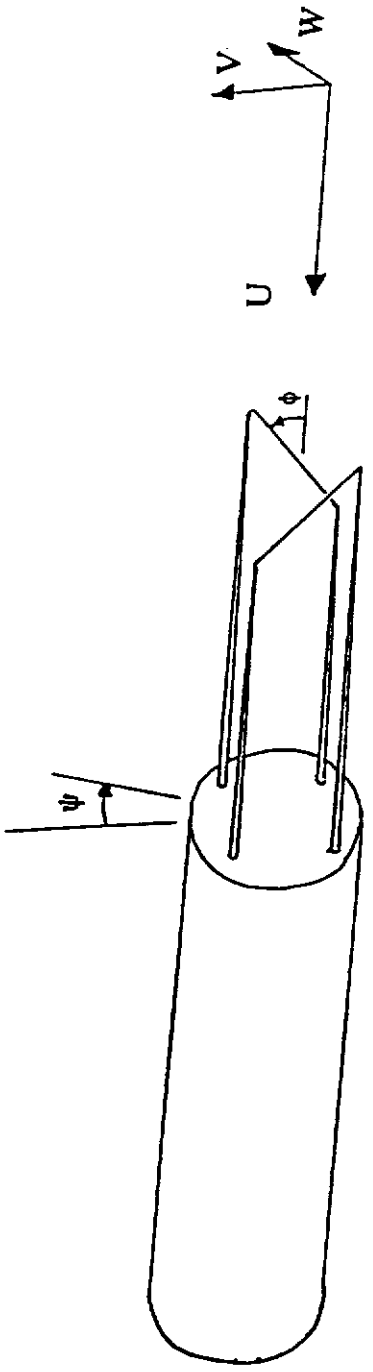

Figure 2-8. Geometry of the Dantec 55P51 X-array hot-wire probe.

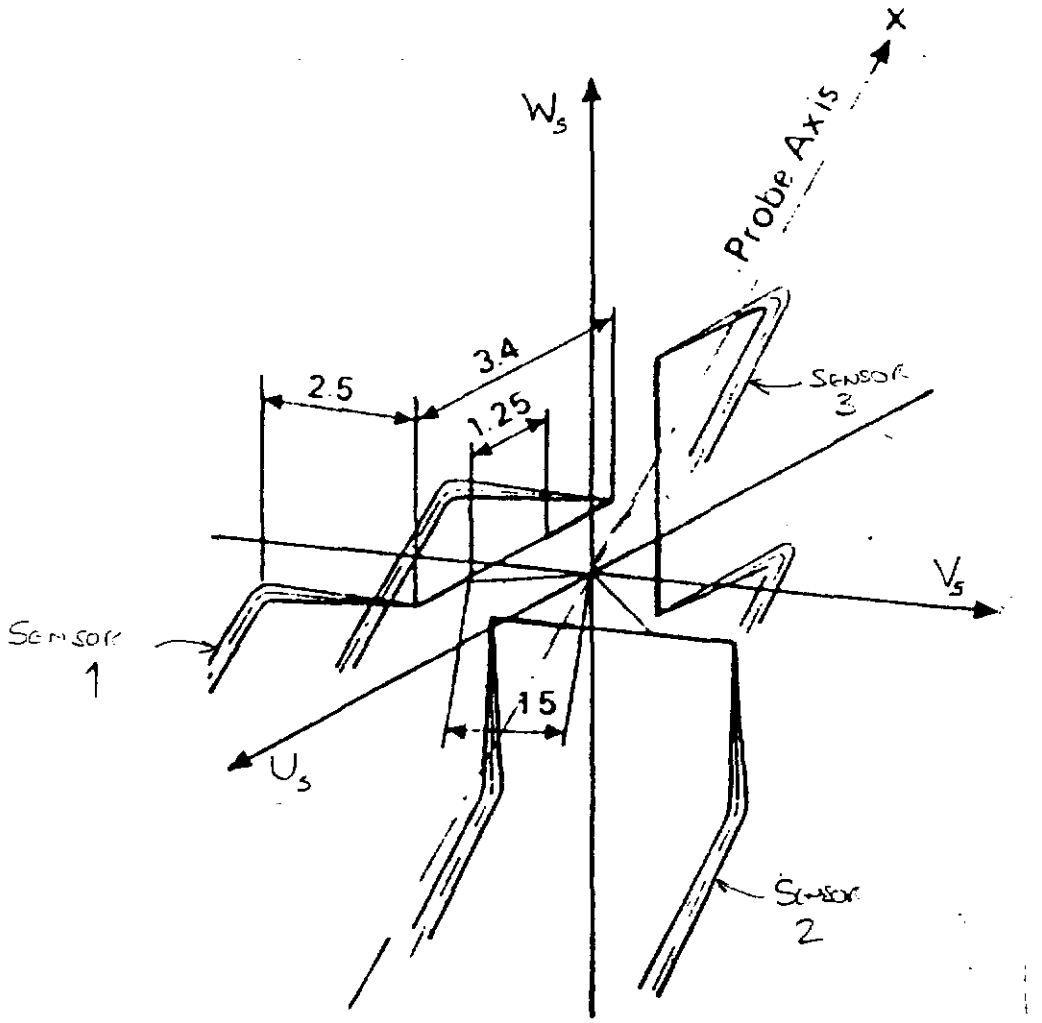

Figure 2-9. Geometry of the Dantec 55P91 triple hot-wire probe.

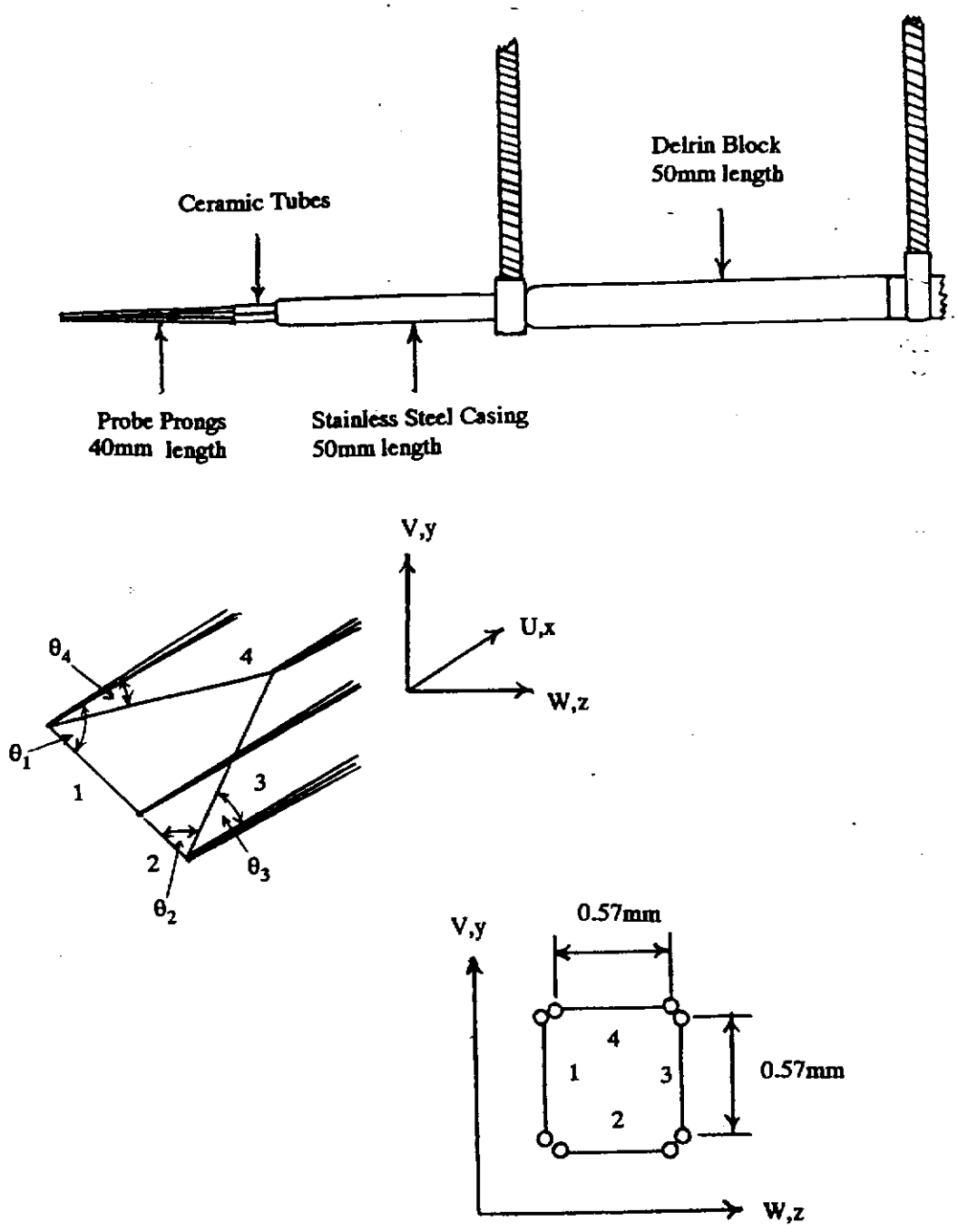

Figure 2-10. Geometry of the Auspex Corporation AVOP-4-100 quad hot-wire probe.

3. RESULTS AND DISCUSSION

3.1 Coordinate system, Measurement conditions

Most measurements will be presented using the coordinate system (x,y,z) and corresponding velocity components (U,V,W) shown in figure 2.3. x is measured along the axis of the test section downstream from the wing leading edge at zero angle of attack. y is measured parallel to the wing span and z completes a right-handed system. Most velocity measurements will be normalized on U_{ref} the local free-stream velocity, most distances on the wing chord 'c' equal to .203m.

The conditions and positions at which hot-wire measurements were made are listed in tables 3.1 and 3.2 in terms of wing angle of attack α (measured positive rotating from the x to the z axis) and chord Reynolds number $Re_c = U_{ref}c/\nu$. Conditions were selected with the following intentions:-

(i) To examine the flow immediately downstream of the wing trailing edge in the two-dimensional region away from the tip for α = 0 to 7.5°, Re_c = 130000 to 530000. Also, to examine the effects of removing the trip on the flow here. These were accomplished through single hot-wire measurements made in profiles parallel to the z axis.

(ii) To examine the far wake of the wing (at x/c = 30) for zero angle of attack and Re_c = 400000. This was accomplished through triple hot-wire measurements made in z profiles at a number of y locations.

(iii) To examine the development of the vortex structure between x/c = 20 to 30 for α = 5° and Re_c = 400000.

(iv) To examine changes in the vortex structure with changes in Reynolds number from 130000 to 530000 at x/c = 30 for α = 5°.

(v) To examine changes in the vortex structure with changes in angle of attack from 2.5° to 7.5° at x/c = 30 for α = 5° and Re_c = 400000.

(vi) To examine changes in the vortex structure brought about by removing the wing trip at x/c = 30 for α = 5° and Re_c = 530000.

Items (iii) through (vi) were accomplished primarily through cross and triple hot-wire measurements made in z profiles through the vortex center. Some profiles were measured using both techniques. The quad hot-wire probe was used to measure only one z profile through the vortex center at x/c = 30 for α = 5° and Re_c = 260000. Note that a y profile was also measured with the triple wire at x/c = 30 for α = 5° and Re_c = 400000.

A full set of data, representing all conditions and locations is available on computer disk.

3.2 The near-wake of the wing

The single hot wire was used to make velocity measurements immediately (1mm) downstream of the wing trailing edge. These measurements, which were expected to reveal the structure of the boundary layers leaving the wing were made at a range of Reynolds numbers and angles of attack, table 3.1 contains a complete list. At each condition a profile was measured across the wing wake at y/c=1.2 (measured from the tip) where the flow was expected to be fairly two-dimensional. At zero angle of attack for a Reynolds number of 400000, profiles were also measured at y/c=2.4 and 3.6.

The axial mean velocity U/U_e and turbulence normal stress $\overline{u^2}/U_e^2$ measurements made at zero angle of attack, Re_c=400000 are plotted vs. $(z-z_o)/c$ in figures 3.1a and b. Here z_o is the position of the wake center, defined as the point of minimum U, and U_e is the edge velocity of the wake measured at the point where $\sqrt{\overline{u^2}}/U = 1\%$. (Note that U_e could not be defined using only the mean velocity profiles because of inviscid velocity gradients in the vicinity of the trailing edge.) Uncertainties in U/U_e and $\overline{u^2}/U_e^2$ are, respectively, 1% and 5%. Power spectra of U, measured at representative z locations at y/c=1.2 are plotted in figure 3.5a as $G_{uu}U_e/\delta\overline{u^2}$ against frequency normalized as $f\delta/U_e$. They thus all have an area of unity.

3.3 The far wake of the wing at zero angle of attack

The triple hot wire was used to make velocity measurements in the wake of the wing at zero angle of attack. A series of profiles at different y locations were measured across the wake 30 chordlengths downstream of the wing at a Reynolds number of 400000. Mean-velocity and turbulence stress profiles are plotted in figures 3.6a-i. Velocity power spectra are shown in figures 3.7a-c. Uncertainty estimates for these measurements are presented in the appendix. The origin of the y and z coordinates used in these figures is nominally the intersection of the quarter chord line and the wing tip. Note, however, that due to the long streamwise distance between the wing and measurement locations there is an uncertainty in the position of this origin of about $\pm 0.05c$ in both directions.

Away from $y=0$ we would expect these data to reveal a flow structure much like that observed in two-dimensional wakes by Wygnanski et al. (1986) and others. According to these authors a fully developed two-dimensional wake can be described by a single velocity scale u_o, the maximum axial velocity deficit, and a single length scale L_o, the distance between the center of the wake and the point where the axial velocity deficit is half its maximum value. These scales are found to vary with streamwise distance x as,

$$\left(\frac{U_{ref}}{u_o}\right)^2 \sim \left(\frac{x-x_o}{\theta}\right), \quad \left(\frac{L_o}{\theta}\right)^2 \sim \left(\frac{x-x_o}{\theta}\right) \tag{1}$$

where x_o is the origin of the wake, located close to the trailing edge of the wing, and θ is the momentum thickness of the wake (a constant). For example, we would expect the turbulent stress distributions measured in similarly produced wakes to be identical when plotted as

$$\overline{u^2}/u_o^2 \quad vs. \quad (z-z_o)/L_o \tag{2}$$

where $\overline{u^2}$ may be substituted by any turbulent stress and z_o locates the center of the wake.

The mean axial velocity profiles measured in the present flow (figure 3.6a) are fairly similar above y/c=0 and have a form much like profiles presented by Wygnanski et al. for an airfoil wake. They show the wake to be centered near z/c=-.03 (zero to within the uncertainty), to have a maximum velocity deficit of about 3% U_e and a width L_o of about 0.15c. At y/c=0, where the wake closes, the profile has a much smaller deficit and appears in a slightly different position, centered near z/c=.05. The other mean velocity components, V and W, (figures 3.6b and c) remain negligibly small at all locations.

Above y/c=0.313, the turbulence stress profiles are likewise all similar in shape. Those of $\overline{u^2}$ and $\overline{v^2}$ (figures 3.6d and e) have two maxima separated by a distance approximately equal to $1.5L_o$, much like the $\overline{u^2}$ profiles presented by Wygnanski et al. However, the peak value of $\overline{u^2}/u_o^2$ is about 0.11, significantly less than their value of about 0.17. This difference may simply reflect the fact, demonstrated by Wygnanski et al., that the structure of even a fully developed wake is not independent of its initial conditions. The profiles of $\overline{w^2}$ (figure 3.6f) have a single peak. Those of $\overline{uw}$ (figure 3.6i) show the same antisymmetric distribution observed by Wygnanski et al., but again the peak value of $\overline{uw}/u_o^2$ is low, about 0.039 compared to Wygnanski et al.'s 0.045. Above y/c=0.313, $\overline{uv}$ and $\overline{vw}$ (figures 3.6g and h) are both negligible.

As y/c=0 is approached the stress profiles reveal the closing of the wake. The peak normal stresses and $\overline{uw}$ shear stress all drop. Figure 3.6g shows significant levels of $\overline{uv}$ at y/c=0.313. These would be expected since the closing of the wake is associated with a y gradient of mean velocity. One interesting feature of the profiles at y/c=0 is that they all show the bottom edge of the wake to be off center, by about .08c (16mm) from the rest. This is probably a result of the wing not being exactly at zero angle of attack. We may estimate its angle by using the small values of V and W in figures 3.6(b and c) to place an upper limit on the circulation. This calculation gives an angle of .025°, well within the accuracy with which the wing could be positioned.

The power spectra of velocity components shown in figure 3.7 were measured at representative z locations, within the turbulent region, during the profile at y/c=0.313. They have been plotted in terms of

$$\frac{G_{uu}U_e}{\overline{u^2}c} \quad vs. \quad \frac{fc}{U_e} \tag{3}$$

and likewise for v and w. The area under each spectrum has thus been normalized to unity. Note that the spectra have been contaminated with electrical noise at frequencies above $fc/U_e = 20$. Also note that since these measurements were made at one streamwise location only, normalizing the spectra on L_o instead of c would not change the form of these results. Perhaps the most striking feature of these results is the near perfect collapse of the spectra. This collapse is not an inevitable result of the wake becoming fully developed, since in that case the shape of the spectrum can still be a function of $(z-z_o)/L_o$. Indeed, Wygnanski et al. show a considerable difference in the shape of U power spectra measured at $(z-z_o)/L_o$ = 0 and 3, the latter location being outside the region of turbulent flow. This leaves only one possibility, assuming the present results and Wygnanski et al.'s are consistent, i.e. that within the turbulent region the spectral shape is almost independent of position.

The curves to which the spectra collapse are worth noting. The U spectra have a very clear inertial subrange, beginning at a frequency fc/U_e of about 2. The inertial subrange is less clear in the V and W components. These spectra show a fairly distinct peak at a frequency fc/U_e of about 1.5. Assuming this to be the passage frequency of large structures in the wake, and assuming Taylor's hypothesis, this implies a streamwise length scale for large structures of 0.67c, approximately the width of the wake as seen in the normal stress profiles (figure 3.6d), and about $4.4L_o$.

3.4 The trailing vortices

In this section the velocity measurements detailed in table 3.2 will be presented. Where possible we shall present cross-wire measurements, since as discussed the appendix, these are more accurate. The appendix includes a full discussion of cross and triple-wire errors and uncertainties.

3.4.1 The baseline case.

Figures 3.8 through 3.12 show mean-velocities, Reynolds stresses and spectra measured during a z-wise traverse through the center of the vortex at x/c = 30, Re_c = 400000, α = 5° with the trip attached. This set of conditions will be referred to as the baseline case. Note that the center of the vortex was located before the traverse by searching for the point of zero mean W and V component velocities.

In the vicinity of the vortex center the mean-velocity field (figure 3.8a) is much as would be expected given the results of Mason and Marchman (1972). The tangential velocities associated with the vortex are clearly visible in the V component profile. These increase to a peak at the edge of the vortex core, which appears to have a diameter of about .09c. The small core size is circumstantial evidence for the relative stability of the vortex and its insensitivity to probe interference. The U profile shows an axial velocity deficit of about $0.14U_{ref}$ here. The normal and shear stress profiles (figures 3.8b and c) are dominated in this region by a strong central peaks. $\overline{v^2}/U_{ref}^2$ and $\overline{w^2}/U_{ref}^2$, by far the largest normal stresses, reach peak values of 0.019 (14% turbulence intensity) and 0.012 (11% turbulence intensity). $-\overline{vw}/U_{ref}^2$, by far the largest shear stress, reaches a value of 0.006.

These large stresses are not representative of turbulence structure but are a consequence of the small lateral wandering of the core observed in the flow visualizations (Devenport and Sharma (1990)). The fact that $\overline{v^2}$ and $\overline{w^2}$ are not equal and $-\overline{vw}$ is not zero at the vortex center indicates, surprisingly, that this unsteadiness is not entirely isotropic. The nature of the core motions is revealed in velocity power spectra measured at the vortex center (figure 3.9a). These broad frequency range spectra are composites obtained by combining spectra measured with the triple-wire probe at two different sampling frequencies. They are plotted in terms of non-dimensional frequency fc/U_{ref} and, for example, $G_{uu}/U_{ref}c$, where f is in Hertz. Because of the implied scales it is unlikely that turbulent velocity fluctuations are associated with frequencies much below fc/U_{ref} = 1. However, this is where the spectra contain the vast bulk of their energy. The peak frequency is remarkably low in all components - at or below 0.001 - implying streamwise length scales greater than 1000 chord lengths (200m). These spectra and the corresponding coherence function for V and W (figure 3.9b) demonstrate that the anisotropy observed in the

Reynolds stresses is produced only at very low frequencies <.01. Only here is there any significant VW coherence (contributing to $-\overline{vw}$) and any difference between G_{vv} and G_{ww}. Above fc/U_{ref} = 1 both G_{vv} and G_{ww} show distinct spike at $fc/U_{ref}=5$. For $fc/U_{ref}>5$ all three autospectra appear to collapse to a single curve.

Away from the vortex center the effects of the motions are smaller and the true turbulence structure is visible (figure 3.10). However, this is somewhat different from that we had expected. Here the measurements show two, if not three, distinct half turns of the wing wake as it spirals around the vortex. These appear as peaks in the normal- and shear-stress profiles (figures 3.10b and c) and inflections and depressions the V and U profiles (figure 3.10a) respectively, centered at z/c = +.75, -.31 and +.19. In contrast to the results and discussions of previous workers studying split-wing vortices (in particular of Phillips and Graham (1984)) there appears to be little region surrounding the core where successive turns of the wing wake have merged to form a continuous axisymmetric structure. As discussed by Zsoldos (1992) this is a consequence of initial conditions. With a split wing two wing wakes, and in some circumstances two vortex cores, are produced that spiral around each other and merge forming the a large axisymmetric region of turbulent flow. This mechanism is absent in a conventional tip vortex.

To illustrate this point figure 3.11a shows a cross section through the vortex at x/c=30. This figure contains contours of $\overline{u^2}/U_{ref}^2$ drawn by interpolating y and z profiles measured with the triple-wire probe along a spiral path deduced from the positions of peaks in the $\overline{u^2}$ profiles. Note that contours have not been drawn in the region y/c>0, z/c>0.5 since this would have involved extrapolation of the data. Figure 3.11b shows $\overline{u^2}/U_{ref}2$ contours from Zsoldos (1992) for a vortex produced by a configuration similar to a split wing. This configuration consisted of two NACA 0012 wings (each identical to the present model) placed tip to tip, with a separation of 0.25c, at opposite angles of attach of 5°. The differences in flow structure, particularly the size and shape of the turbulent region are self evident.

Apart from the non-axisymmetric nature of the flow, the most striking feature revealed in figure 3.11a is the continuous reduction in $\overline{u^2}$ with distance along the spiral wake towards the vortex center. (This is despite the fact that turbulence levels in the wake

are already very low.) A similar reduction, by about 40% on each half turn of the spiral, is also visible in the other normal stresses (see figure 3.10b). The largest shear stress $-\overline{uw}$ drops even more rapidly (figure 3.10c). This may indicate that the greater circumferential shear and curvature experienced by the wing wake towards the vortex center inhibits the development of, or breaks up, large stress-producing turbulent eddies. Figures 3.10 and 3.11(a) do not show whether the reduction in turbulence stresses continues into the core of the vortex, since the true turbulence levels here are obscured by the core motions.

This issue is resolved by examining of more velocity autospectra. Figure 3.12(c) shows autospectra of W-component fluctuations (G_{ww}). These cover a narrower frequency band than those of figure 3.9a but were measured using the over a range of z locations from the spiral wake to the core center. G_{ww} and frequency f have been normalized on U_{ref} and c. Note that at frequencies fc/U_{ref} above about 40, the spectra are contaminated by electrical noise, visible because of the very low overall turbulence levels at some locations. These data were measured using the cross hot-wire probe. Triple-wire measurements are also available at these locations but are not presented here since they suffered from greater contamination by electrical noise.

The spectra measured z/c=-.5 and -.25, to either side of the spiral wake, are almost identical in shape, having a broad peak centered near $fc/U_{ref} = 2$. This similarity is surprising considering the difference in turbulence levels (more than a factor of two) between these locations. The peak frequency $fc/U_{ref} = 2$ implies a streamwise length scale (assuming Taylor's hypothesis) of about c/2, a distance aproximately equal to the width of the spiral wake. It is an open question as to whether such large structures truly do exist in this region of circumferential shear and curvature.

Moving in towards the vortex center, the unsteady motions of the vortex begin to dominate the spectra at low frequencies, the energy here increasing by almost three orders of magnitude. At higher frequencies ($fc/U_{ref} > 10$), however, where the velocity fluctuations are most likely generated by turbulence, energy levels actually fall and are almost an order of magnitude smaller at the vortex center than in the spiral wake. This is remarkable considering that the overall turbulence intensity in this part of the spiral wake is never greater than 1%. It suggests that the flow in the core is non-turbulent. It is therefore

possible that viscous stresses may play a role here. Another clue to the dynamics of the core is the spike that appears in those spectra measured at z/c=-0.09 and -0.04 at frequencies close to $fc/U_{ref}=5$. This could be consequence of viscous instability of the type observed by Singh and Uberoi (1976) at a frequency, for their vortex of $fc/U_{ref}=3.5$. Note that there is a discrepancy in the data concerning the existence of the spike in the core center. The spectra shown in figure 3.12, measured with the cross-wire probe, show at most a slight bump at $fc/U_{ref}=5$ for z/c=0.0. However, those of figure 3.9a, measured with the triple wire, show the spike clearly. This difference is seen at some other conditions but only at the core center, spectra measured with both techniques at other locations (z/c=-.04,-.09,-.16,-.25,-.5) being almost identical. It could be due to the uncertainty in absolute probe position, about ±.01c for the spectra. Another possibility is an, as yet, unexplained bias error in one of these techniques. Whatever the explanation there seems no doubt the spike is a genuine feature of the flow in and around the core.

U and V component autospectra, plotted in similar form in figures 3.12(a) and (b), show much the same effects seen in the W component. Note that the spike appearing in G_{ww} near $fc/U_{ref} = 1.5$ in those spectra measured outside the core region is not a flow feature but is a result of probe vibration. Although the vibration was barely visible to the naked eye it can be seen in the spectra because of the low overall level of the turbulent velocity fluctuations.

3.4.2 Comparison with other cases.

Figures 3.13 through 3.20 compare the mean velocity, normal stress and shear stress profiles of the baseline case with those measured at other conditions listed in table 3.2. Comparisons covering the core and wake regions are made separately in these figures. Note that in both cases only the most significant of the Reynolds shear stresses is plotted i.e. $-\overline{vw}$ in the core region and $-\overline{uw}$ in the wake region. Spectra measured in these cases are presented in figures 3.21 through 3.27, which show broad frequency-range spectra at the core center, and figures 3.28 through 3.35, which show spectra over a narrower frequency band but at several different radial positions extending into the wake region. In studying the profile comparisons take note of the uncertainty estimates listed in the appendix.

Before embarking on a detailed discussion some general observations can be made concerning all of these flows.

(i) In every case the measurements clearly show the wing wake forming a spiral around the vortex (see for example figures 3-14c, 16c, 18c and 20c).

(ii) In no case does there appear to be any large merged region axisymmetric flow outside the core.

(iii) Regardless of conditions turbulence stresses in the wake fall as the core is approached (e.g. figure 3-14c).

(iv) In the core region the basic shapes of the tangential (V) velocity profiles and the corresponding normal and shear stresses $\overline{v^2}$, $\overline{w^2}$ and $-\overline{vw}$ are qualitatively identical in all cases (e.g. figures 3-15b,d,e,and f). These stresses are always fairly large in the core center suggesting that they are primarily a consequence of core motions rather than turbulence.

(v) In none of the cases is $-\overline{vw}$ zero or $\overline{v^2}=\overline{w^2}$ at the center of the vortex cores indicating, as in the baseline case, that these motions are at least partly anisotropic.

(vi) While the form of the axial velocity profiles varies there remains in all cases a small axial velocity deficit of between 8% and 18% U_{ref} at the core center.

(vii) Spectra measured at the core center (figures 3.21-27) show, regardless of conditions, G_{vv} and G_{ww} to be identical except at frequecies $fc/U_{ref}<0.01$. Here, in all cases, there is a significant VW coherence indicating, as in the baseline case, that the anisotropic component of the core motions is confined to very low frequencies.

(viii) In all cases except one ($\alpha=2.5^o$, $Re_c=400000$, $x/c=30$) those spectra measured at a range of radial positions (figures 3.28 to 35) show much lower spectral levels at high frequencies in the core than in the spiral wake. The implication, again, is that in these cases the flow in the core is non turbulent.

3.4.2.1 Effects of streamwise distance x/c.

Figures 3.13 and 3.14 compare the baseline case results with measurements made further upstream in the same vortex at $x/c=25$ and 20. In the core region (figure 3.13) the flow appears to change little over this range of x/c. The mean axial velocity profiles all have

the same form (figure 3.13a) and, bearing in mind the uncertainty in this measurement due to calibration drift, all indicate about the same deficit at the core center. The mean tangential (V) velocity profiles (figure 3.13b) show some growth of the core diameter and corresponding reduction in peak tangential velocity but both effects are quite small being only just observable on this plot. The shapes of the normal and shear stress profiles in the core (figure 3.13c-f) also change little though the magnitudes of these stresses are slightly higher at x/c=25 and 30 than at x/c=20. This could indicate some development of the turbulence structure within the core but it is more probably a consequence of development in the core motions and mean velocity gradients. Several previous workers have observed the unsteadiness of tip vortex cores to increase with downstream distance. Spectra measured at the core center (figure 3.9, 3.21 and 3.22) show no perceptible effect of x/c.

In the wake region (figure 3.14) the measurements show more substantial changes. Those features associated with the wing wake - local dips in the U profile, inflections in the V profile and peaks in the profiles of turbulence stresses all move outward from the core center between x/c=20 and 30. As illustrated in figure 3.36 this is consistent with the rolling up of the wake about the core. By analogy with two-dimensional wakes of the type studied by Wygnanski et al. (1986) we would expect the spiral wake surrounding the core to gradually dissipate with distance downstream, the axial velocity deficit and turbulence levels within it falling. This appears to happen. At most positions in the spiral wake turbulence stress levels fall by about a factor of 2 between x/c=20 and 30 (an exception here is the $\overline{w^2}$ on the negative z side of the core, figure 3.14(e)). Despite the comparatively large uncertainty in U/U_{ref} due to calibration drift (particularly noticeable at x/c=25, figure 3.14a) these profiles also shows a gradual reduction in the wake deficit. The velocity spectra of figure 3.12 and 3.28 and 3.29 show no significant effects of x/c. The levels of some of the spectra measured in and around the wake change with x but this is merely a consequence of the roll up process which moves the wake relative to the fixed locations at which the spectra were measured.

3.4.2.2 Effects of Reynolds number Re_c.

Figures 3.15 and 3.16 compare profiles measured at x/c=30 in four vortices generated at four different Reynolds numbers 1.3, 2.6, 4.0 and $5.3x10^{-5}$ (4.0 being the baseline case) with the wing at 5° angle of attack.

In the core region (figure 3.15) Reynolds number has little or no significant effect on the shape and magnitude of the mean axial velocity deficit (figure 3.15a). The same can be said of the tangential velocity profiles here (figure 3.15b) between Re_c = 260000 and 530000. However, a substantial increase in the core radius and corresponding reduction in the peak tangential velocity occurs as Re_c is lowered from 260000 to 130000. This change may be a consequence of the rather low momentum thickness Reynolds number of the wing boundary layer at Re_c=130000 (see table 3.3) since it is the roll up of the this layer determines the initial size and circulation of the core. Further Reynolds number effects are seen in the normal and shear stresses (figures 3.15c-f). With the exception of $\overline{u^2}$ the magnitude of all the stresses increases monotonically with Reynolds number, the largest changes occuring between Re_c=260000 and 400000. These effects may well be entirely a consequece of core motions, their amplitude increasing with Re_c. However, examination of the $\overline{u^2}$ profiles suggests that coherent wandering of the vortex may only play a part other types of motion, possibly inviscid waves or viscous instabilities also being present. Coherent wandering would be expected to produce peaks in the $\overline{u^2}$ profiles in regions where the radial gradient of U is greatest, i.e. near z/c= ±0.3 (figure 3.15a) towards the edge of the core. However, this does not happen. Peaks are only clearly seen here at the highest Reynolds number (figure 3.15c). At the other Reynolds numbers a central peak dominates. Reynolds number has surprisingly little influence on the shapes of the autospectra at the core center (figures 3.9, 3.23 to 3.25). In terms of fc/U_{ref} the frequency of the spike toward the high frequency side of the spectrum is almost constant, increasing only very slightly with Re_c.

In the wake region (figure 3.16) the flow appears Reynolds number independent, consistent with the idea that the spiral wake is a fully developed turbulent flow. With one exception the profiles of the two mean velocity and four Reynolds streses plotted are quantitatively the same to within the measurement uncertainty at all four Reynolds numbers.

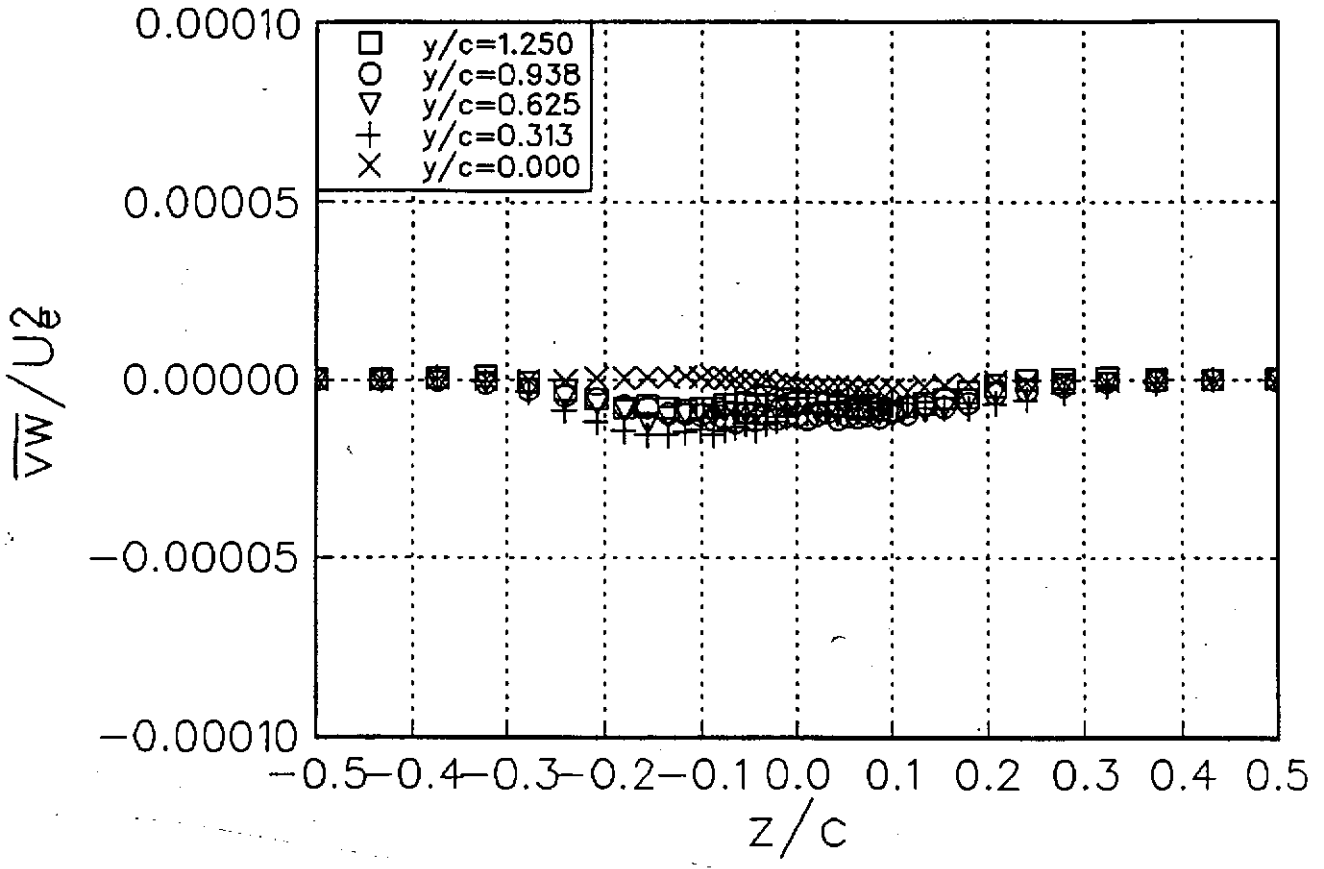

(h) Turbulence shear stress $\overline{vw}/U_e^2$

Figure 3.6 Velocity profiles measured at x/c=30 in the wing wake at zero angle of attack. Re_c=400000.

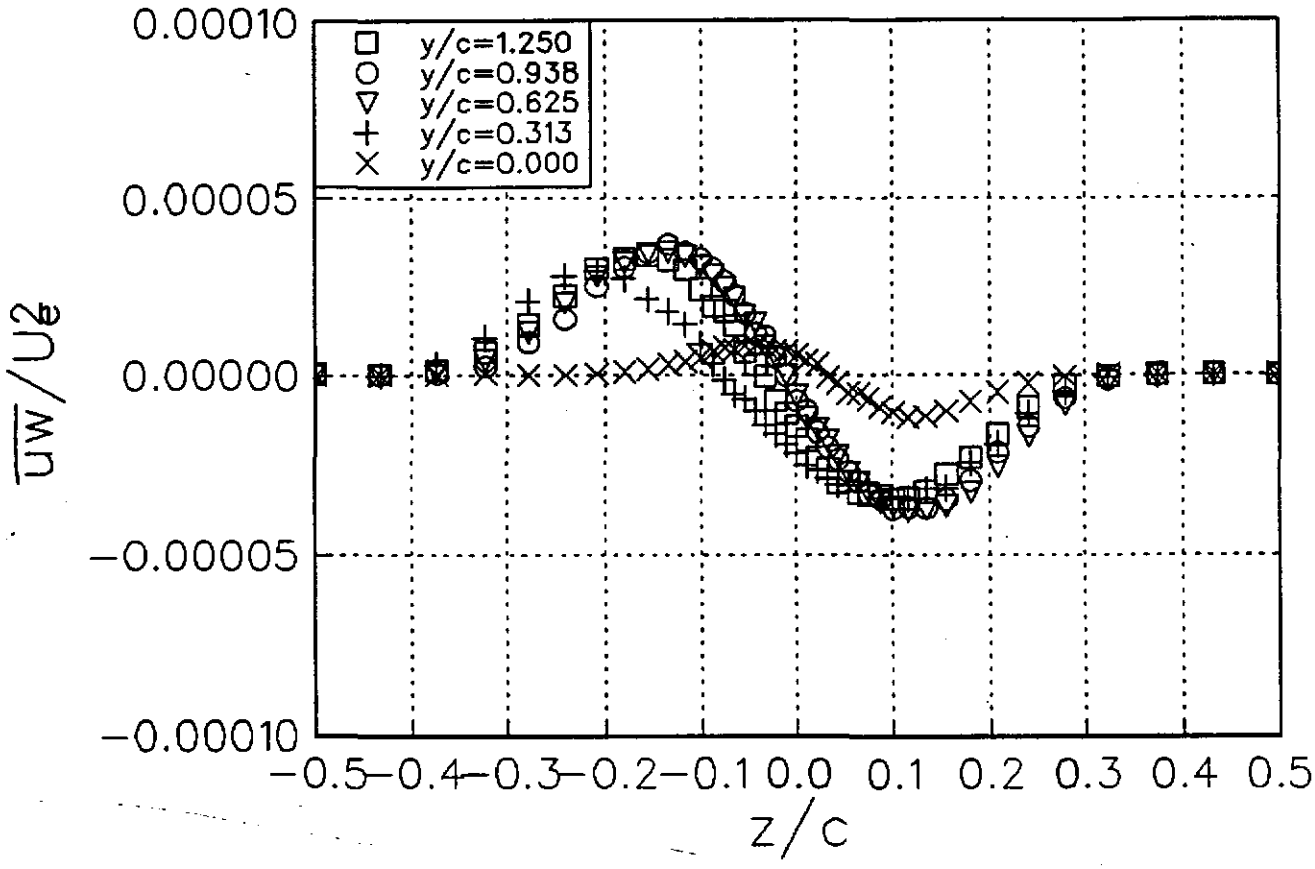

(i) Turbulence shear stress $\overline{uw}/U_e^2$

Figure 3.6 Velocity profiles measured at x/c=30 in the wing wake at zero angle of attack. Re_c=400000.

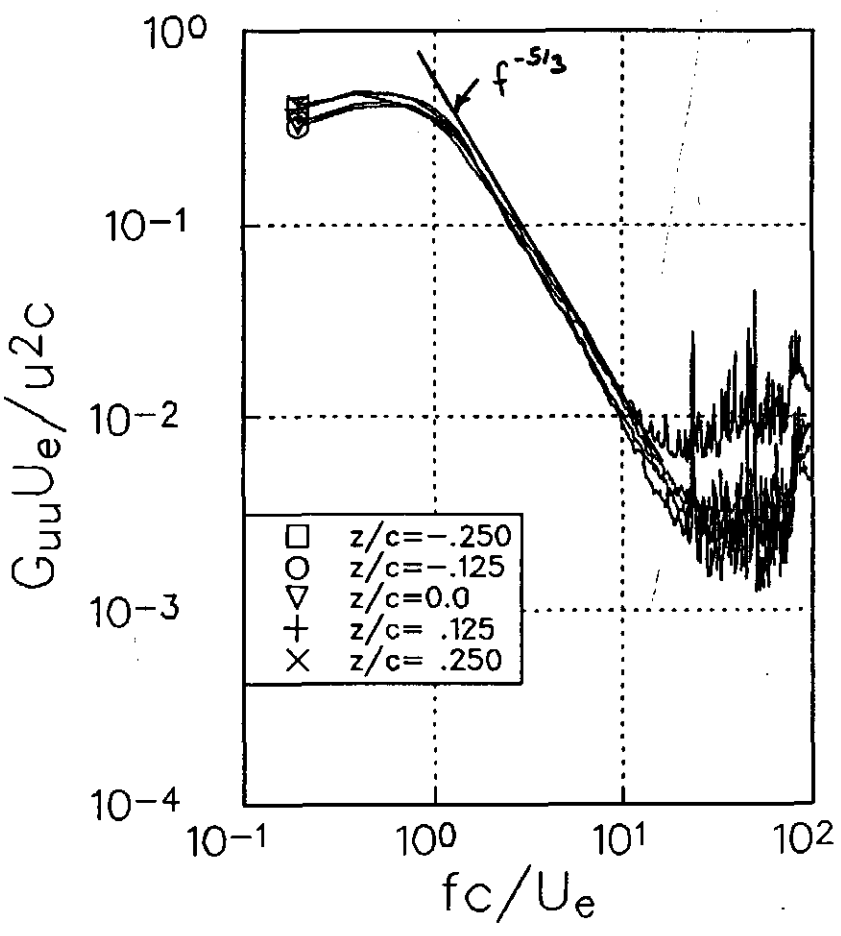

(a) U component

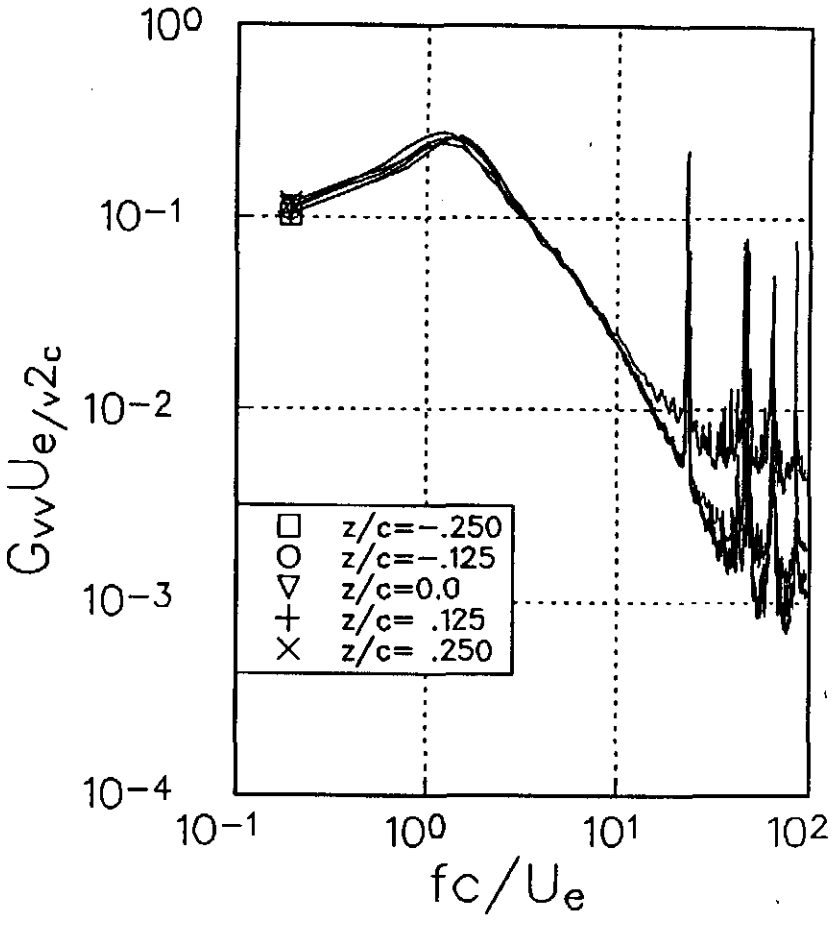

(b) V component

Figure 3.7 Power spectra of velocity fluctuations in the wing wake at zero angle of attack. Re_c=400000, y/c=0.313.

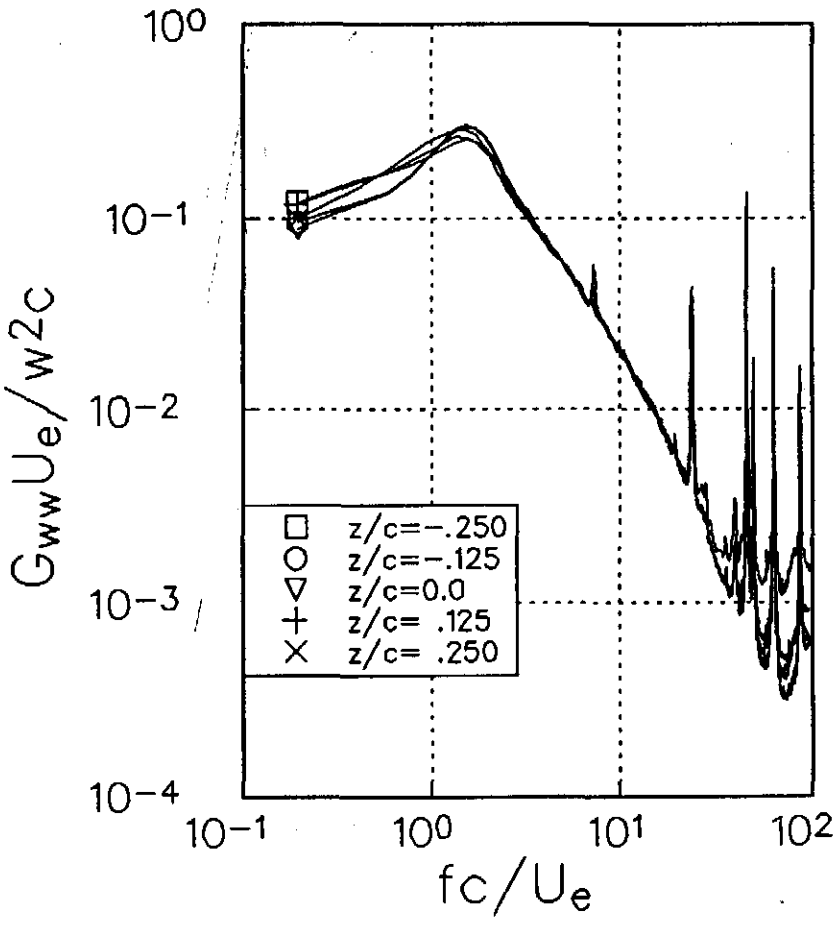

(c) W component

Figure 3.7 Power spectra of velocity fluctuations in the wing wake at zero angle of attack. Re_c=400000, y/c=0.313.

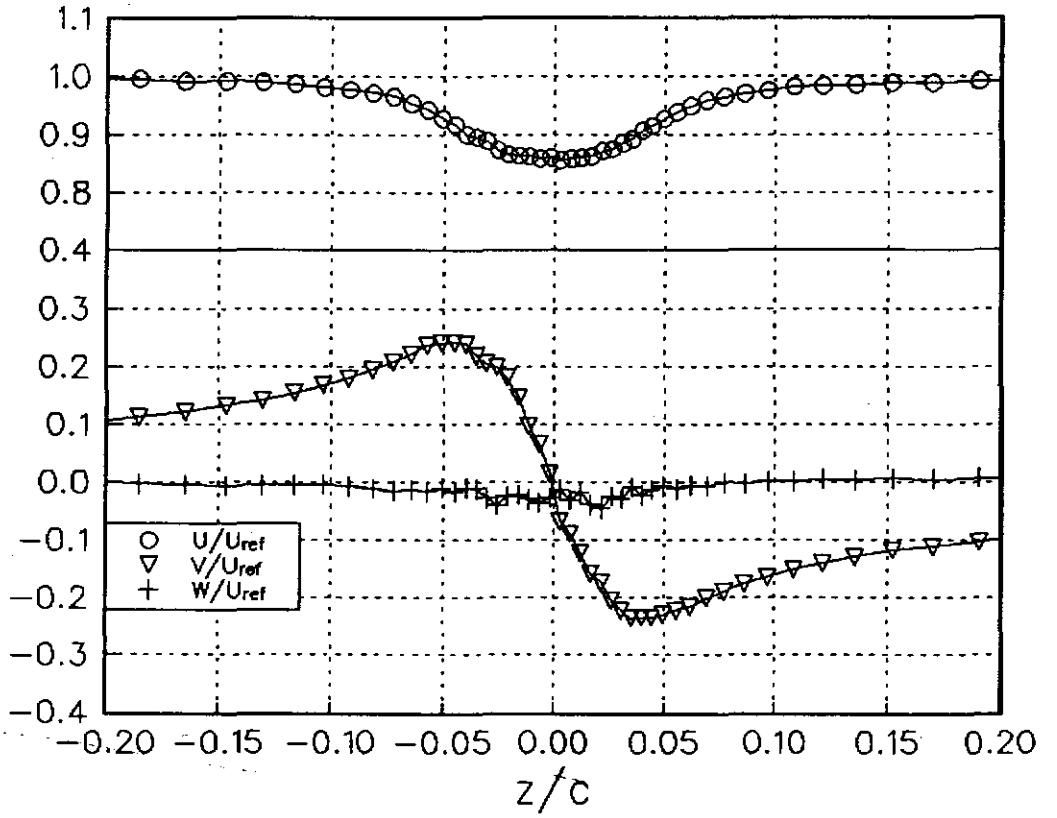

(a) Mean velocities

Figure 3.8 Velocity profiles in the vicinity of the vortex core normalized on U_{ref}. Baseline case.

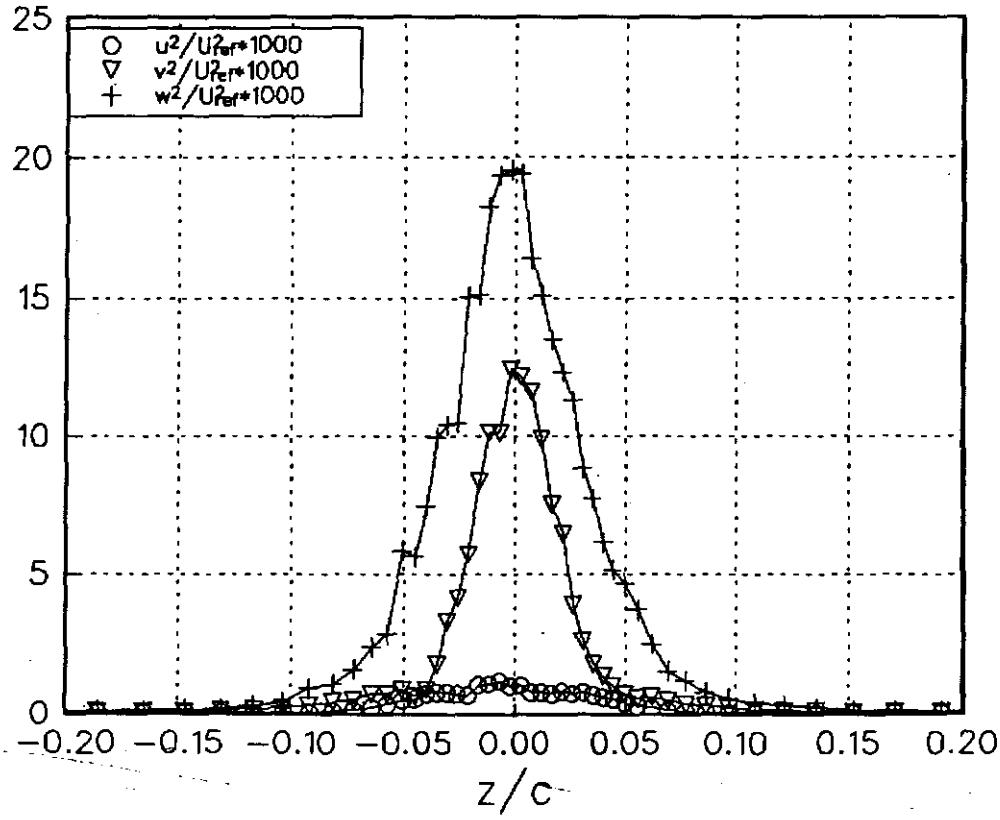

(b) Reynolds normal stresses

Figure 3.8 Velocity profiles in the vicinity of the vortex core normalized on U_{ref}. Baseline case.

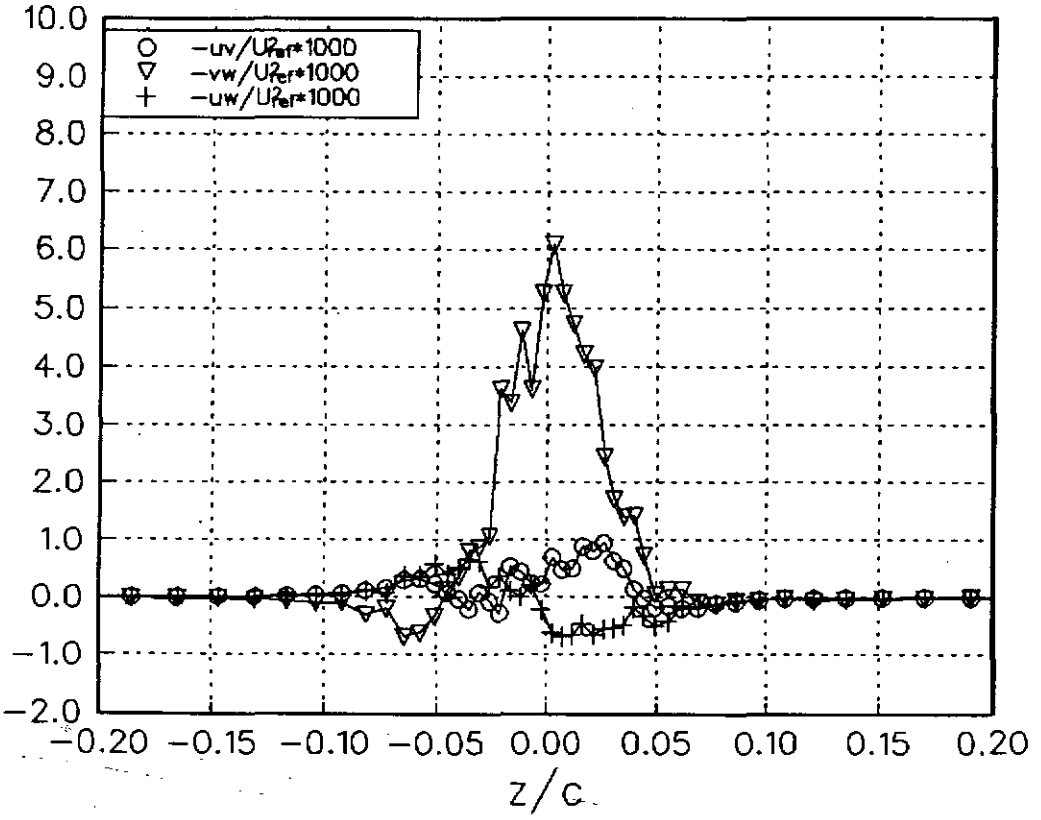

(c) Reynolds shear stresses

Figure 3.8 Velocity profiles in the vicinity of the vortex core normalized on U_{ref}. Baseline case.

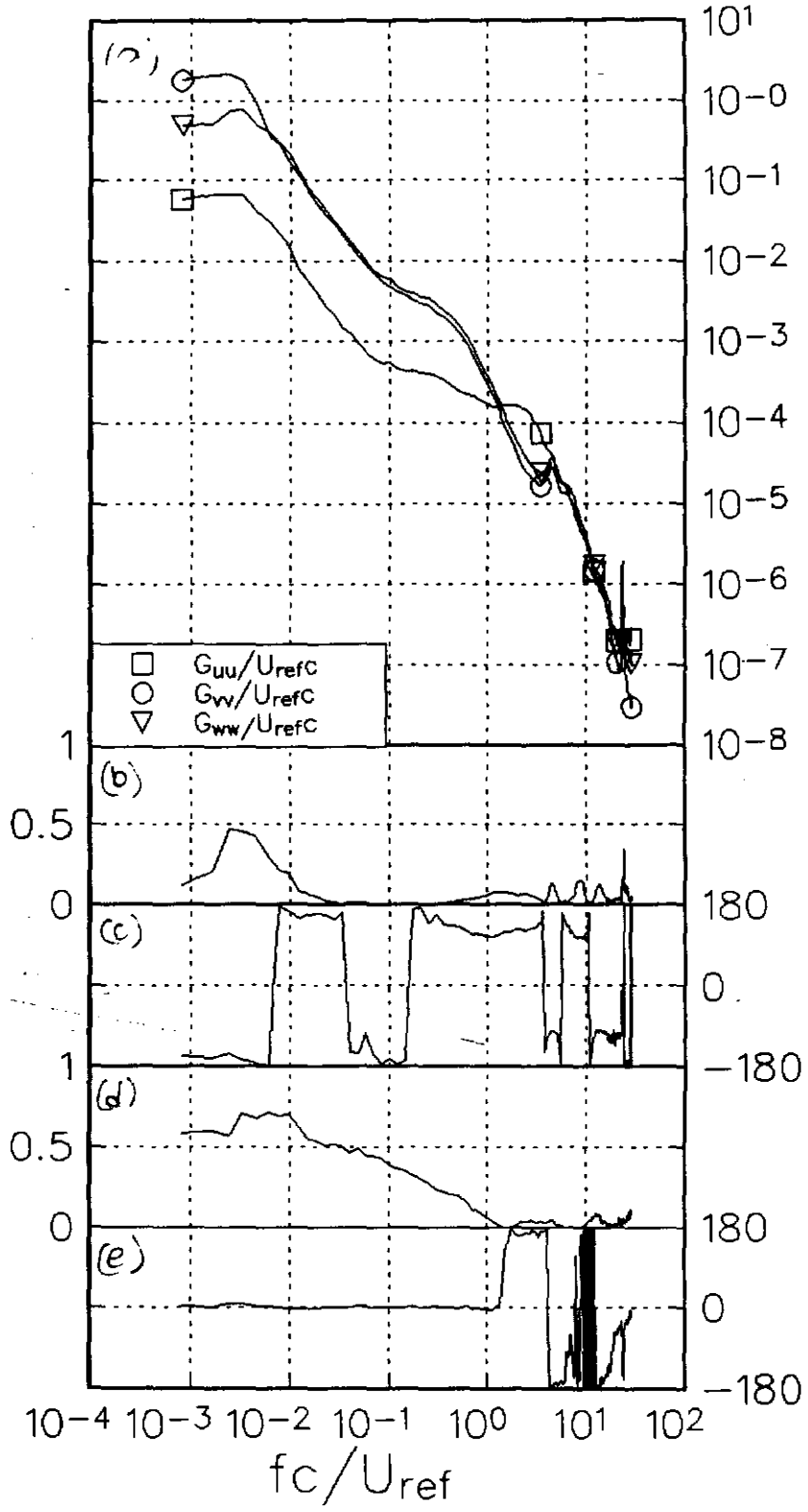

Figure 3.9 Composite spectra of velocity fluctuations at the core center. Baseline case. (a) autospectra, (b) VW coherence, (c) VW phase, (d) UQ coherence, (e) UQ phase. Note, Q is the magnitude of the instantaneous circumferencial velocity defined as $Q = \sqrt{V^2+W^2}$.

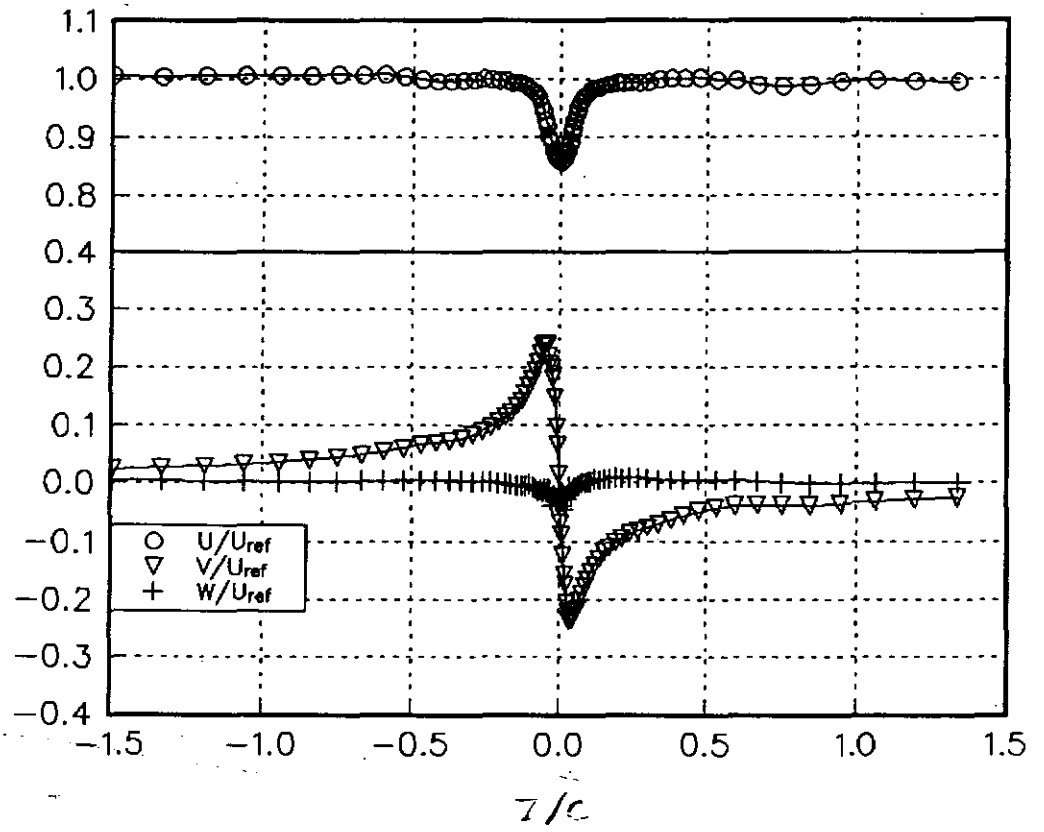

(a) Mean velocities

Figure 3.10 Velocity profiles over the entire vortex normalized on U_{ref}. Baseline case.

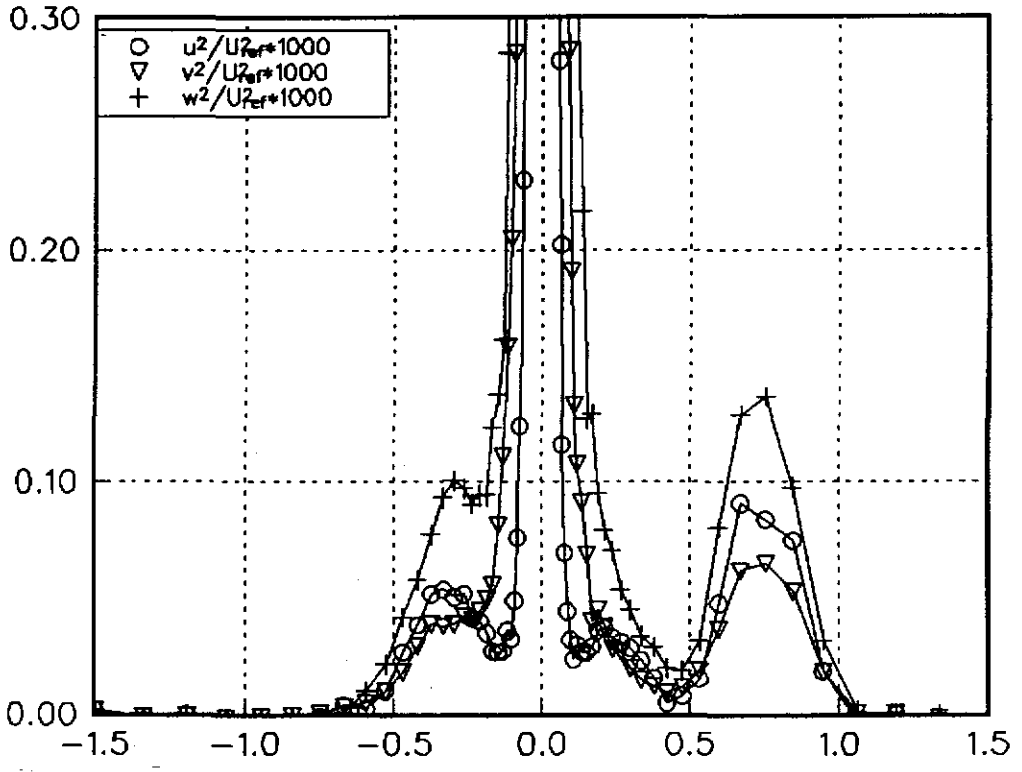

(b) Reynolds normal stresses

Figure 3.10 Velocity profiles over the entire vortex normalized on U_{ref}. Baseline case.

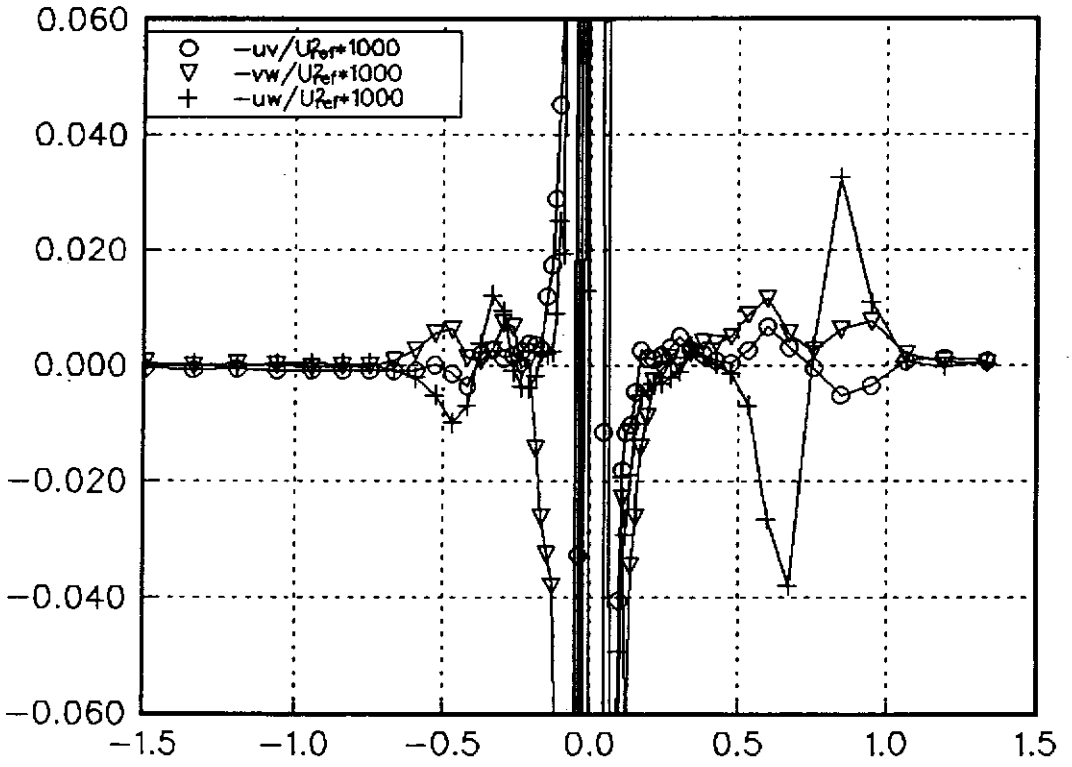

(c) Reynolds shear stresses

Figure 3.10 Velocity profiles over the entire vortex normalized on U_{ref}. Baseline case.

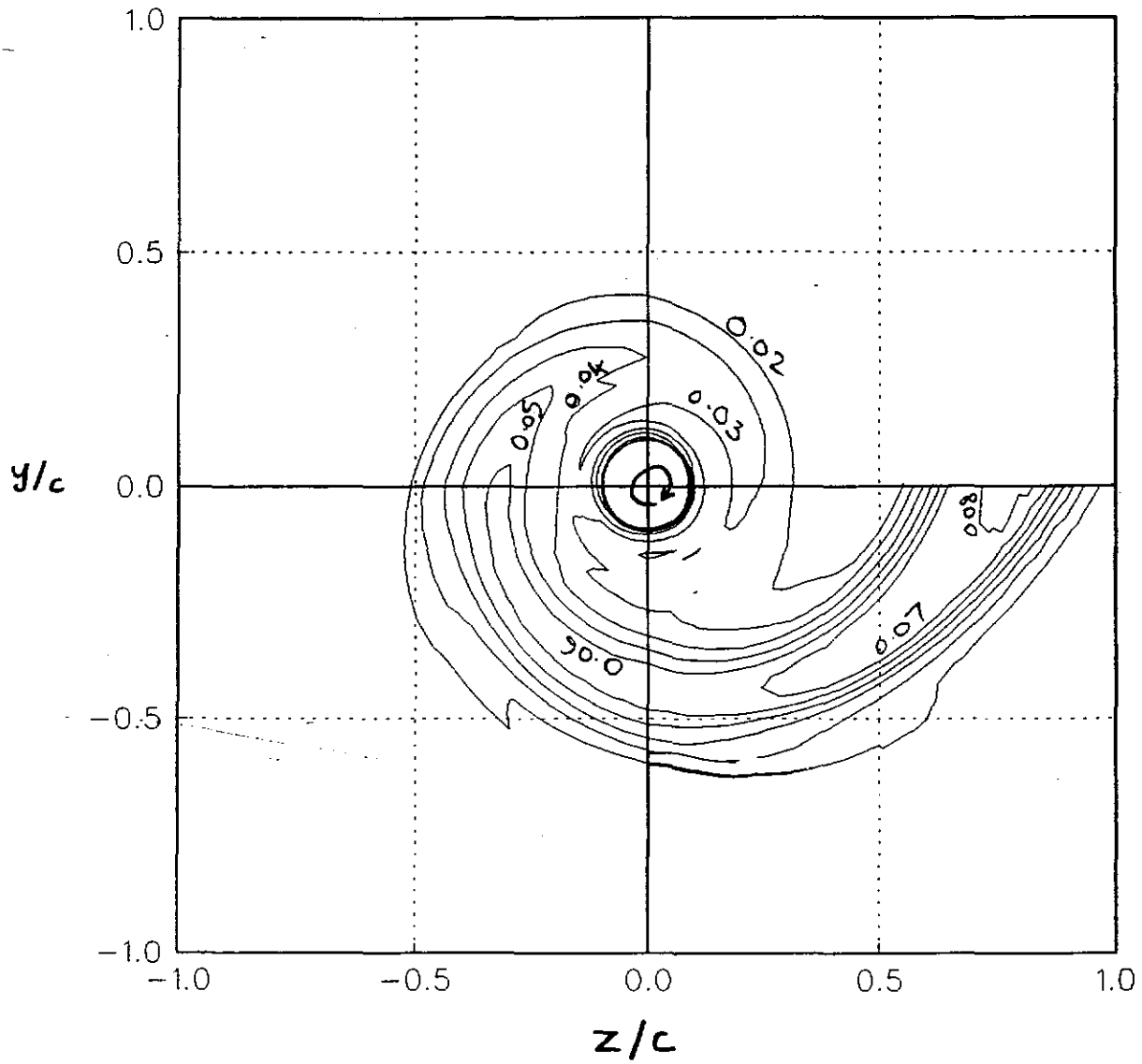

Figure 3.11(a) Contours of $\overline{u^2}/U_{ref}^2$ x 1000 in the baseline case drawn by interpolating triple hot-wire profiles measured along the Y and Z profiles along spiral paths.

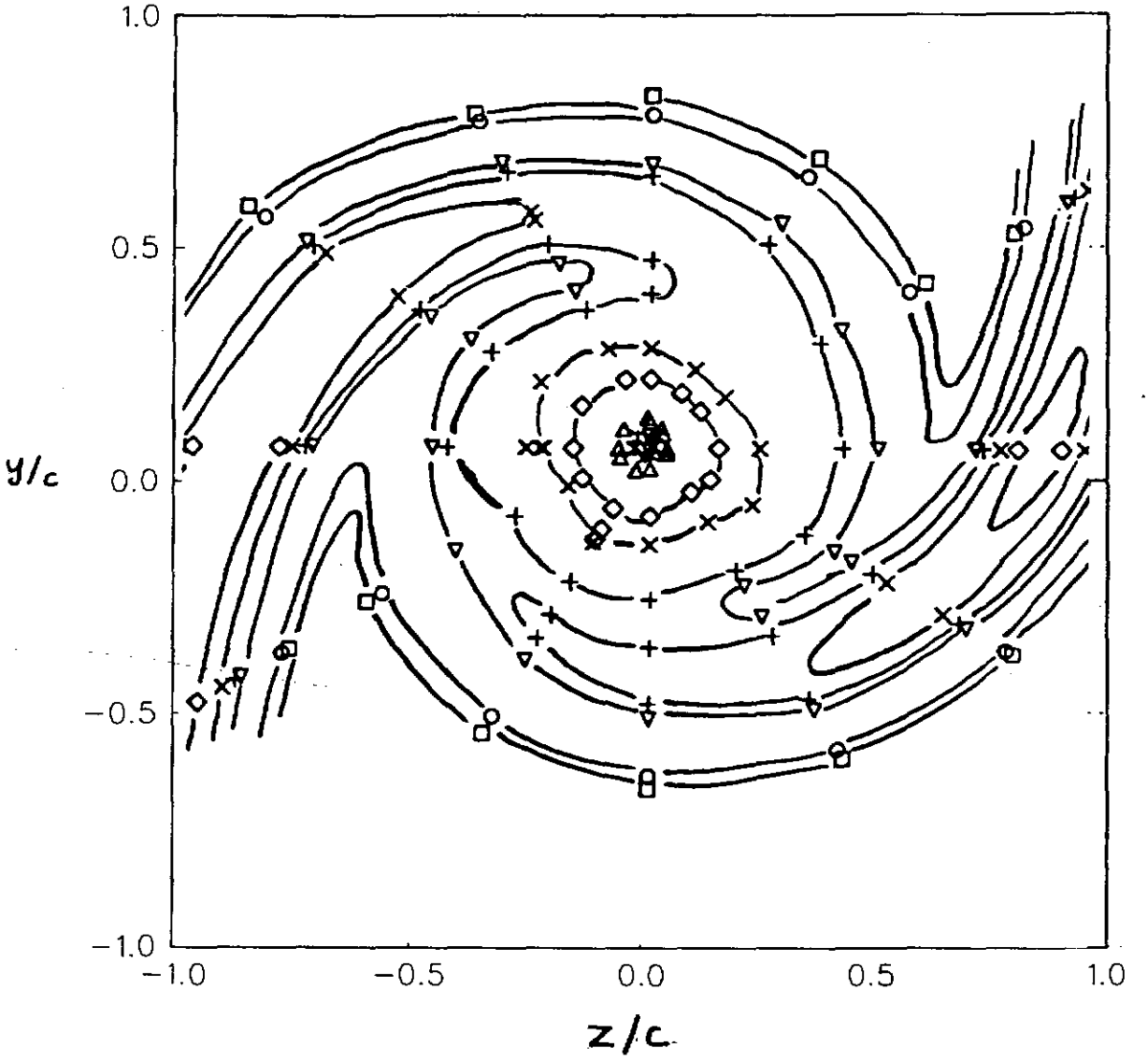

Figure 3.11(b) Contours of u^2/U_{ref}^2 in the merged vortex produced by a split wing configuration under similar conditions to the baseline case, from Zsoldos (1992).

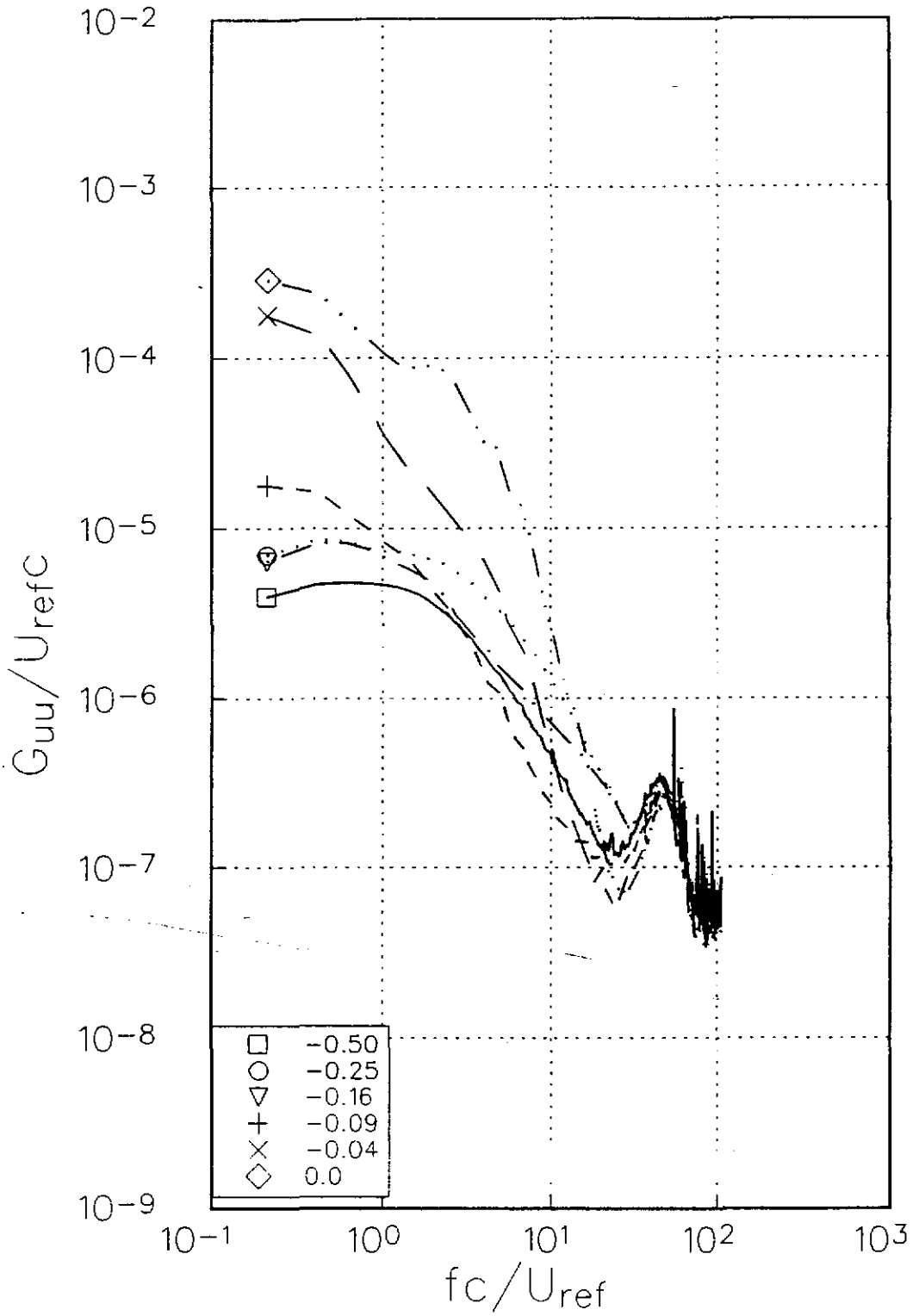

Figure 3.12(a) Autospectra of U component velocity fluctuations measured at various z/c locations in the baseline case.

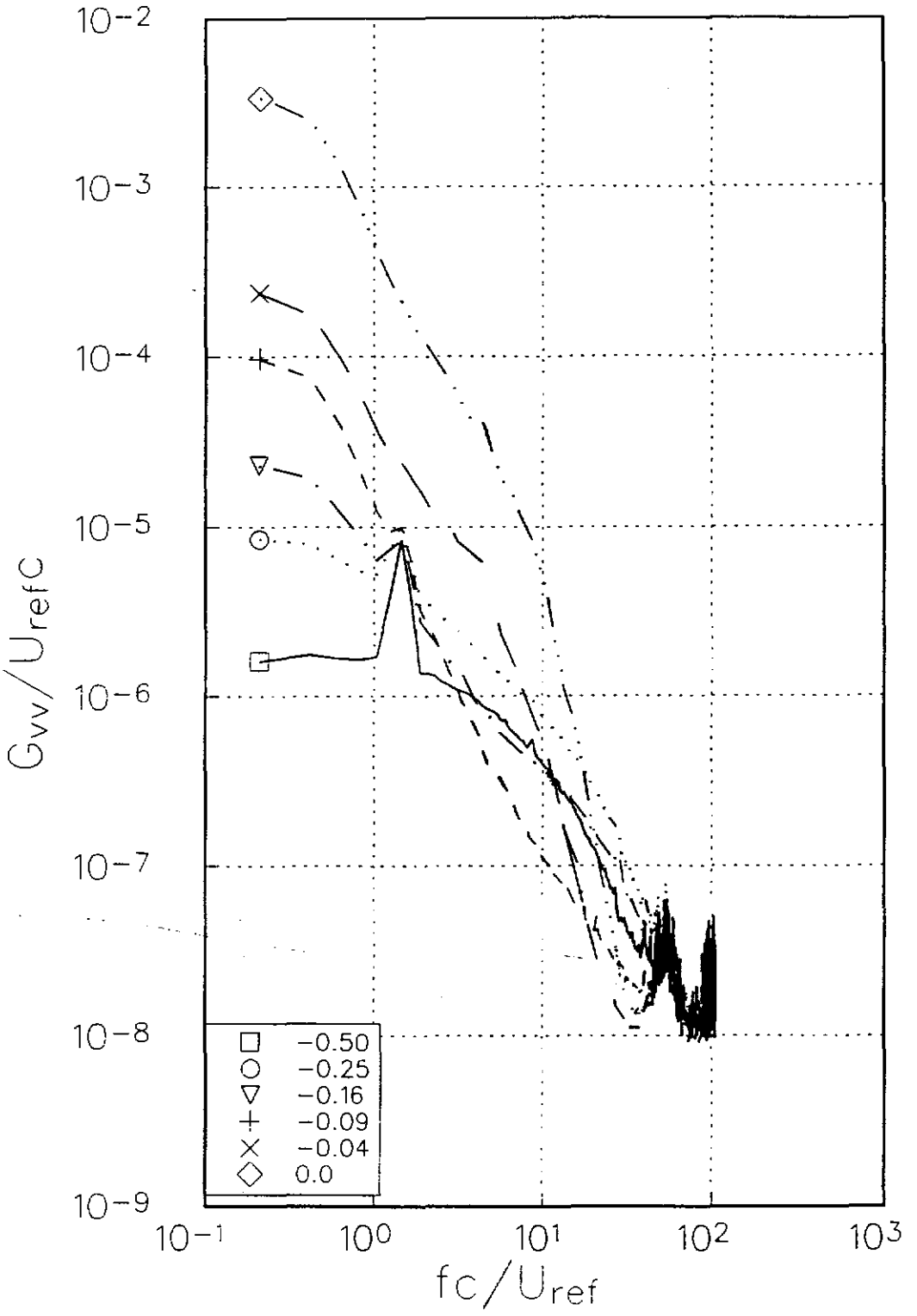

Figure 3.12(b) Autospectra of V component velocity fluctuations measured at various z/c locations in the baseline case.

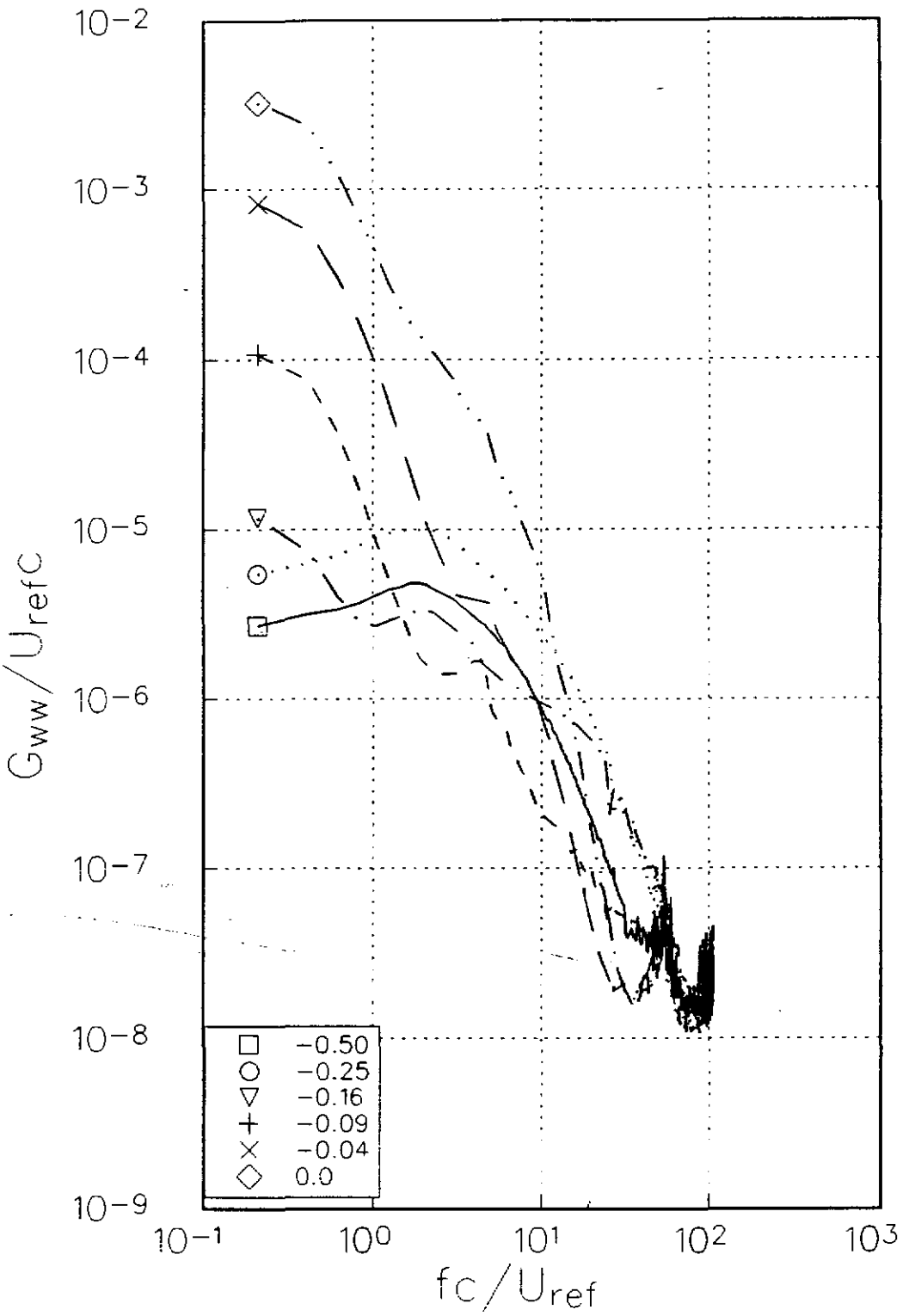

Figure 3.12(c) Autospectra of W component velocity fluctuations measured at various z/c locations in the baseline case.

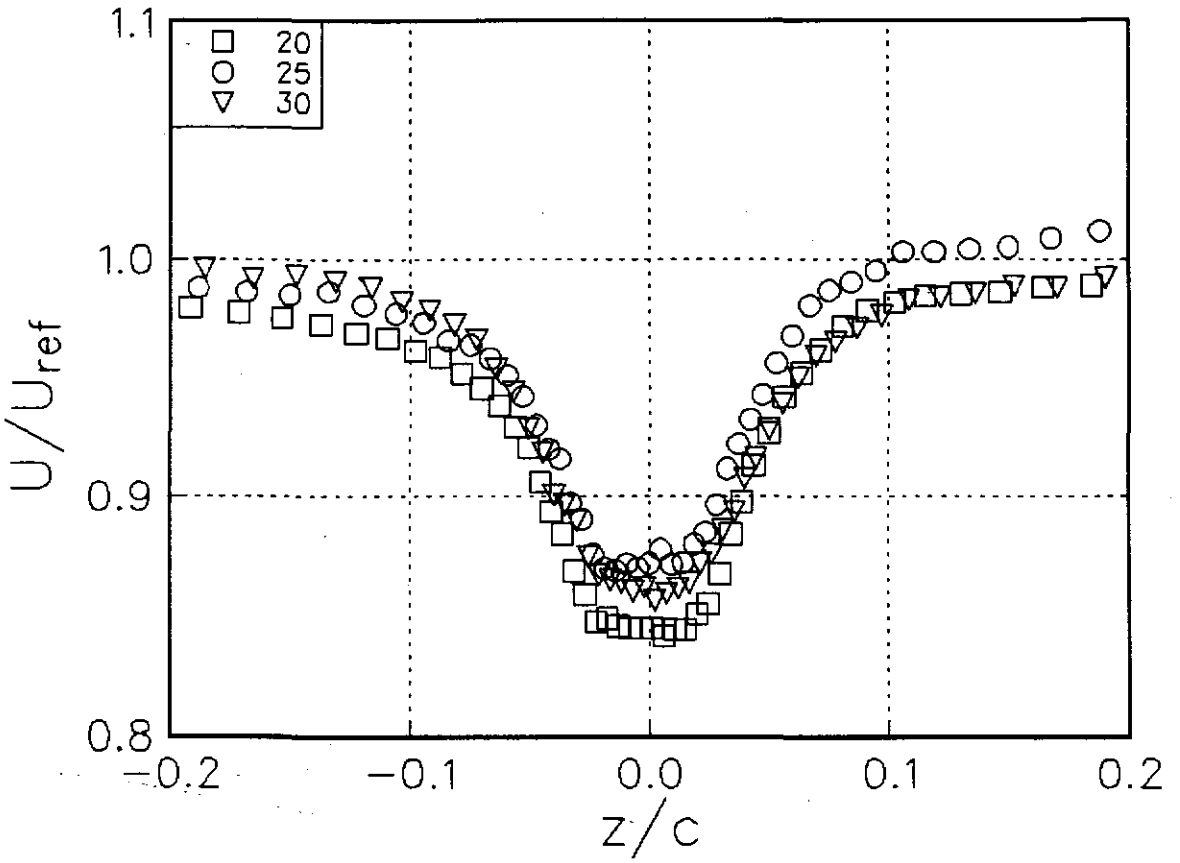

(a) U/U_{ref}

Figure 3.13 Velocity profiles in the core region as a function of streamwise distance x/c for Re_c=400000, α=5.0°.

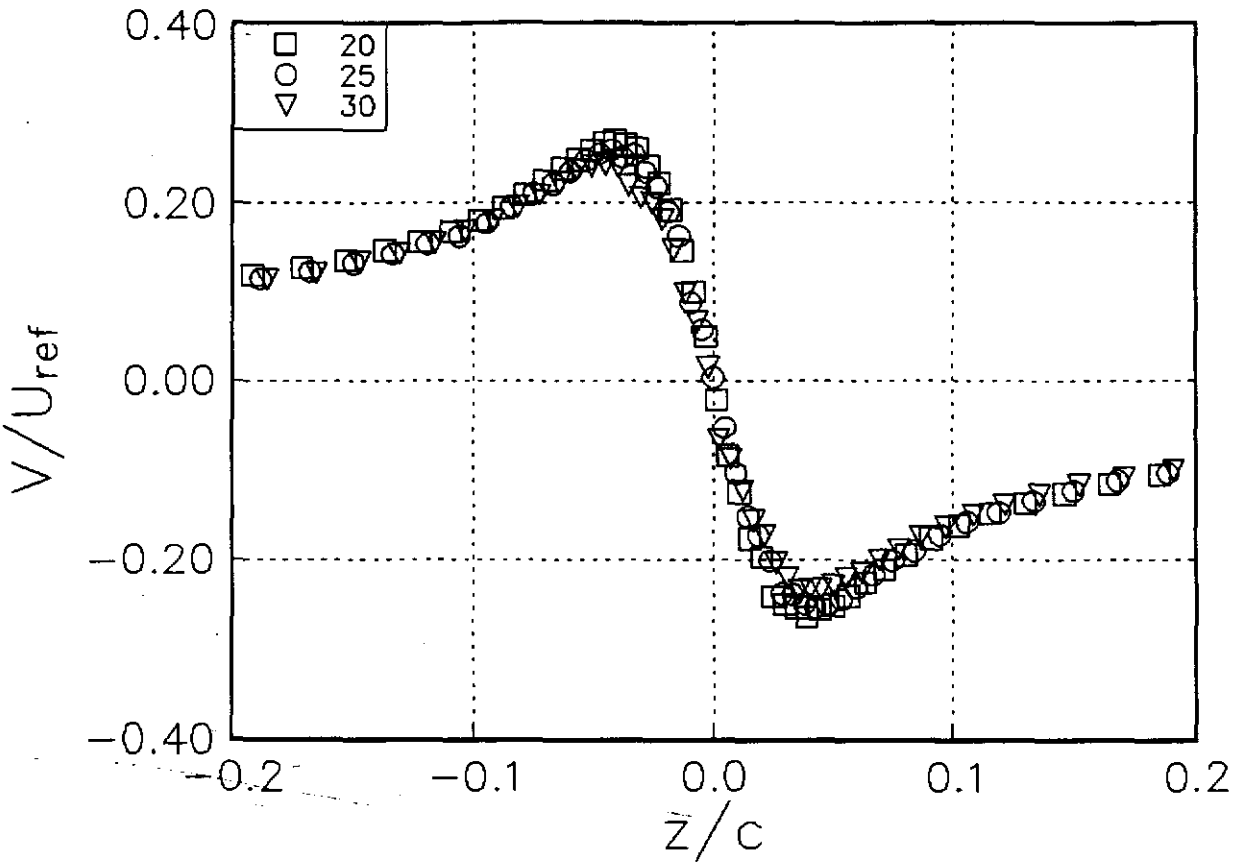

(b) V/U_{ref}

Figure 3.13 Velocity profiles in the core region as a function of streamwise distance x/c for $Re_c = 400000$, $\alpha = 5.0°$.

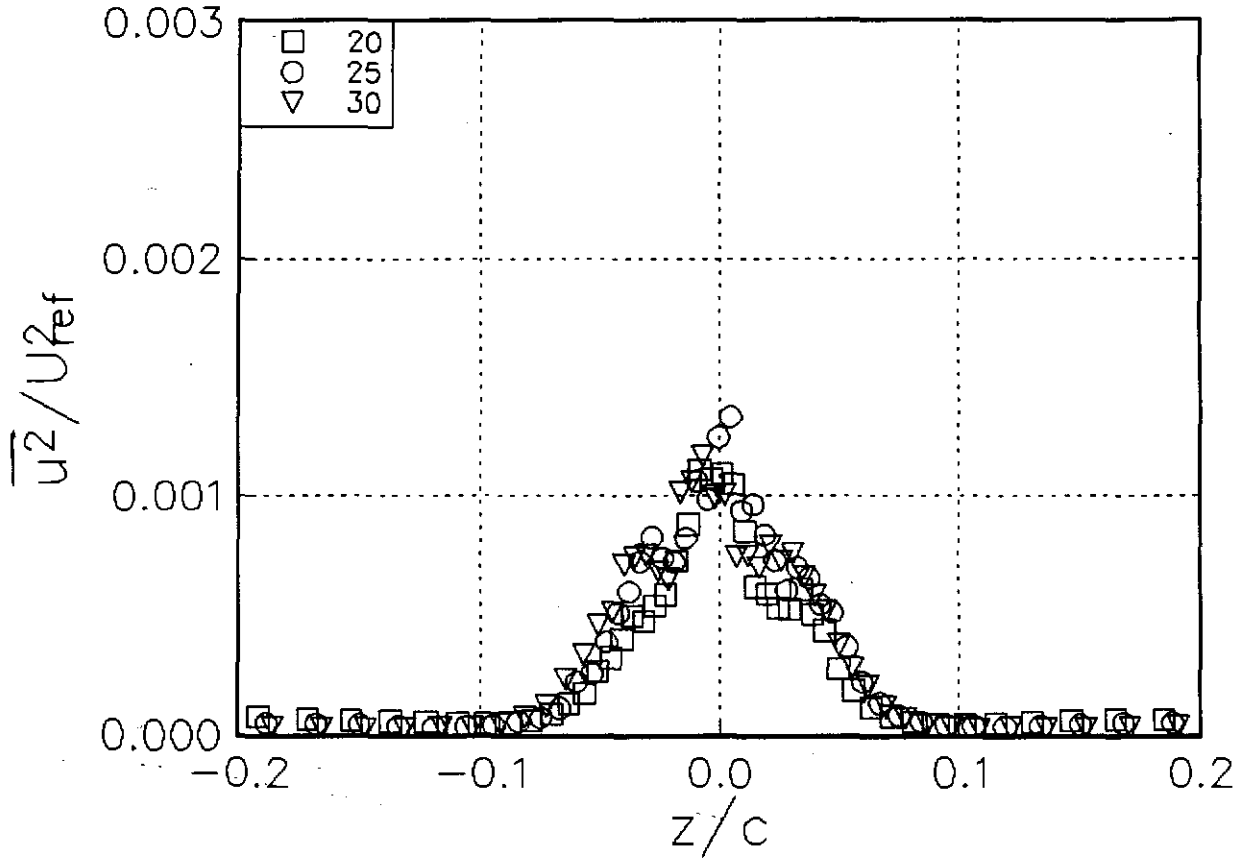

(c) $\overline{u^2}/U_{ref}^2$

Figure 3.13 Velocity profiles in the core region as a function of streamwise distance x/c for $Re_c = 400000$, $\alpha = 5.0°$.

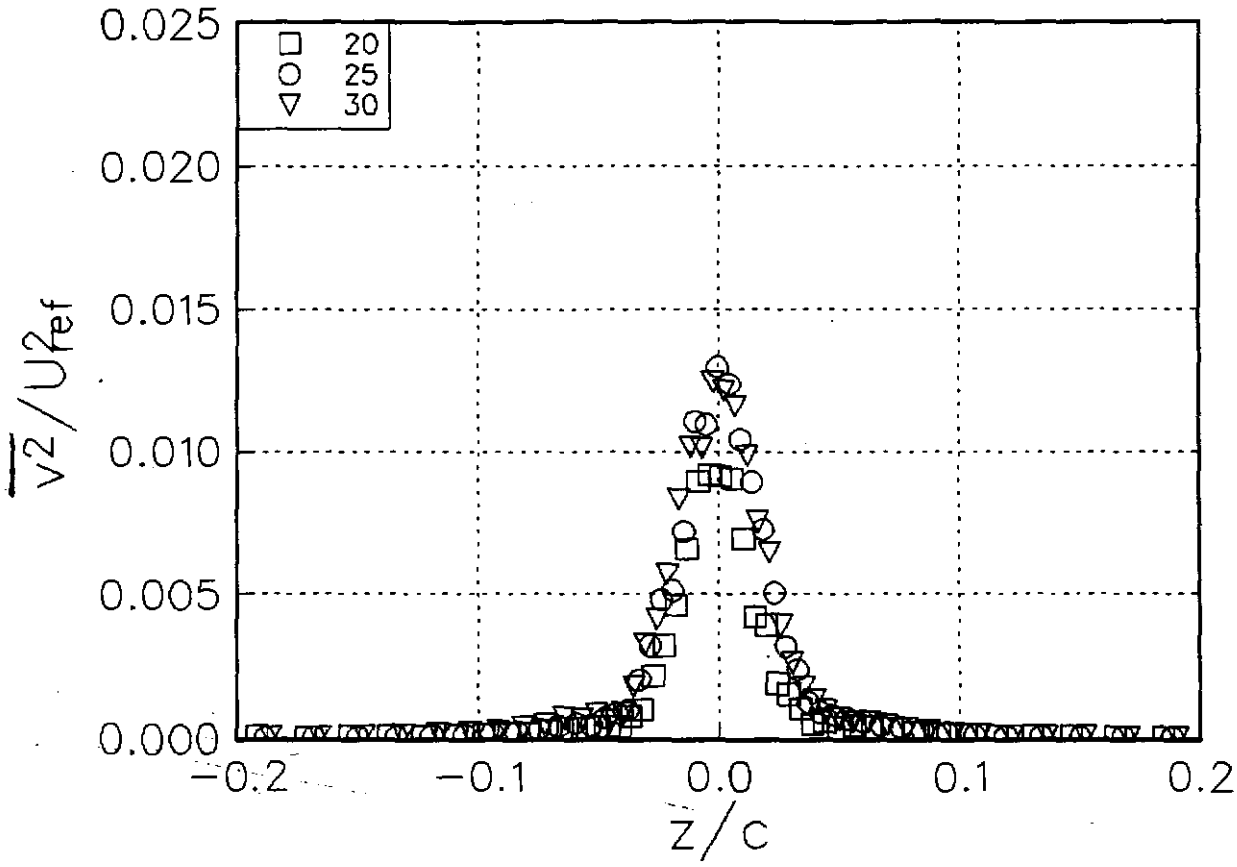

(d) $\overline{v^2}/U_{ref}^2$

Figure 3.13 Velocity profiles in the core region as a function of streamwise distance x/c for Re_c=400000, α=5.0°.

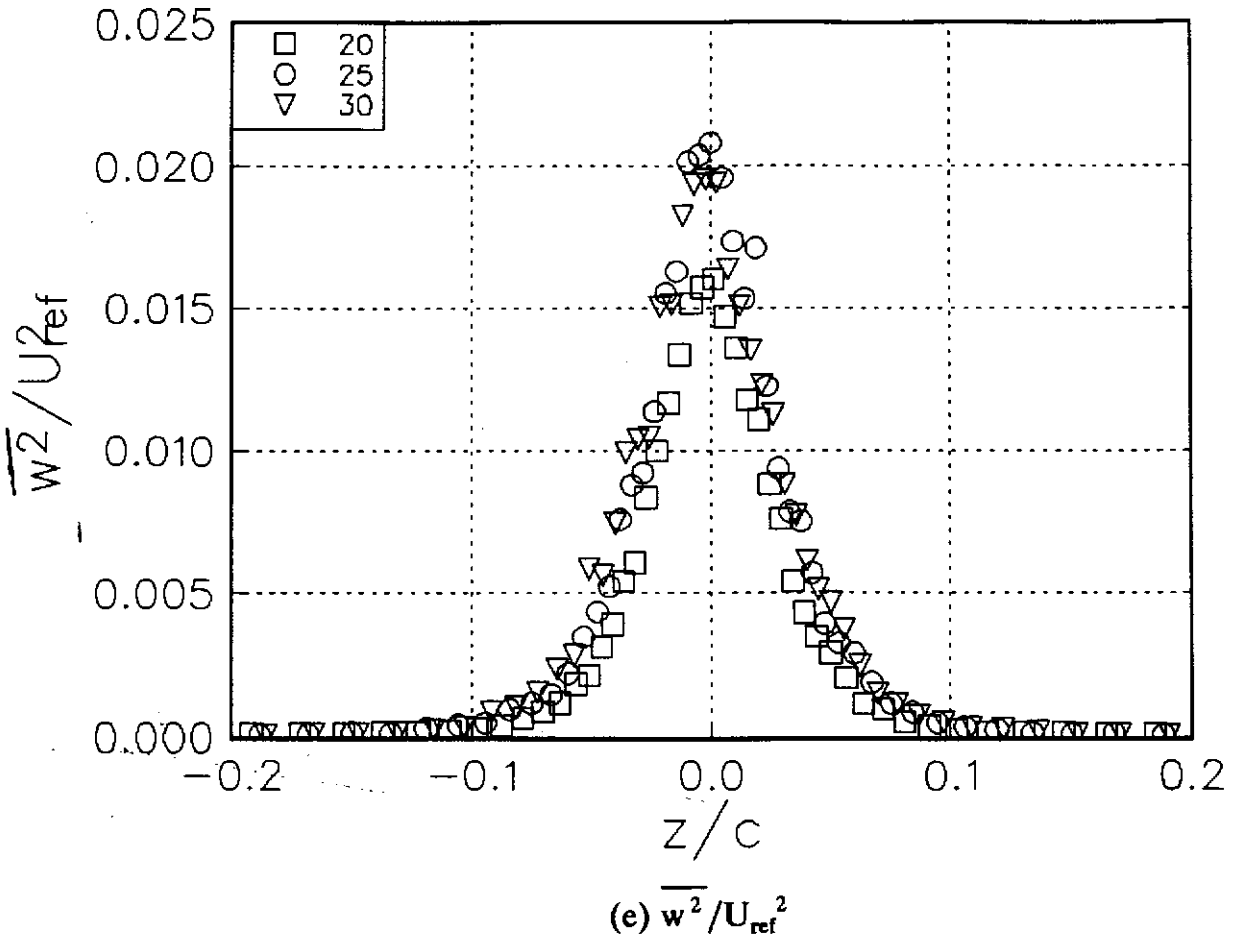

(e) $\overline{w^2}/U_{ref}^2$

Figure 3.13 Velocity profiles in the core region as a function of streamwise distance x/c for Re_c=400000, α=5.0°.

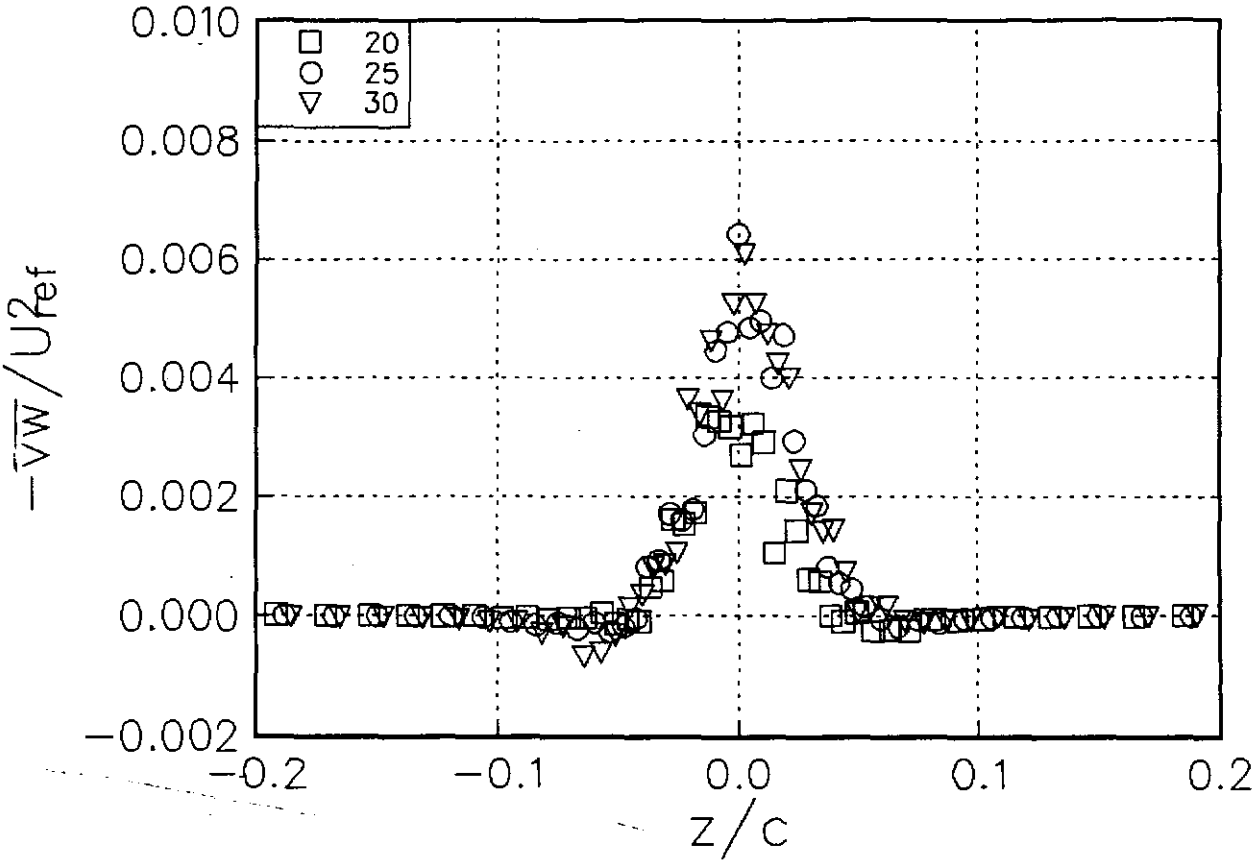

(f) $-\overline{vw}/U_{ref}^2$

Figure 3.13 Velocity profiles in the core region as a function of streamwise distance x/c for $Re_c = 400000$, $\alpha = 5.0^o$.

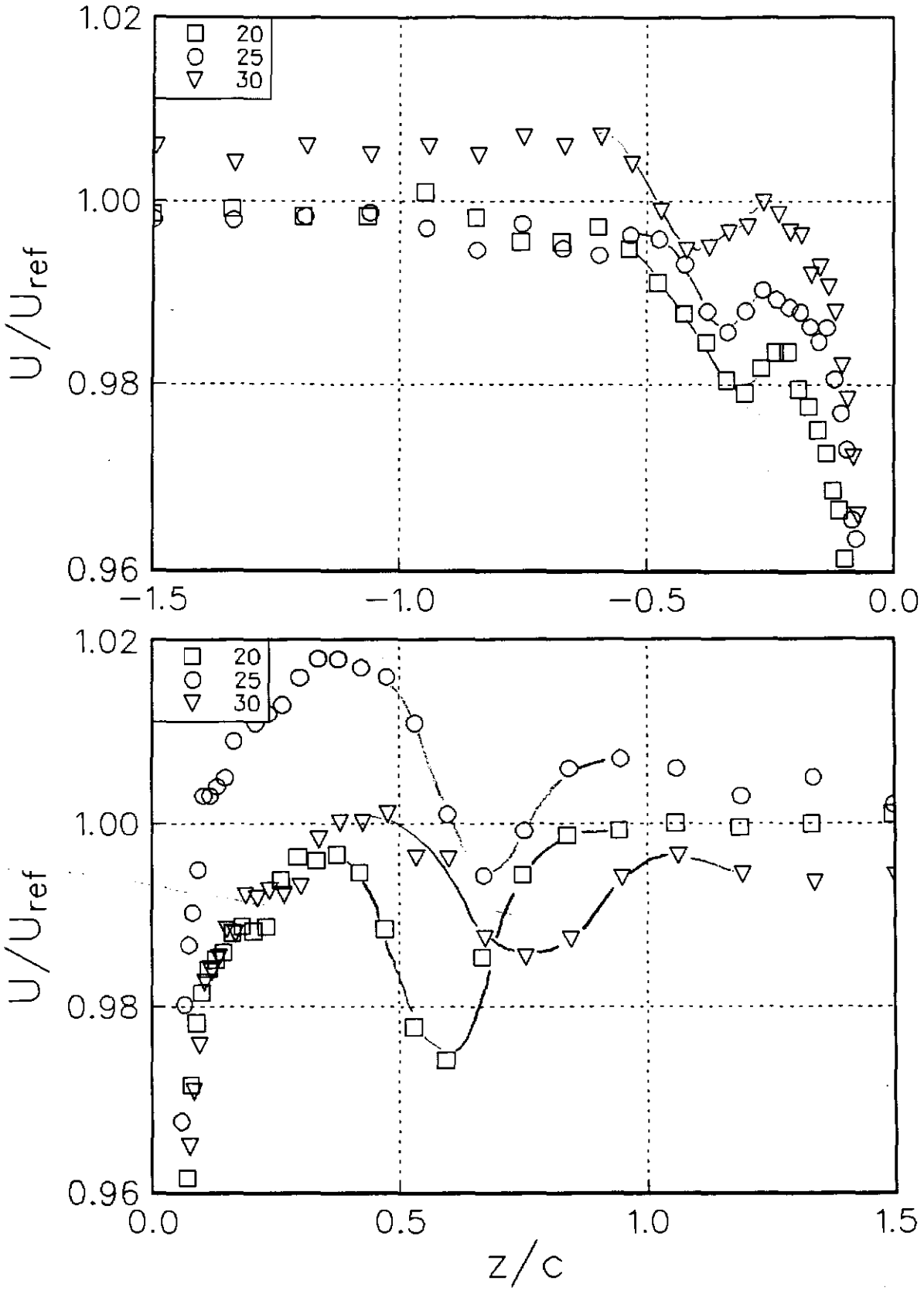

(a) U/U_{ref}

Figure 3.14 Velocity profiles in the wake region as a function of streamwise distance x/c for Re_c=400000, α=5.0°.

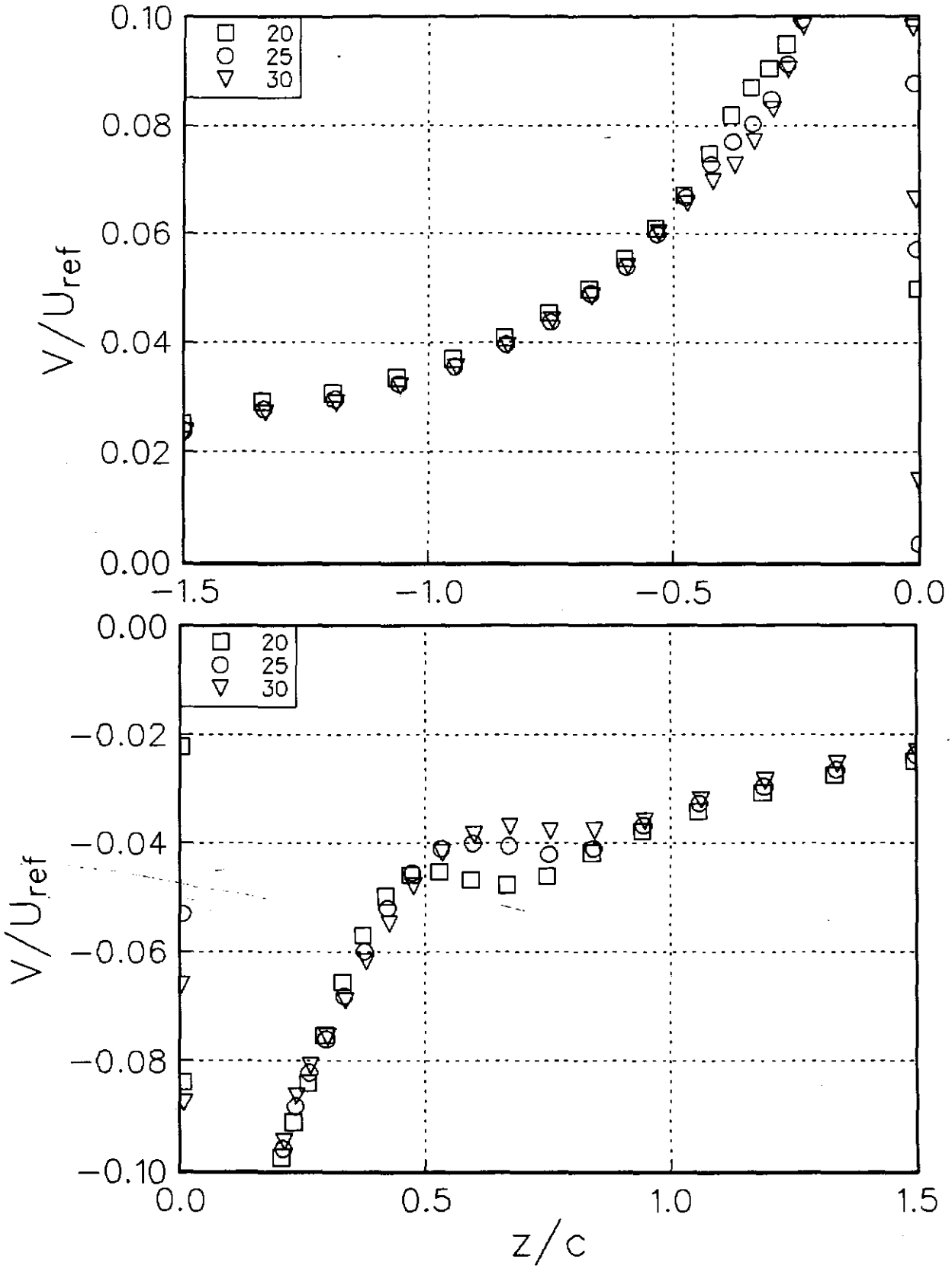

(b) V/U_{ref}

Figure 3.14 Velocity profiles in the wake region as a function of streamwise distance x/c for Re_c=400000, α=5.0°.

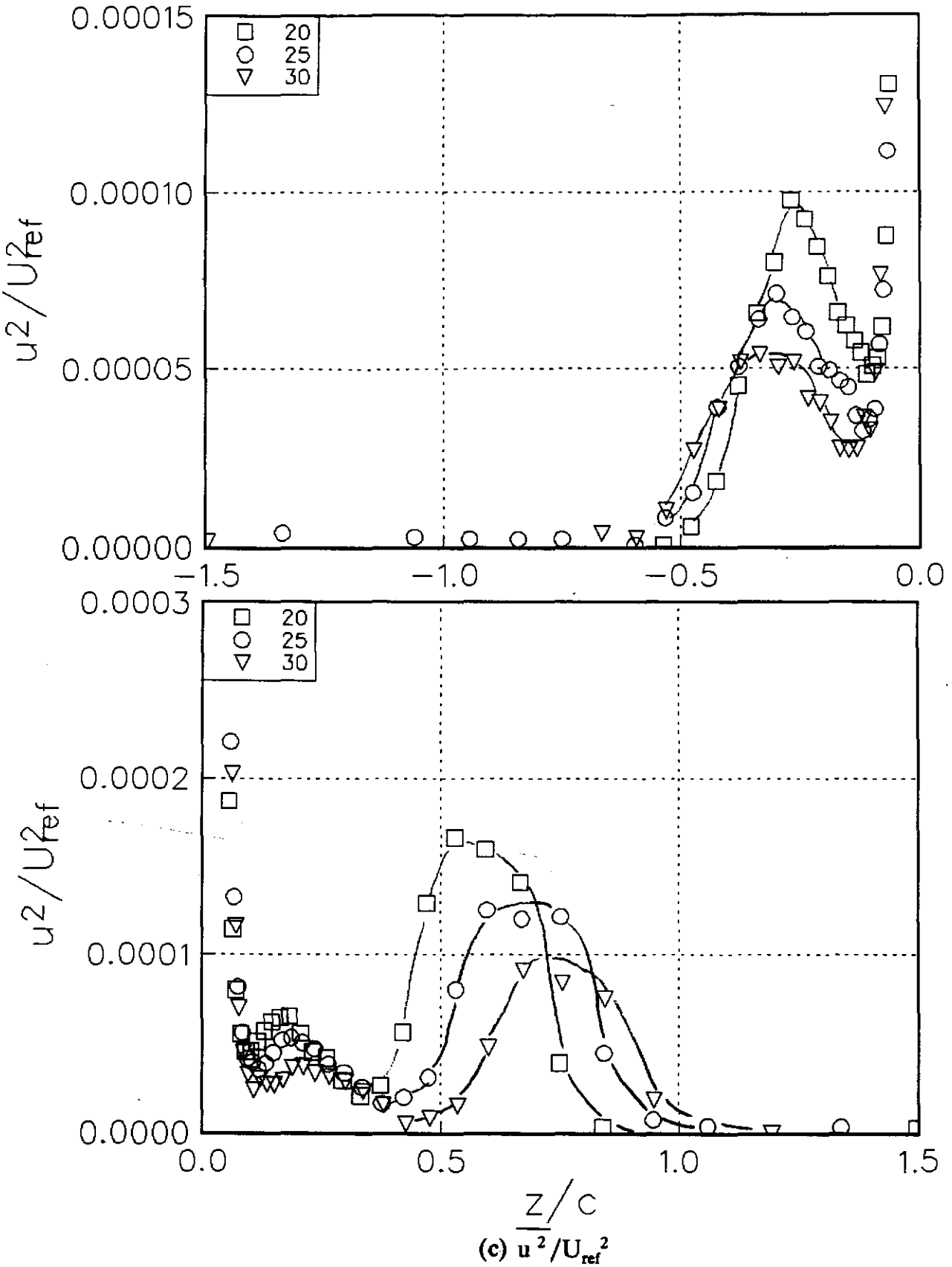

(c) $\overline{u^2}/U_{ref}^2$

Figure 3.14 Velocity profiles in the wake region as a function of streamwise distance x/c for Re_c=400000, α=5.0°.

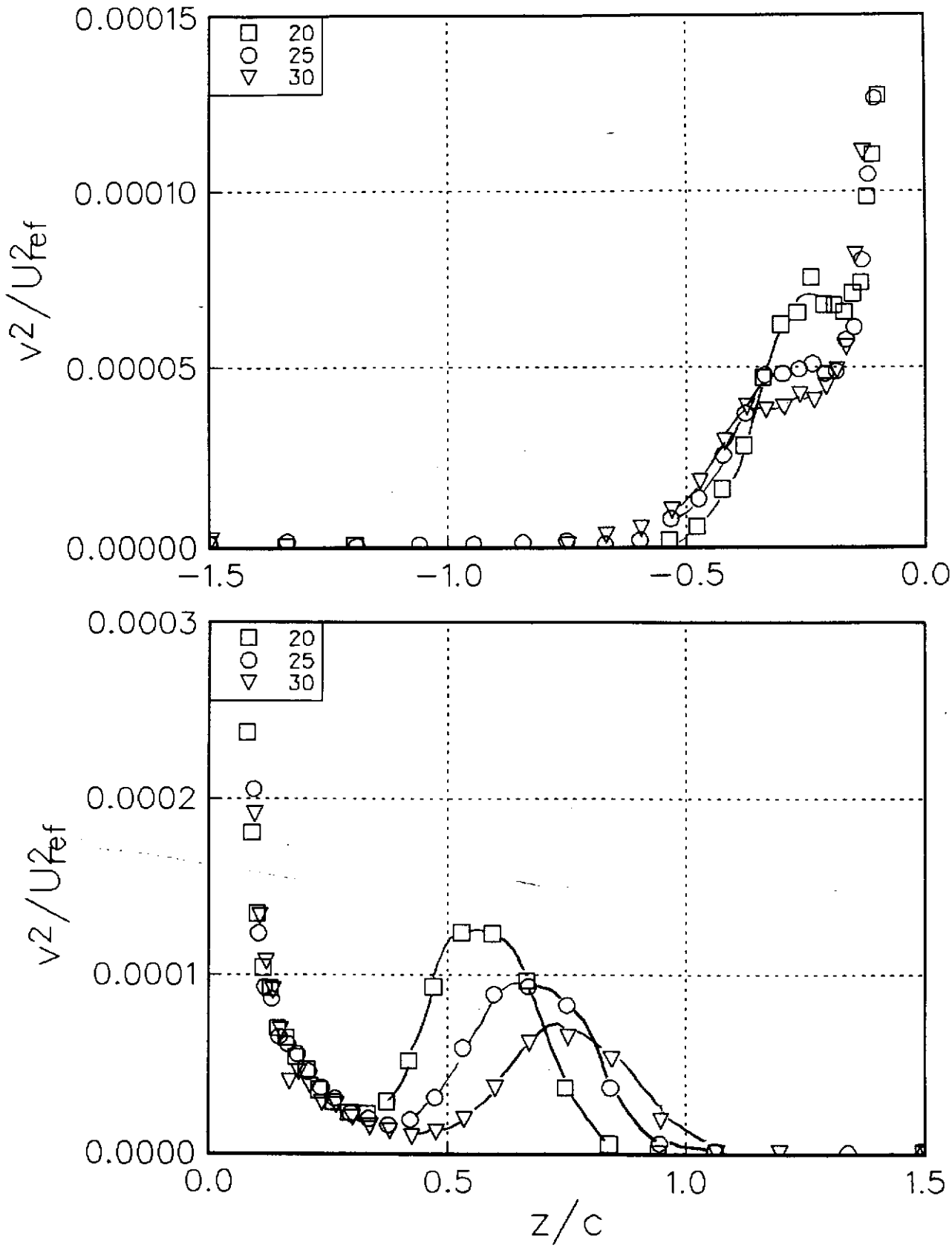

(d) $\overline{v^2}/U_{ref}^2$

Figure 3.14 Velocity profiles in the wake region as a function of streamwise distance x/c for Re_c=400000, α=5.0°.

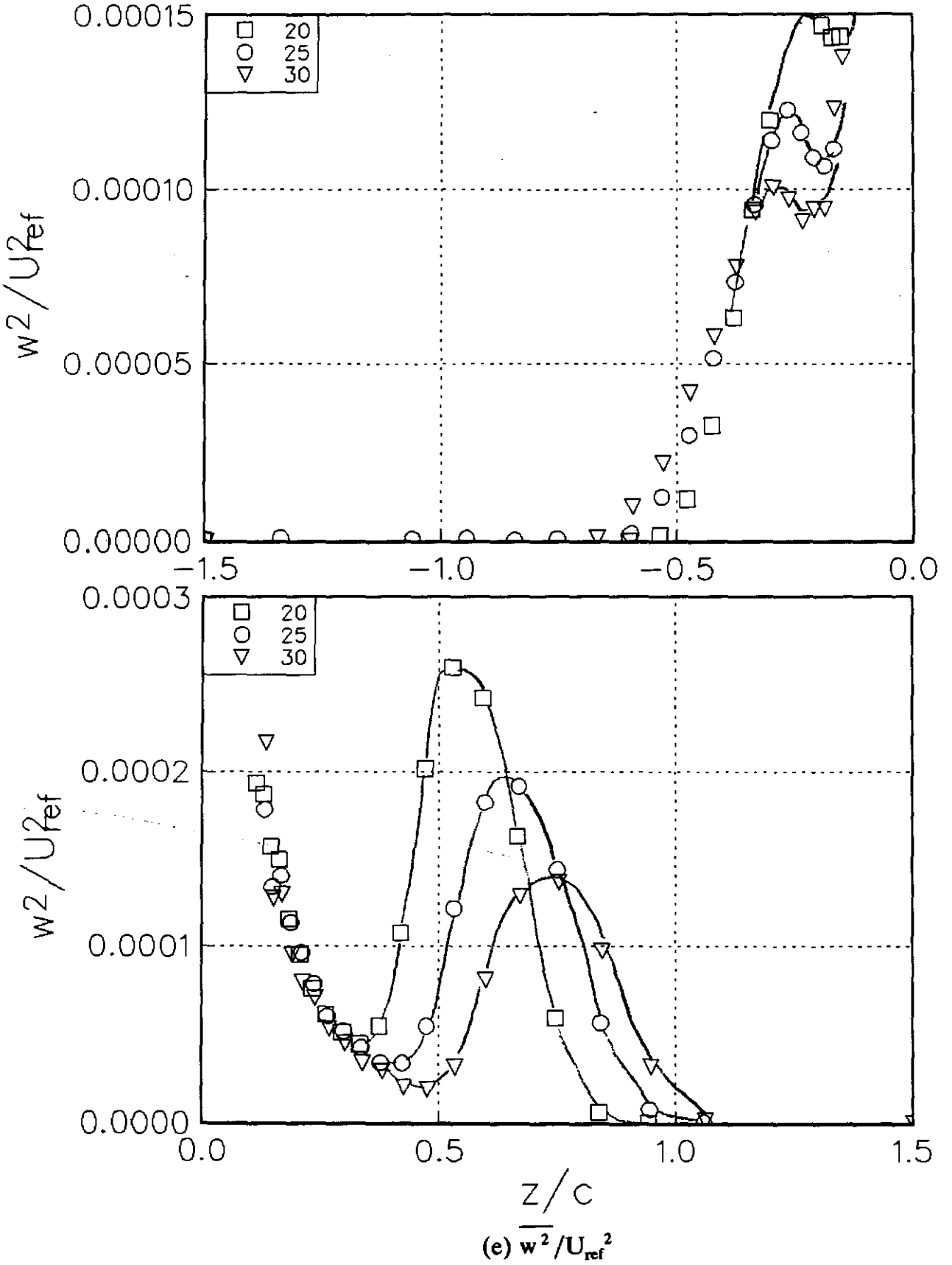

Figure 3.14 Velocity profiles in the wake region as a function of streamwise distance x/c for Re_c=400000, α=5.0°.

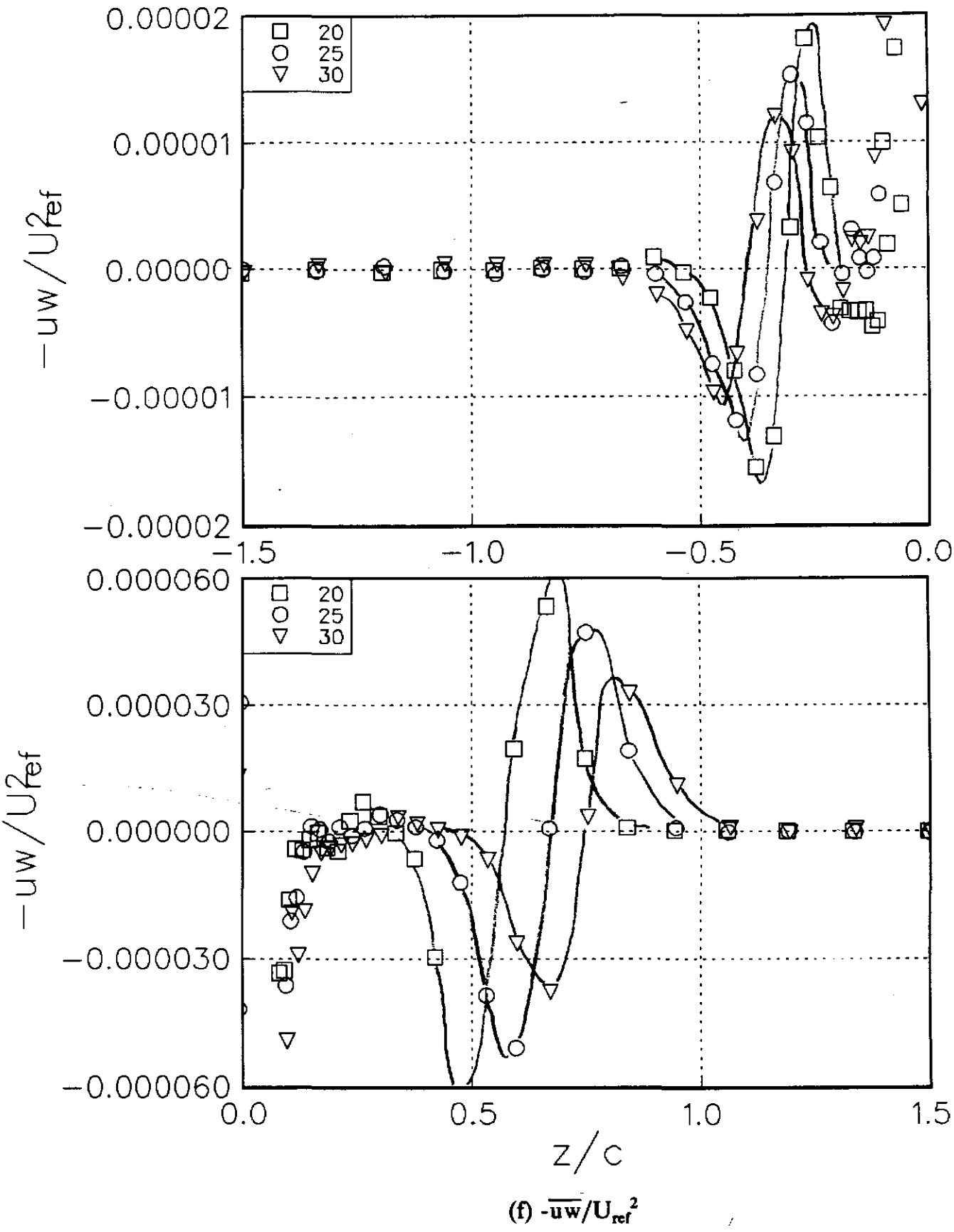

(f) $-\overline{uw}/U_{ref}^2$

Figure 3.14 Velocity profiles in the wake region as a function of streamwise distance x/c for $Re_c = 400000$, $\alpha = 5.0°$.

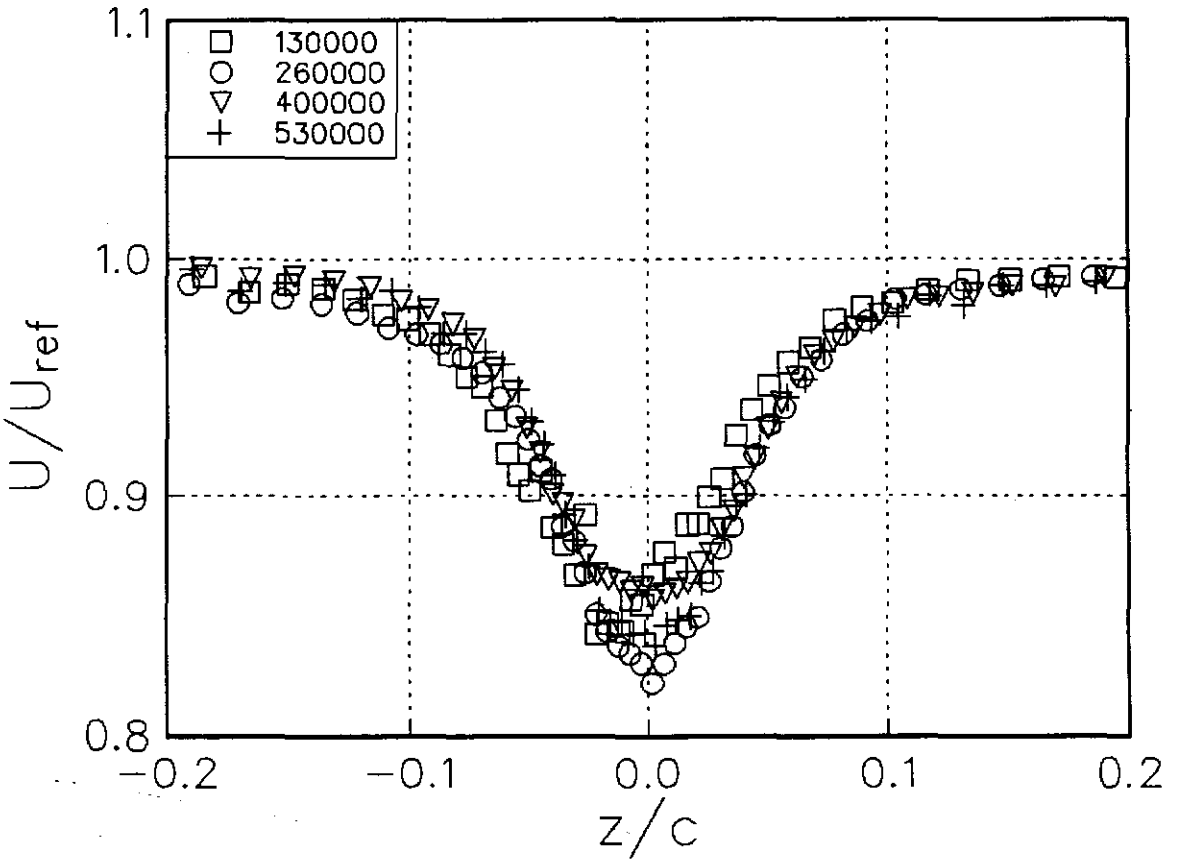

(a) U/U_{ref}

Figure 3.15 Velocity profiles in the core region as a function of Reynolds number Re_c for $x/c=30$, $\alpha=5.0°$.

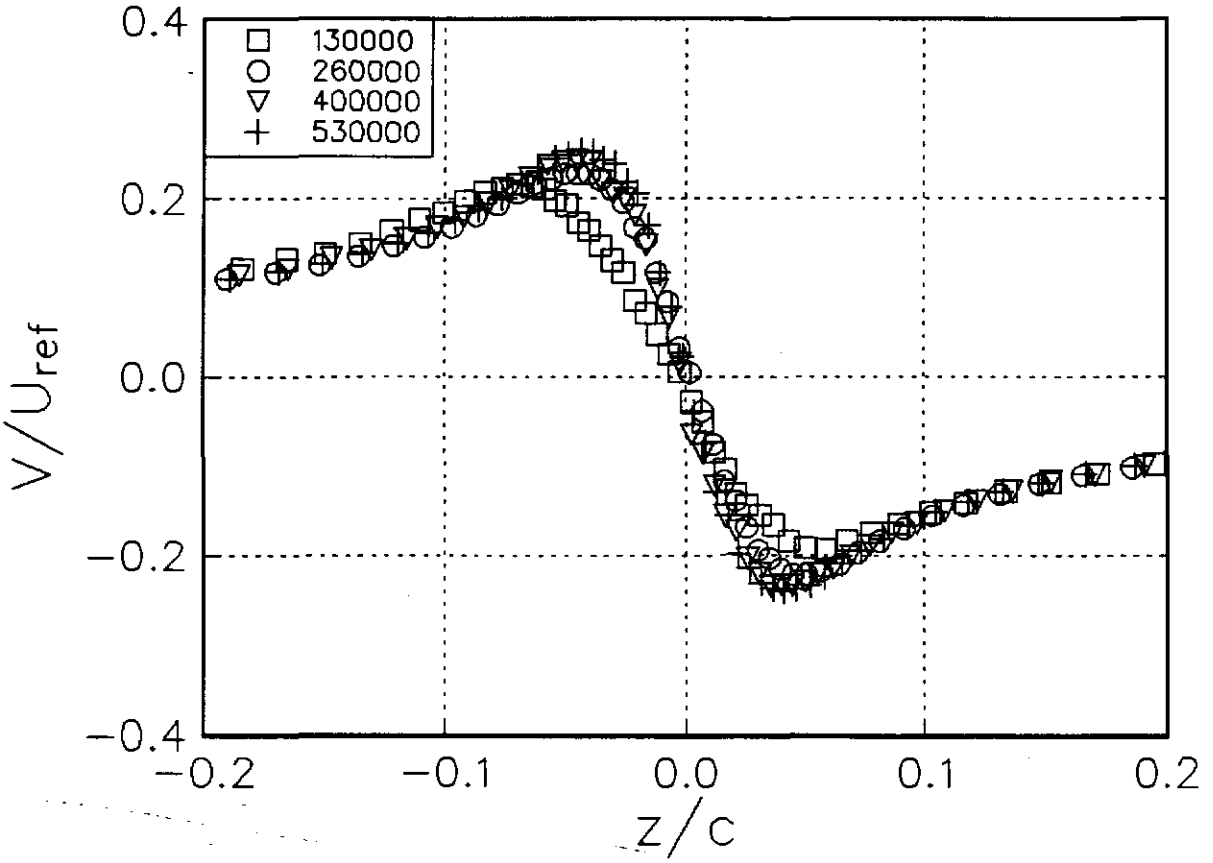

(b) V/U_{ref}

Figure 3.15 Velocity profiles in the core region as a function of Reynolds number Re_c for $x/c=30$, $\alpha=5.0°$.

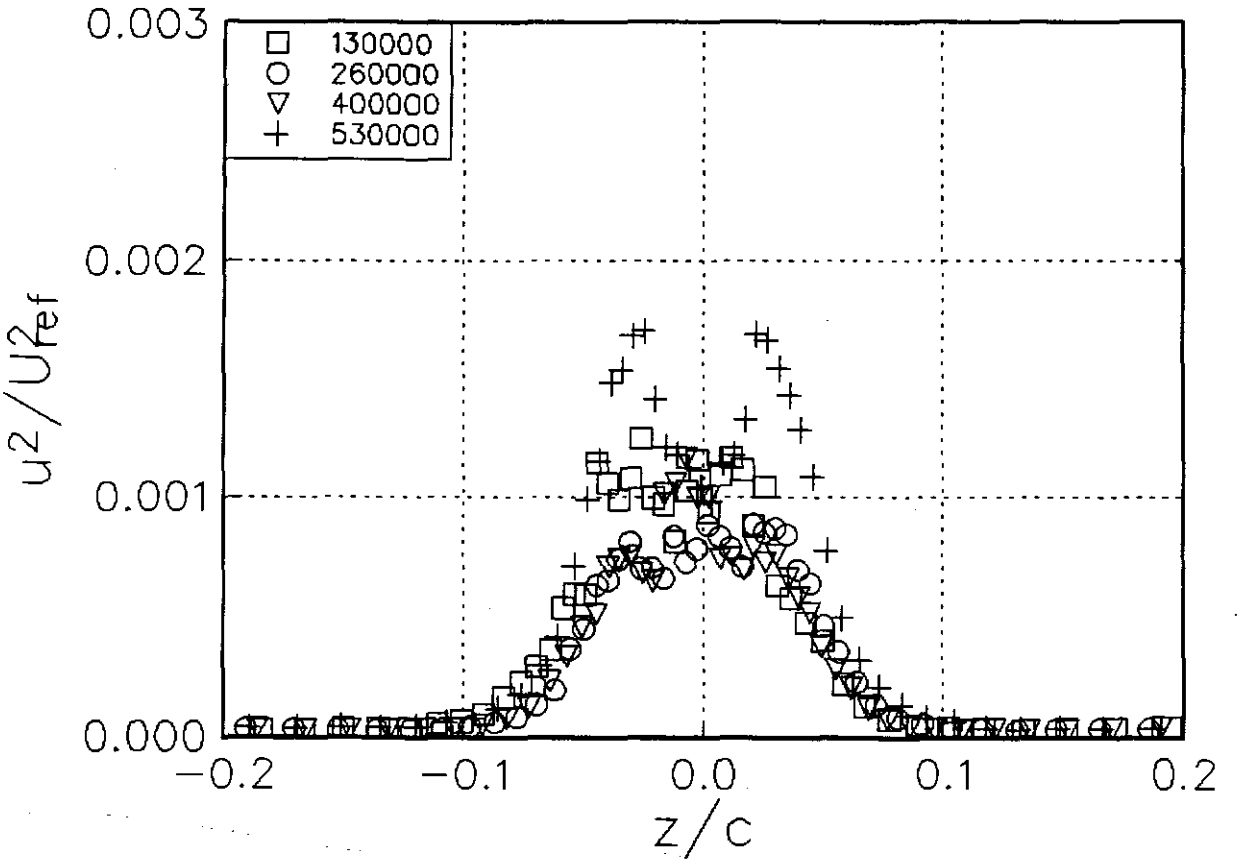

(c) $\overline{u^2}/U_{ref}^2$

Figure 3.15 Velocity profiles in the core region as a function of Reynolds number Re_c for $x/c=30$, $\alpha=5.0°$.

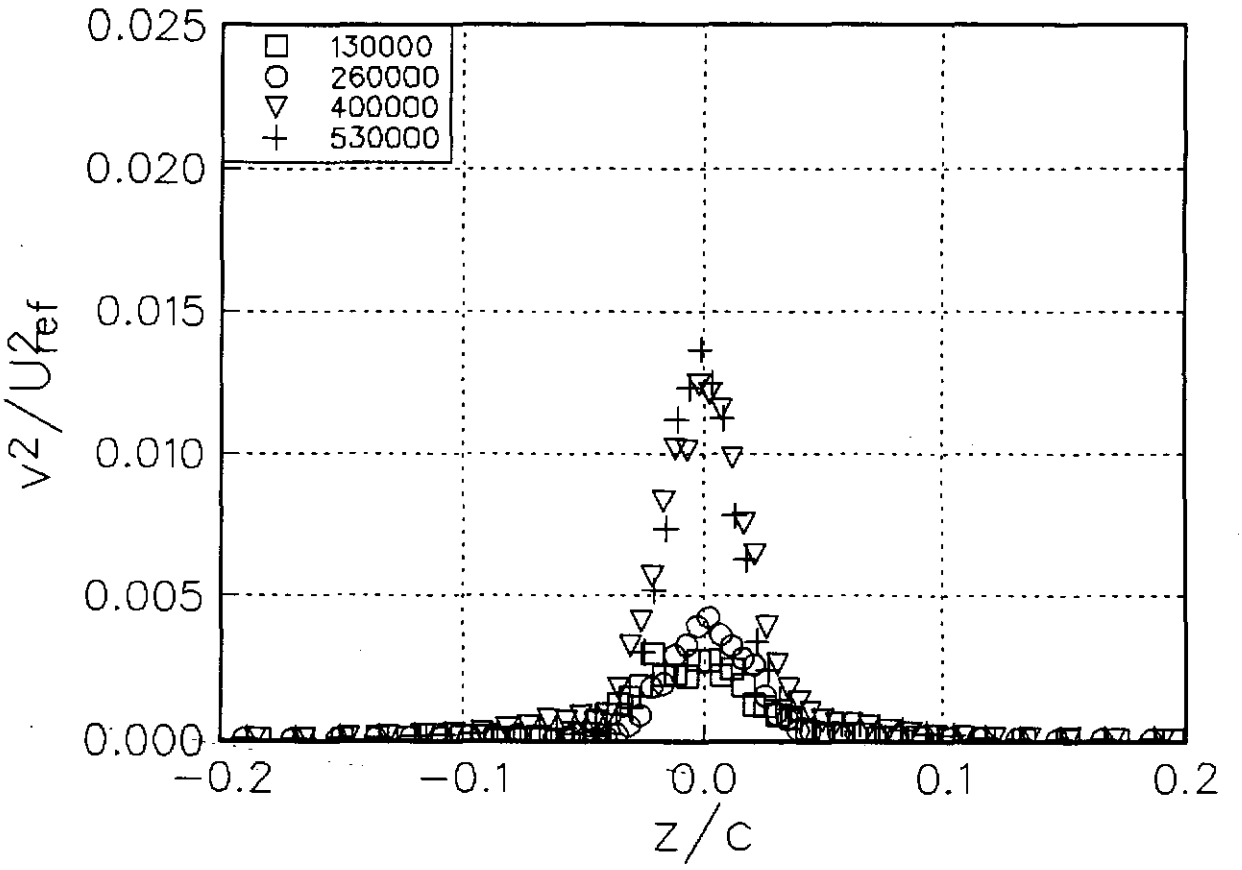

(d) $\overline{v^2}/U_{ref}^2$

Figure 3.15 Velocity profiles in the core region as a function of Reynolds number Re_c for $x/c=30$, $\alpha=5.0°$.

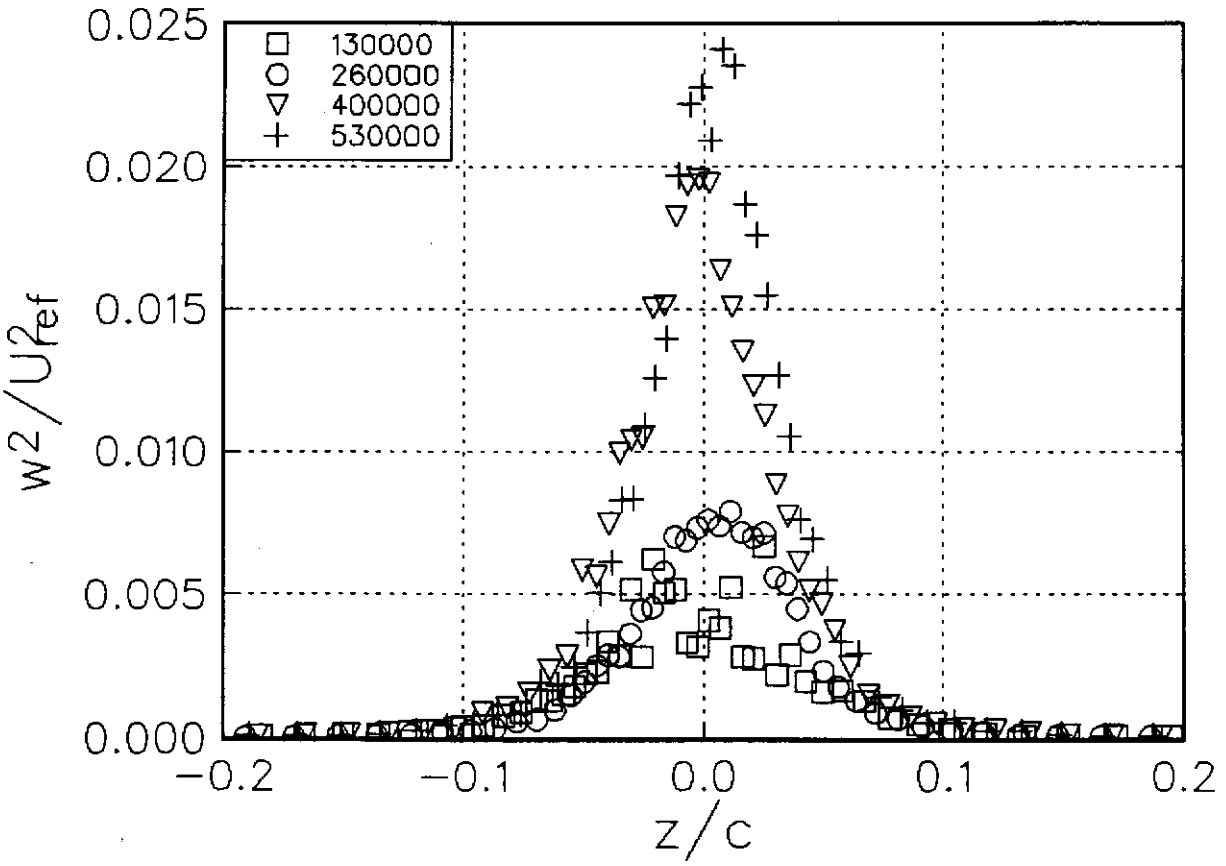

(e) $\overline{w^2}/U_{ref}^2$

Figure 3.15 Velocity profiles in the core region as a function of Reynolds number Re_c for $x/c=30$, $\alpha=5.0°$.

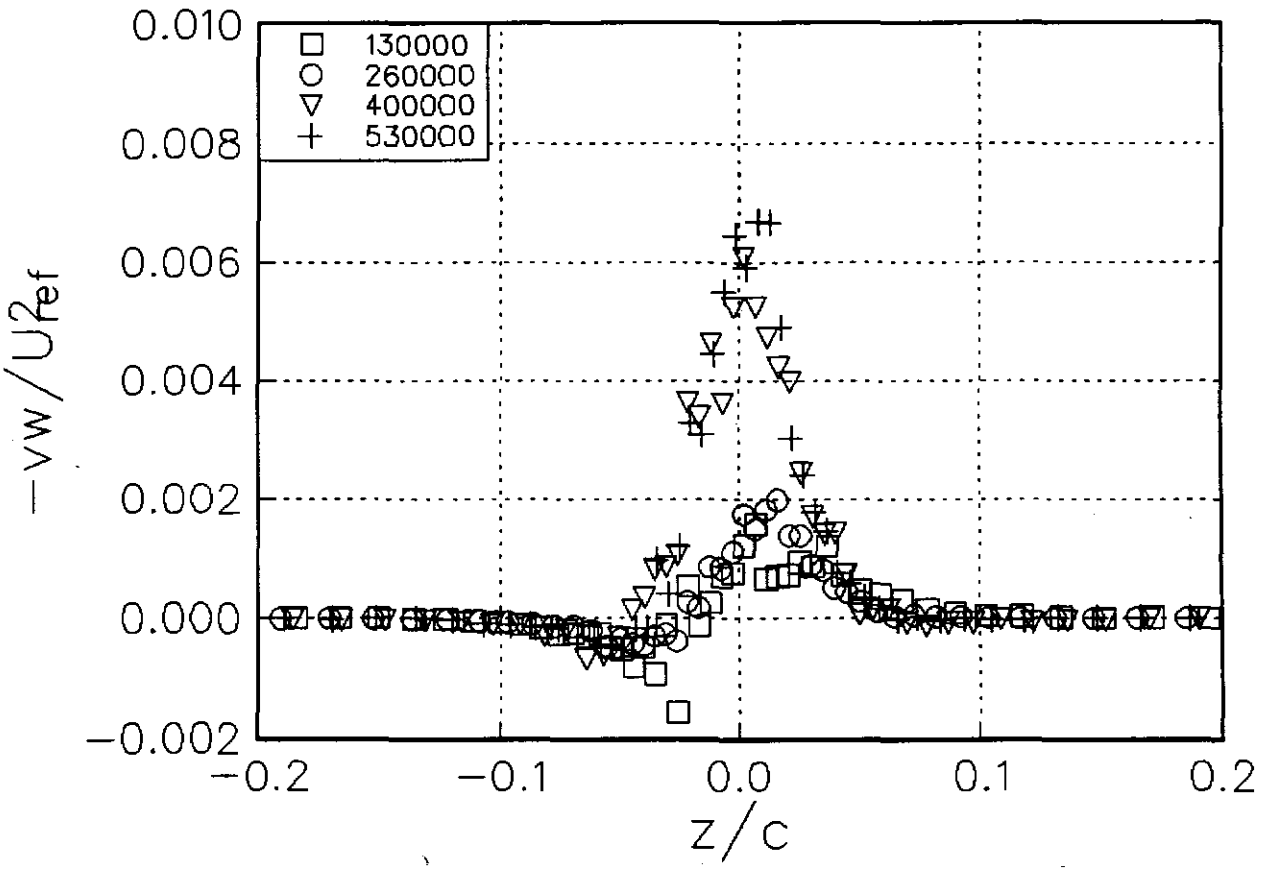

(f) $-\overline{vw}/U_{ref}^2$

Figure 3.15 Velocity profiles in the core region as a function of Reynolds number Re_c for $x/c=30$, $\alpha=5.0°$.

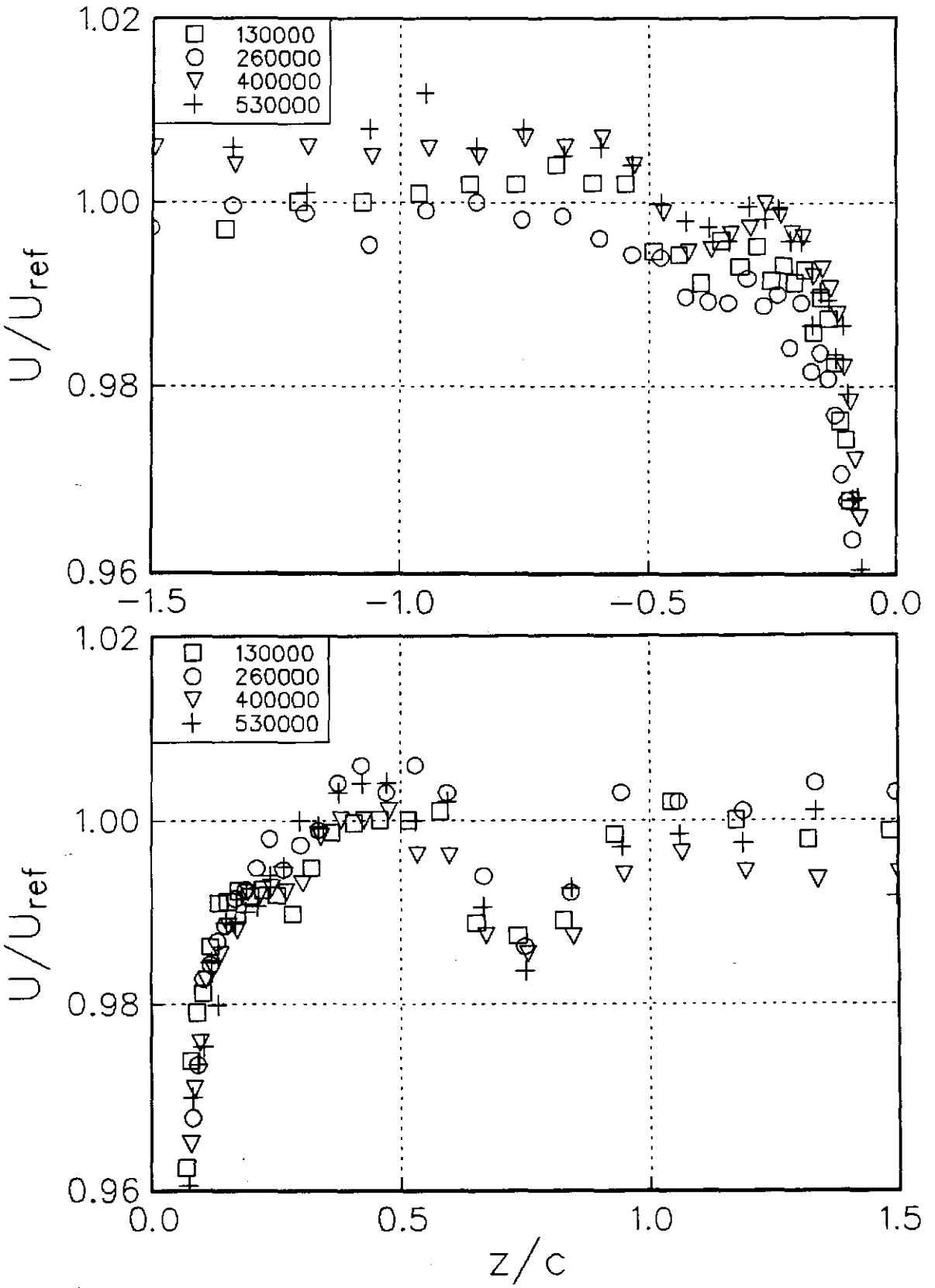

(a) U/U_{ref}

Figure 3.16 Velocity profiles in the wake region as a function of Reynolds number Re_c for $x/c=30$, $\alpha=5.0°$.

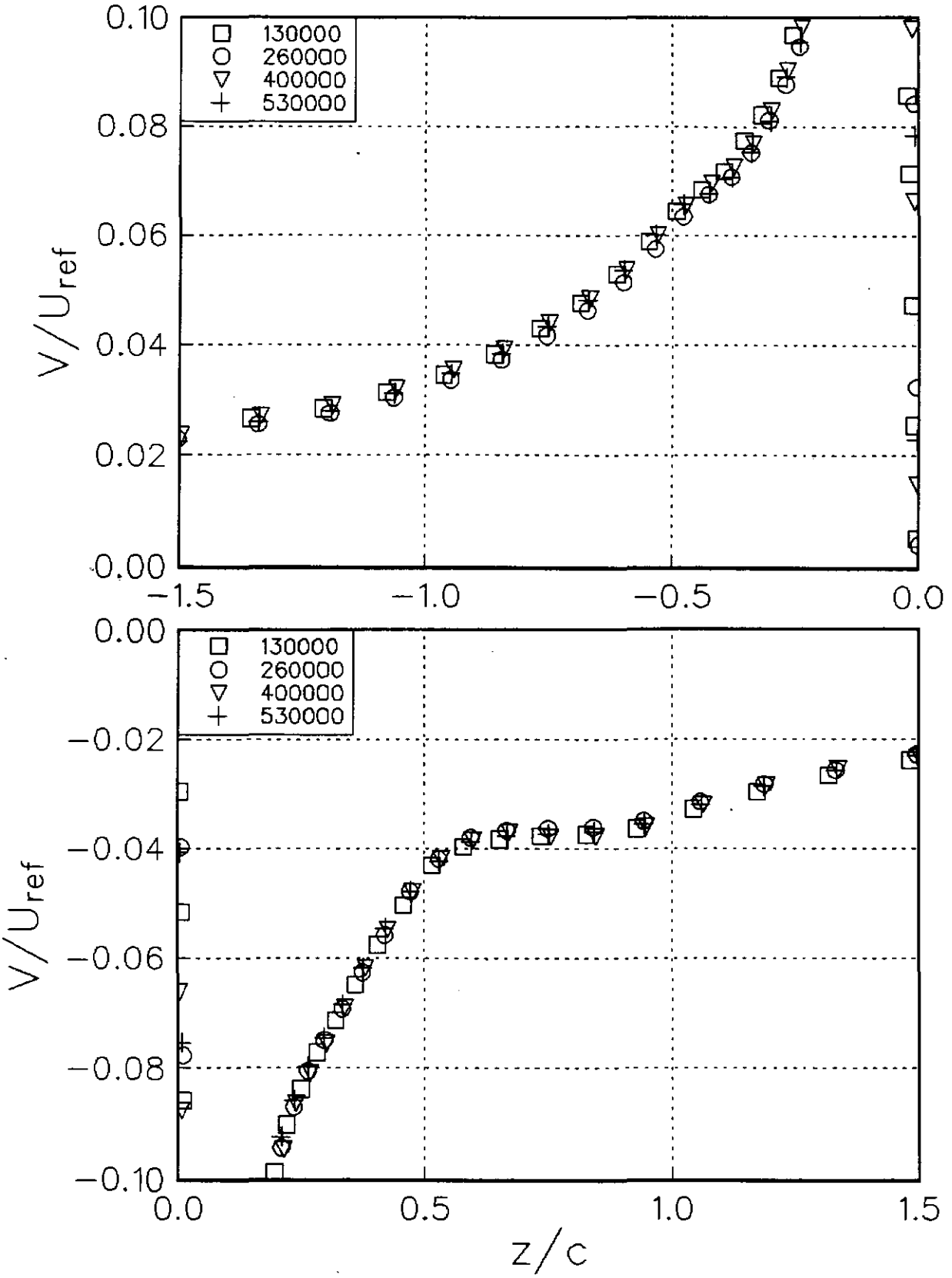

(b) V/U_{ref}

Figure 3.16 Velocity profiles in the wake region as a function of Reynolds number Re_c for $x/c=30$, $\alpha=5.0°$.

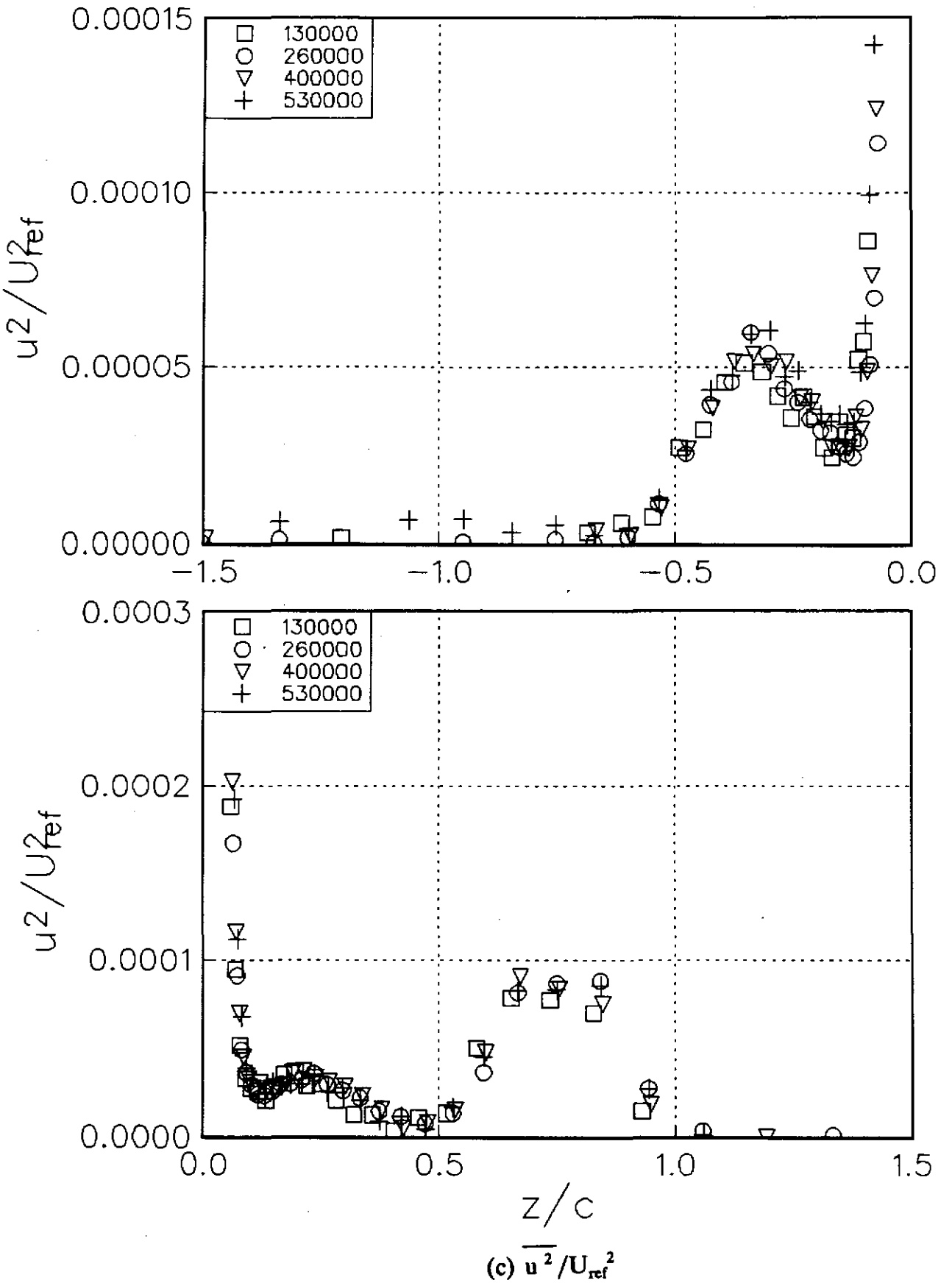

(c) $\overline{u^2}/U_{ref}^2$

Figure 3.16 Velocity profiles in the wake region as a function of Reynolds number Re_c for $x/c=30$, $\alpha=5.0°$.

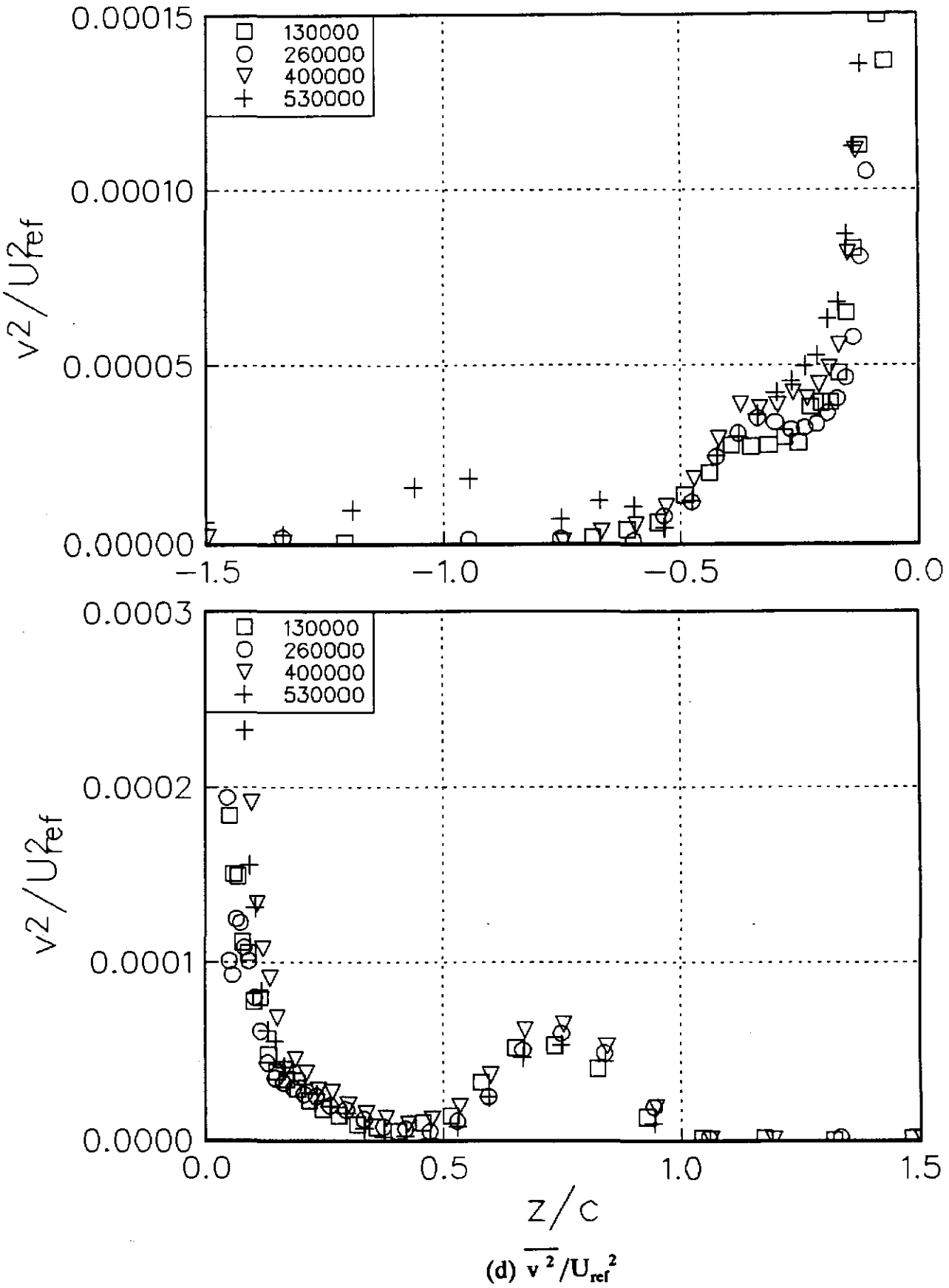

(d) $\overline{v^2}/U_{ref}^2$

Figure 3.16 Velocity profiles in the wake region as a function of Reynolds number Re_c for x/c=30, α=5.0°.

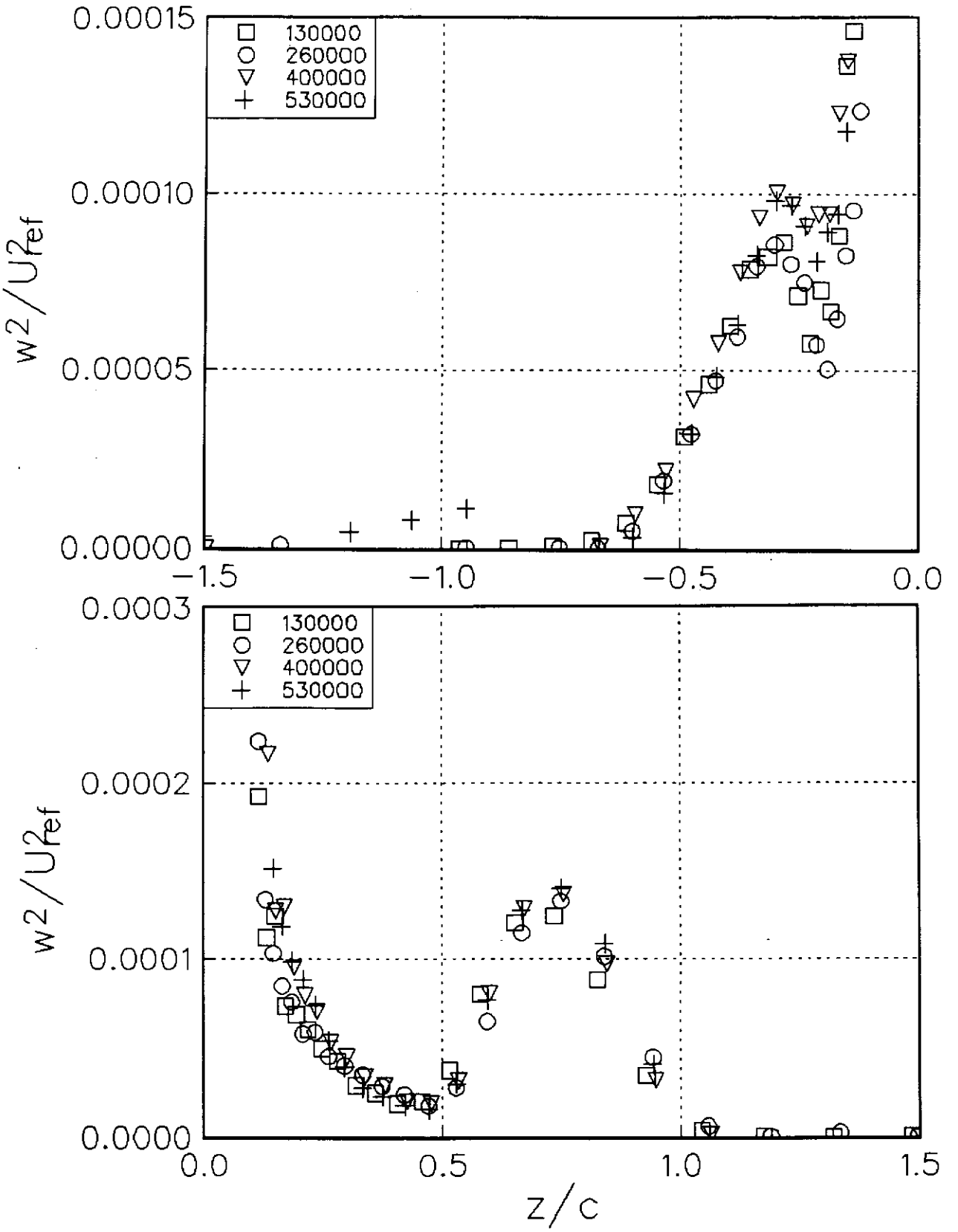

(e) $\overline{w^2}/U_{ref}^2$

Figure 3.16 Velocity profiles in the wake region as a function of Reynolds number Re_c for x/c=30, α=5.0°.

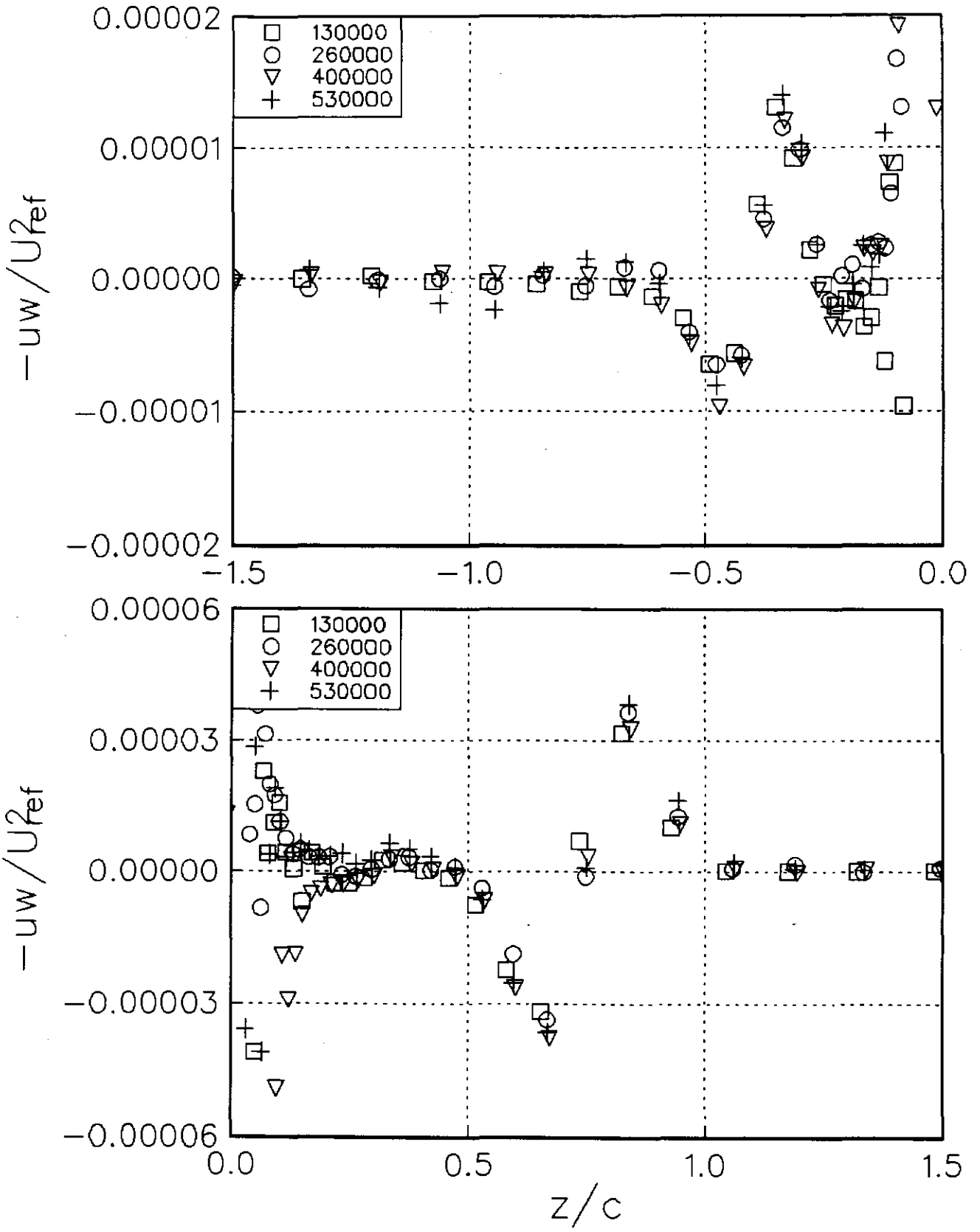

(f) $-\overline{uw}/U_{ref}^2$

Figure 3.16 Velocity profiles in the wake region as a function of Reynolds number Re_c for $x/c=30$, $\alpha=5.0°$.

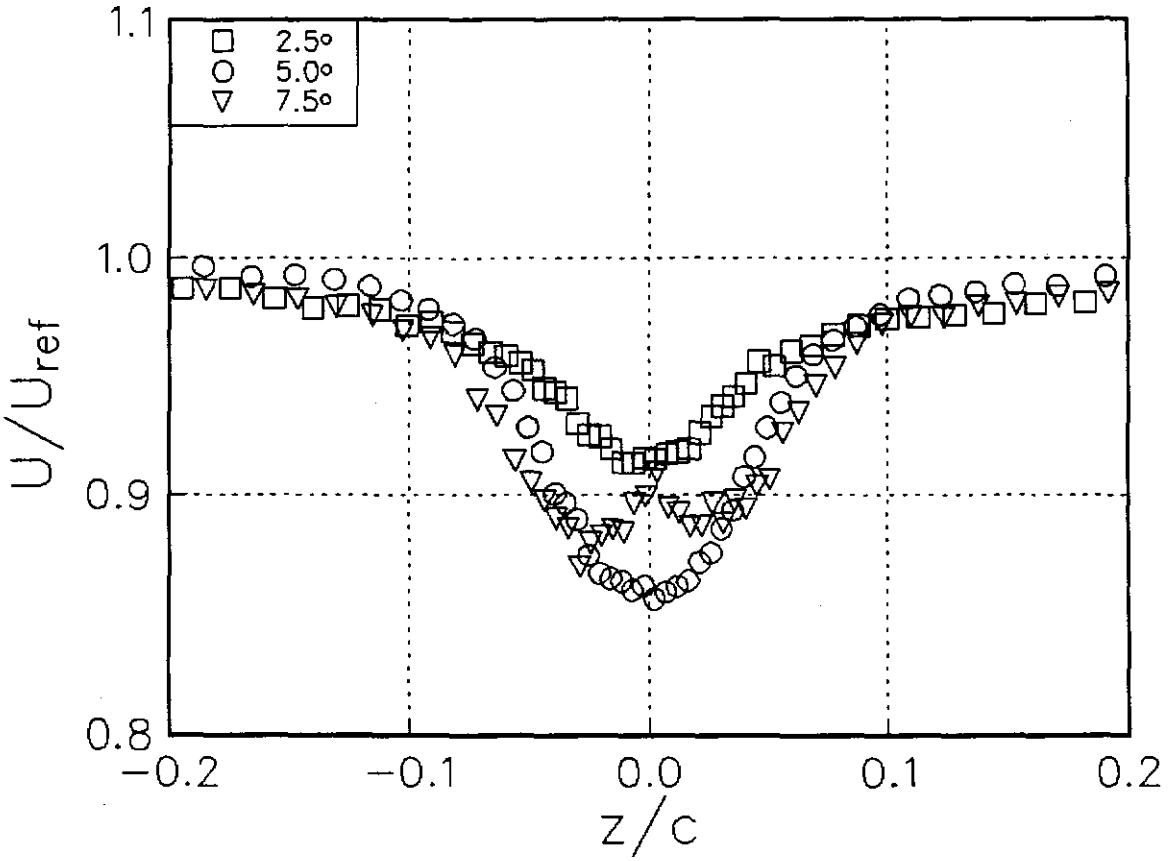

(a) U/U_{ref}

Figure 3.17 Velocity profiles in the core region as a function of angle of attack α for Re_c=400000, x/c=30.

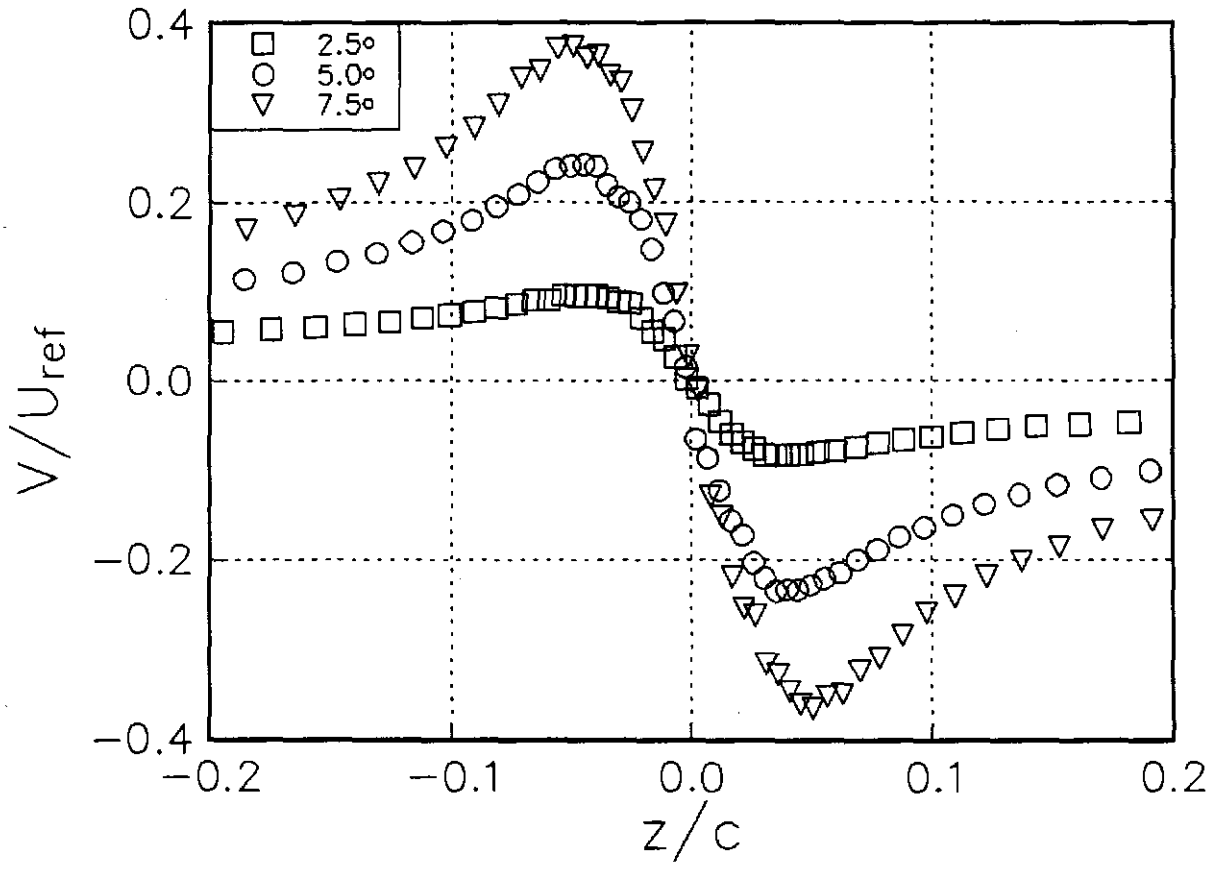

(b) V/U_{ref}

Figure 3.17 Velocity profiles in the core region as a function of angle of attack α for Re_c=400000, x/c=30.

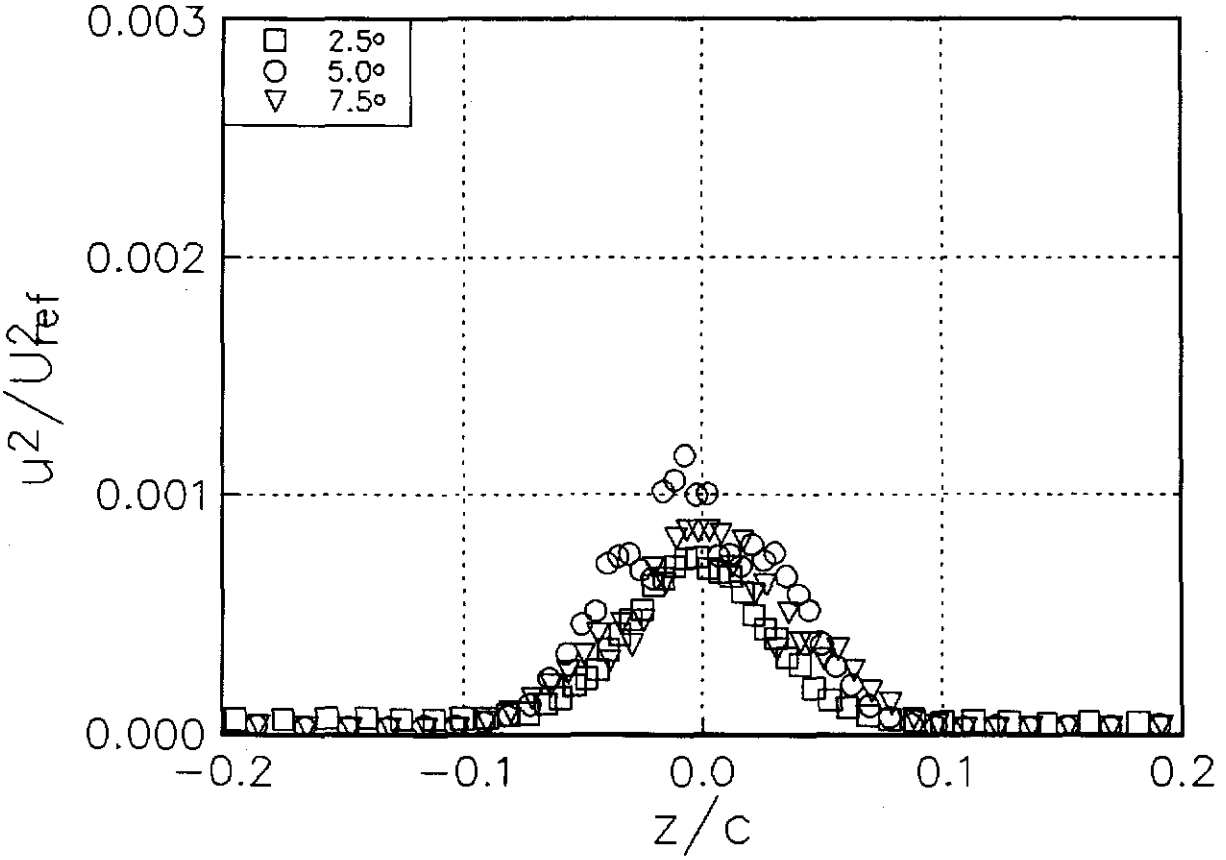

(c) $\overline{u^2}/U_{ref}^2$

Figure 3.17 Velocity profiles in the core region as a function of angle of attack α for Re_c=400000, x/c=30.

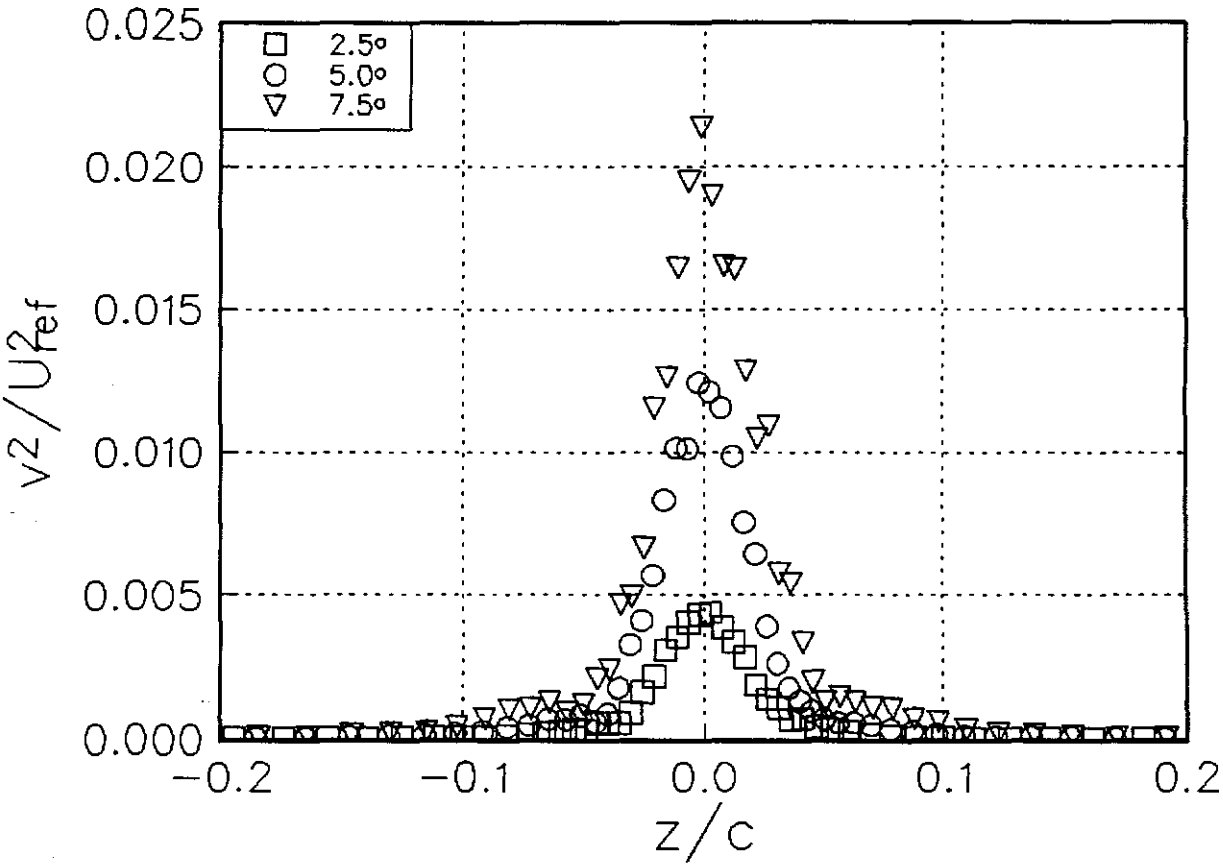

(d) $\overline{v^2}/U_{ref}^2$

Figure 3.17 Velocity profiles in the core region as a function of angle of attack α for Re_c=400000, x/c=30.

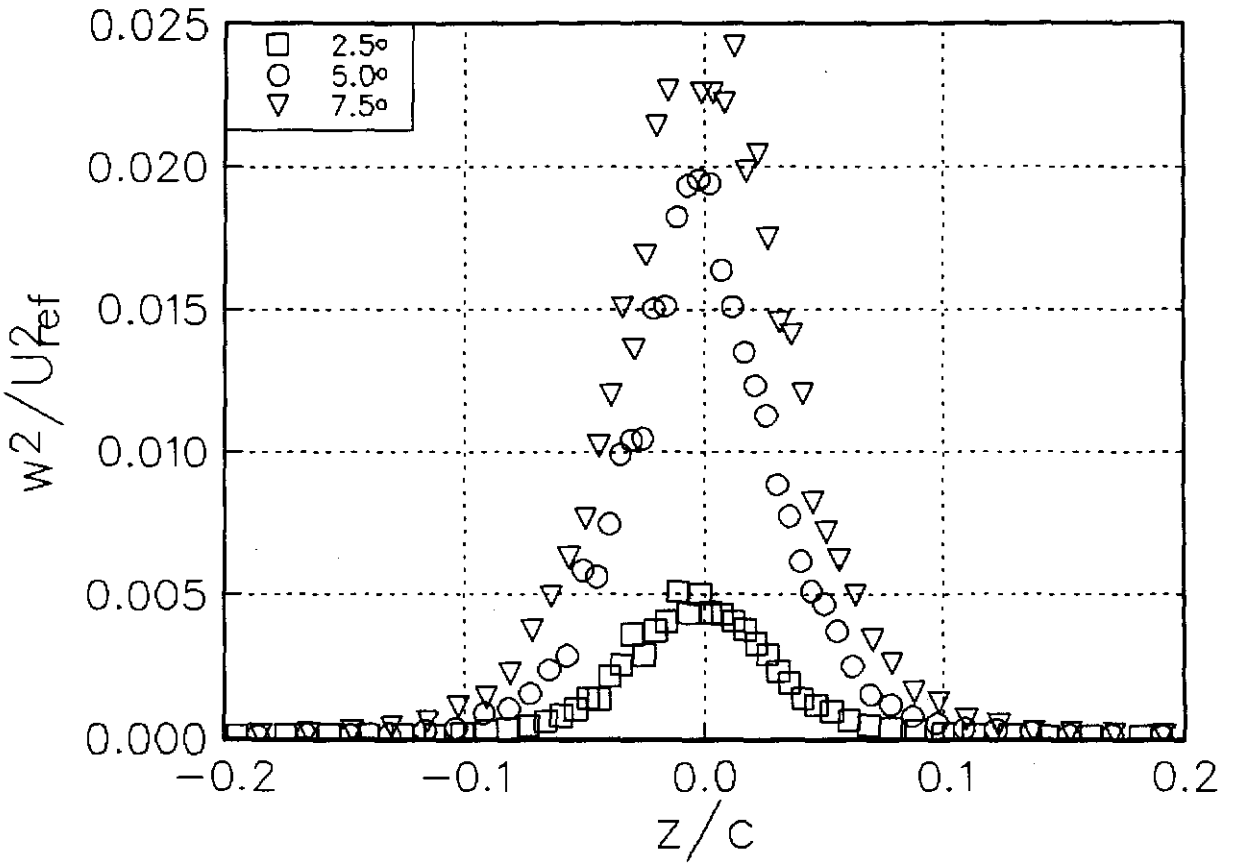

(e) $\overline{w^2}/U_{ref}^2$

Figure 3.17 Velocity profiles in the core region as a function of angle of attack α for Re_c=400000, x/c=30.

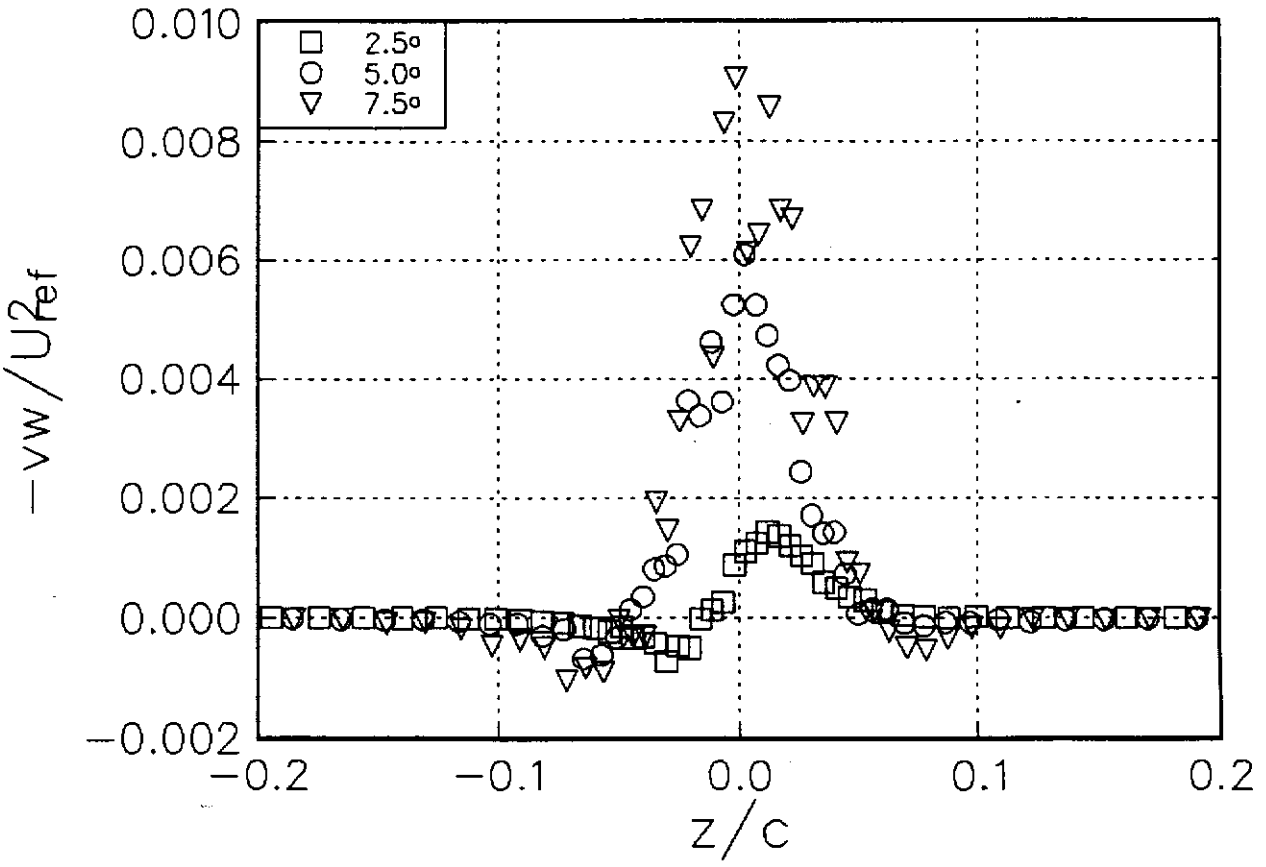

(f) $-\overline{vw}/U_{ref}^2$

Figure 3.17 Velocity profiles in the core region as a function of angle of attack α for Re_c=400000, x/c=30.

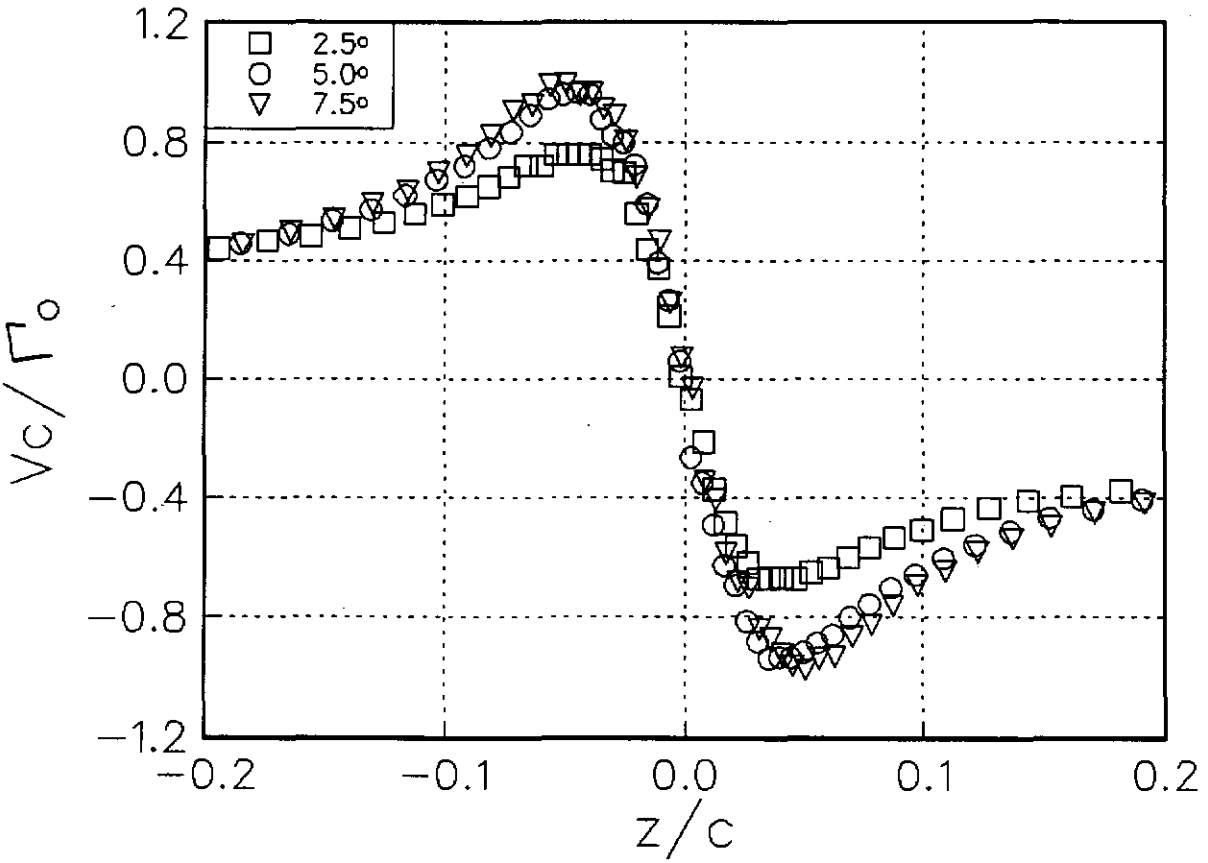

(g) Vc/Γ_0

Figure 3.17 Velocity profiles in the core region as a function of angle of attack α for Re_c=400000, x/c=30.

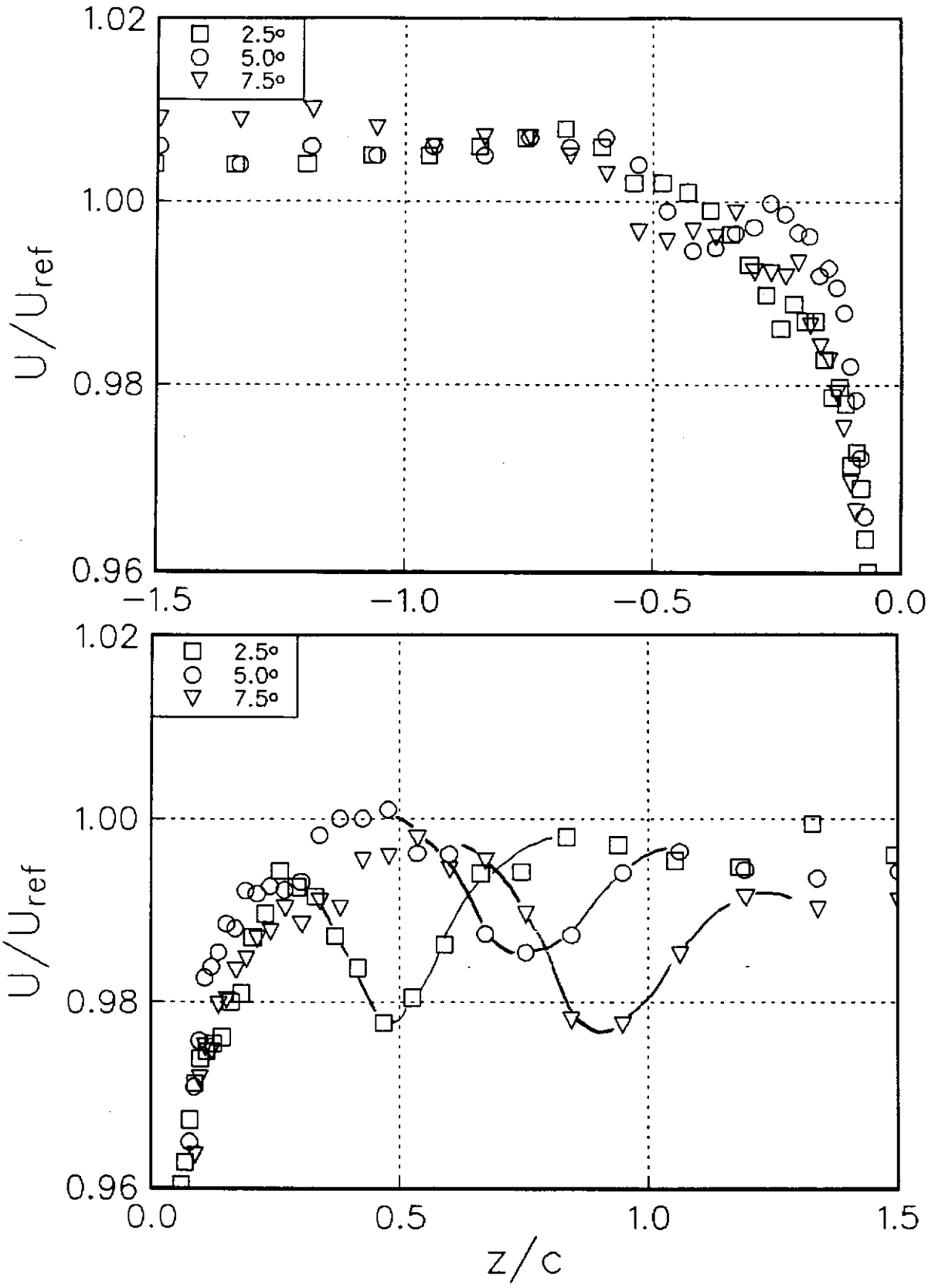

(a) U/U_{ref}

Figure 3.18 Velocity profiles in the wake region as a function of angle of attack α for $Re_c = 400000$, $x/c = 30$.

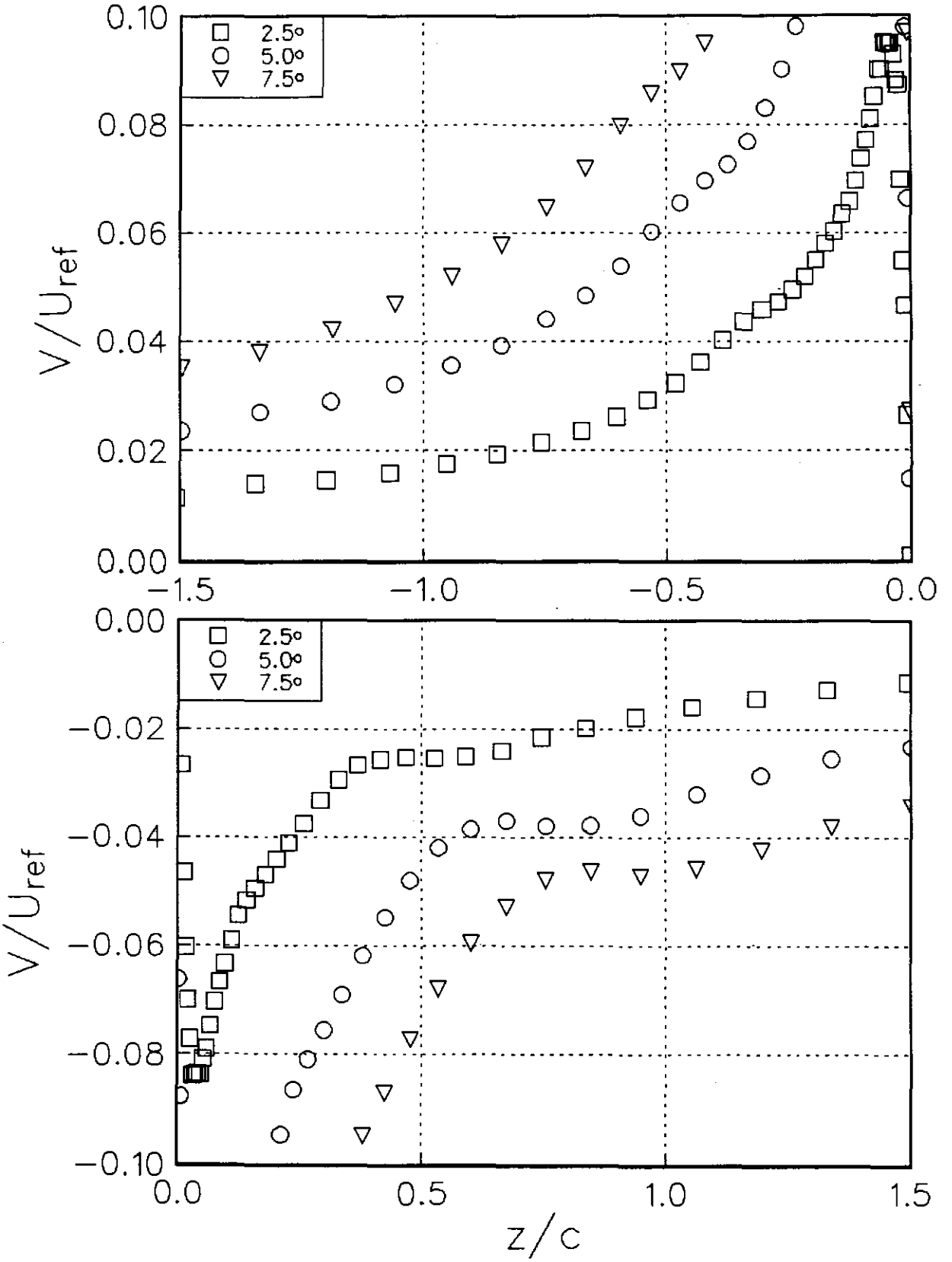

(b) V/U_{ref}

Figure 3.18 Velocity profiles in the wake region as a function of angle of attack α for $Re_c = 400000$, $x/c = 30$.

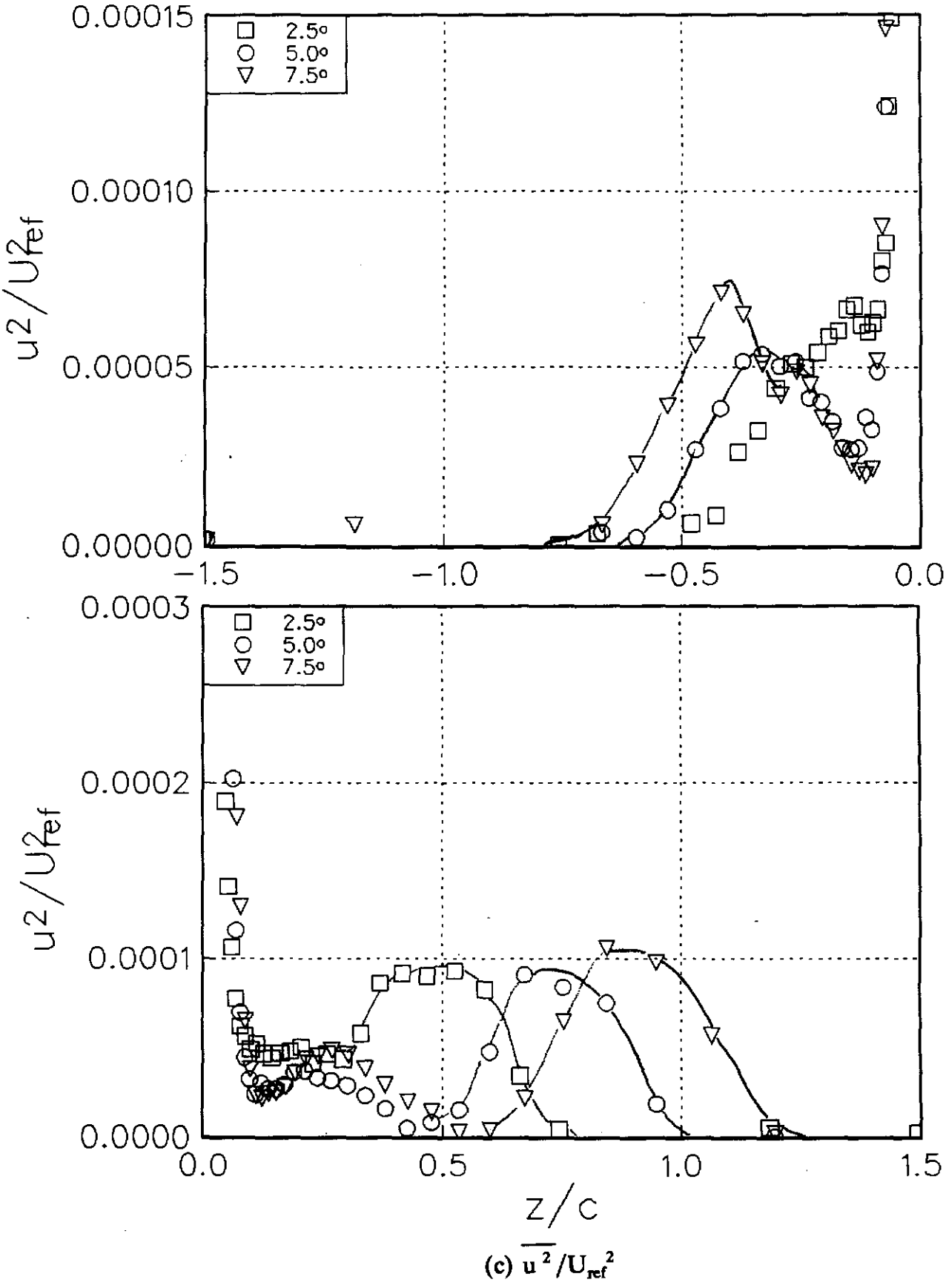

(c) $\overline{u^2}/U_{ref}^2$

Figure 3.18 Velocity profiles in the wake region as a function of angle of attack α for Re_c=400000, x/c=30.

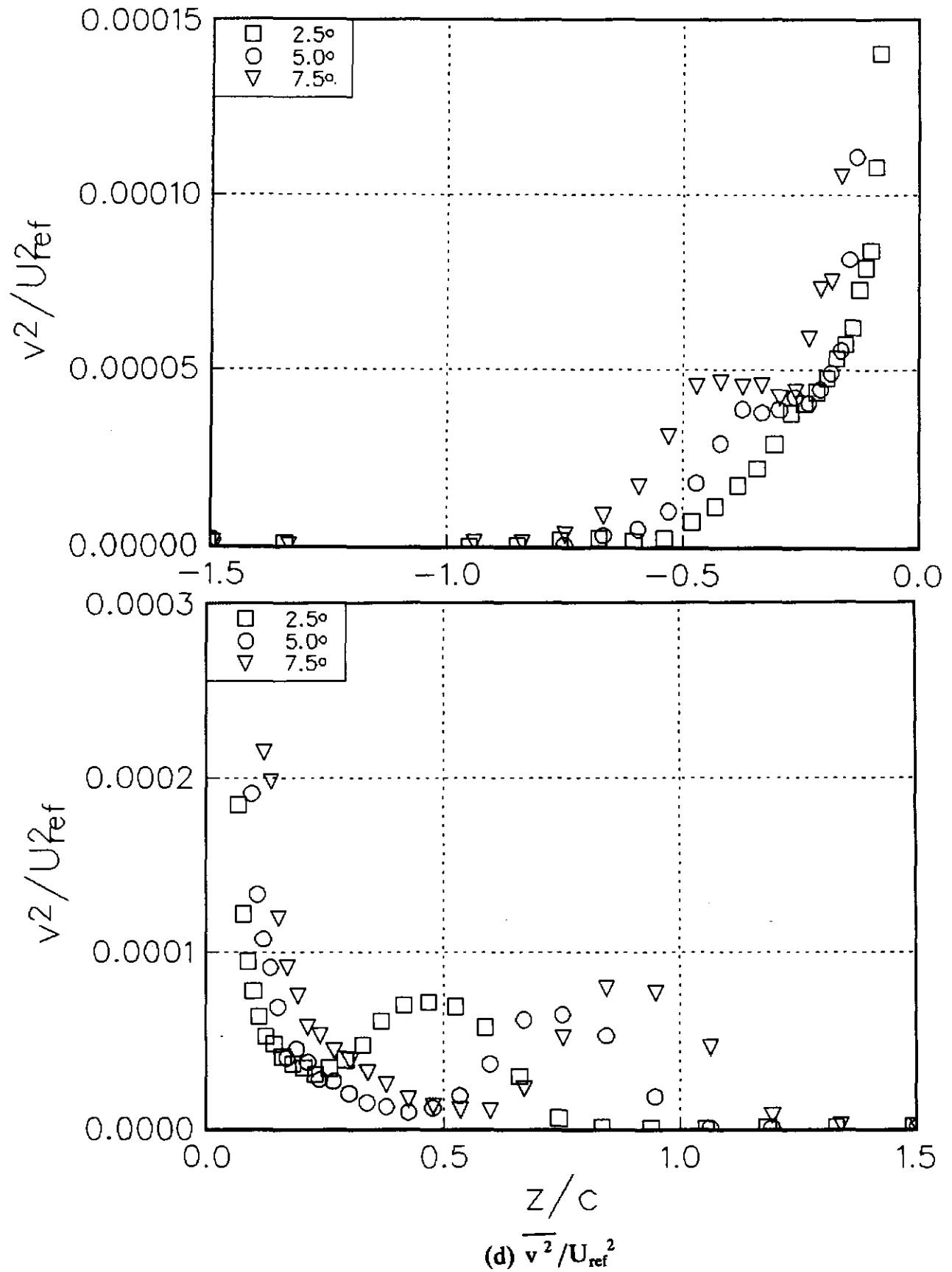

(d) $\overline{v^2}/U_{ref}^2$

Figure 3.18 Velocity profiles in the wake region as a function of angle of attack α for Re_c=400000, x/c=30.

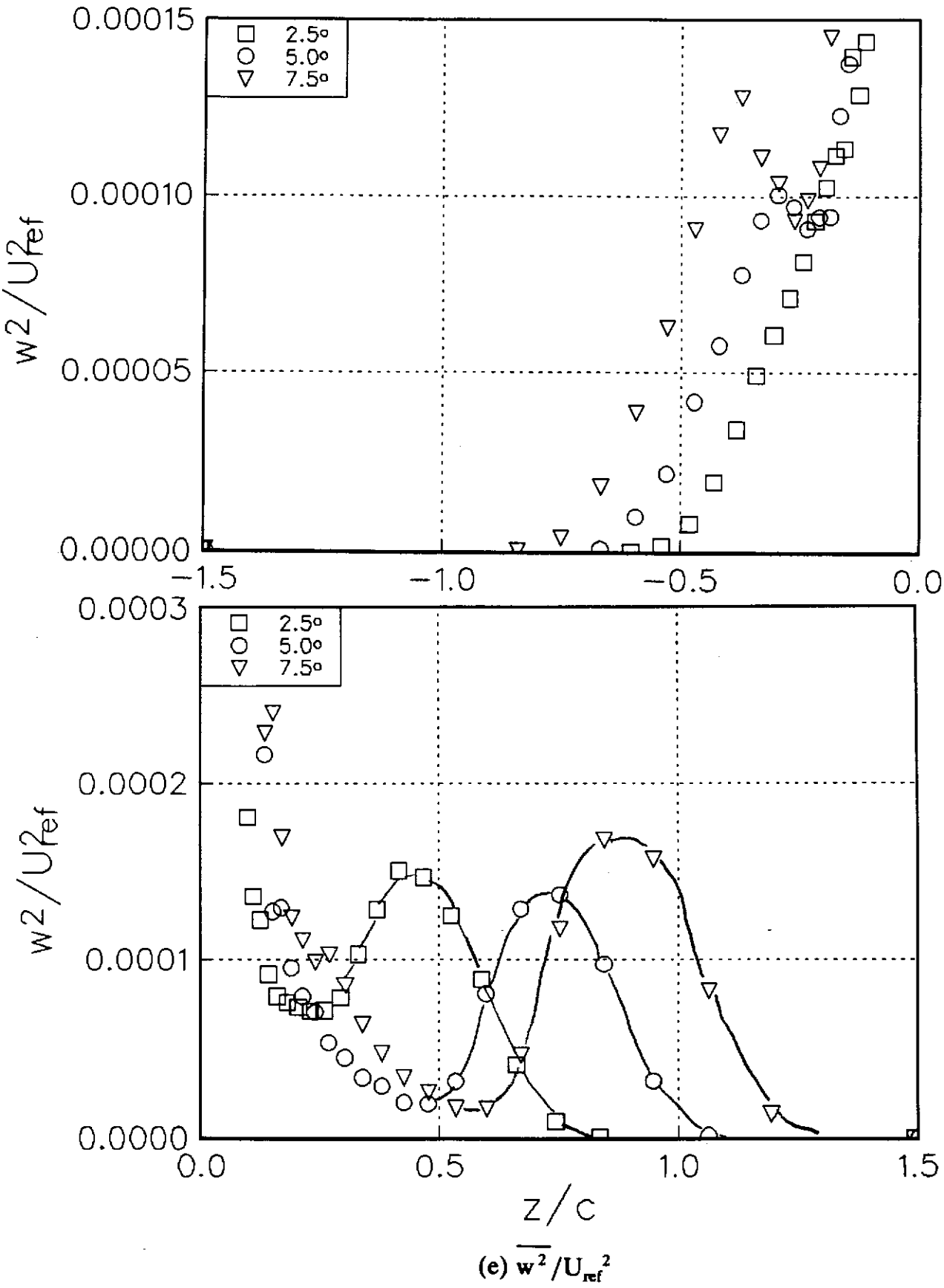

(e) $\overline{w^2}/U_{ref}^2$

Figure 3.18 Velocity profiles in the wake region as a function of angle of attack α for Re_c=400000, x/c=30.

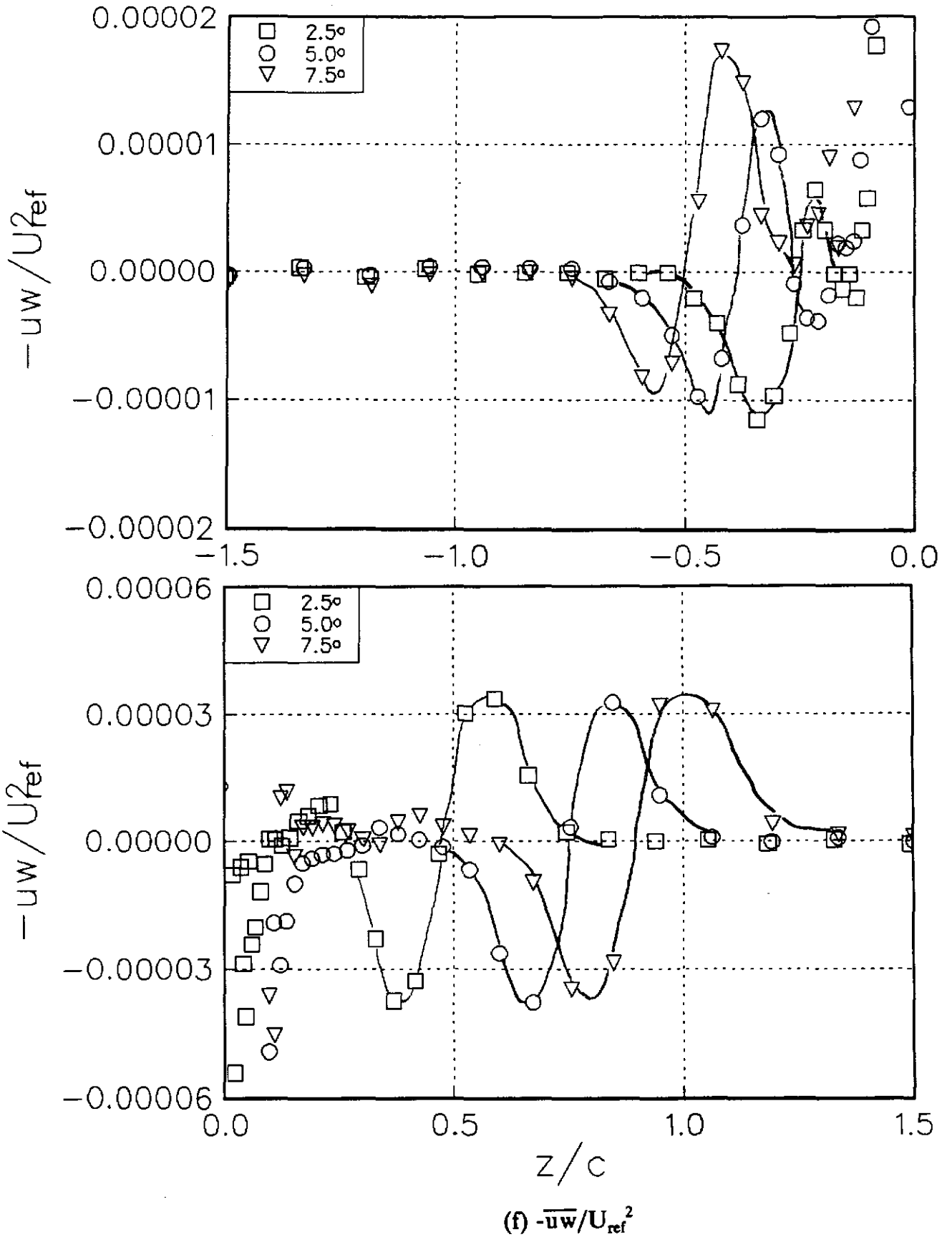

(f) $-\overline{uw}/U_{ref}^2$

Figure 3.18 Velocity profiles in the wake region as a function of angle of attack α for Re_c=400000, x/c=30.

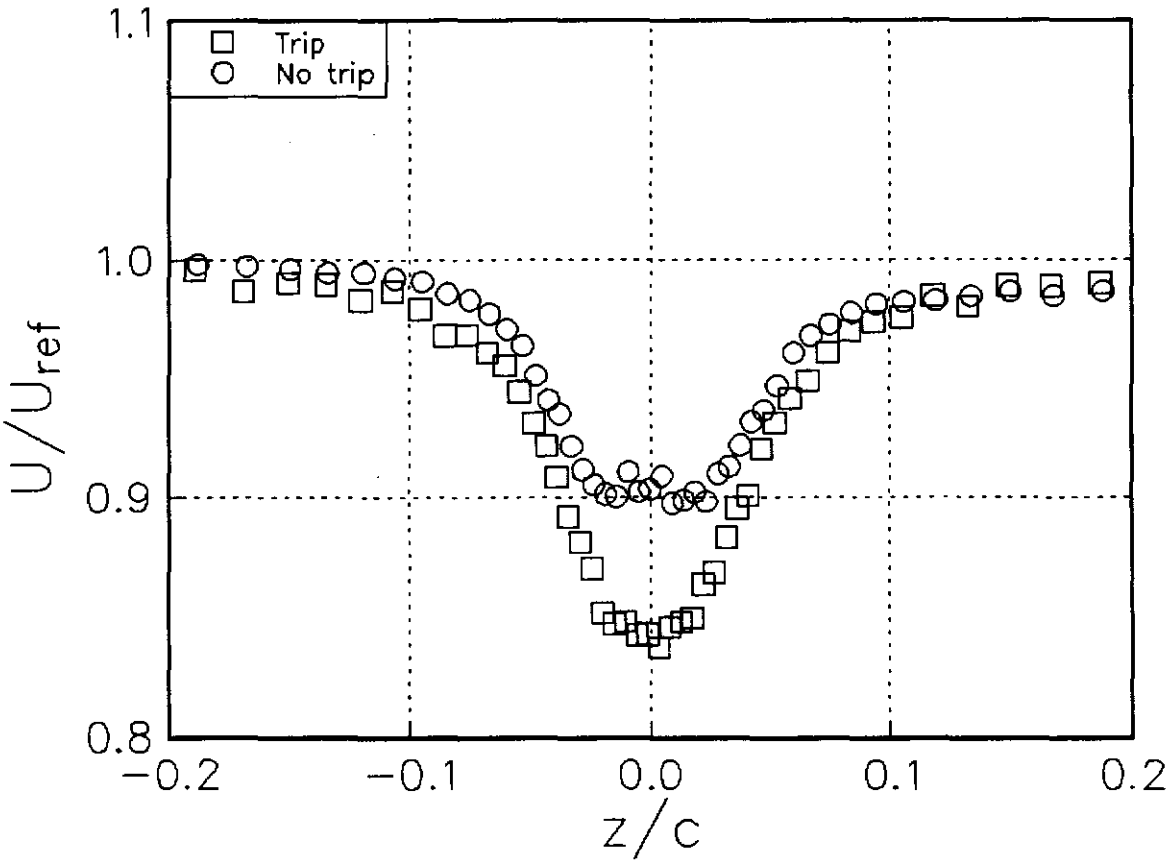

(a) U/U_{ref}

Figure 3.19 Velocity profiles in the core region as a function of wing trip for $\alpha=5.0°$, $Re_c=530000$, $x/c=30$.

The exception is the $\overline{v^2}$ profile measured on the negative z side of the vortex (figure 3.16d) which in the spiral wake shows some increase in this stress with Re_c. Since here the spiral wake lies close to the core this may well be a consequence of contamination of the profiles by the core motions which, as discussed above, appear to increase with Re_c. Autospectra measured in the spiral wake (figures 3.12,30,31 and 32) also show no substantial Reynolds number effects.

3.4.2.3 Effects of angle of attack α.

Figures 3.17 and 3.18 compare profiles measured at x/c=30 in three vortices generated at with the wing at three different angles of attack 2.5°, 5.0° and 7.5° (5.0 being the baseline case) for a chord Reynolds number of 400000.

In the core region (figure 3.17) angle of attack, i.e. total vortex circulation, has a strong effect on the axial mean velocity profiles (figure 3.17a). Between α=2.5° and 5.0° the axial velocity deficit increases substantially by a factor of about 1.7. The shape of the profile at these two conditions appears very similar, containing a single minimum. Between 5.0° and 7.5° however, the profile develops a small maximum at its center. The increase in angle of attack still produces an increase in velocity deficit at the core edge, but in the center a reduction is seen. We are not certain at this stage of the cause of this peak but we are reasonably confident that it is not a consequence of measurement errors. Re-examining the profiles measured at x/c=20 and 25 for Re_c=400000, α=5.0° (figure 3.13a) and looking forward to the axial velocity profile measured without the trip (figure 3.19a) we see some suggestion of less pronounced peaks at other conditions.

The tangential velocity comparison in the core region also shows an interesting effect. In terms of V/U_{ref} (figure 3.17b) the comparison reveals the expected change in core circulation with angle of attack. Normalized on the root circulation of the wing Γ_o, computed using a lifting-line theory model, (figure 3.17g) we see that the profiles measured at α=5.0° and 7.5° are almost identical in shape. That measured at 2.5°, however, is not, the relative core circulation being more than 30% smaller than in the other two cases. All the turbulence stresses except $\overline{u^2}$ (figures 3.17(c-f)) show large increases in their maximum values at the core center with angle of attack. Qualitatively this is what would be expected

if these peaks were a consequence of core motions. Spectra measured at the center of the core (figure 3.9, 26 and 27) show the effects of angle of attack in several ways. Between 5.0° and 2.5° there is a qualitative change in shape. The high frequency spike (presumed to be associated with core waves) disappears or becomes swamped by an overal rise in spectral levels at higher frequencies relative to U_{ref}. An possible inertial subrange even begins to appear here. At lower frequencies the difference in the spectral levels of U and of V and W becomes smaller. Between 5.0° and 7.5° the reverse trend is seen. The high frequency spike becomes more distinct and shifts to a slightly higher frequency. There is a suggestion of a second spike which appears near a frequency $fc/U_{ref} = 7.5$. The difference between the spectral levels of U and the other two components increases between 5.0° and 7.5°.

The effects of angle of attack on the flow in the wake region (figure 3.18) are in some ways similar to those of x/c since both increase the degree to which the wing wake rolls up around the core. Features associated with the wing wake - local dips in the U profile, inflections in the V profile and peaks in the profiles of turbulence stresses all move outward from the core center between α=2.5° and 7.5°. On the positive z side of the vortex the magnitude of the turbulence stresses in the wing wake changes little with α suggesting that corresponding changes in the circumferential shear and flow curvature experienced by the wake here are insufficient to significantly alter its structure. The same is not true on on the negative z side, where the wake is much closer to the vortex core. Here there appears to be a significant increase in turbulence levels with α. Despite this effect autospectra measured in the wake region on the negative z side (figures 3.12, 33 and 34) show little change in shape. The difference between spectral levels in the wake and in the core region does change however. At 5.0° and 7.5° V and W spectral levels at higher frequencies in the core ($z/c> = -0.04$) are about an order of magnitude smaller than in the wake. As noted above this may be an indication of laminar flow in the core. At 2.5° they are, however, approximately the same suggesting that turbulence may penetrate the core in this case. This result, together with other observations made above, indicate that there may be a substantial difference between in the core dynamics in the 2.5° case and in that of all others. This will be discussed further in chapter 4.

3.4.2.4 Effects of the wing trip.

Profiles measured through vortices generated with and without the wing trip at $Re_c = 530000$, $\alpha = 5°$ and $x/c = 30$ are compared in figures 3.19 and 3.20. In the core region the mean axial velocity deficit (figure 3.19a) is significantly reduced by the removal of the trip. This may well be a simple consequence of conservation of axial momentum since without the trip the momentum deficit of the wing boundary layers (table 3.3), from which the core is formed, is much smaller. Tangential velocity profiles in this region (figure 3.19b) are almost identical in shape but the velocity magnitude is consistently about 10% higher without the trip. That this factor appears constant across the profile suggests that the trip may influence the root circulation of the wing. Since the trip increases the boundary layer displacement thickness more on the suction side than on the pressure side (table 3.3) it is possible that it, in effect, introduces a small negative camber and thus reduces the circulation. The changes in the profiles of $\overline{u^2}$, $\overline{v^2}$, $\overline{w^2}$ and $-\overline{vw}$ (figures 3.19c to f) appear consistent with the effects of the trip on the mean profiles coupled with some coherent vortex wandering. $\overline{v^2}$, $-\overline{vw}$ and, except at its maximum $\overline{w^2}$ are all slightly larger without the trip. By contrast, $\overline{u^2}$ is as much as a factor of 4 smaller without the trip, consistent with lower axial velocity gradients and deficit seen in figure 3.19a.

In the wake region the effects of the trip very pronounced in the turbulence stresses (figure 3.20c to f). Removal of the trip reduces the apparent wake width by a factor of about 1.5 and decreases the magnitude of the stresses uniformly by a factor of about 2. These effects are no different than would be seen in a fully developed two-dimensional wing wake. Removal of the trip reduces the total momentum thickness of the near wing wake (table 3.3) by a factor of slightly over 2. From equation (1) we would therefore expect, in a two dimensional wake, the square of the velocity scale u_o^2, which determines the magnitude of the Reynolds stresses, also to fall by a factor of 2. In addition the length scale L_o, which determines the total wake width, should decrease by a factor of $\sqrt{2}$. These estimates are obviously consistent with the present results.

The sensitivity of the Reynolds stress distributions in the wake region to the precise momentum thickness of the wake makes repeatability a problem. Figure 3.37 compares profile measurements made in the wake region with the triple and quad hot wires. These

measurements were made at the same nominal conditions ($\alpha = 5.0^{o}$, $Re_c = 260000$, $x/c = 30$). The quad hot-wire measurements were made some six months after those of the triple hot wire. (All the single, triple and cross hot-wire measurements presented in this report were made during the same experimental run). During that time the trip was removed and remade by a different researcher. The results of figure 3.37 show the turbulence stresses in the wake region to be smaller as measured by the quad wire than the triple wire by a fairly constant factor of about 20%. We believe this difference is a consequence of differences in the trip since fabrication of the trip is a relatively imprecise process involving the scattering of the glass beads on to a coat of wet lacquer.

Due to equipment malfunctions during the experiment, broad frequency range spectra were not measured in the core center without the wing trip. Furthermore those spectra measured at various radial locations with the cross wire (figure 3.35) were contaminated with electrical noise much more than at other conditions. However, a careful comparison of these spectra with the corresponding set measured with the trip (figure 3.32) appears to show that the trip had little, if any, influence on the shapes of the spectra.

α (degrees)	Re_c	Trip	y/c (measured from tip)[1]	Data file name[2]
0	400000	Yes	1.2	E097140
			2.4	E093140
			3.6	E094140
2.5	400000	Yes	1.2	E101140
5.0	130000	Yes	1.2	E122113
	260000	Yes	1.2	E115126
	400000	Yes	1.2	E108140
	530000	Yes	1.2	E129153
		No	1.2	E316153
7.5	400000	Yes	1.2	E136140

Notes

1. Mean velocity and normal stress measurements made in z profiles at x/c = 1.006. Spectra measured at representative z locations on both sides of the wake.
2. Data files containing mean velocity and normal stress profiles, available on accompanying diskette.

Table 3.1 Conditions and locations of single hot-wire measurements.

α (degrees)	Re_c	Trip	x/c[1]	Data file X-wire[2]	Data file Triple wire
0	400000	Yes	30		E210340
2.5	400000	Yes	30	E276240	
5.0	130000	Yes	30		E184313
	260000	Yes	30		E178326[3]
	400000	Yes	20	E249240	E239340
			25	E254240	E236340
			30	E261240	E194340
			30[4]		E199340
	530000	Yes	30		E190353
		No	30	E305253	
7.5	400000	Yes	30	E284240	

Notes

1. Mean velocity and turbulence stress measurements made in z profiles passing through (or very close to) the vortex center. High-frequency range spectra during profile at z/c = -0.5, -0.25, -0.16, -0.09, -0.04 and 0.0. Low frequency range spectra measured at z/c = -1.4 and 0.0.
2. Data files containing mean velocity and turbulence stress profiles, available on accompanying diskette.
3. This profile also measured with the quad-wire probe, data file E160426.
4. y profile through the vortex center.

Table 3.2 Conditions and locations of cross, triple and quad hot-wire measurements.

			Positive $z-z_o$				Negative $z-z_o$			
α deg.	Re_c x10^{-5}	y/c	δ/c x100	δ^*/c x100	θ/c x100	Re_θ	δ/c x100	δ^*/c x100	θ/c x100	Re_c
0°	4.0	1.2	5.05	1.35	0.71	2690	5.00	1.31	0.70	2784
		2.4	5.25	1.33	0.72	2755	5.40	1.33	0.73	2940
		3.6	5.78	1.43	0.76	2877	4.91	1.29	0.67	2692
2.5°	4.0	1.2	4.68	1.14	0.64	2417	5.50	1.42	0.76	2888
5.0°	1.3	1.2	4.12	0.88	0.50	621	6.13	1.40	0.79	976
	2.6	1.2	4.41	0.98	0.57	1398	5.92	1.54	0.82	2023
	4.0	1.2	4.31	1.10	0.58	2200	5.96	1.57	0.84	3181
	5.3	1.2	4.35	0.99	0.58	2900	6.22	1.61	0.87	4355
	5.3[1]	1.2	3.23	0.54	0.25	1244	3.70	0.97	0.46	2301
7.5°	4.0	1.2	4.13	1.04	0.52	1984	7.62	2.22	1.00	3800

Notes
1. Without trip.

Table 3.3 Boundary layer thicknesses (δ), displacement thicknesses (δ^*), momentum thicknesses (θ) and momentum thickness Reynolds numbers ($Re_\theta = U_e\theta/\nu$) for the wing boundary layers, estimated from near-wake profile measurements at $x/c = 1.05$.

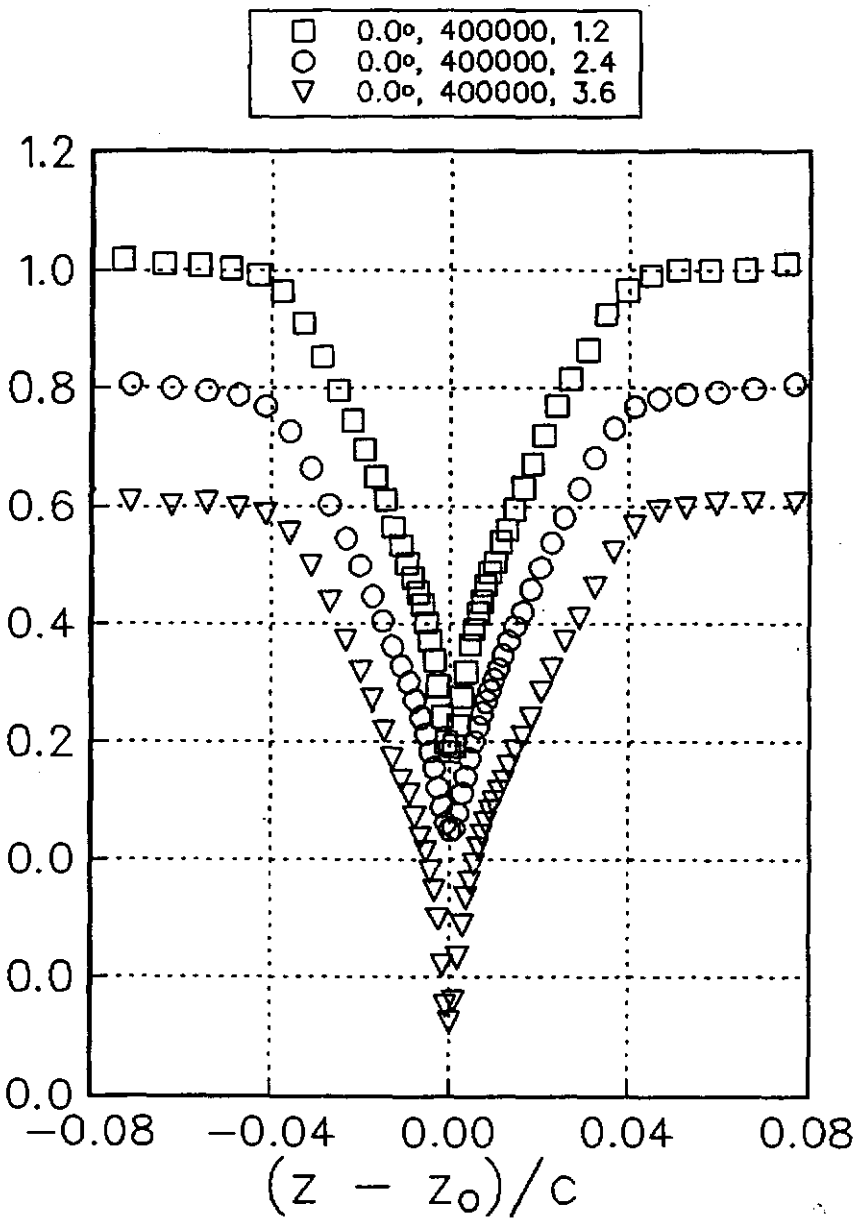

(a) Mean velocity U/U_e.

Figure 3.1 Velocity profiles measured at x/c=1.05 immediately downstream of the trailing edge with the wing at zero angle of attack. Numbers in legend indicate, respectively, angle of attack, Reynolds number and y location.

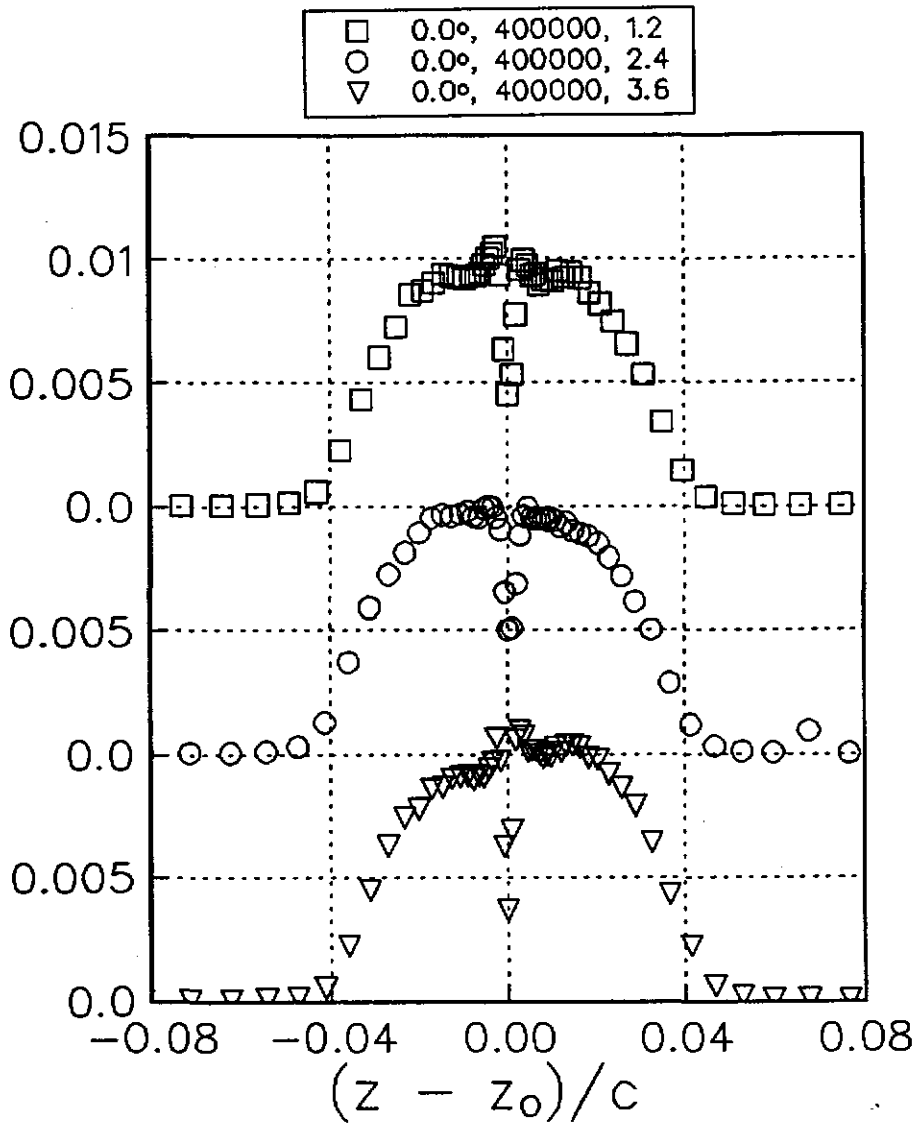

(b) Turbulence normal stress $\overline{u^2}/U_e^2$.

Figure 3.1 Velocity profiles measured at x/c=1.05 immediately downstream of the trailing edge with the wing at zero angle of attack. Numbers in legend indicate, respectively, angle of attack, Reynolds number and y location.

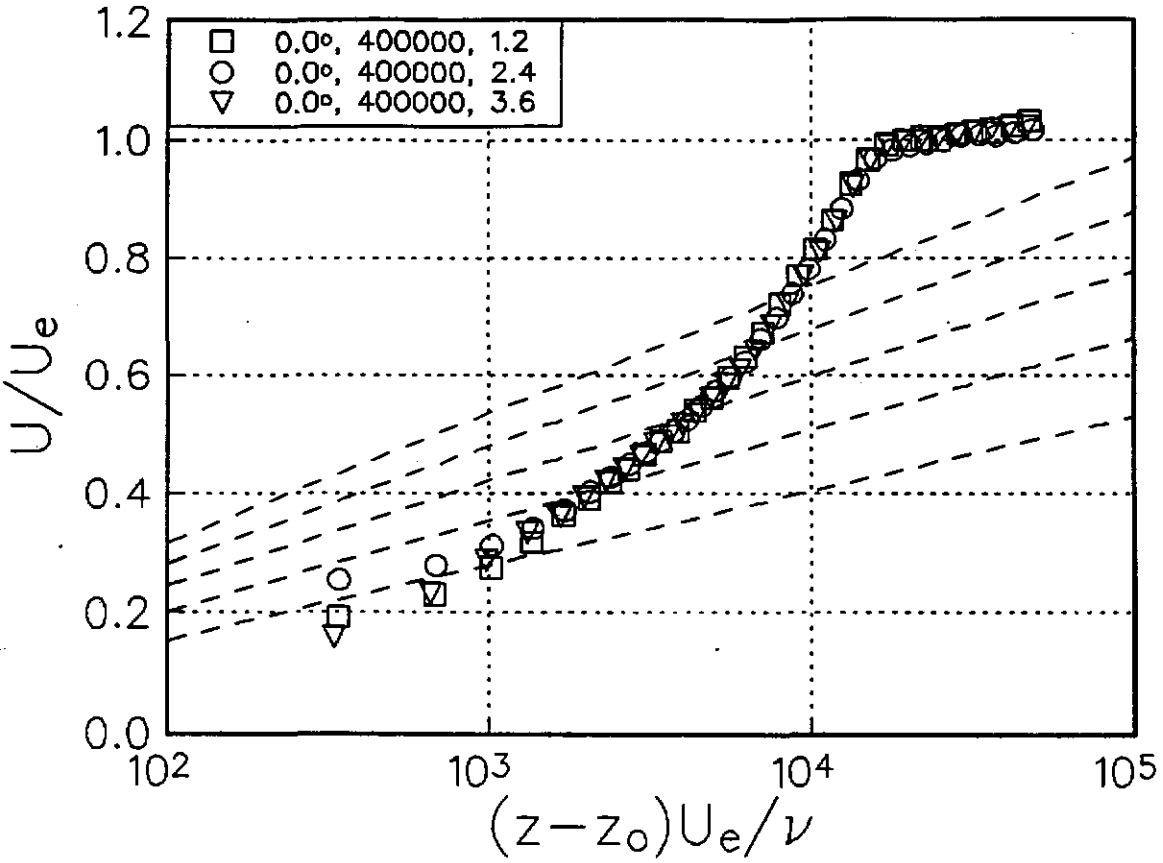

(c) Clauser plot of mean velocity, pressure (+z) side.

Figure 3.1 Velocity profiles measured at x/c=1.05 immediately downstream of the trailing edge with the wing at zero angle of attack. Numbers in legend indicate, respectively, angle of attack, Reynolds number and y location.

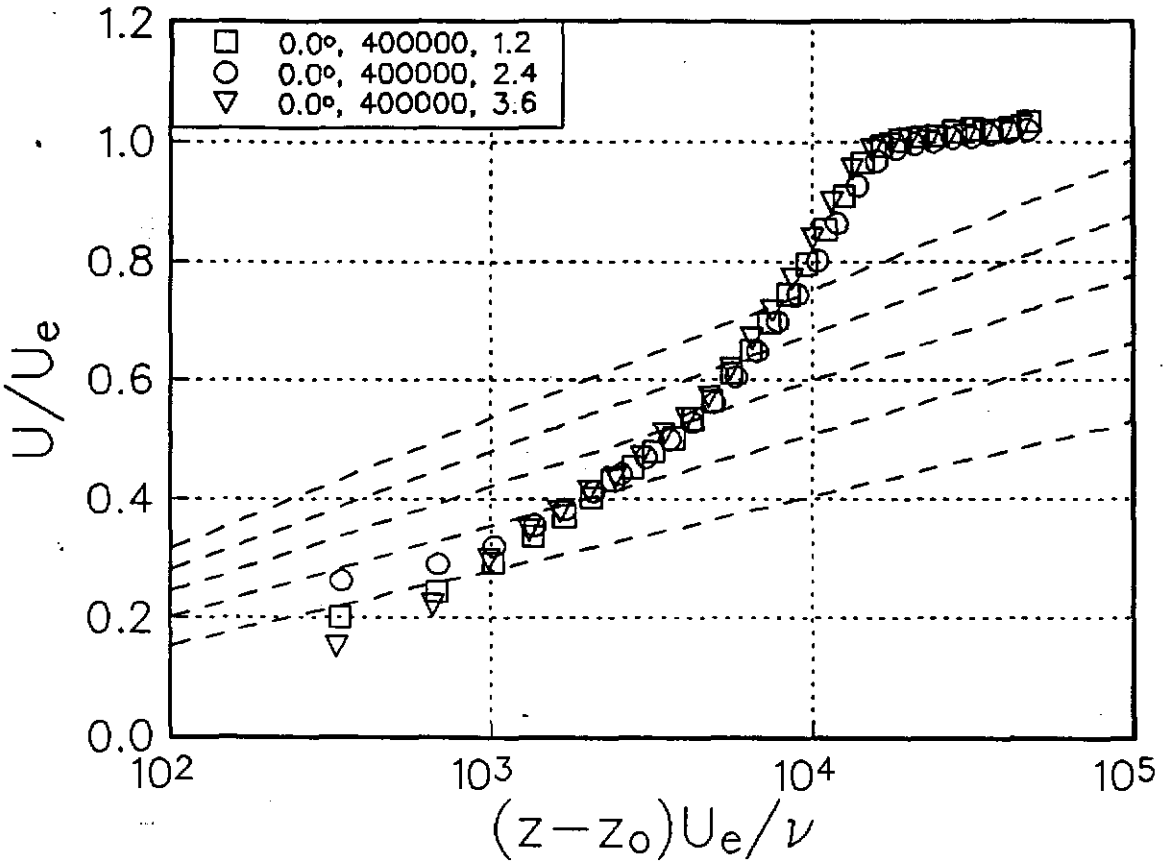

(d) Clauser plot of mean velocity, suction (-z) side.

Figure 3.1 Velocity profiles measured at x/c=1.05 immediately downstream of the trailing edge with the wing at zero angle of attack. Numbers in legend indicate, respectively, angle of attack, Reynolds number and y location.

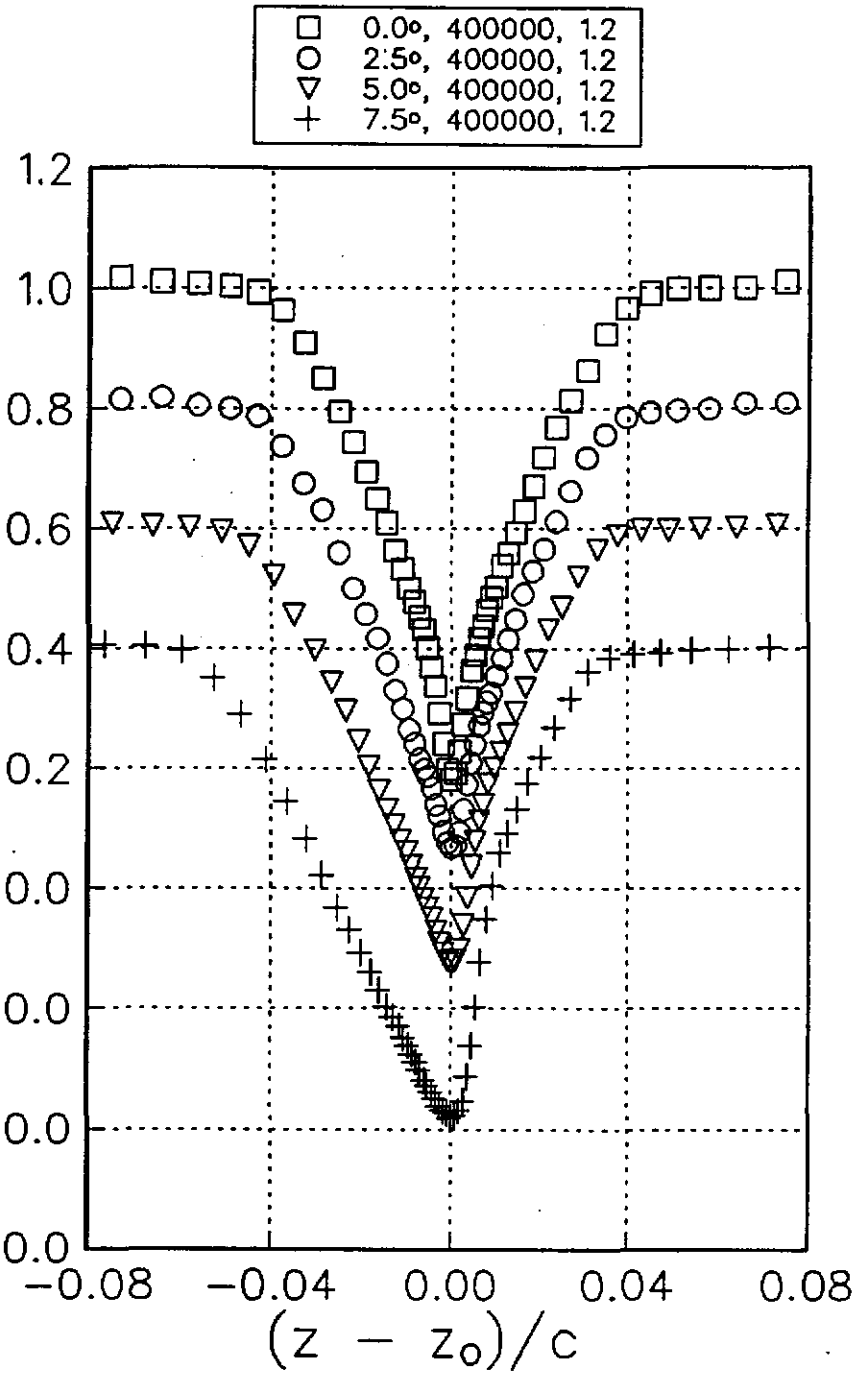

(a) Mean velocity U/U_e.

Figure 3.2 Velocity profiles measured at x/c=1.05 immediately downstream of the trailing edge showing the effects of angle of attack. Numbers in legend indicate, respectively, angle of attack, Reynolds number and y location.

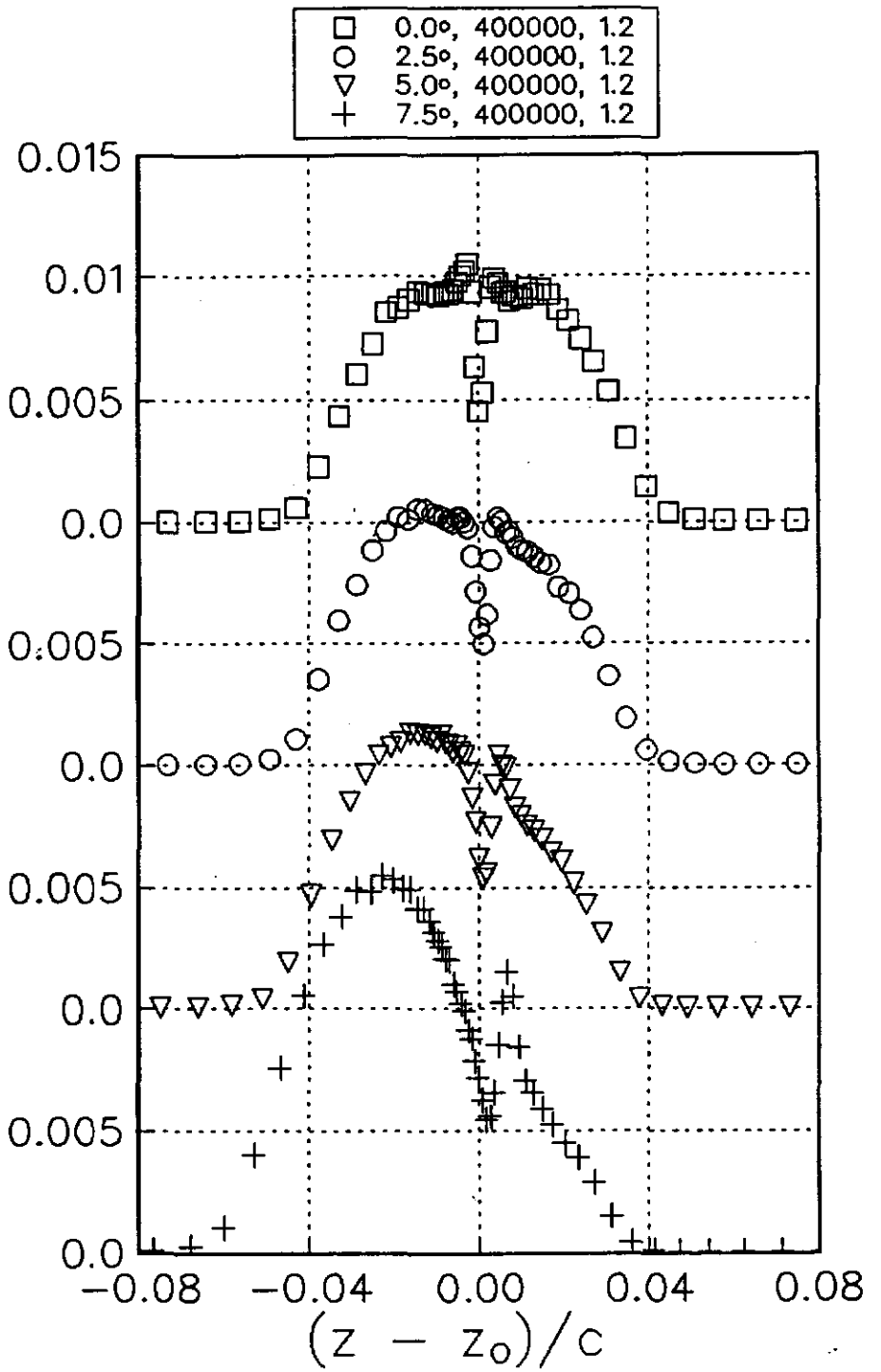

(b) Turbulence normal stress $\overline{u^2}/U_e^2$.

Figure 3.2 Velocity profiles measured at x/c=1.05 immediately downstream of the trailing edge with the wing at zero angle of attack. Numbers in legend indicate, respectively, angle of attack, Reynolds number and y location.

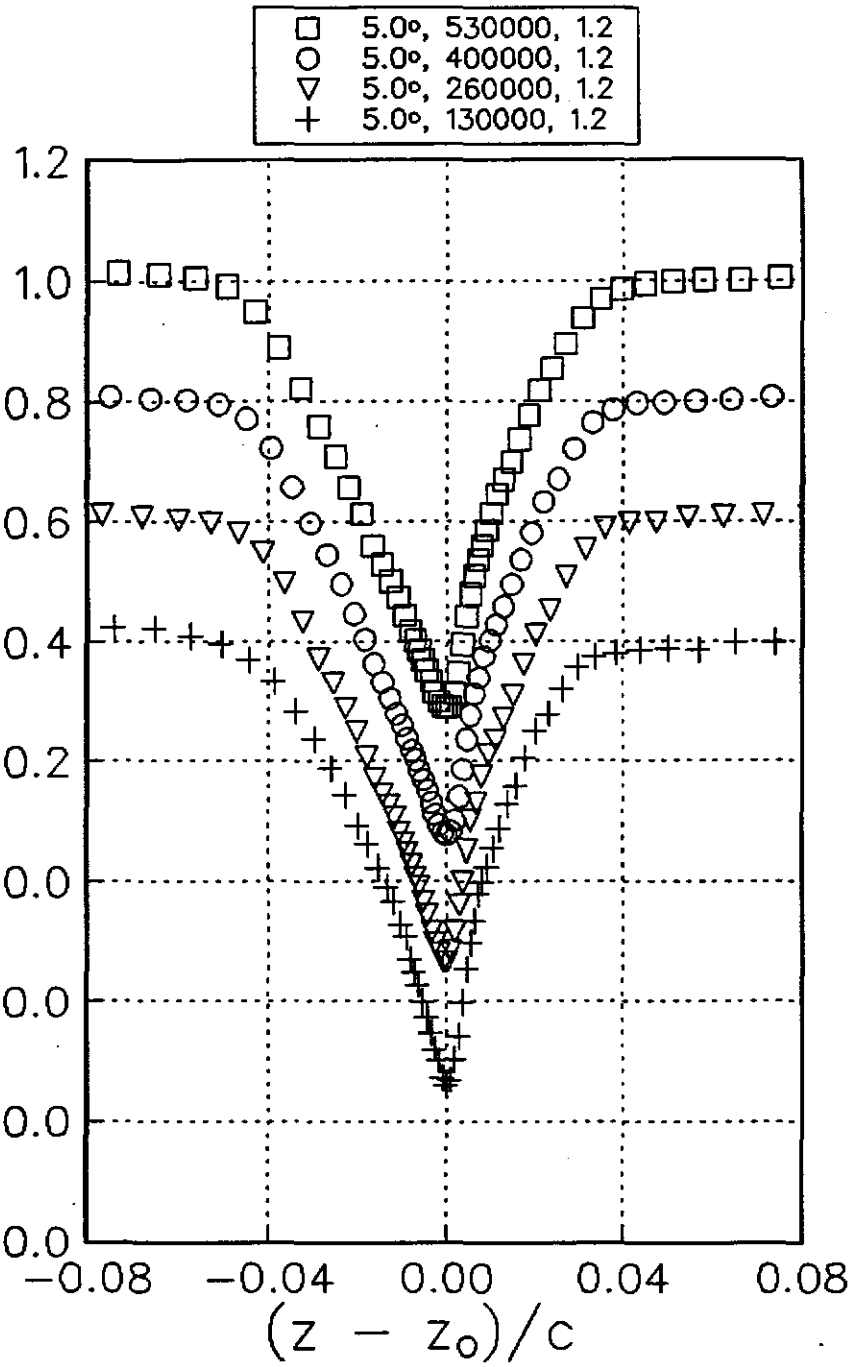

(a) Mean velocity U/U_e.

Figure 3.3 Velocity profiles measured at x/c=1.05 immediately downstream of the trailing edge showing the effects of Reynolds number. Numbers in legend indicate, respectively, angle of attack, Reynolds number and y location.

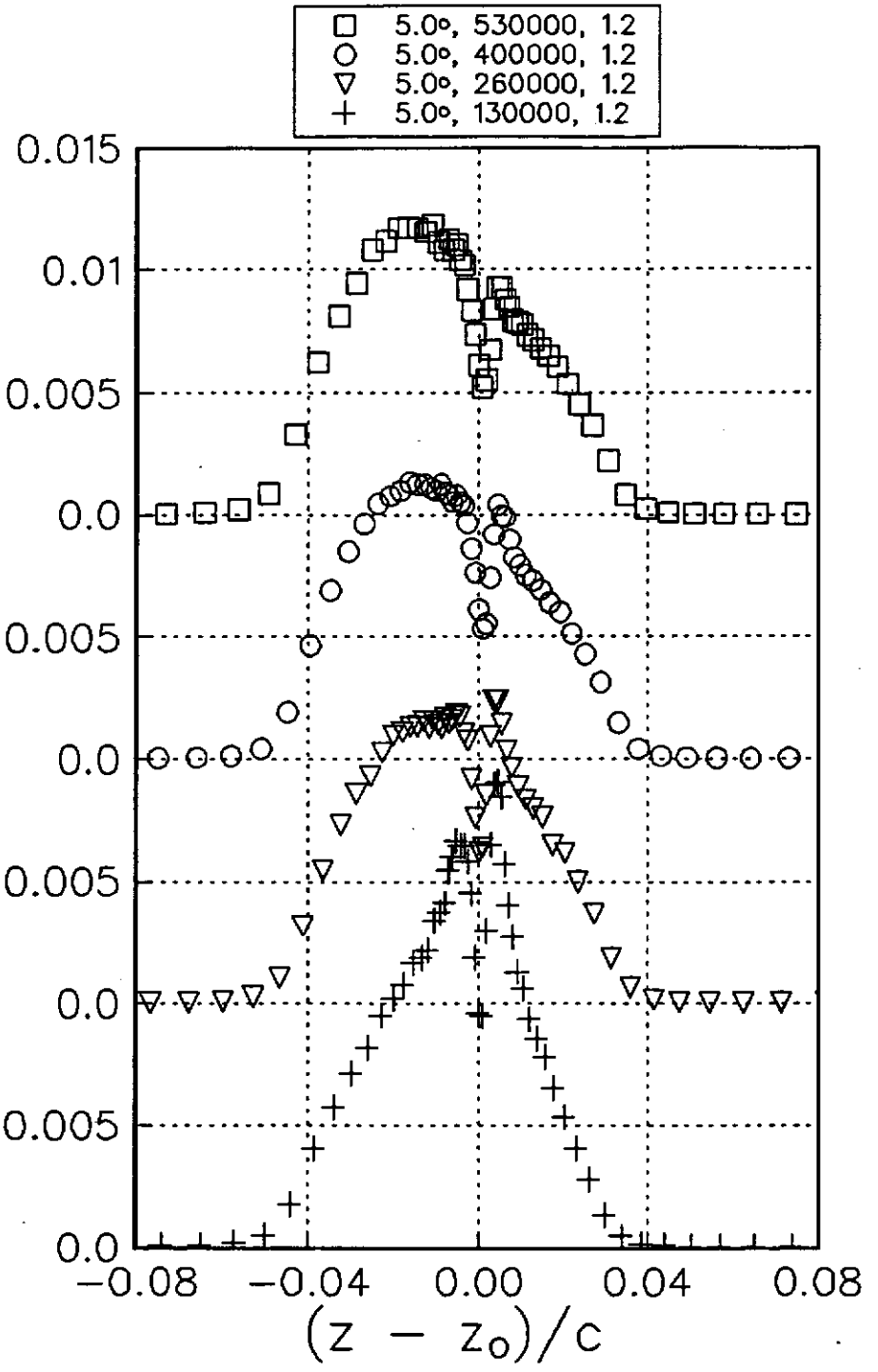

(b) Turbulence normal stress $\overline{u^2}/U_e^2$.

Figure 3.3 Velocity profiles measured at x/c=1.05 immediately downstream of the trailing edge showing the effects of Reynolds number. Numbers in legend indicate, respectively, angle of attack, Reynolds number and y location.

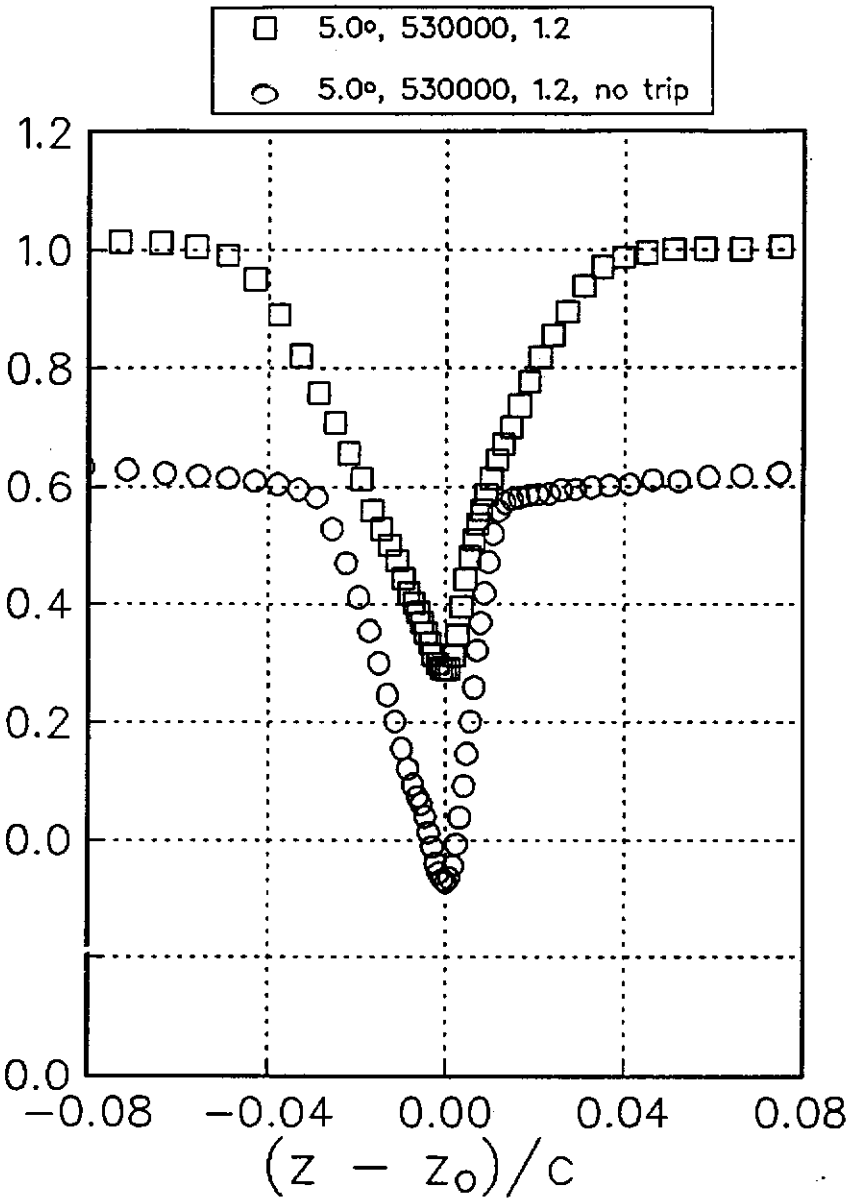

(a) Mean velocity U/U_e.

Figure 3.4 Velocity profiles measured at x/c=1.05 immediately downstream of the trailing edge showing the effects of removing the trip. Numbers in legend indicate, respectively, angle of attack, Reynolds number and y location.

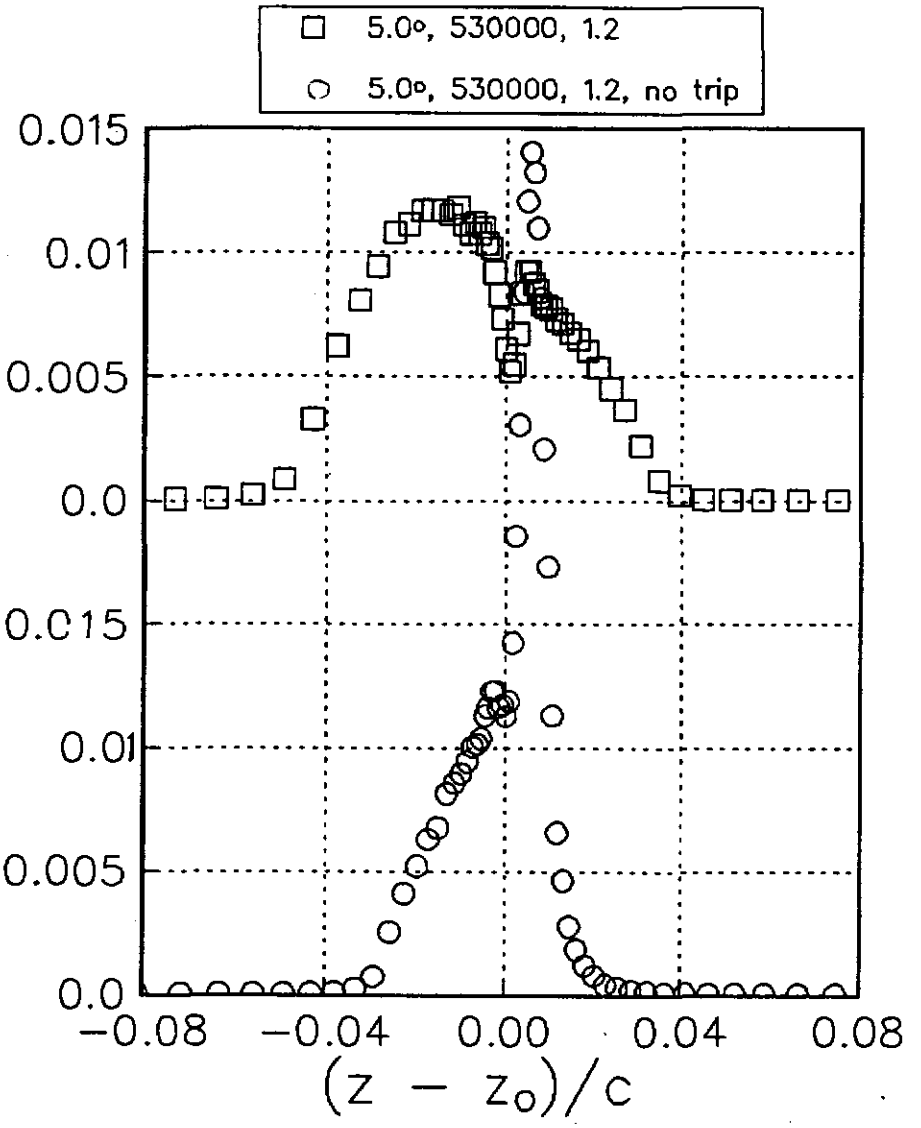

(b) Turbulence normal stress $\overline{u^2}/U_e^2$.

Figure 3.4 Velocity profiles measured at x/c=1.05 immediately downstream of the trailing edge showing the effects of removing the trip. Numbers in legend indicate, respectively, angle of attack, Reynolds number and y location.

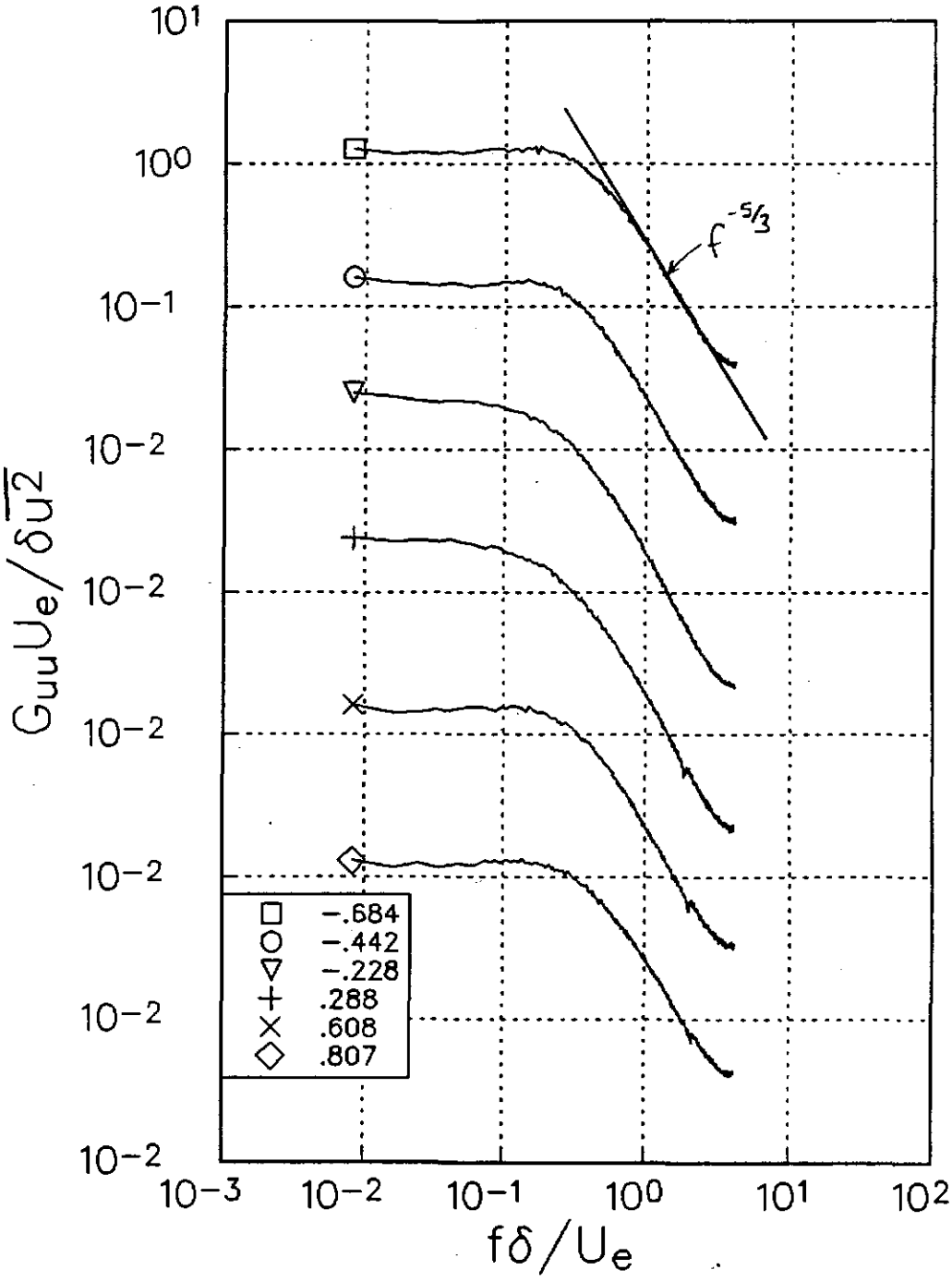

(a) Re_c=400000, α=0°, y/c=1.2

Figure 3.5 Power spectra of U component velocity fluctuations measured immediately downstream of the trailing edge at representative z locations. Numbers in legend indicate position in terms of $(z-z_o)/\delta$ where δ is the relevant boundary layer thickness (i.e. half wake width). Note that adjacent spectra are offset by one decade.

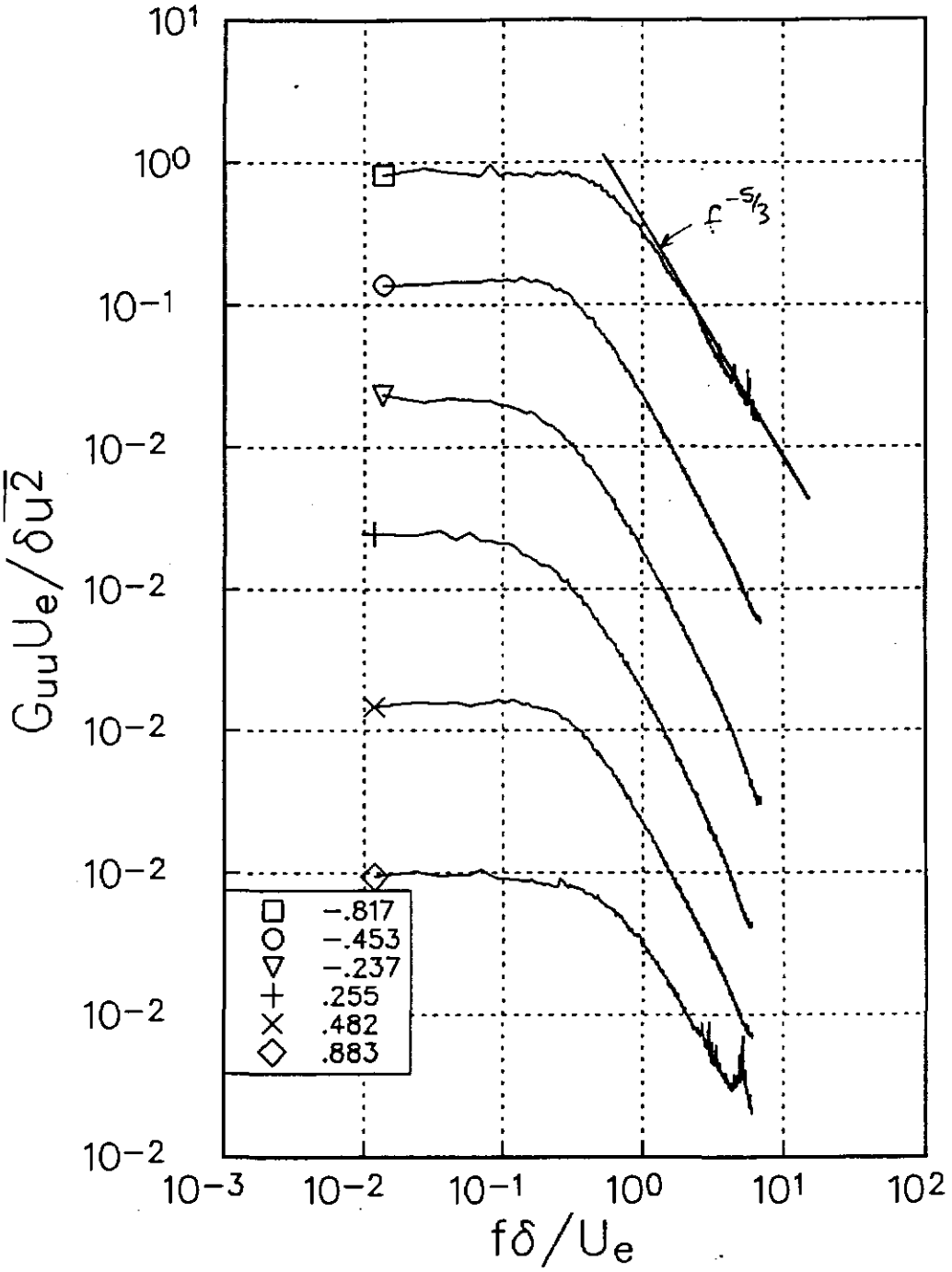

(b) Re_c=400000, α=2.5°, y/c=1.2

Figure 3.5 Power spectra of U component velocity fluctuations measured immediately downstream of the trailing edge at representative z locations. Numbers in legend indicate position in terms of $(z-z_o)/\delta$ where δ is the relevant boundary layer thickness (i.e. half wake width). Note that adjacent spectra are offset by one decade.

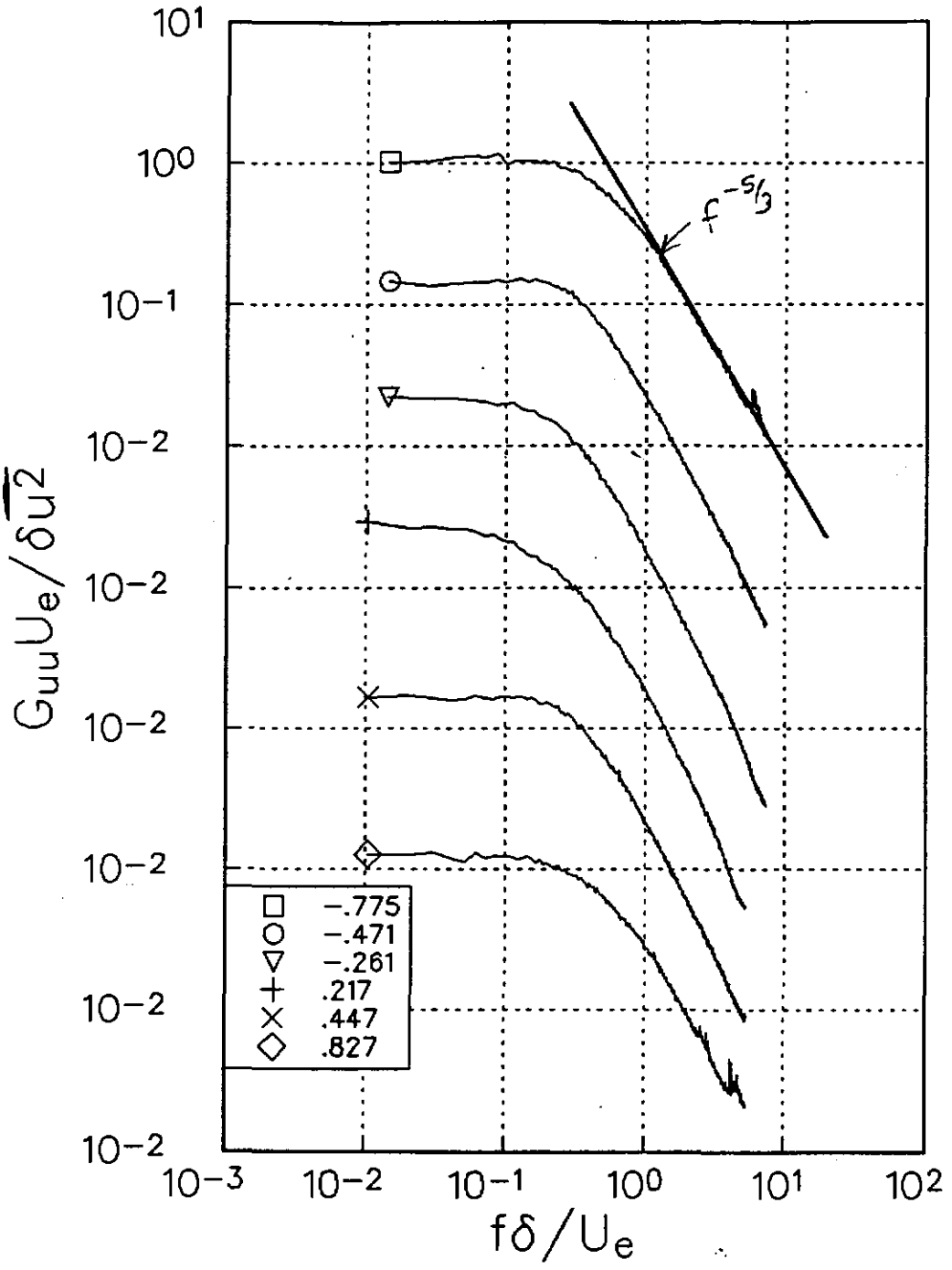

(c) Re_c=400000, α=5.0°, y/c=1.2

Figure 3.5 Power spectra of U component velocity fluctuations measured immediately downstream of the trailing edge at representative z locations. Numbers in legend indicate position in terms of $(z-z_o)/\delta$ where δ is the relevant boundary layer thickness (i.e. half wake width). Note that adjacent spectra are offset by one decade.

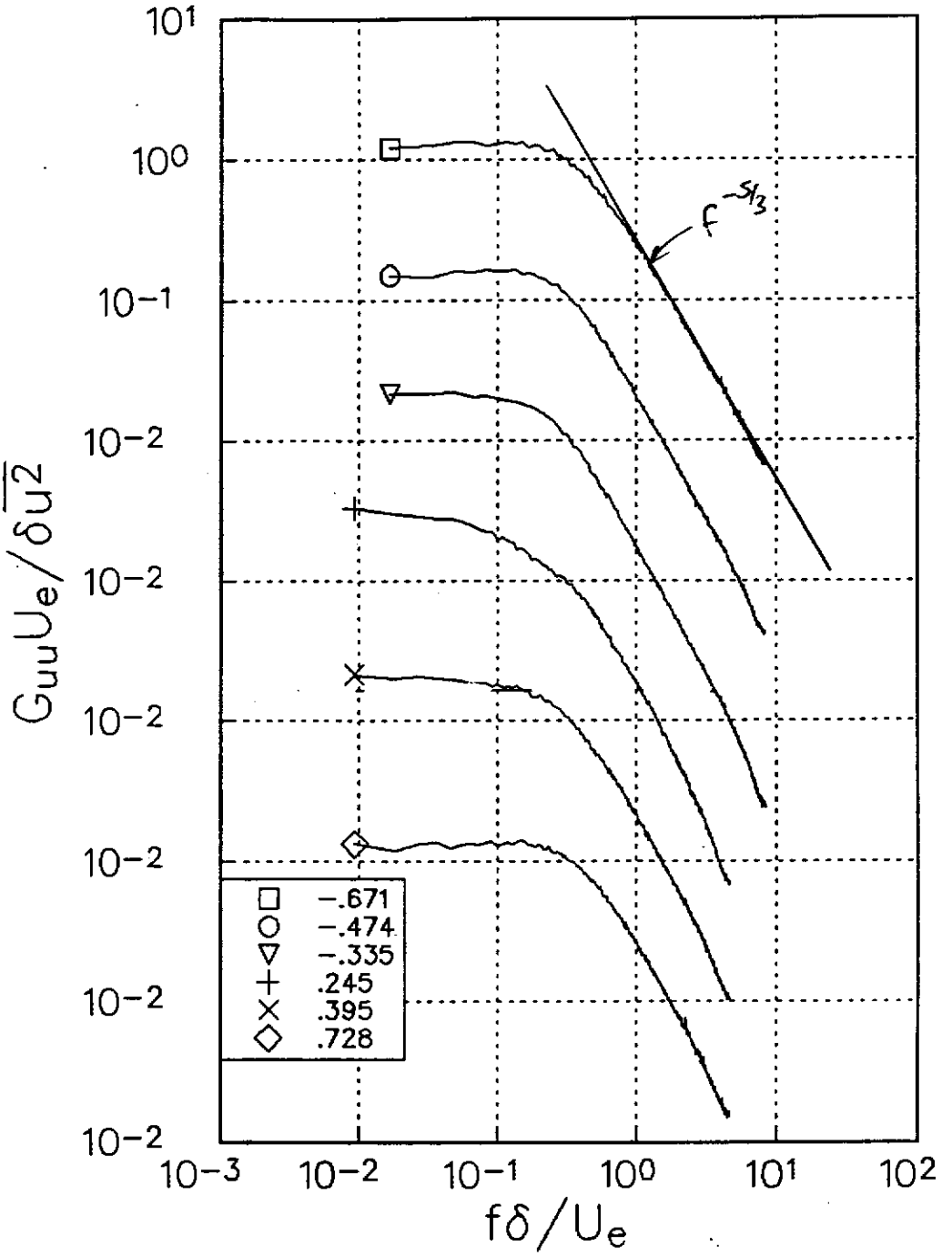

(d) $Re_c = 400000$, $\alpha = 7.5°$, $y/c = 1.2$

Figure 3.5 Power spectra of U component velocity fluctuations measured immediately downstream of the trailing edge at representative z locations. Numbers in legend indicate position in terms of $(z-z_o)/\delta$ where δ is the relevant boundary layer thickness (i.e. half wake width). Note that adjacent spectra are offset by one decade.

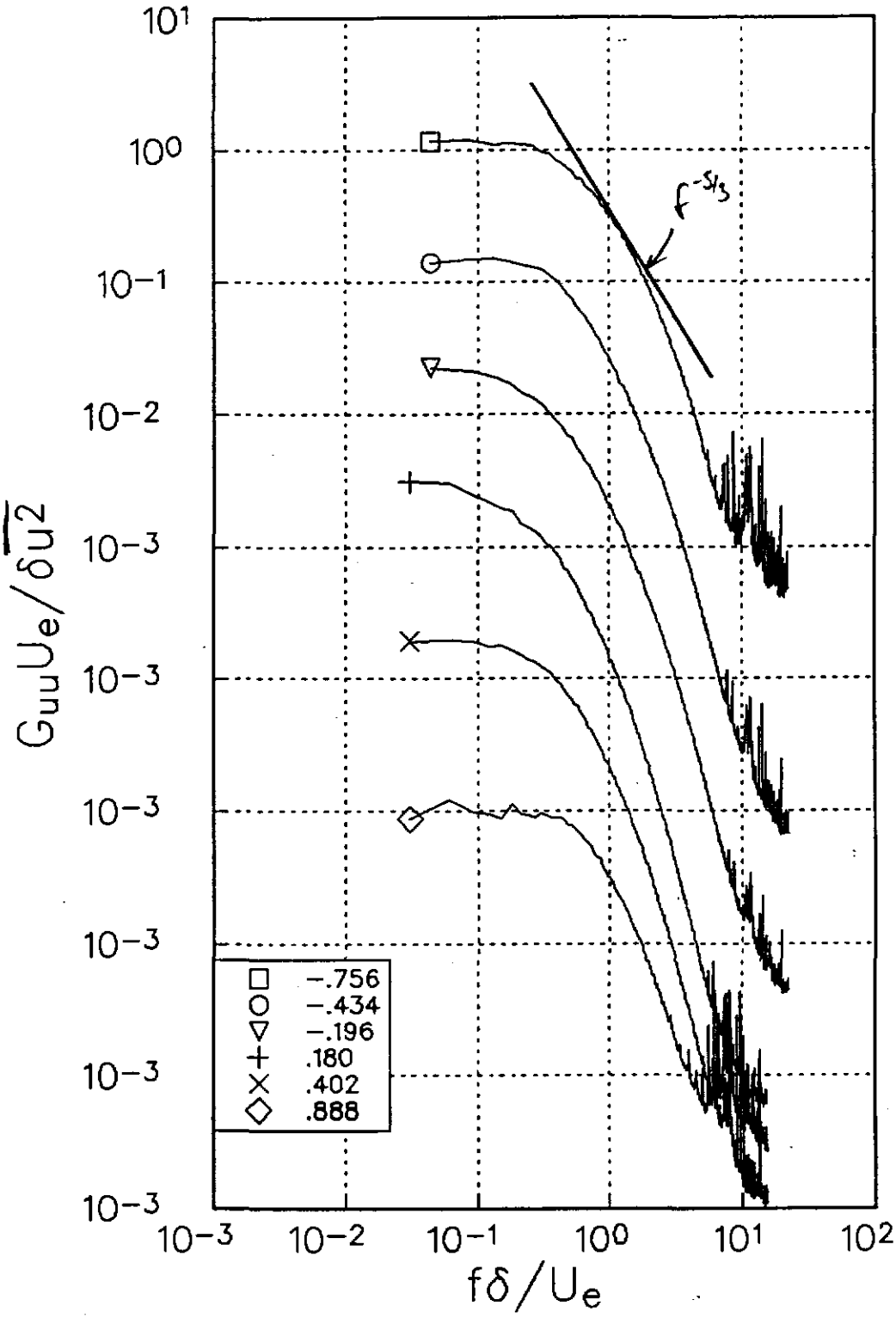

(e) $Re_c = 130000$, $\alpha = 5.0^o$, $y/c = 1.2$

Figure 3.5 Power spectra of U component velocity fluctuations measured immediately downstream of the trailing edge at representative z locations. Numbers in legend indicate position in terms of $(z-z_o)/\delta$ where δ is the relevant boundary layer thickness (i.e. half wake width). Note that adjacent spectra are offset by one decade.

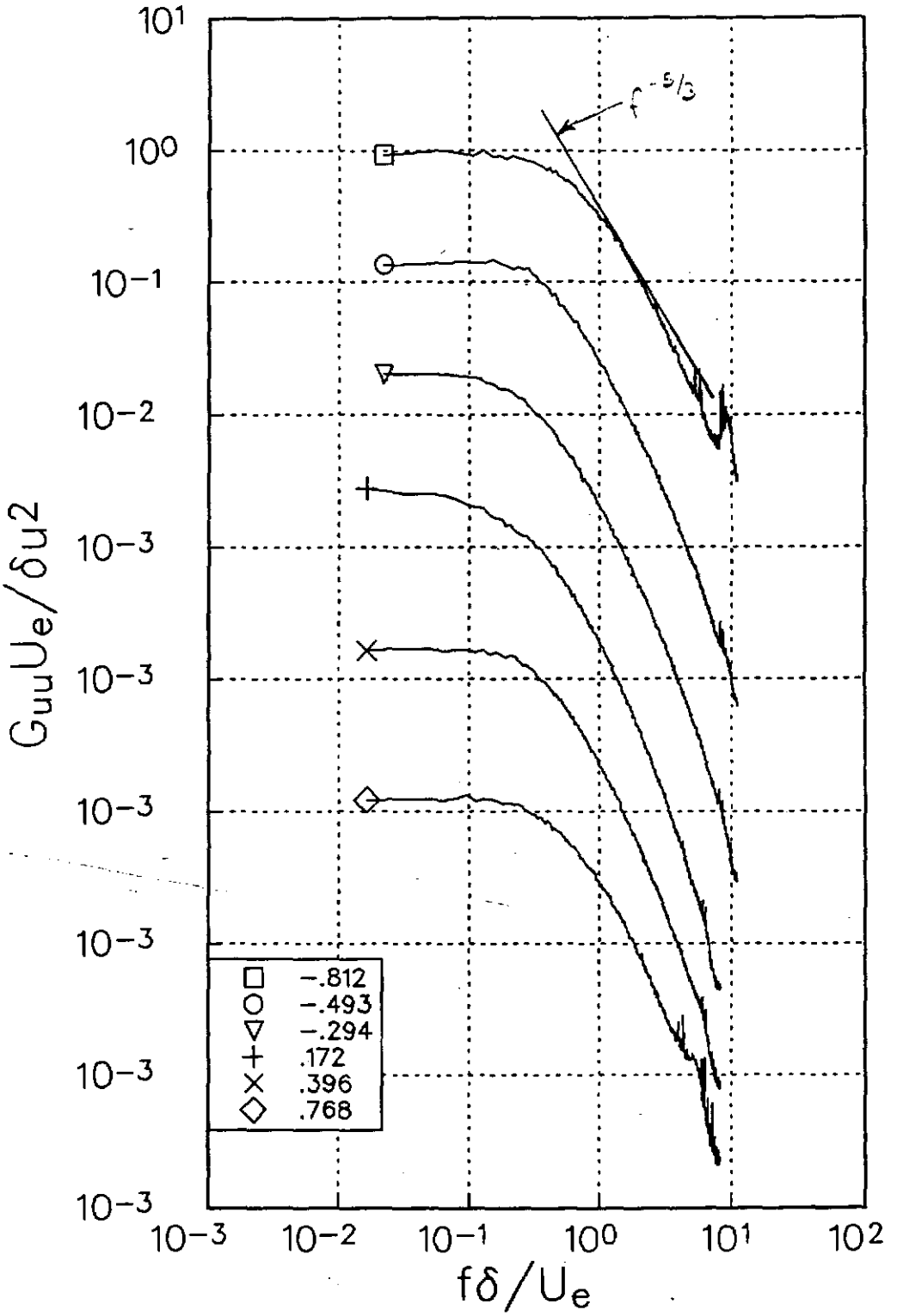

(f) $Re_c = 260000$, $\alpha = 5.0°$, $y/c = 1.2$

Figure 3.5 Power spectra of U component velocity fluctuations measured immediately downstream of the trailing edge at representative z locations. Numbers in legend indicate position in terms of $(z-z_o)/\delta$ where δ is the relevant boundary layer thickness (i.e. half wake width). Note that adjacent spectra are offset by one decade.

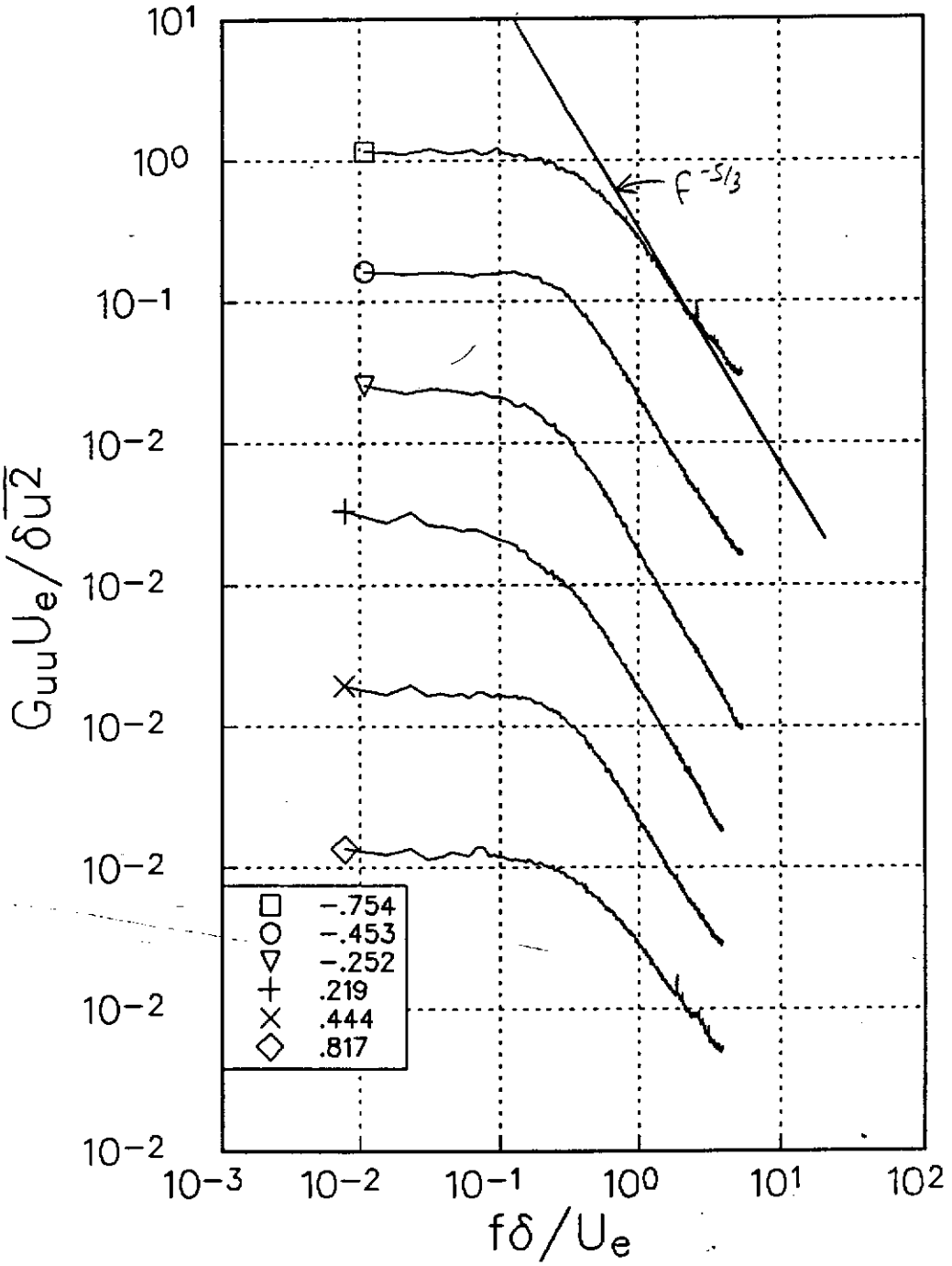

(g) $Re_c = 530000$, $\alpha = 5.0°$, $y/c = 1.2$

Figure 3.5 Power spectra of U component velocity fluctuations measured immediately downstream of the trailing edge at representative z locations. Numbers in legend indicate position in terms of $(z-z_o)/\delta$ where δ is the relevant boundary layer thickness (i.e. half wake width). Note that adjacent spectra are offset by one decade.

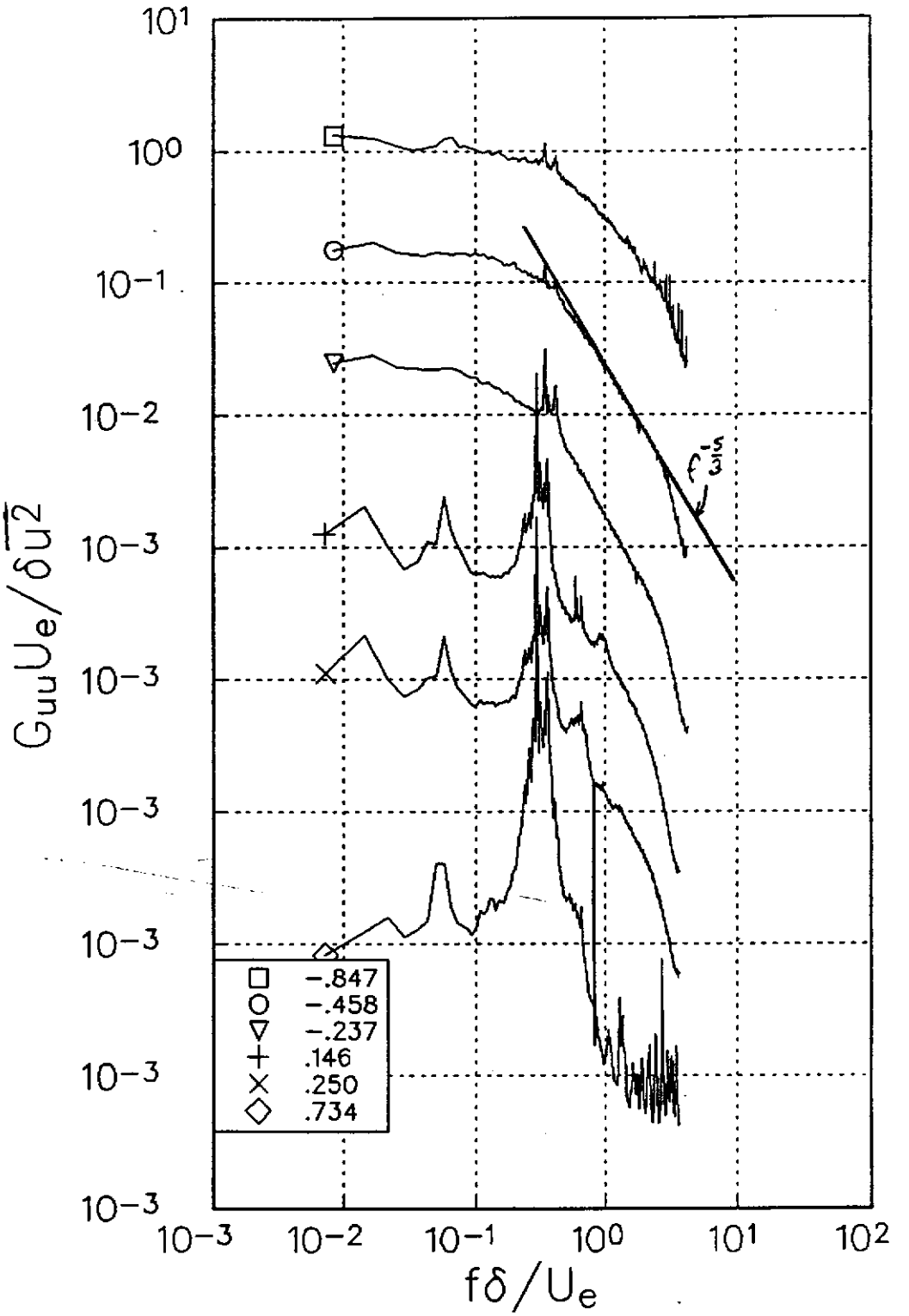

(h) $Re_c = 530000$, $\alpha = 5.0°$, $y/c = 1.2$, no trip

Figure 3.5 Power spectra of U component velocity fluctuations measured immediately downstream of the trailing edge at representative z locations. Numbers in legend indicate position in terms of $(z-z_o)/\delta$ where δ is the relevant boundary layer thickness (i.e. half wake width). Note that adjacent spectra are offset by one decade.

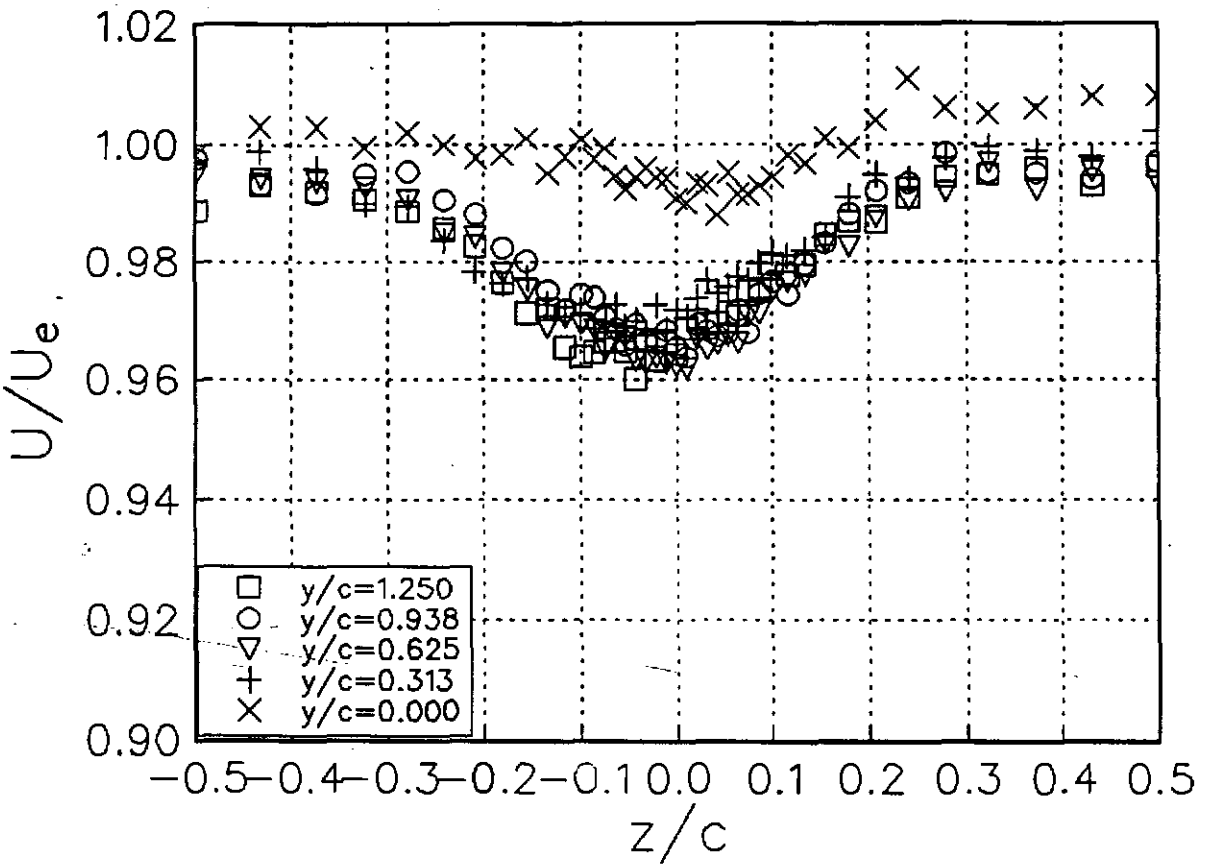

(a) Mean velocity U/U_e

Figure 3.6 Velocity profiles measured at x/c=30 in the wing wake at zero angle of attack. Re_c=400000.

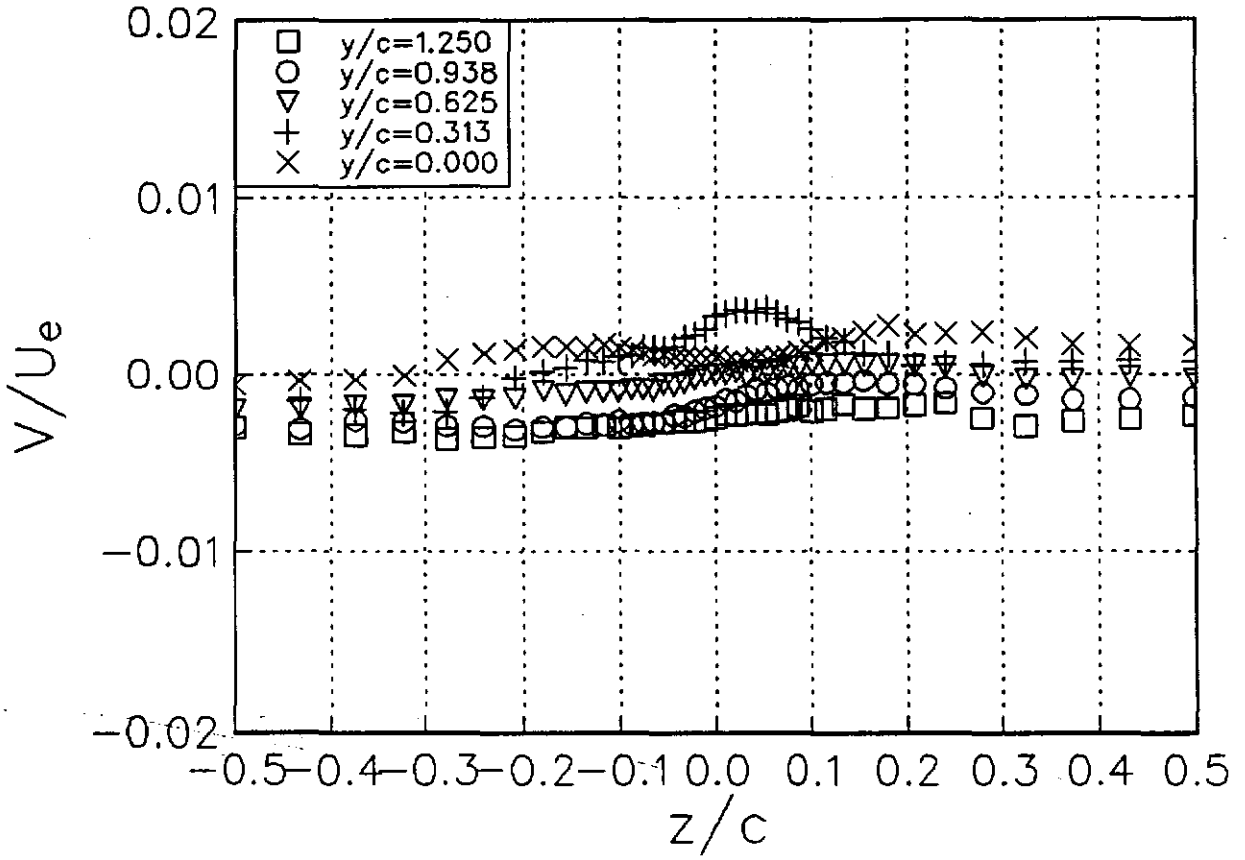

(b) Mean velocity V/U_e

Figure 3.6 Velocity profiles measured at x/c=30 in the wing wake at zero angle of attack. Re_c=400000.

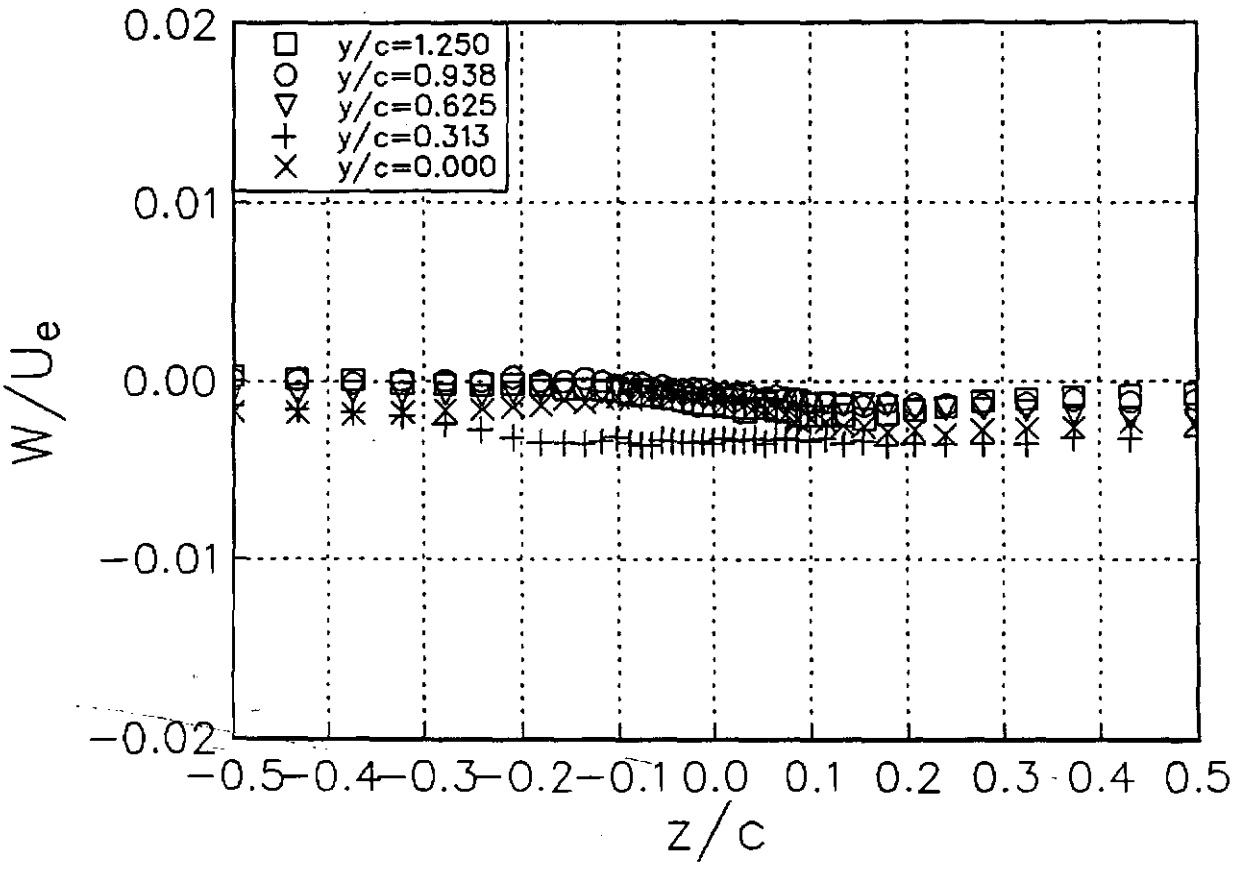

(c) Mean velocity W/U_e

Figure 3.6 Velocity profiles measured at x/c=30 in the wing wake at zero angle of attack. Re_c=400000.

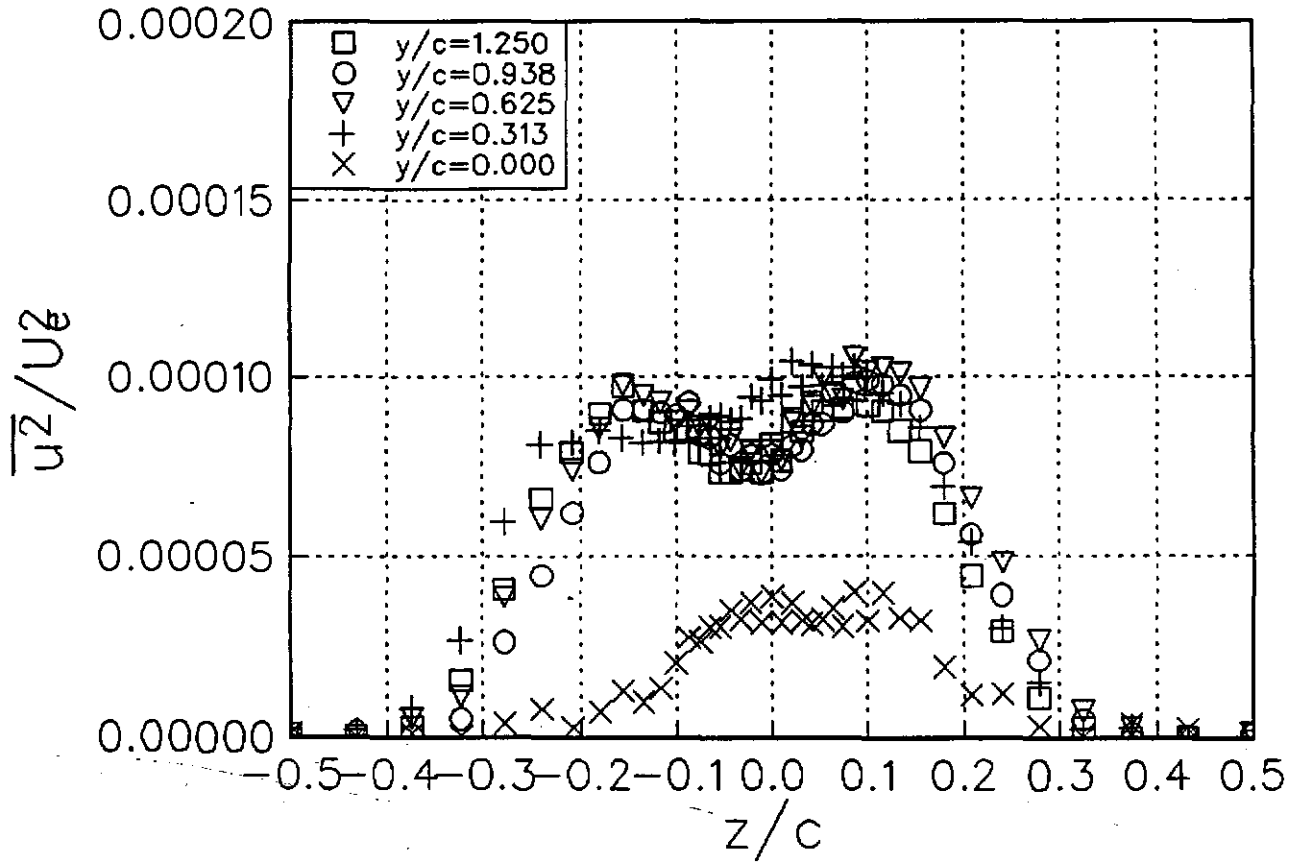

(d) Turbulence normal stress $\overline{u^2}/U_e^2$

Figure 3.6 Velocity profiles measured at x/c=30 in the wing wake at zero angle of attack. Re_c=400000.

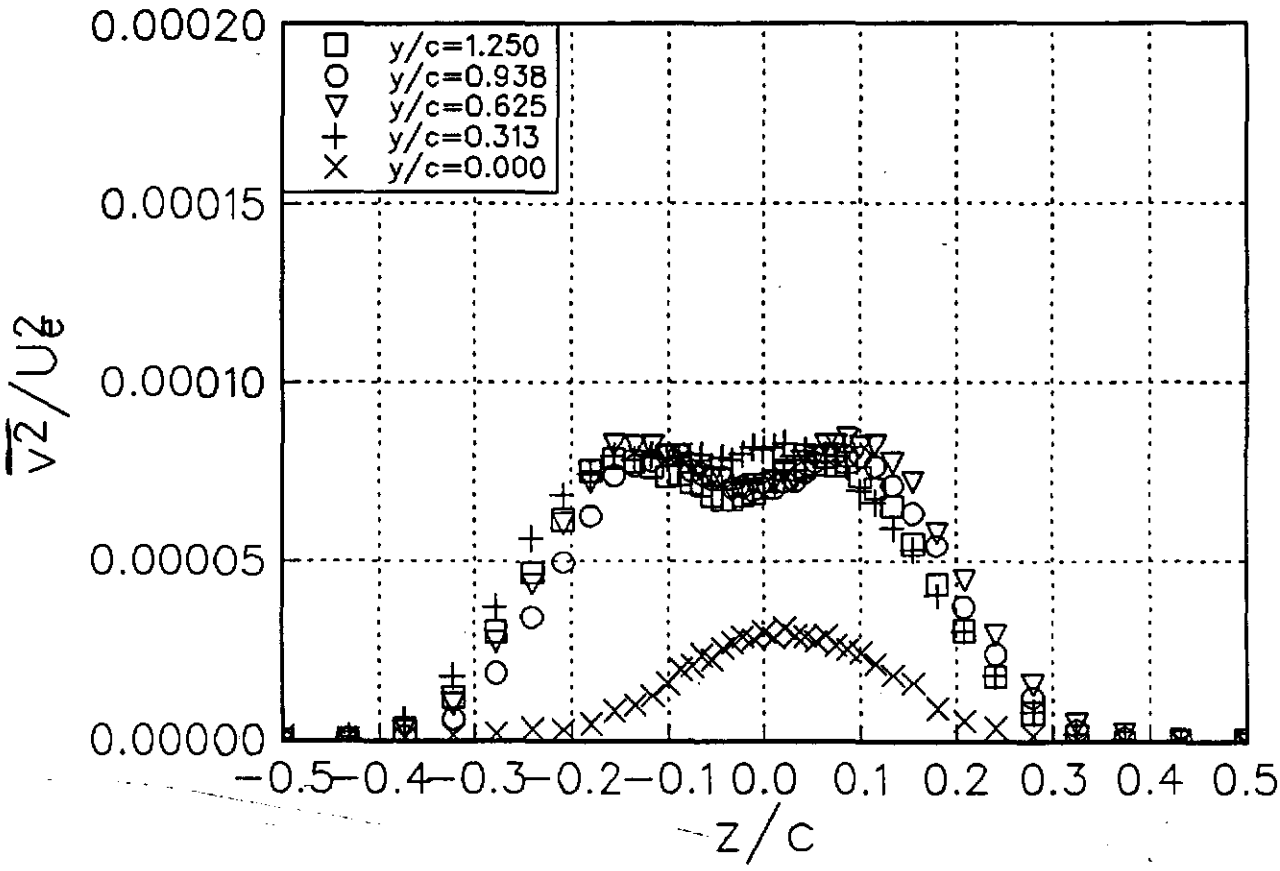

(e) Turbulence normal stress $\overline{v^2}/U_e^2$

Figure 3.6 Velocity profiles measured at x/c=30 in the wing wake at zero angle of attack. Re_c=400000.

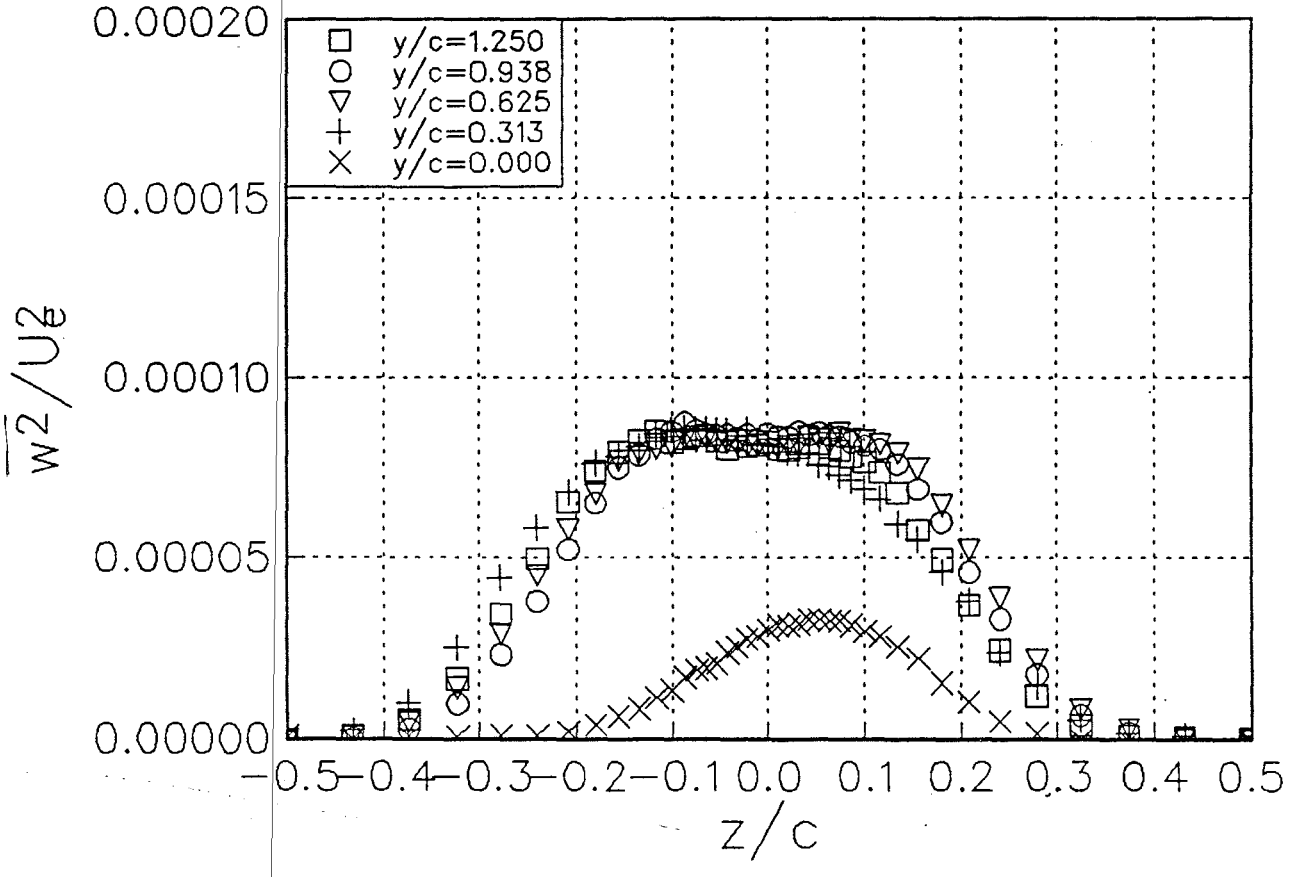

(f) Turbulence normal stress $\overline{w^2}/U_e^2$

Figure 3.6 Velocity profiles measured at x/c=30 in the wing wake at zero angle of attack. Re_c=400000.

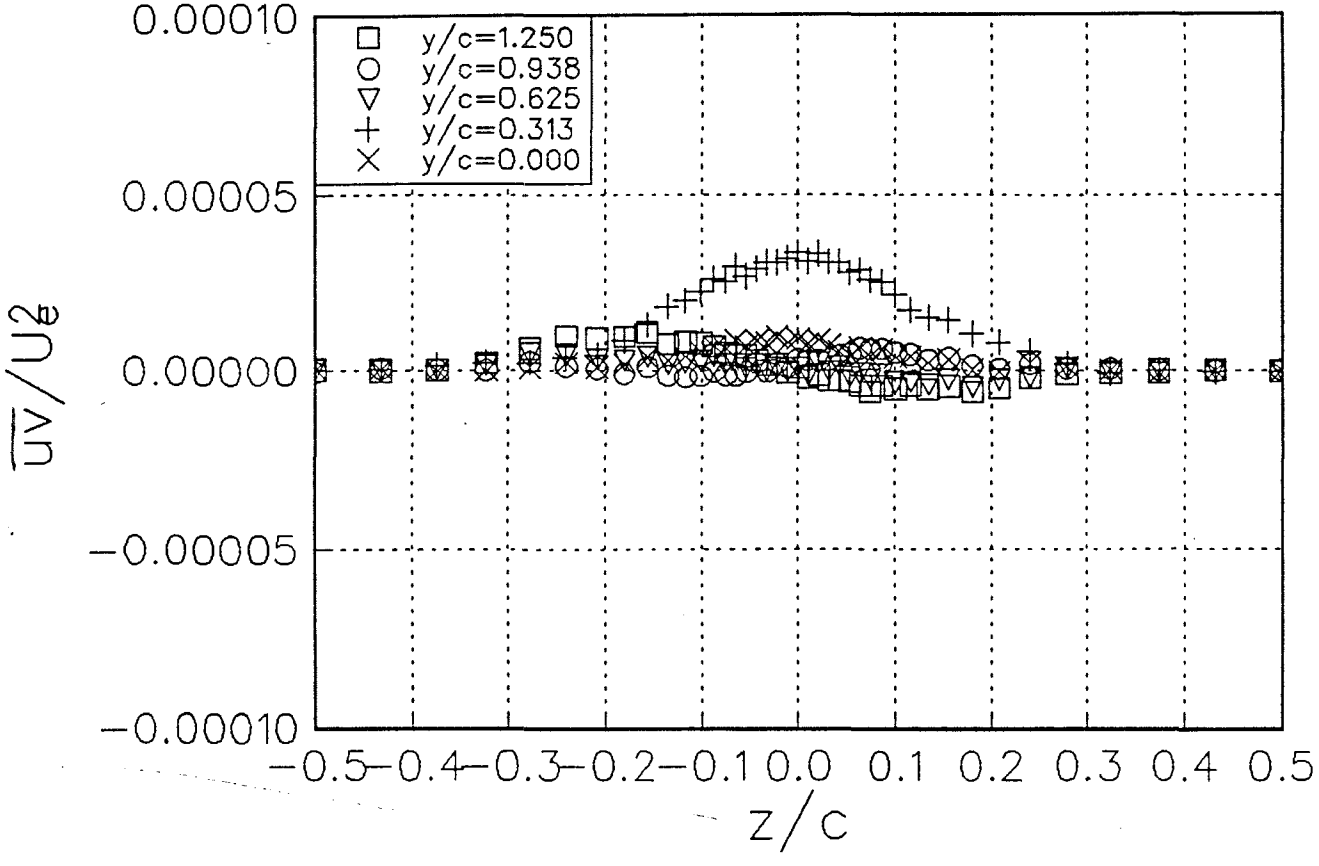

(g) Turbulence shear stress $\overline{uv}/U_e^2$

Figure 3.6 Velocity profiles measured at x/c=30 in the wing wake at zero angle of attack. Re_c=400000.

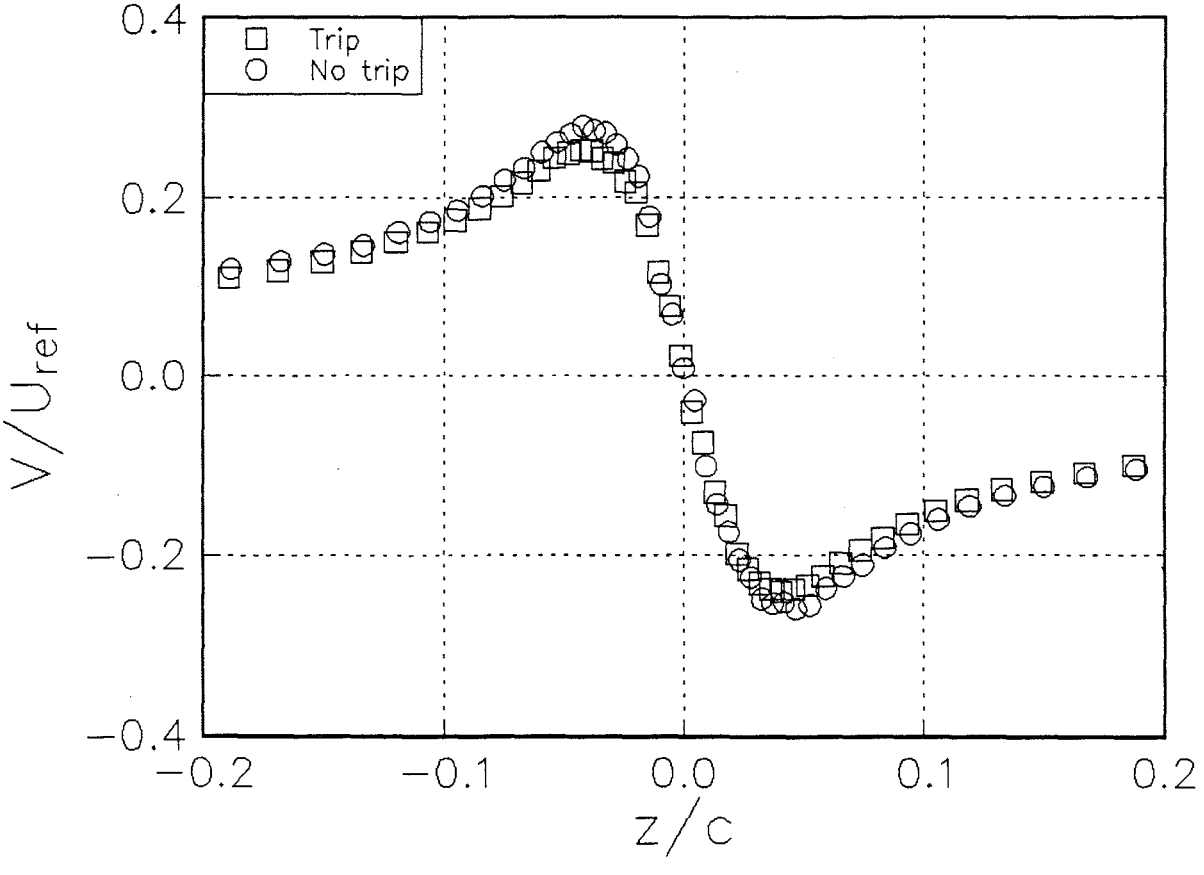

(b) V/U_{ref}

Figure 3.19 Velocity profiles in the core region as a function of wing trip for $\alpha = 5.0°$, $Re_c = 530000$, $x/c = 30$.

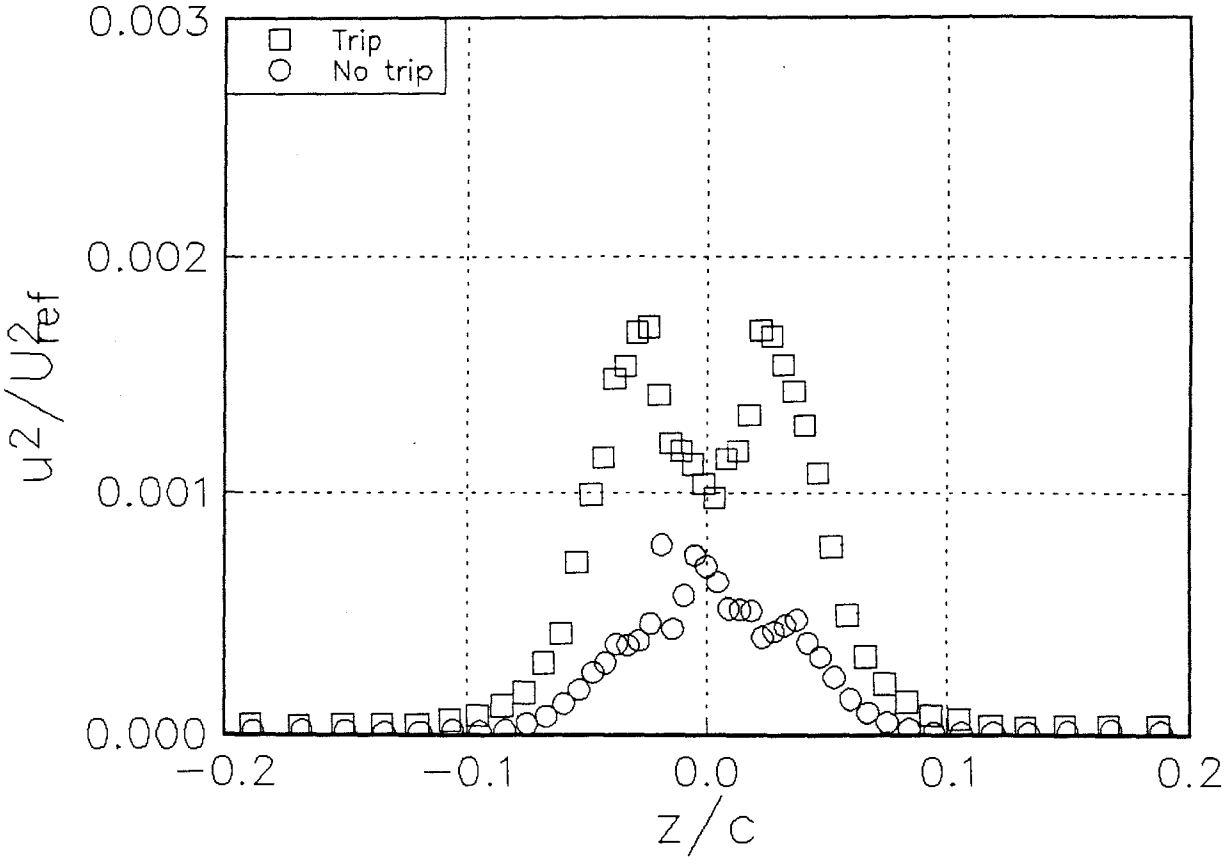

(c) $\overline{u^2}/U_{ref}^2$

Figure 3.19 Velocity profiles in the core region as a function of wing trip for $\alpha = 5.0^o$, $Re_c = 530000$, $x/c = 30$.

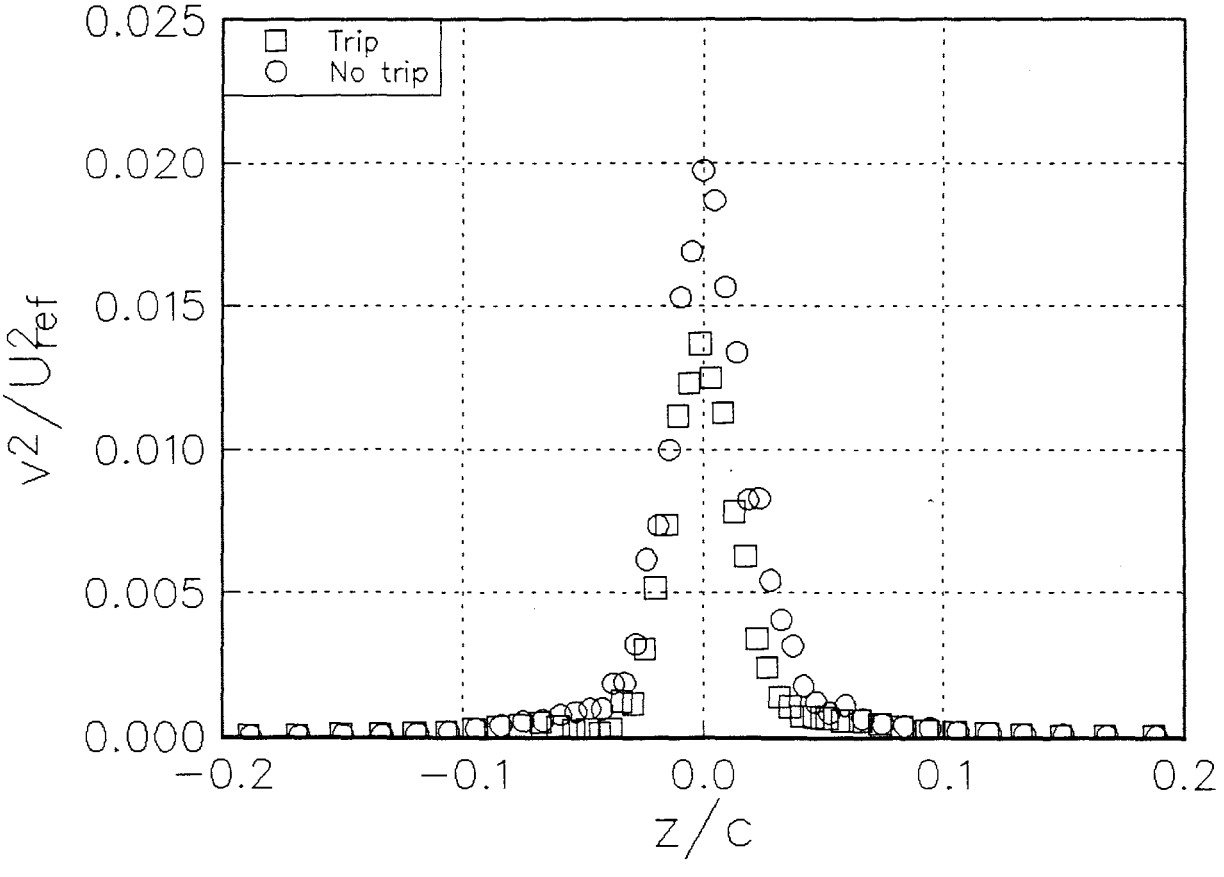

(d) $\overline{v^2}/U_{ref}^2$

Figure 3.19 Velocity profiles in the core region as a function of wing trip for $\alpha = 5.0°$, $Re_c = 530000$, $x/c = 30$.

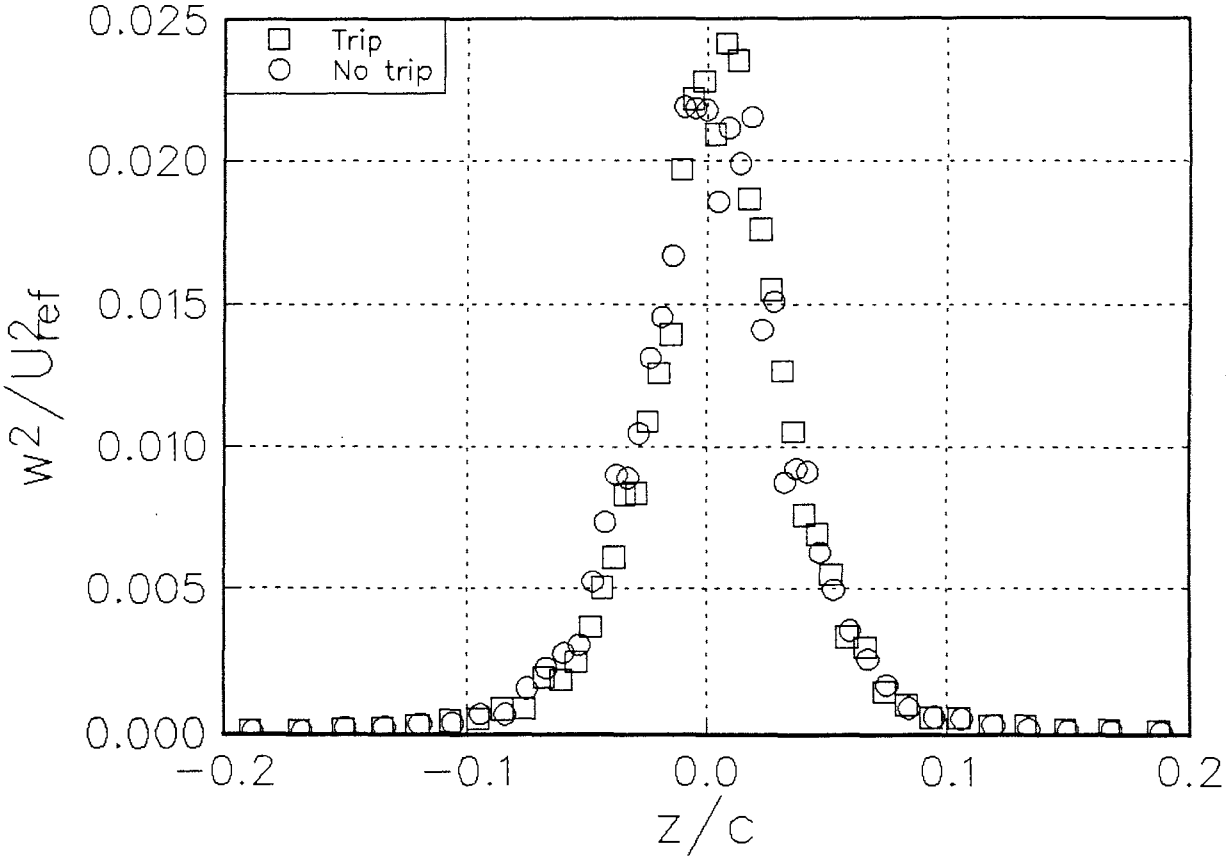

(e) $\overline{w^2}/U_{ref}^2$

Figure 3.19 Velocity profiles in the core region as a function of wing trip for $\alpha = 5.0^o$, $Re_c = 530000$, $x/c = 30$.

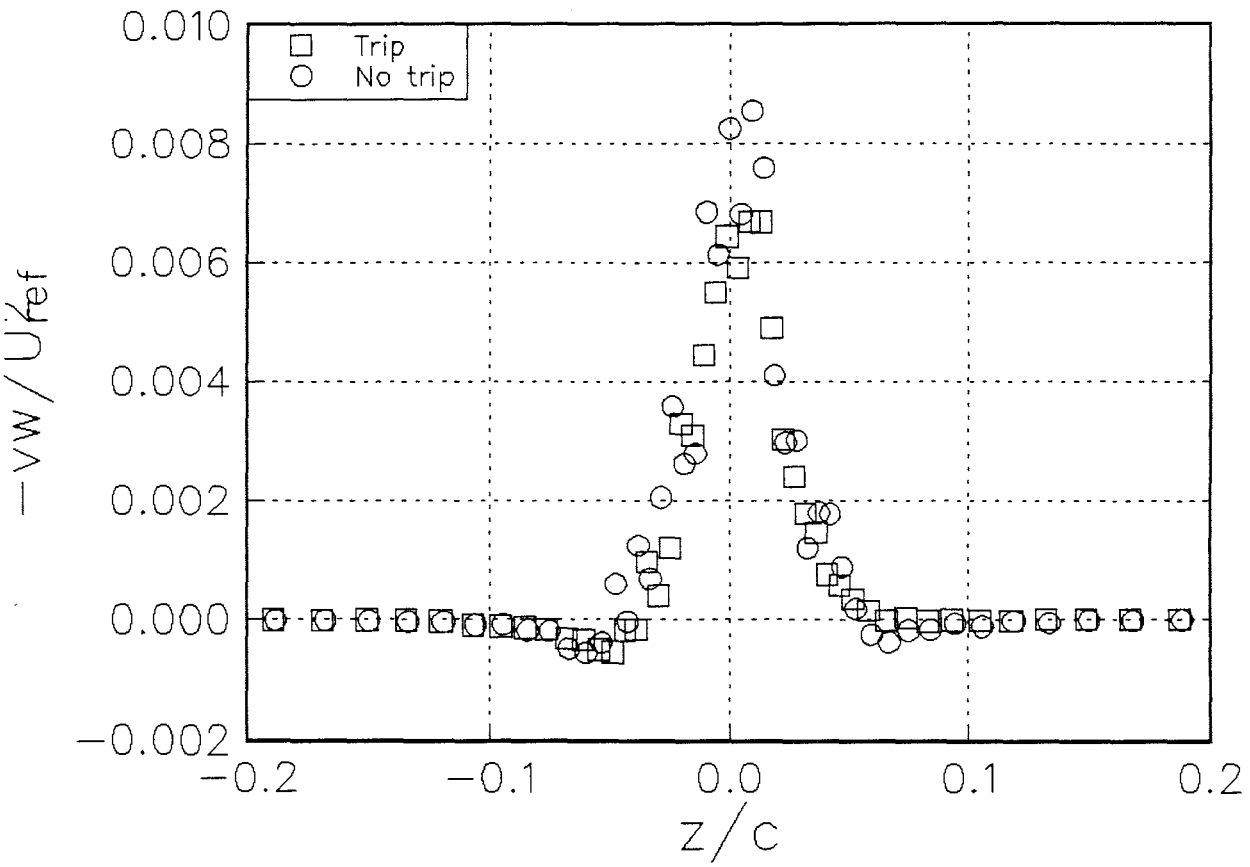

(f) $-\overline{vw}/U_{ref}^2$

Figure 3.19 Velocity profiles in the core region as a function of wing trip for $\alpha=5.0°$, $Re_c=530000$, $x/c=30$.

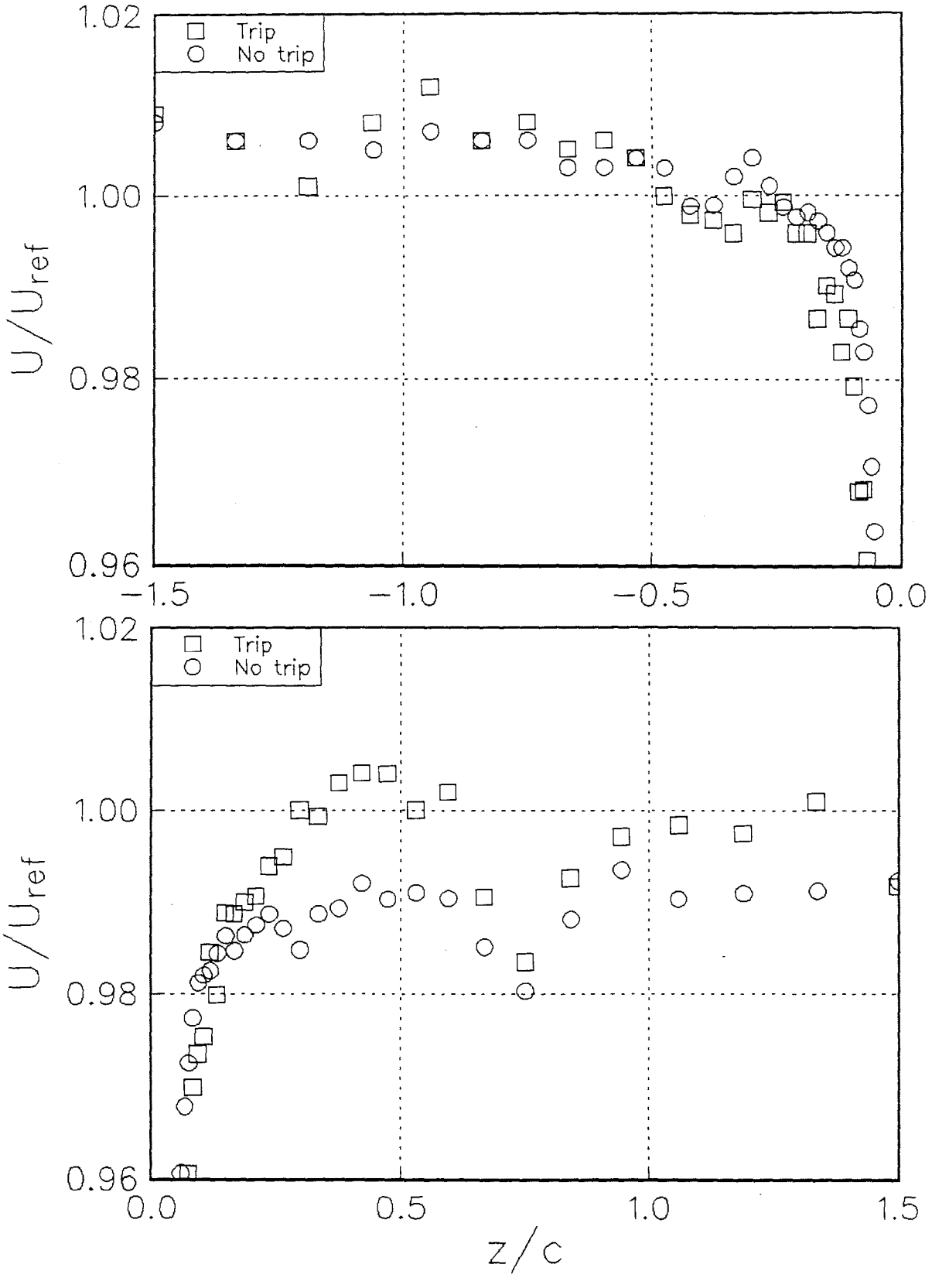

(a) U/U_{ref}

Figure 3.20 Velocity profiles in the wake region as a function of wing trip for $\alpha=5.0°$, $Re_c=530000$, $x/c=30$.

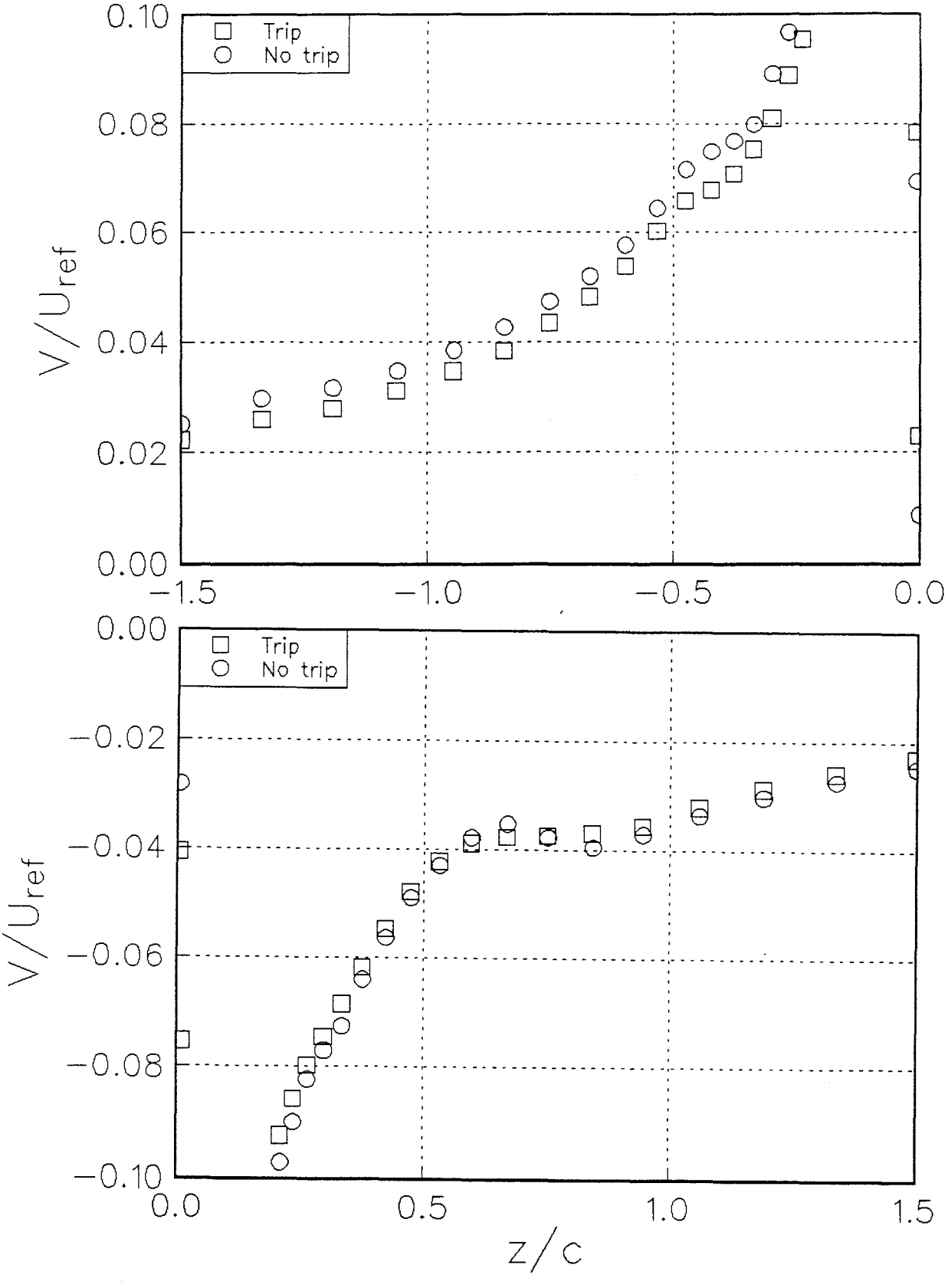

(b) V/U_{ref}

Figure 3.20 Velocity profiles in the wake region as a function of wing trip for $\alpha=5.0^{o}$, $Re_c=530000$, $x/c=30$.

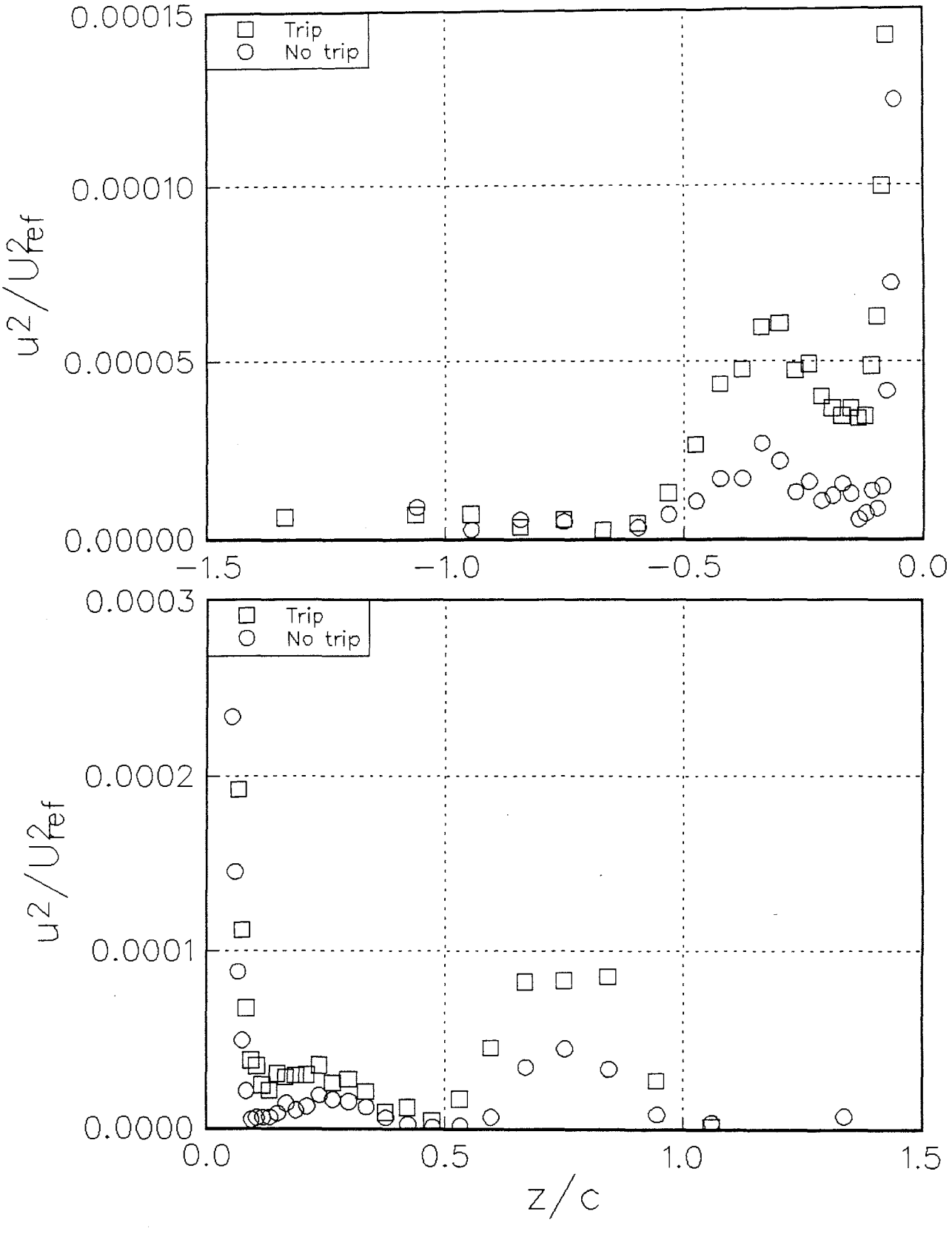

(c) $\overline{u^2}/U_{ref}^2$

Figure 3.20 Velocity profiles in the wake region as a function of wing trip for $\alpha = 5.0°$, $Re_c = 530000$, $x/c = 30$.

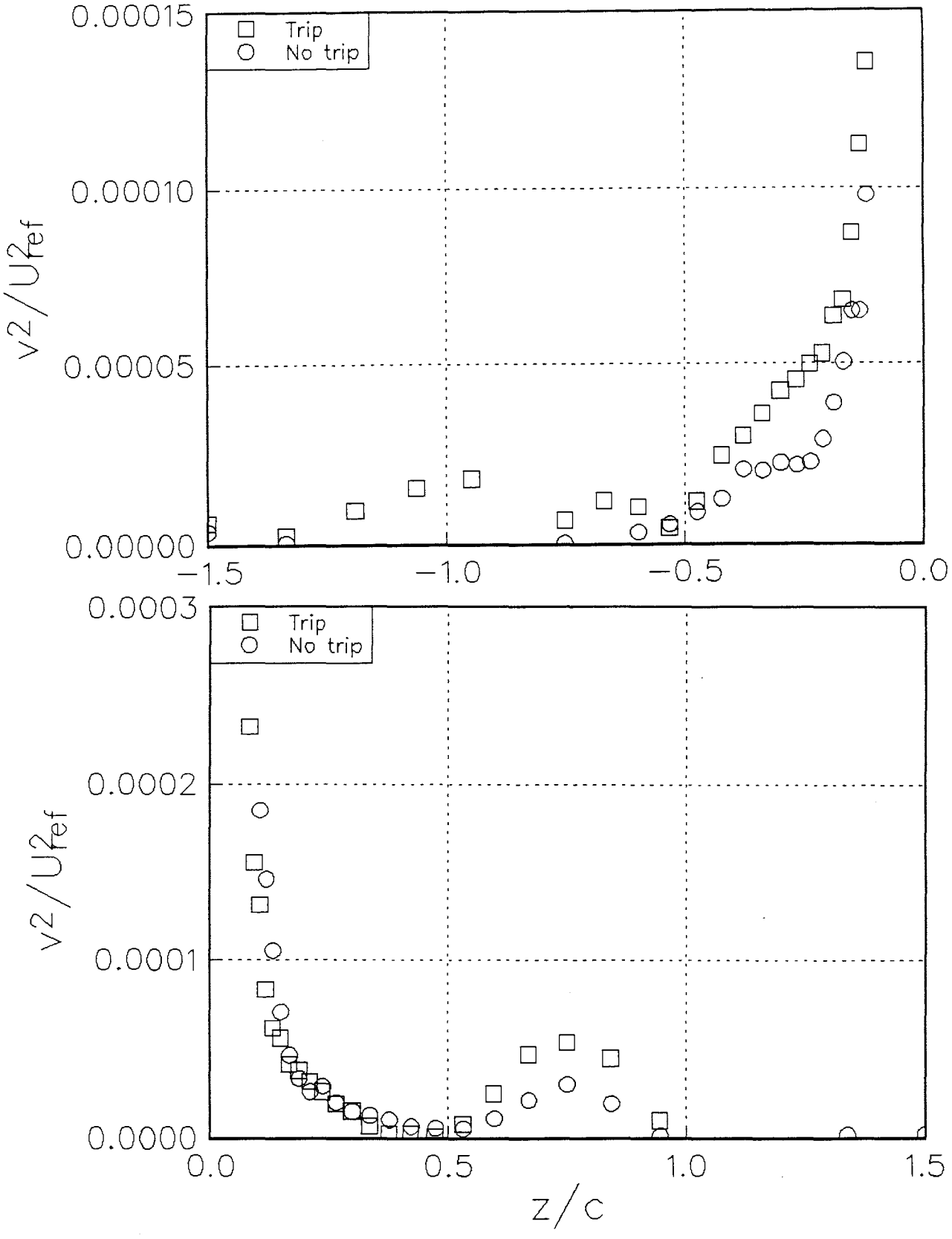

(d) $\overline{v^2}/U_{ref}^2$

Figure 3.20 Velocity profiles in the wake region as a function of wing trip for $\alpha=5.0^o$, $Re_c=530000$, $x/c=30$.

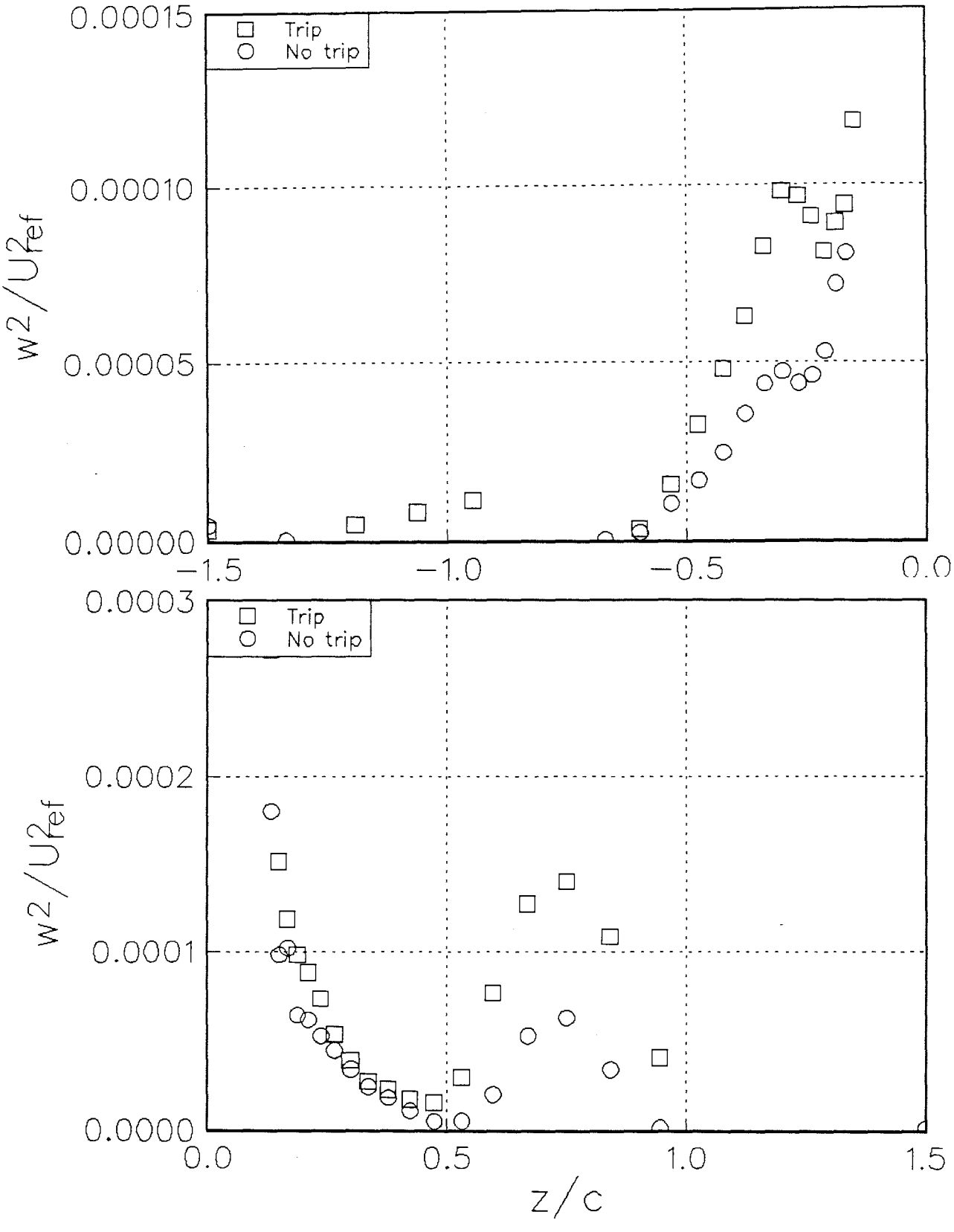

(e) $\overline{w^2}/U_{ref}^2$

Figure 3.20 Velocity profiles in the wake region as a function of wing trip for α=5.0°, Re_c=530000, x/c=30.

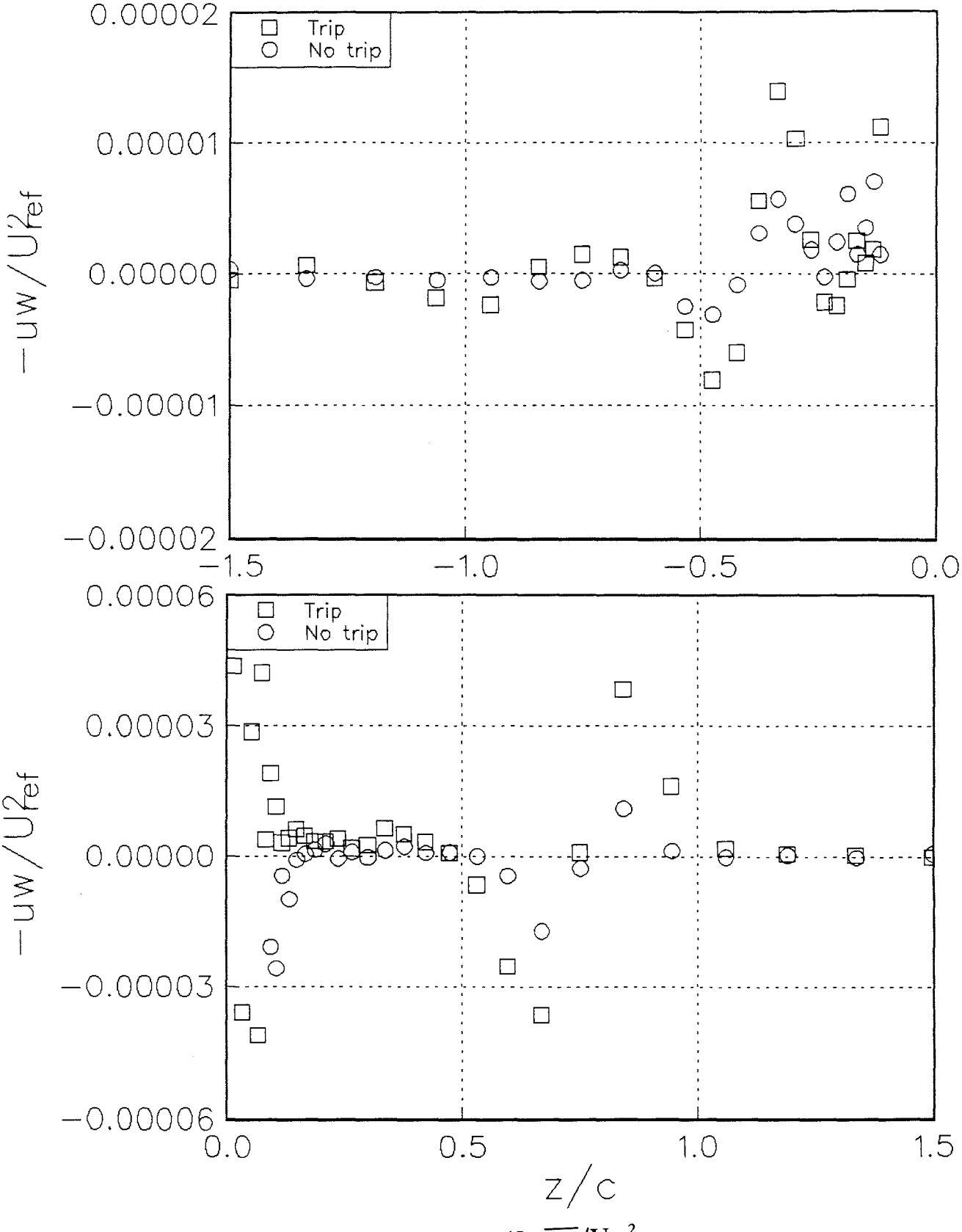

(f) $-\overline{uw}/U_{ref}^2$

Figure 3.20 Velocity profiles in the wake region as a function of wing trip for $\alpha = 5.0°$, $Re_c = 530000$, $x/c = 30$.

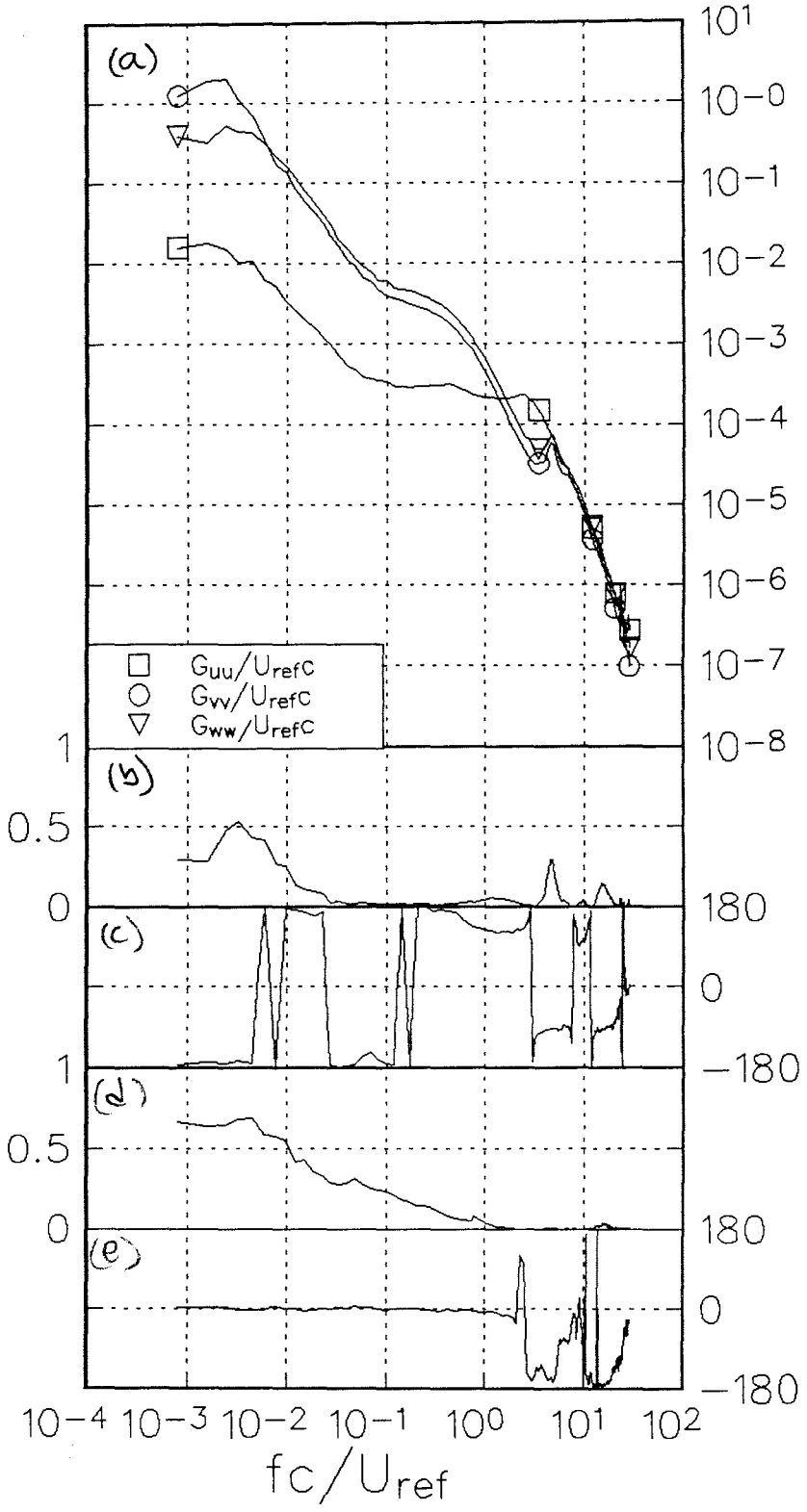

Figure 3.21 Composite spectra of velocity fluctuations at the core center. Re_c=400000, x/c=20, α=5.0°. (a) autospectra, (b) VW coherence, (c) VW phase, (d) UQ coherence, (e) UQ phase. Note, Q is the magnitude of the instantaneous circumferencial velocity defined as $Q = \sqrt{V^2+W^2}$.

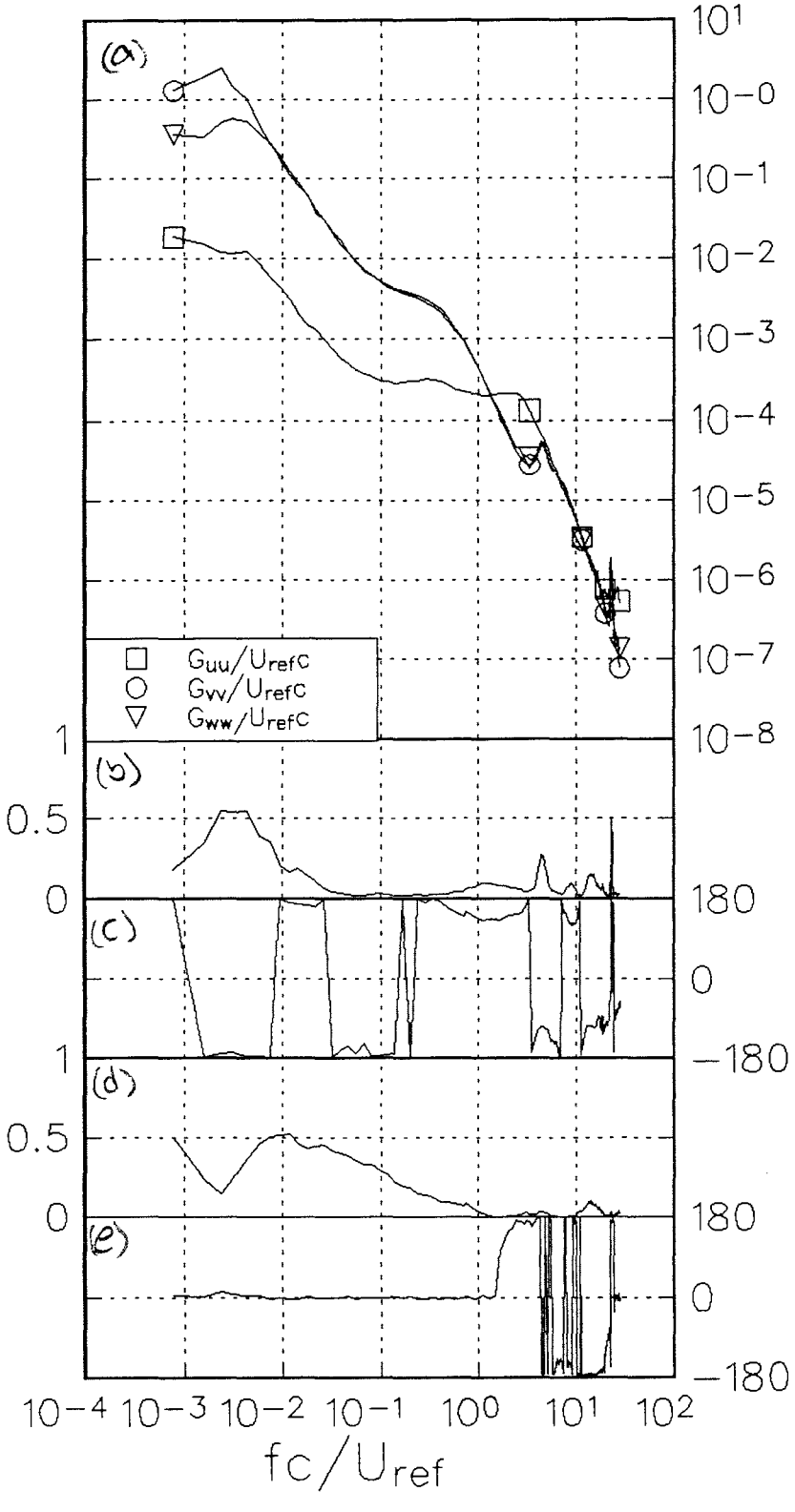

Figure 3.22 Composite spectra of velocity fluctuations at the core center. Re_c=400000, x/c=25, α=5.0°. (a) autospectra, (b) VW coherence, (c) VW phase, (d) UQ coherence, (e) UQ phase. Note, Q is the magnitude of the instantaneous circumferencial velocity defined as $Q = \sqrt{V^2+W^2}$.

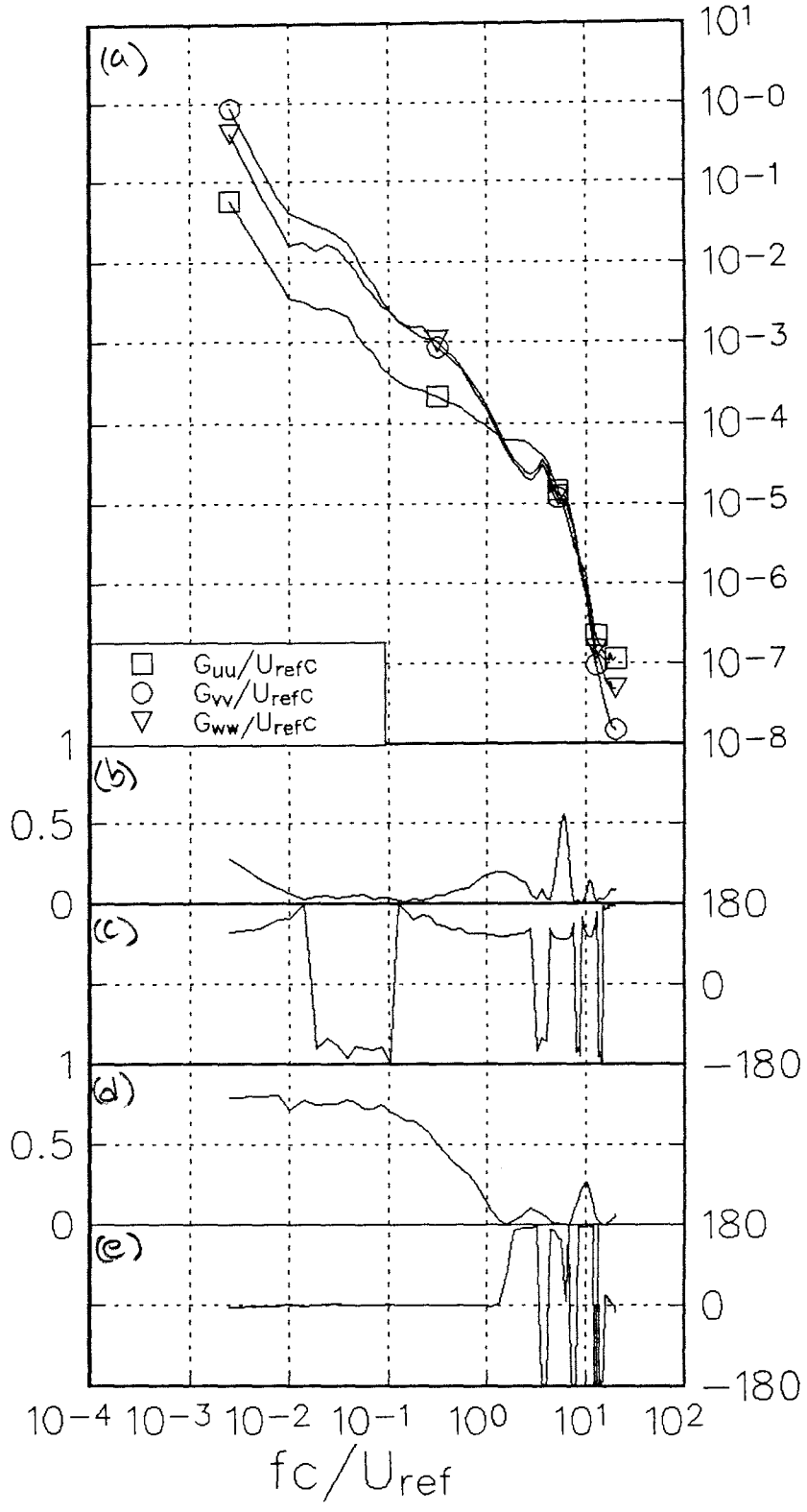

Figure 3.23 Composite spectra of velocity fluctuations at the core center. $Re_c = 130000$, $x/c = 30$, $\alpha = 5.0°$. (a) autospectra, (b) VW coherence, (c) VW phase, (d) UQ coherence, (e) UQ phase. Note, Q is the magnitude of the instantaneous circumferencial velocity defined as $Q = \sqrt{V^2+W^2}$.

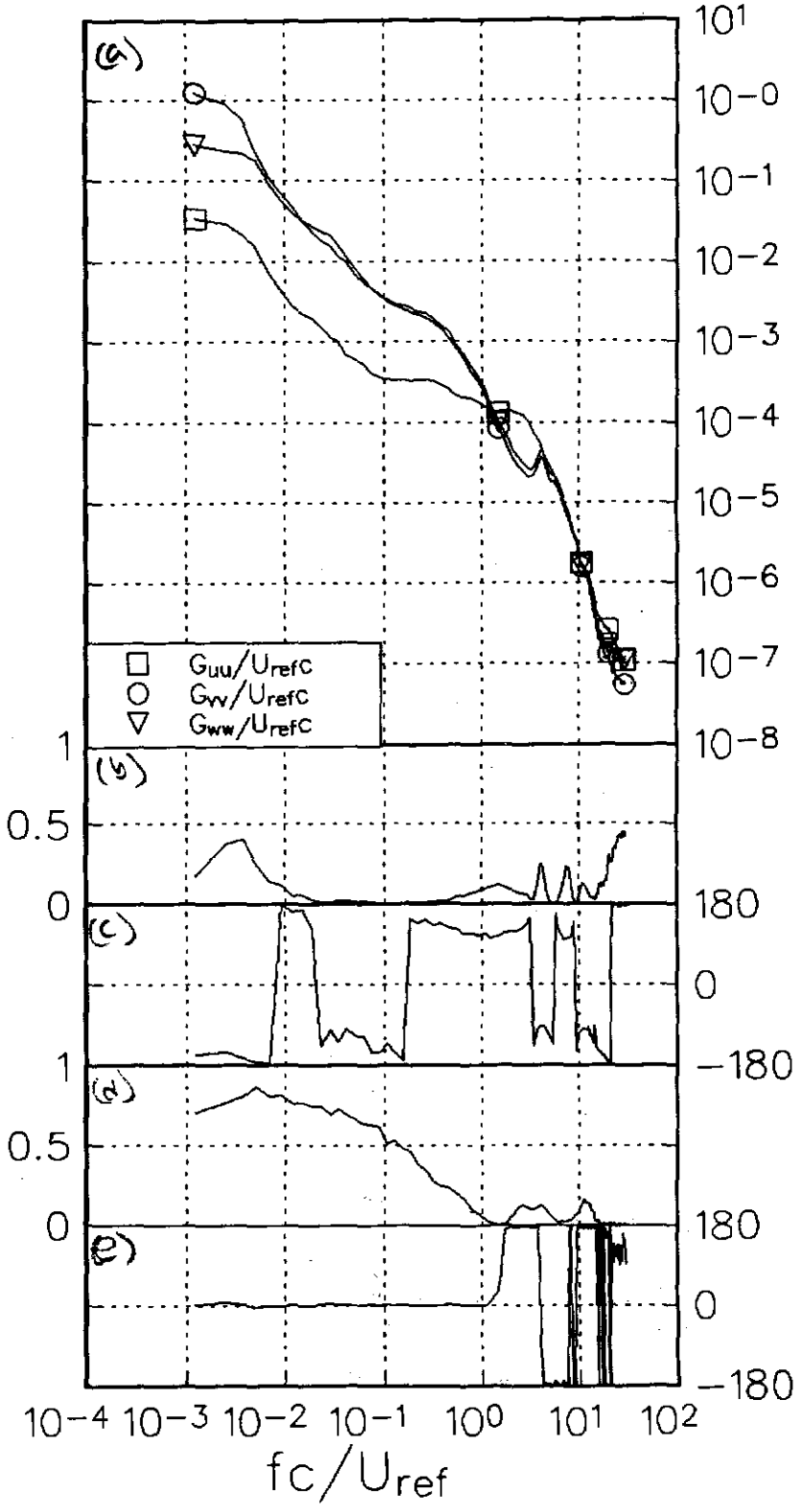

Figure 3.24 Composite spectra of velocity fluctuations at the core center. Re_c=260000, x/c=30, α=5.0°. (a) autospectra, (b) VW coherence, (c) VW phase, (d) UQ coherence, (e) UQ phase. Note, Q is the magnitude of the instantaneous circumferencial velocity defined as $Q = \sqrt{V^2+W^2}$.

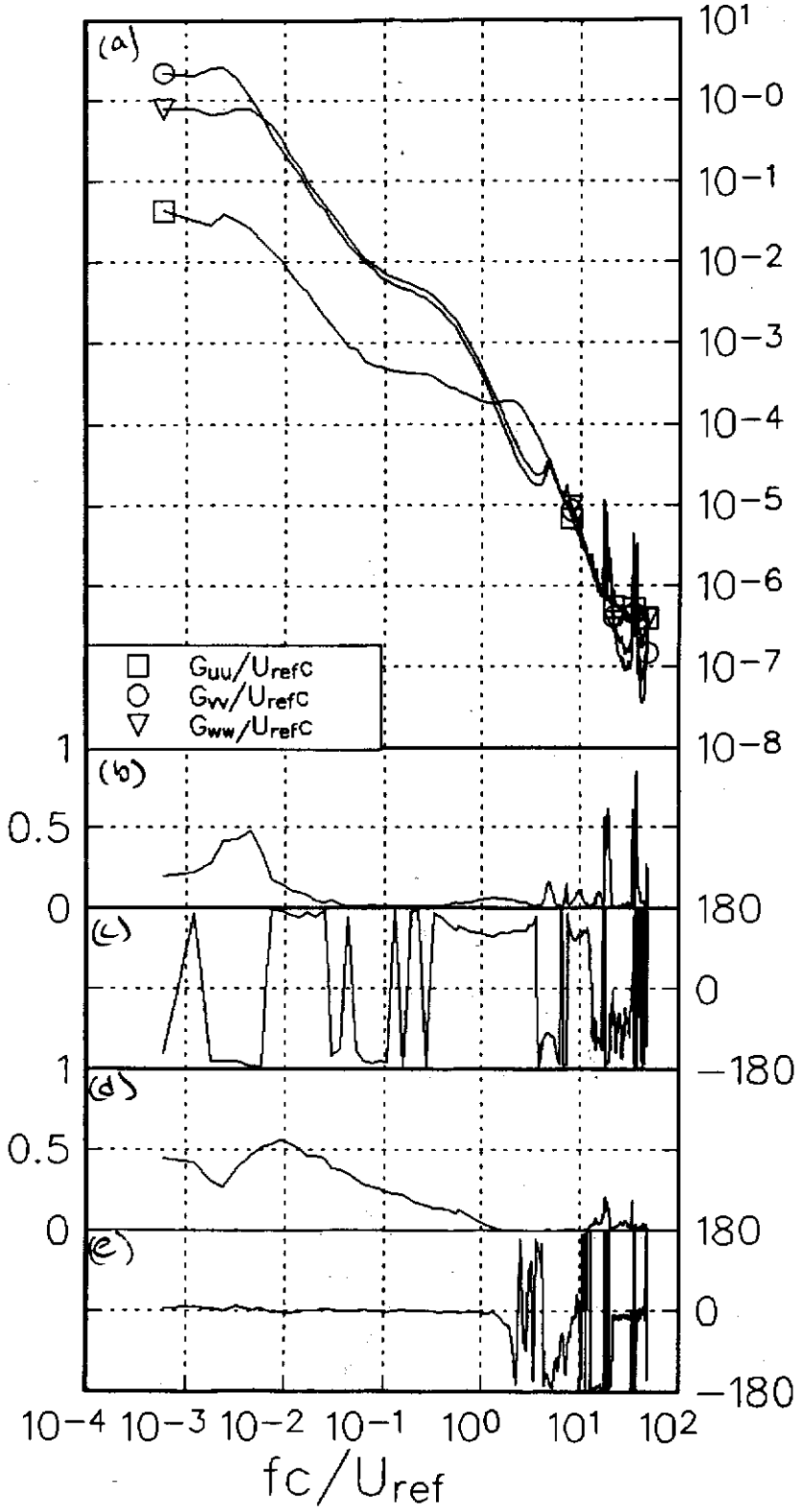

Figure 3.25 Composite spectra of velocity fluctuations at the core center. Re_c=530000, x/c=30, α=5.0°. (a) autospectra, (b) VW coherence, (c) VW phase, (d) UQ coherence, (e) UQ phase. Note, Q is the magnitude of the instantaneous circumferencial velocity defined as $Q = \sqrt{V^2+W^2}$.

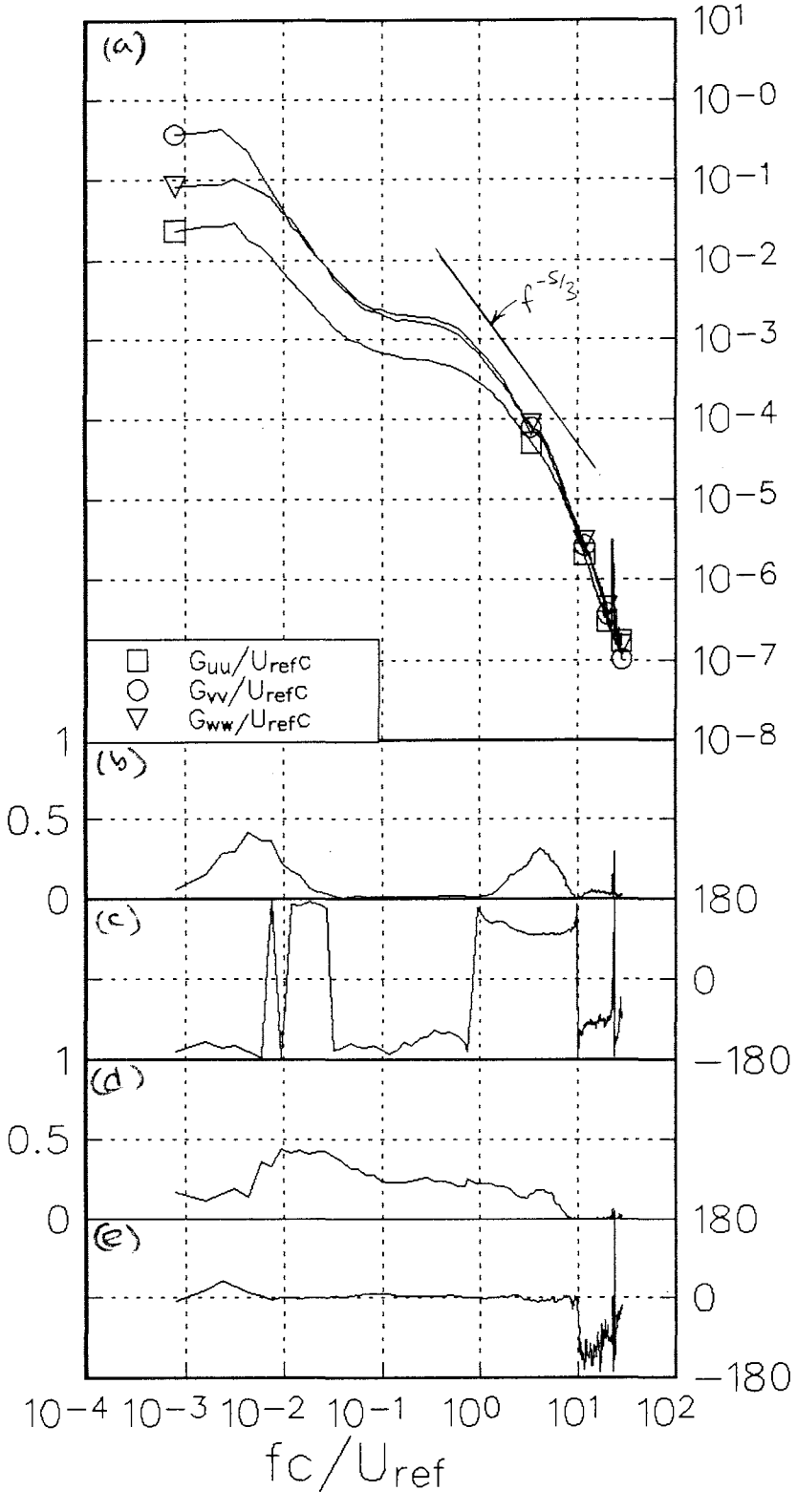

Figure 3.26 Composite spectra of velocity fluctuations at the core center. Re_c=400000, x/c=30, α=2.5°. (a) autospectra, (b) VW coherence, (c) VW phase, (d) UQ coherence, (e) UQ phase. Note, Q is the magnitude of the instantaneous circumferencial velocity defined as $Q = \sqrt{V^2+W^2}$.

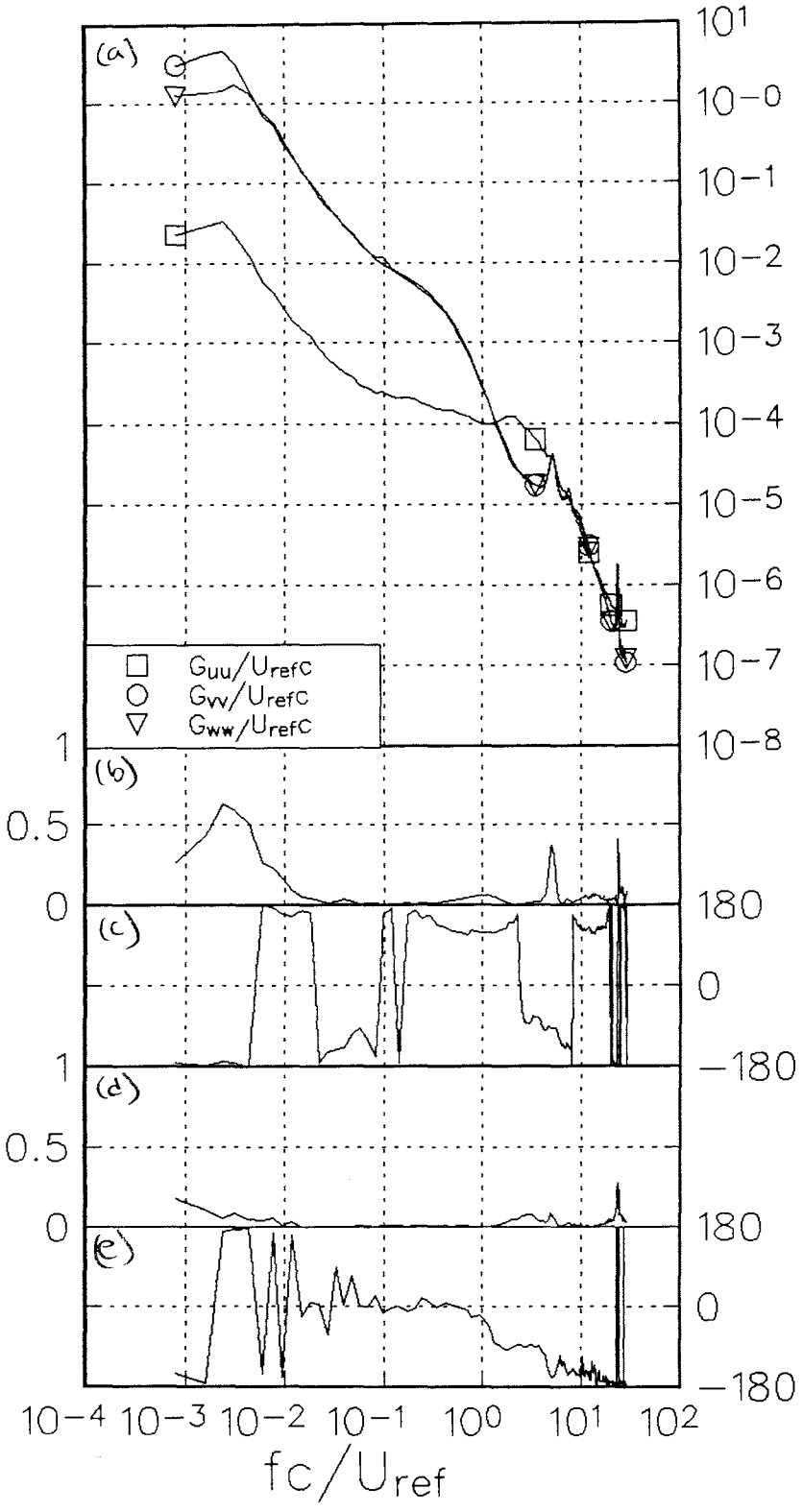

Figure 3.27 Composite spectra of velocity fluctuations at the core center. Re_c=400000, x/c=20, α=7.5°. (a) autospectra, (b) VW coherence, (c) VW phase, (d) UQ coherence, (e) UQ phase. Note, Q is the magnitude of the instantaneous circumferencial velocity defined as $Q = \sqrt{V^2+W^2}$.

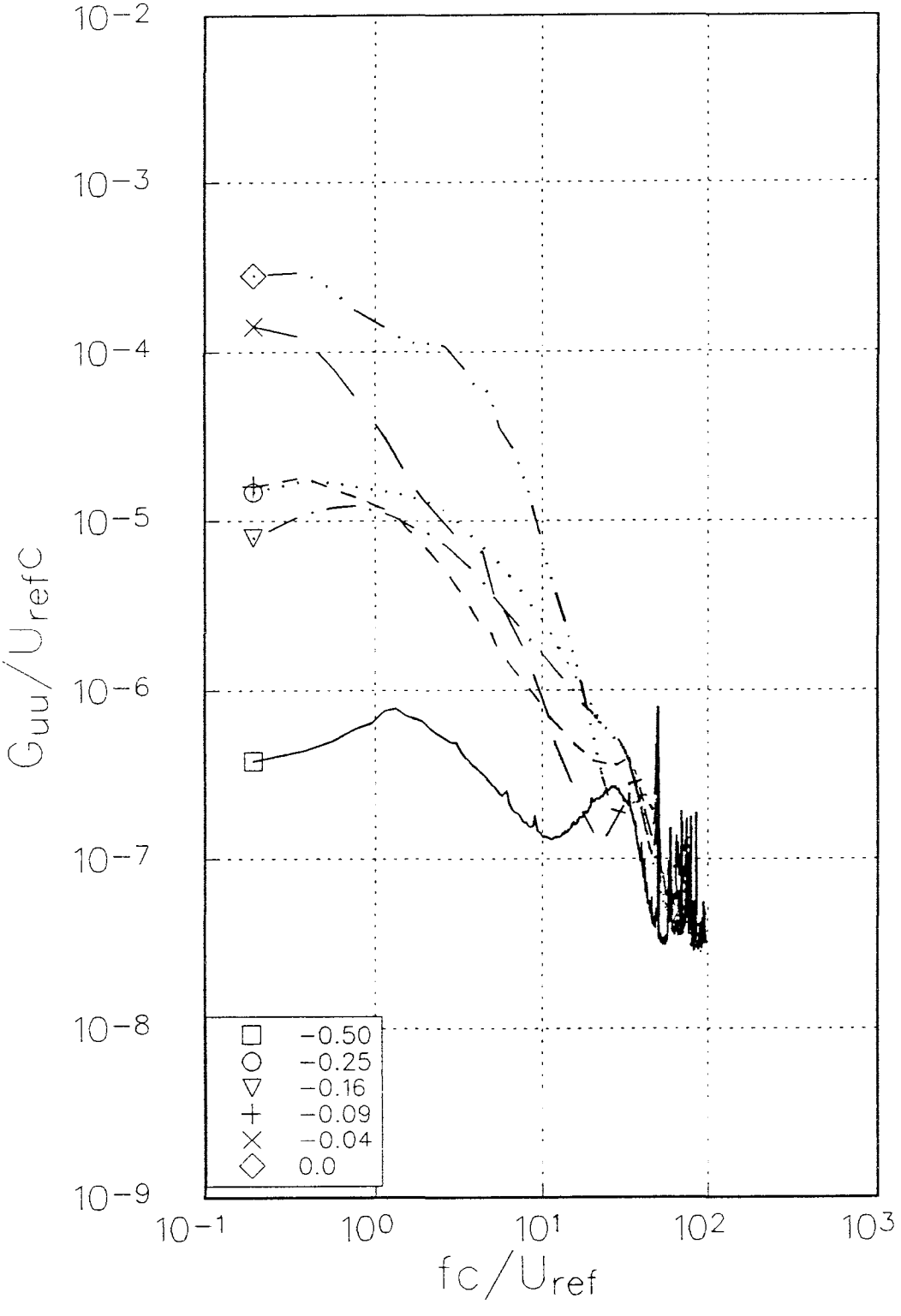

Figure 3.28(a) Autospectra of U component velocity fluctuations measured at various z/c locations for Re_c=400000, x/c=20, α=5.0°.

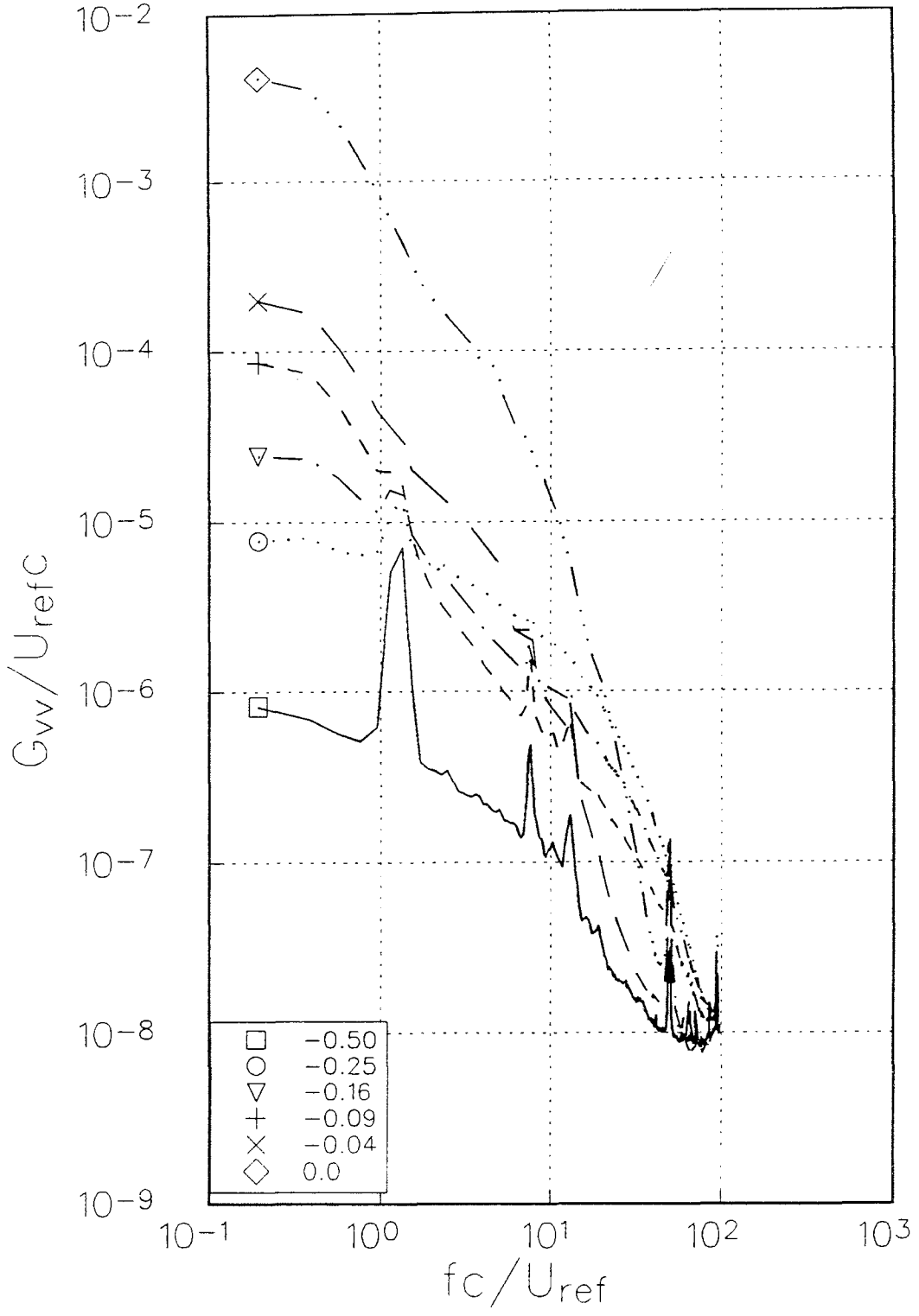

Figure 3.28(b) Autospectra of V component velocity fluctuations measured at various z/c locations for Re_c=400000, x/c=20, α=5.0°.

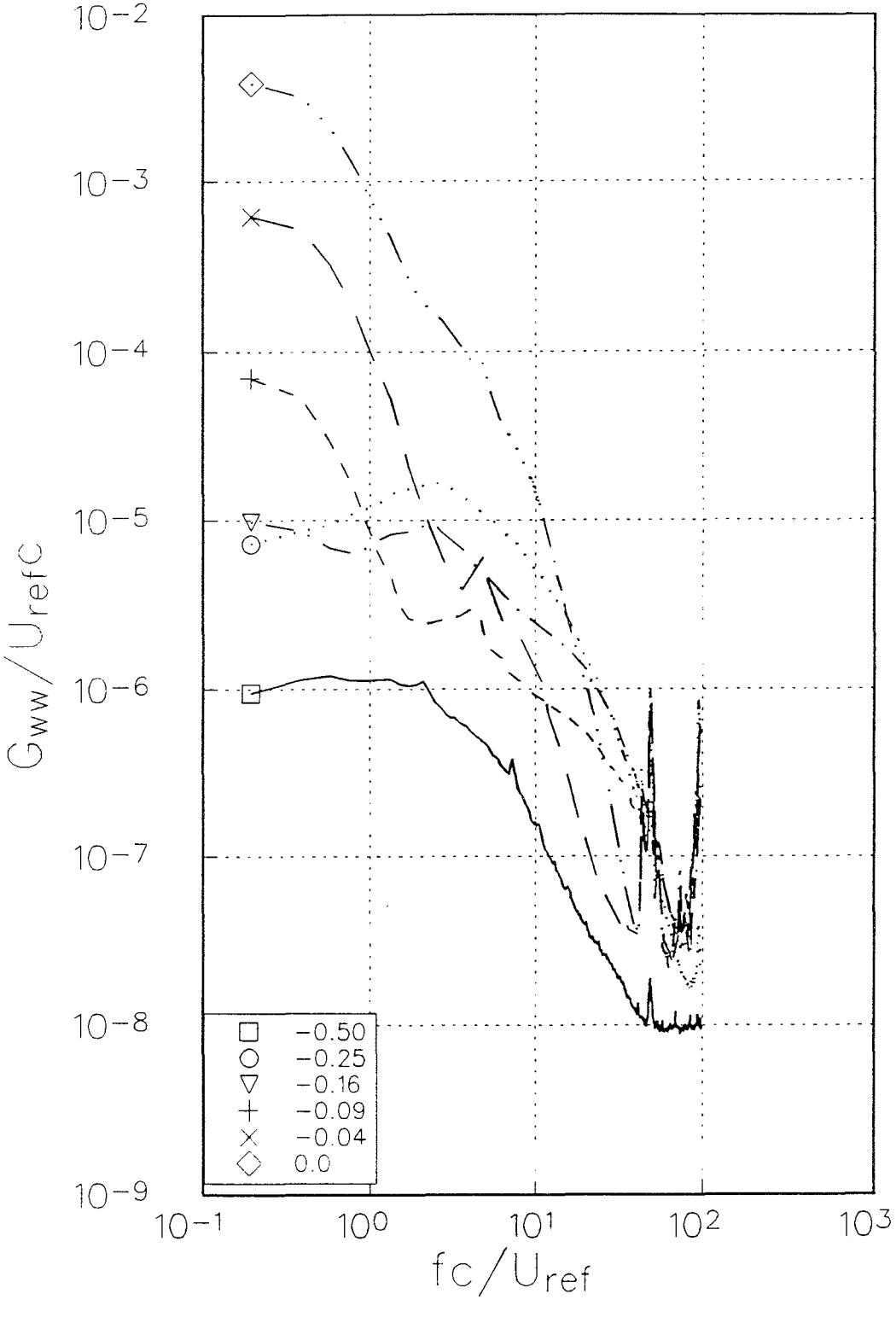

Figure 3.28(c) Autospectra of W component velocity fluctuations measured at various z/c locations for Re_c=400000, x/c=20, α=5.0°.

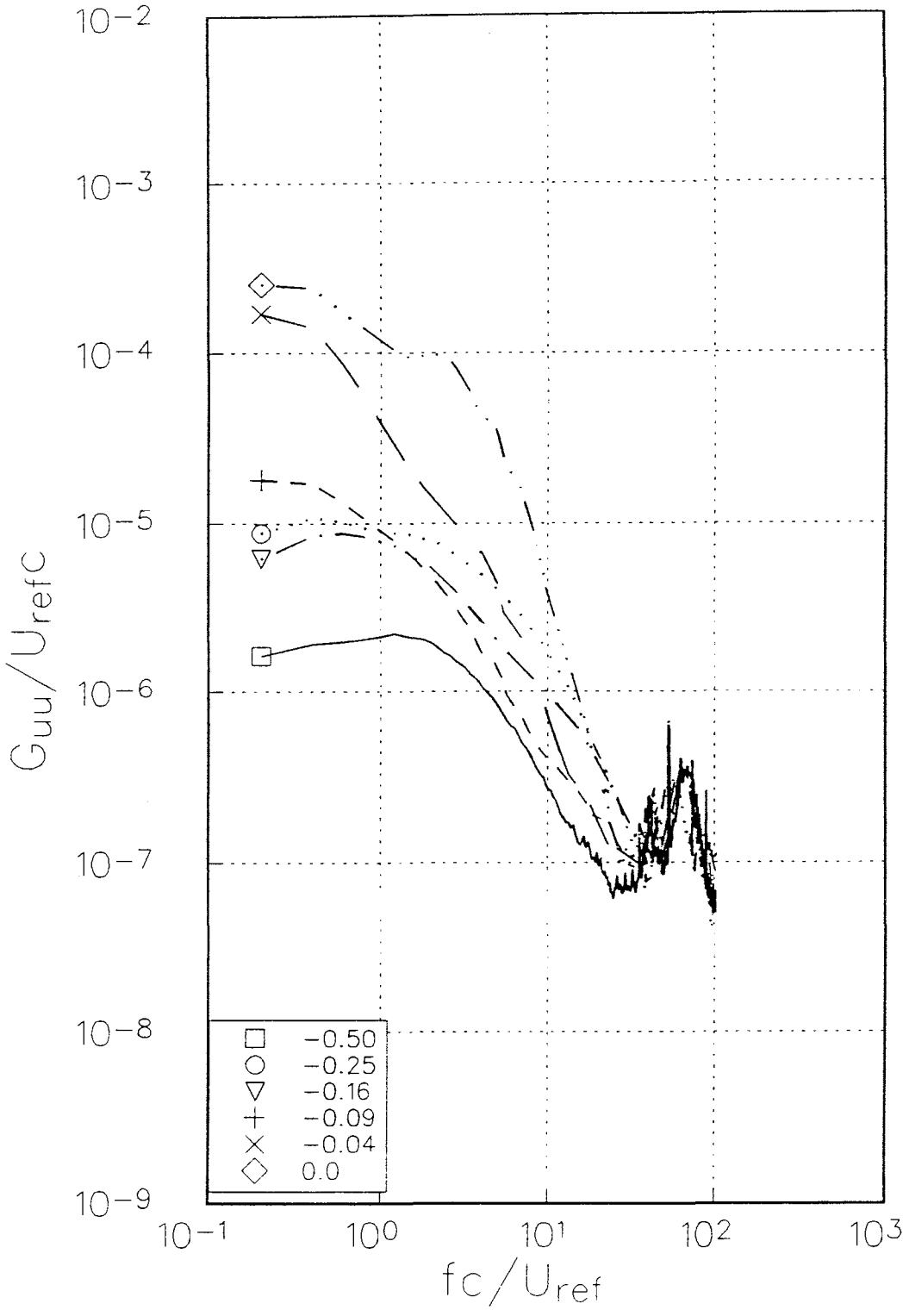

Figure 3.29(a) Autospectra of U component velocity fluctuations measured at various z/c locations for Re_c=400000, x/c=25, α=5.0°.

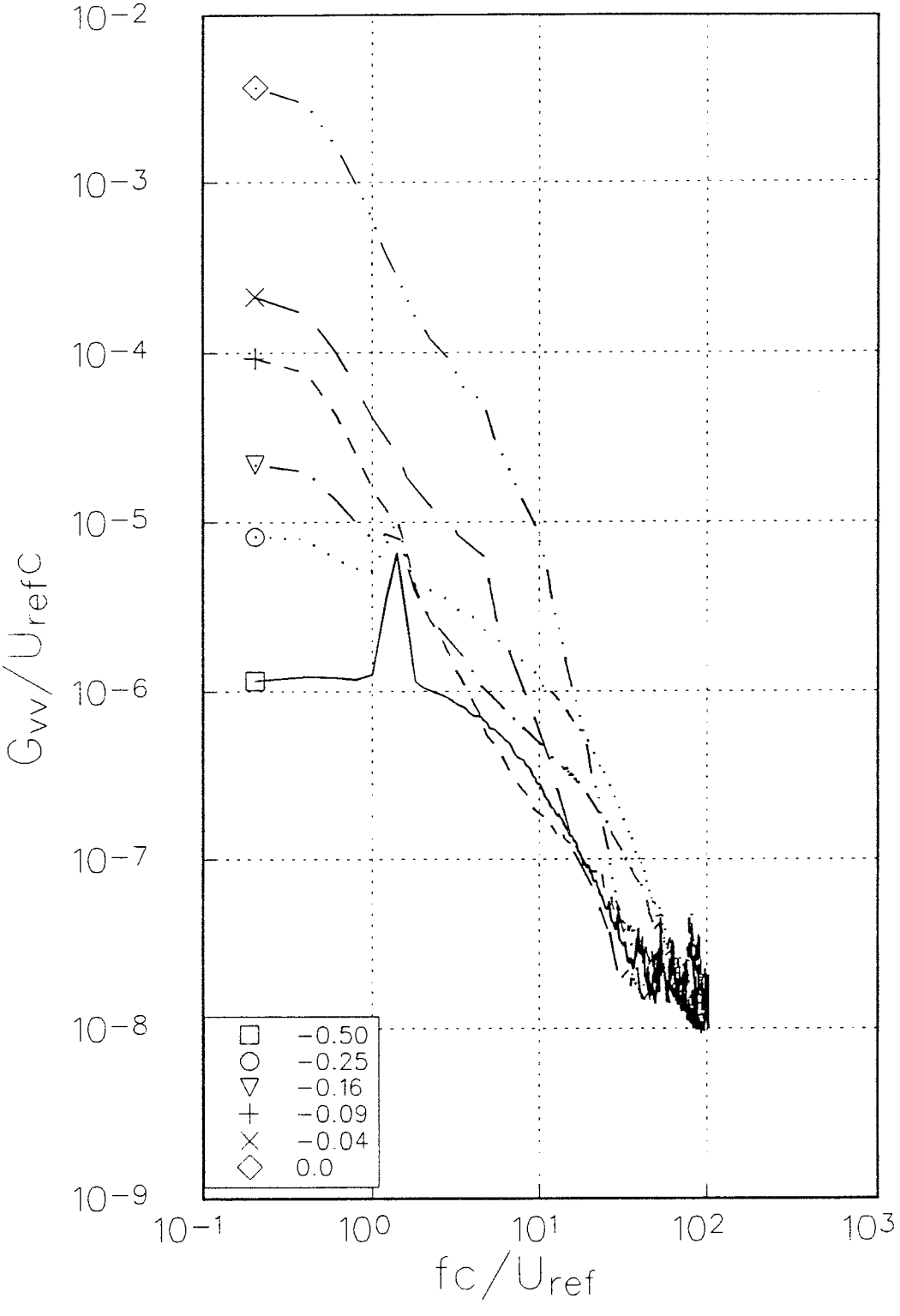

Figure 3.29(b) Autospectra of V component velocity fluctuations measured at various z/c locations for Re_c=400000, x/c=25, α=5.0°.

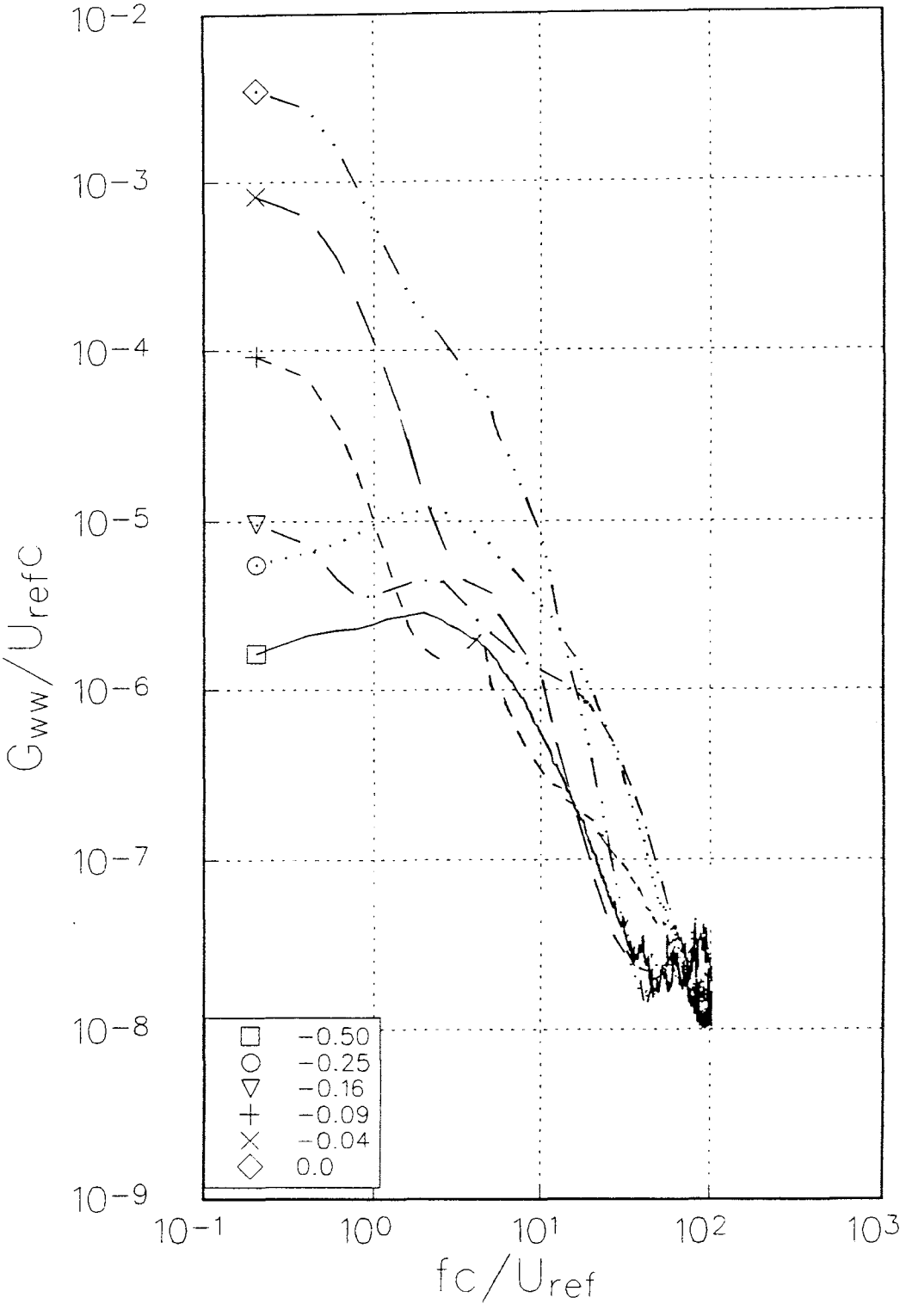

Figure 3.29(c) Autospectra of W component velocity fluctuations measured at various z/c locations for Re_c=400000, x/c=25, α=5.0°.

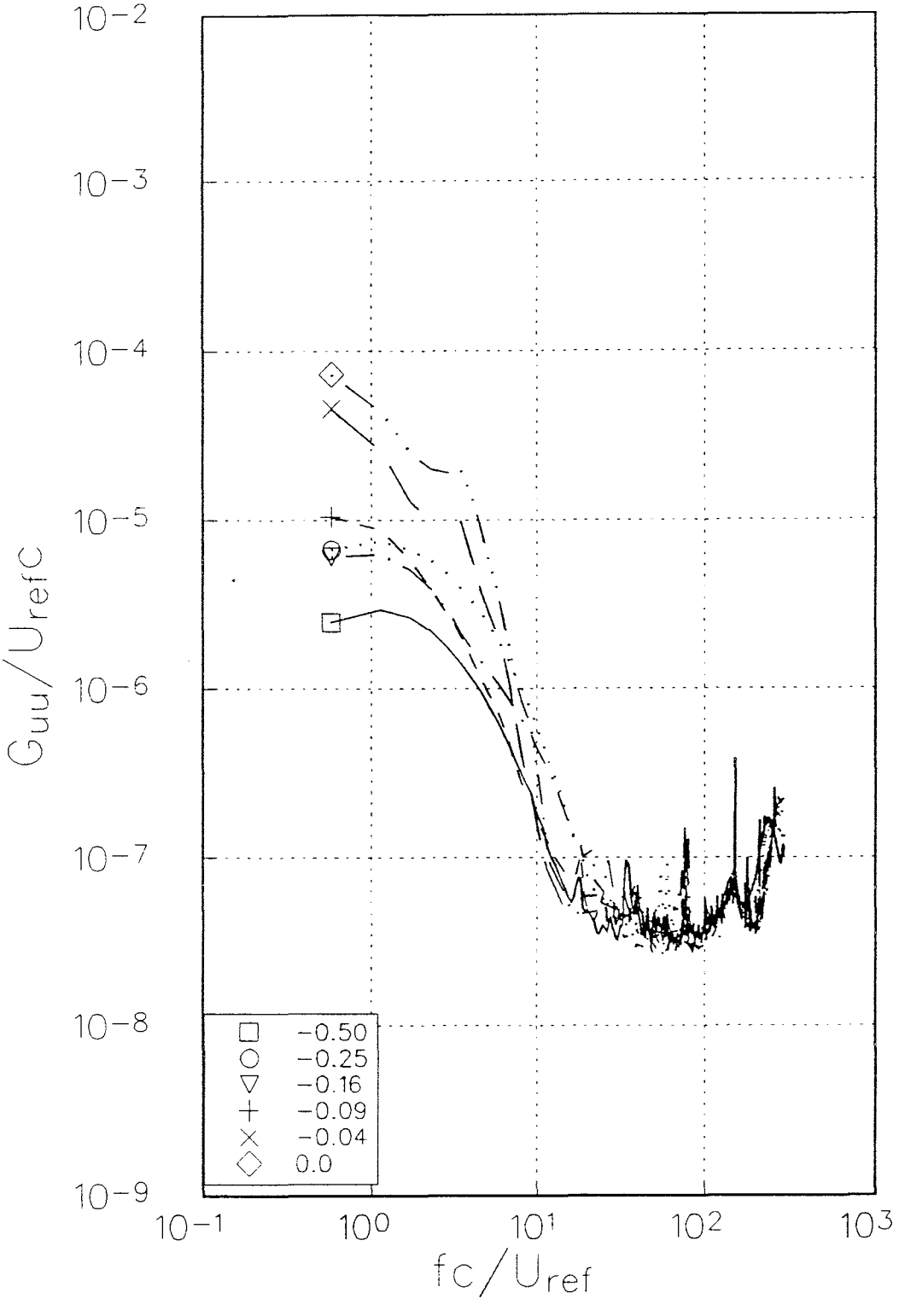

Figure 3.30(a) Autospectra of U component velocity fluctuations measured at various z/c locations for $Re_c = 130000$, $x/c = 30$, $\alpha = 5.0^o$.

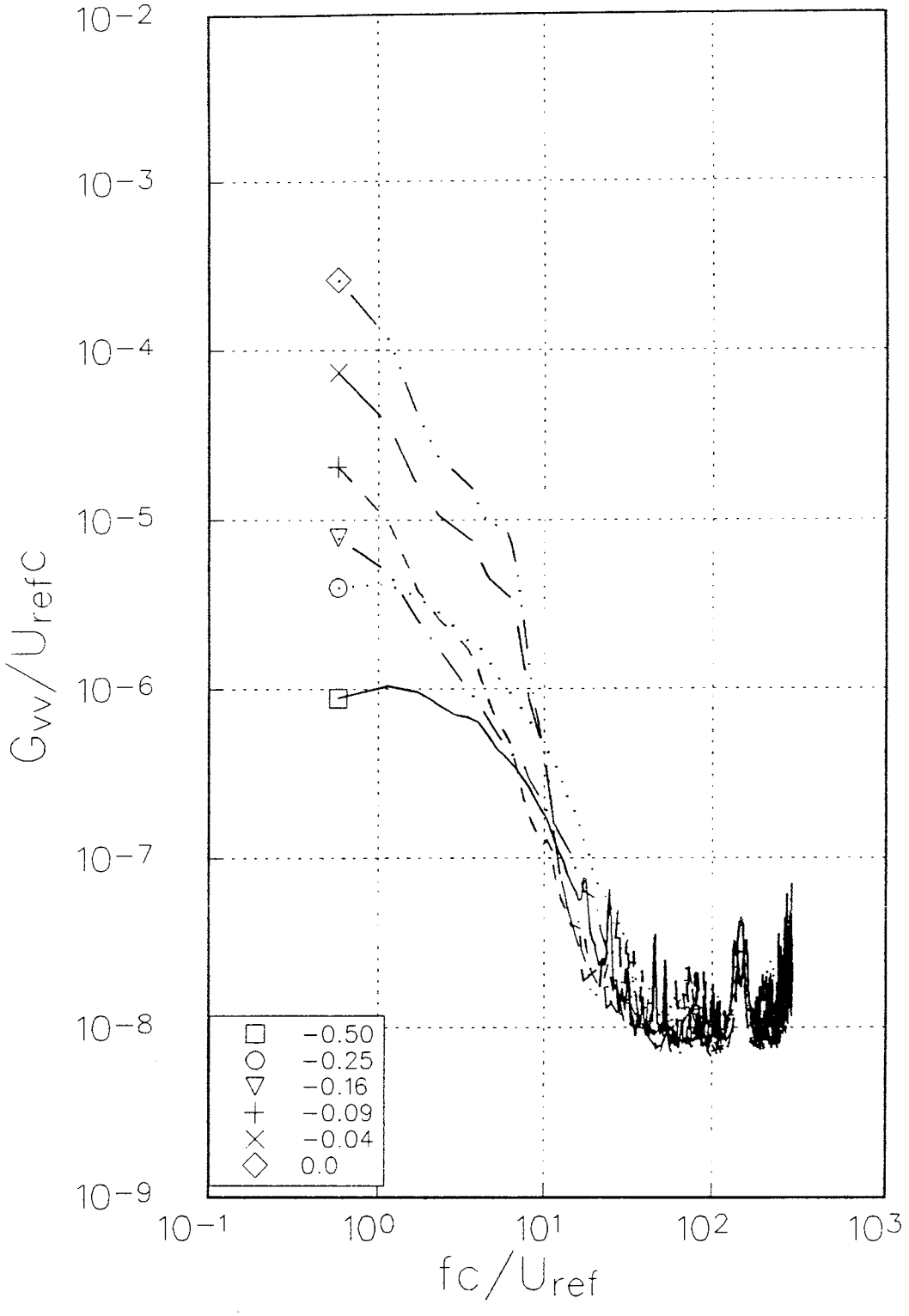

Figure 3.30(b) Autospectra of V component velocity fluctuations measured at various z/c locations for $Re_c = 130000$, x/c=30, $\alpha = 5.0°$.

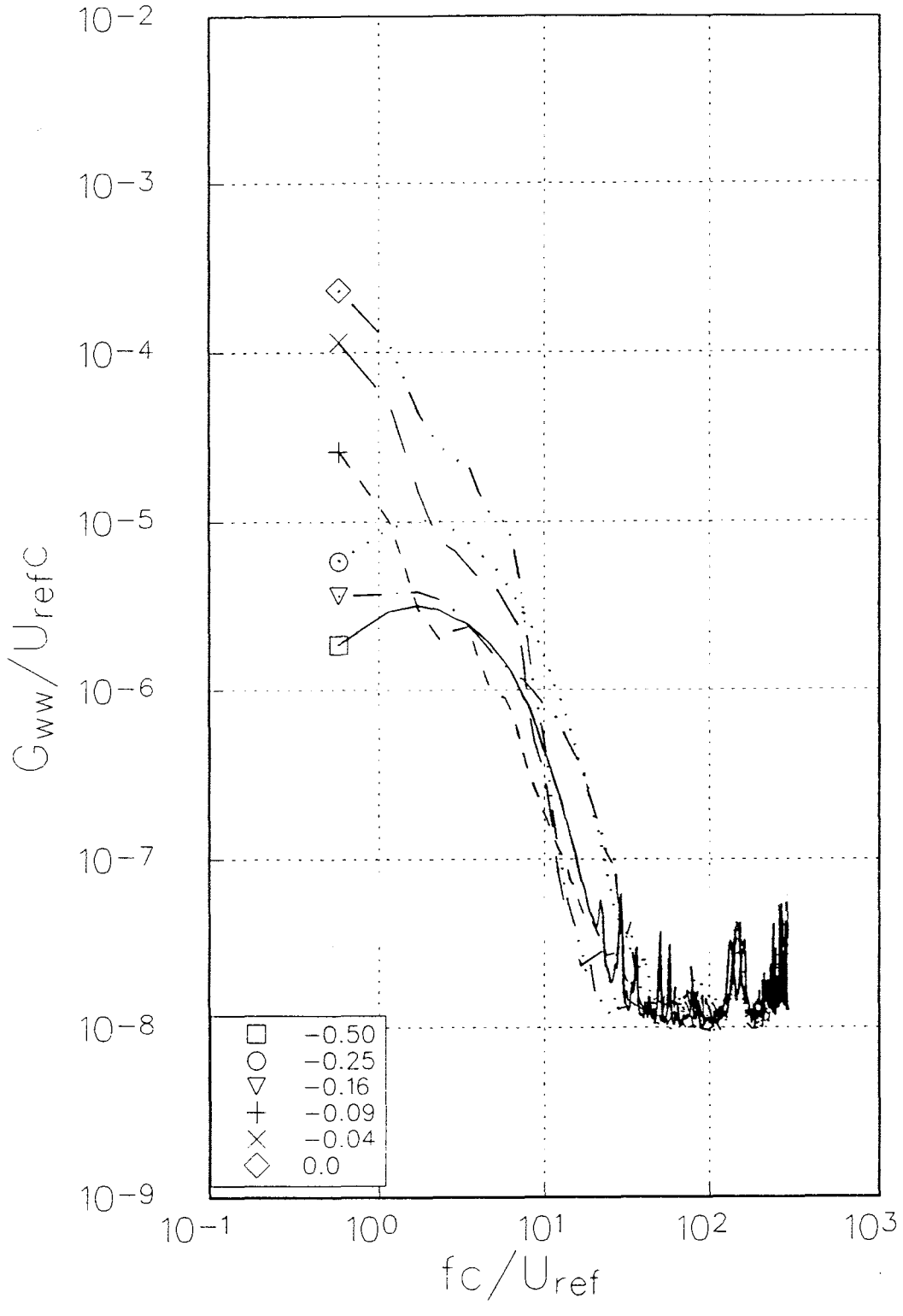

Figure 3.30(c) Autospectra of W component velocity fluctuations measured at various z/c locations for $Re_c = 130000$, x/c=30, $\alpha = 5.0°$.

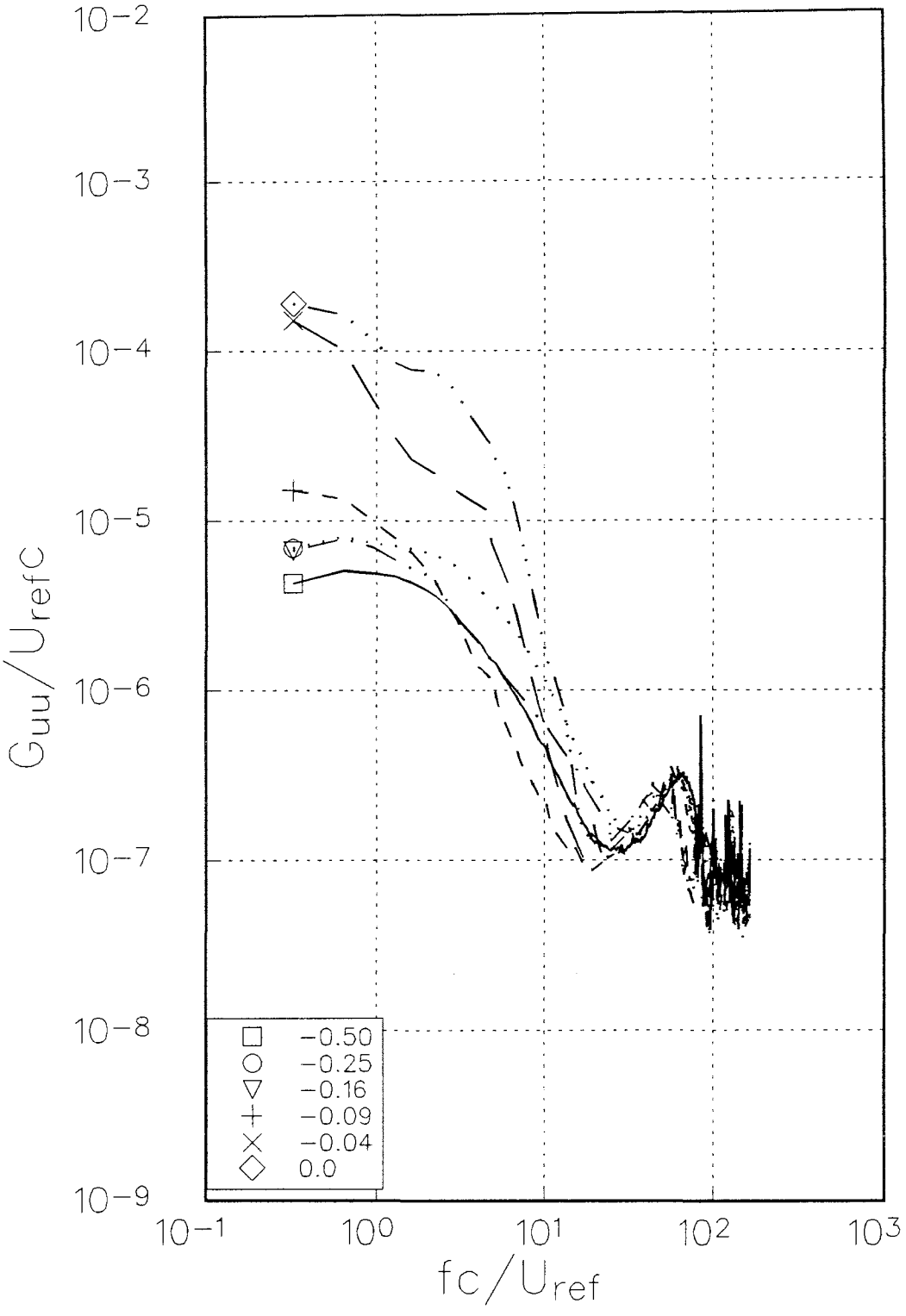

Figure 3.31(a) Autospectra of U component velocity fluctuations measured at various z/c locations for Re_c=260000, x/c=30, α=5.0°.

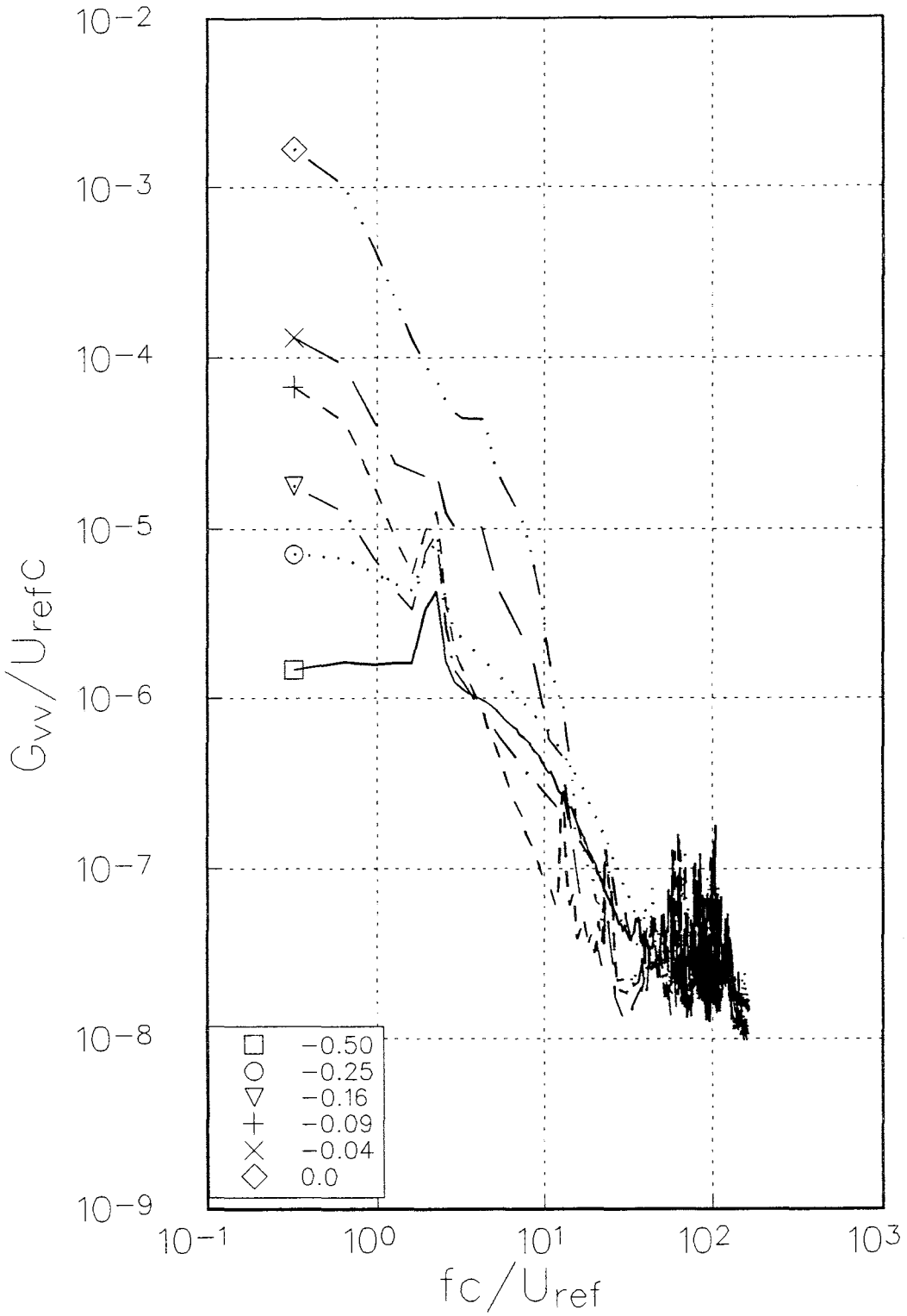

Figure 3.31(b) Autospectra of V component velocity fluctuations measured at various z/c locations for Re_c=260000, x/c=30, α=5.0°.

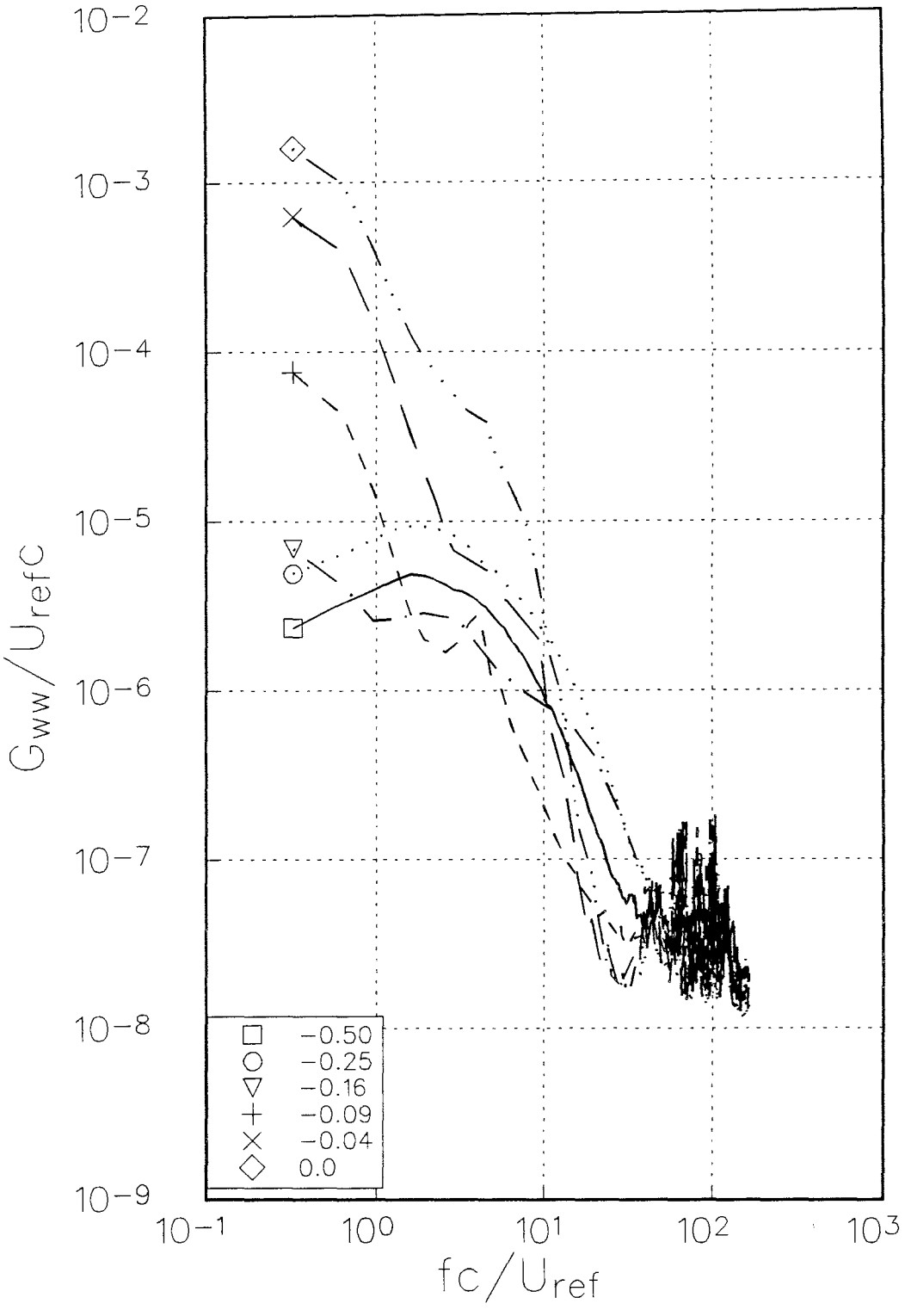

Figure 3.31(c) Autospectra of W component velocity fluctuations measured at various z/c locations for Re_c=260000, x/c=30, α=5.0°.

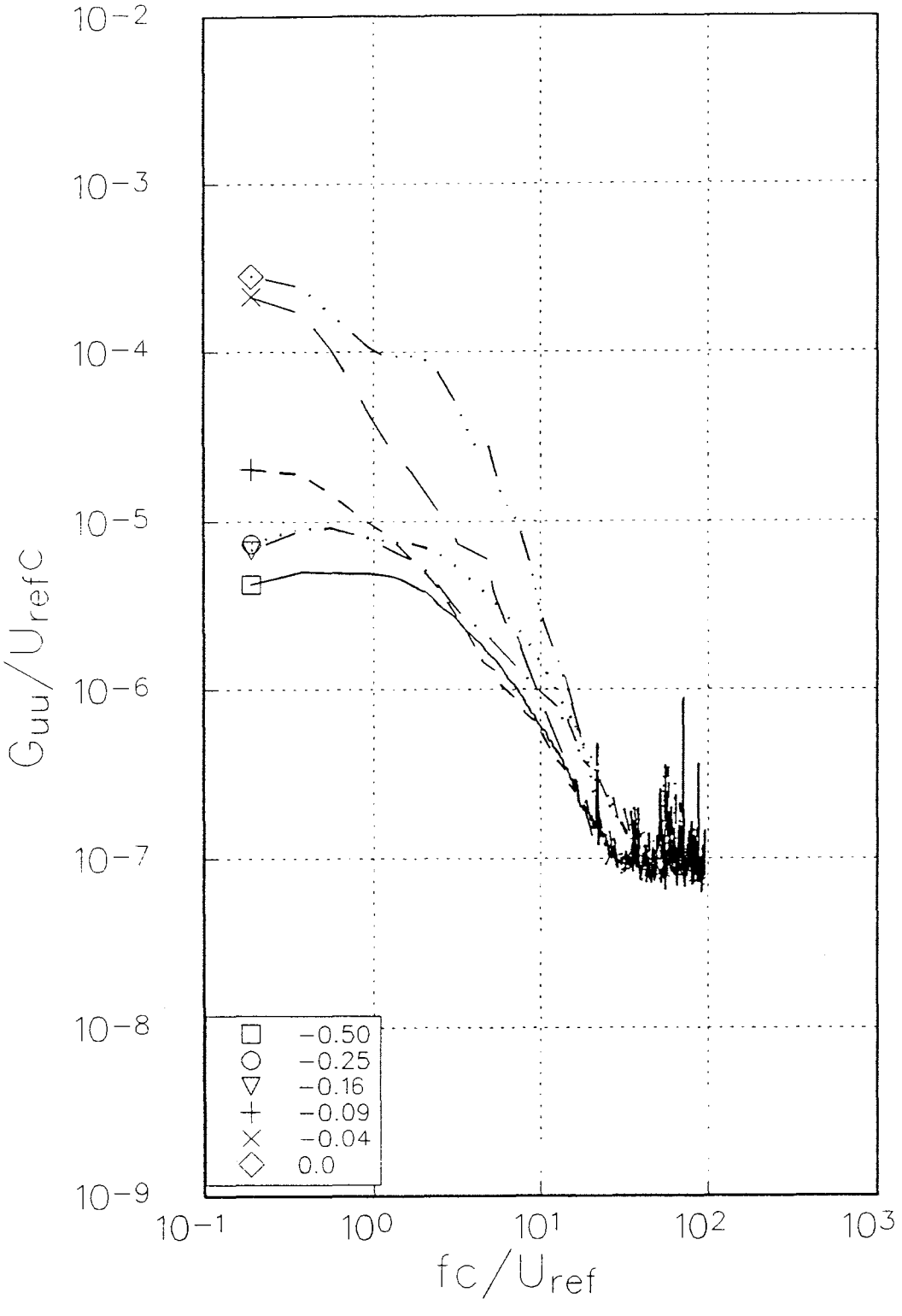

Figure 3.32(a) Autospectra of U component velocity fluctuations measured at various z/c locations for $Re_c = 530000$, $x/c = 30$, $\alpha = 5.0^{\circ}$.

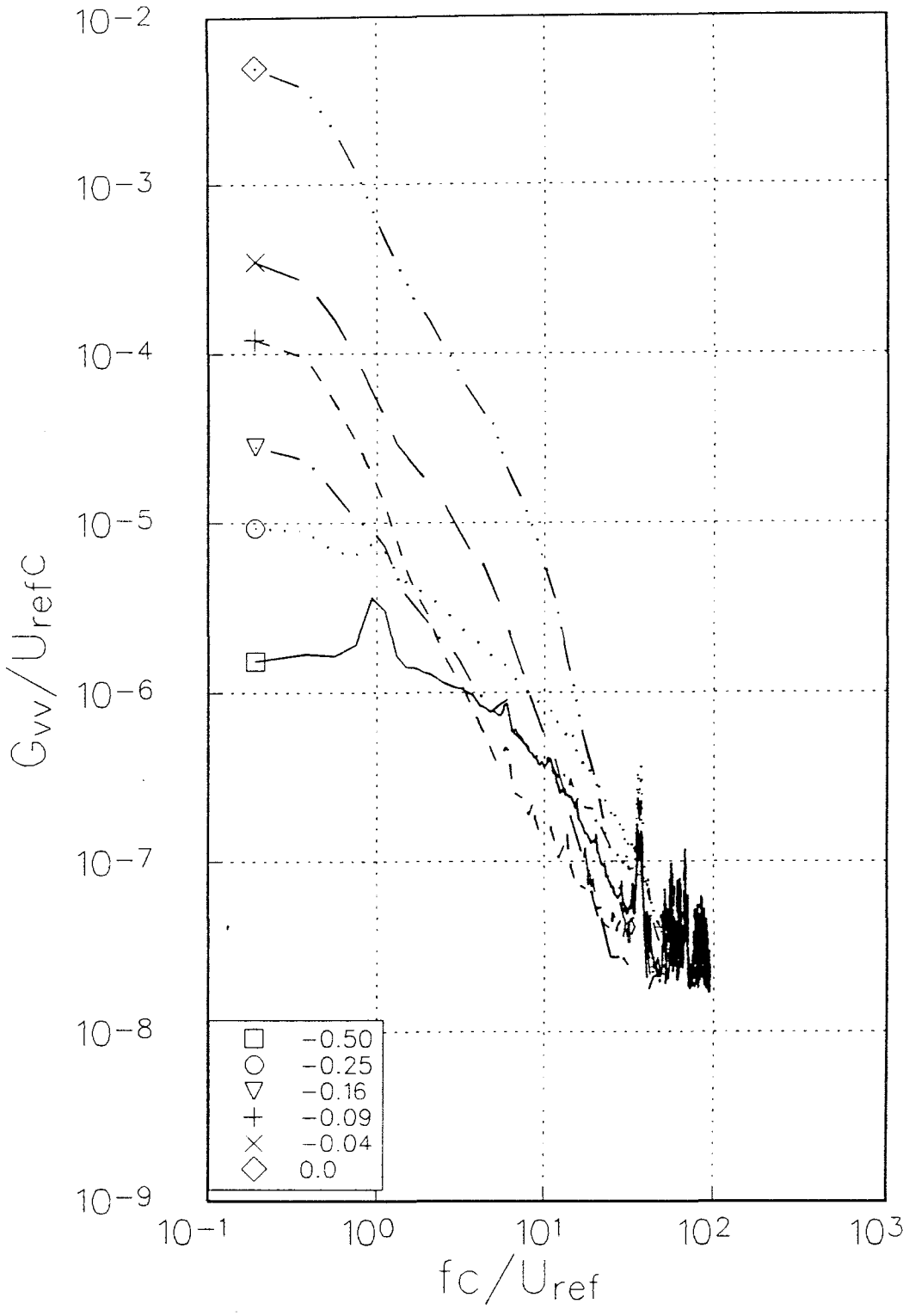

Figure 3.32(b) Autospectra of V component velocity fluctuations measured at various z/c locations for Re_c=530000, x/c=30, α=5.0°.

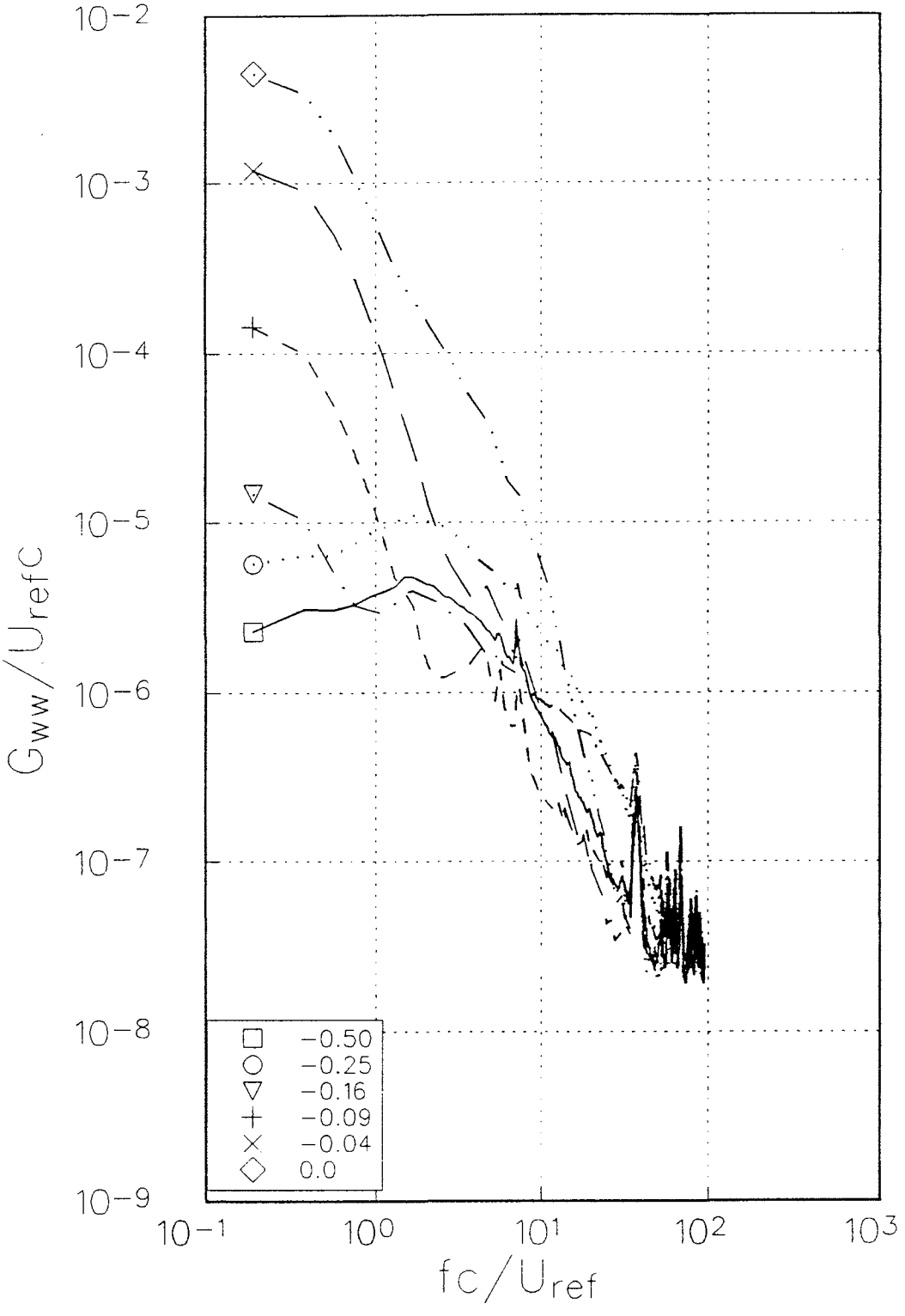

Figure 3.32(c) Autospectra of W component velocity fluctuations measured at various z/c locations for Re_c=530000, x/c=30, α=5.0°.

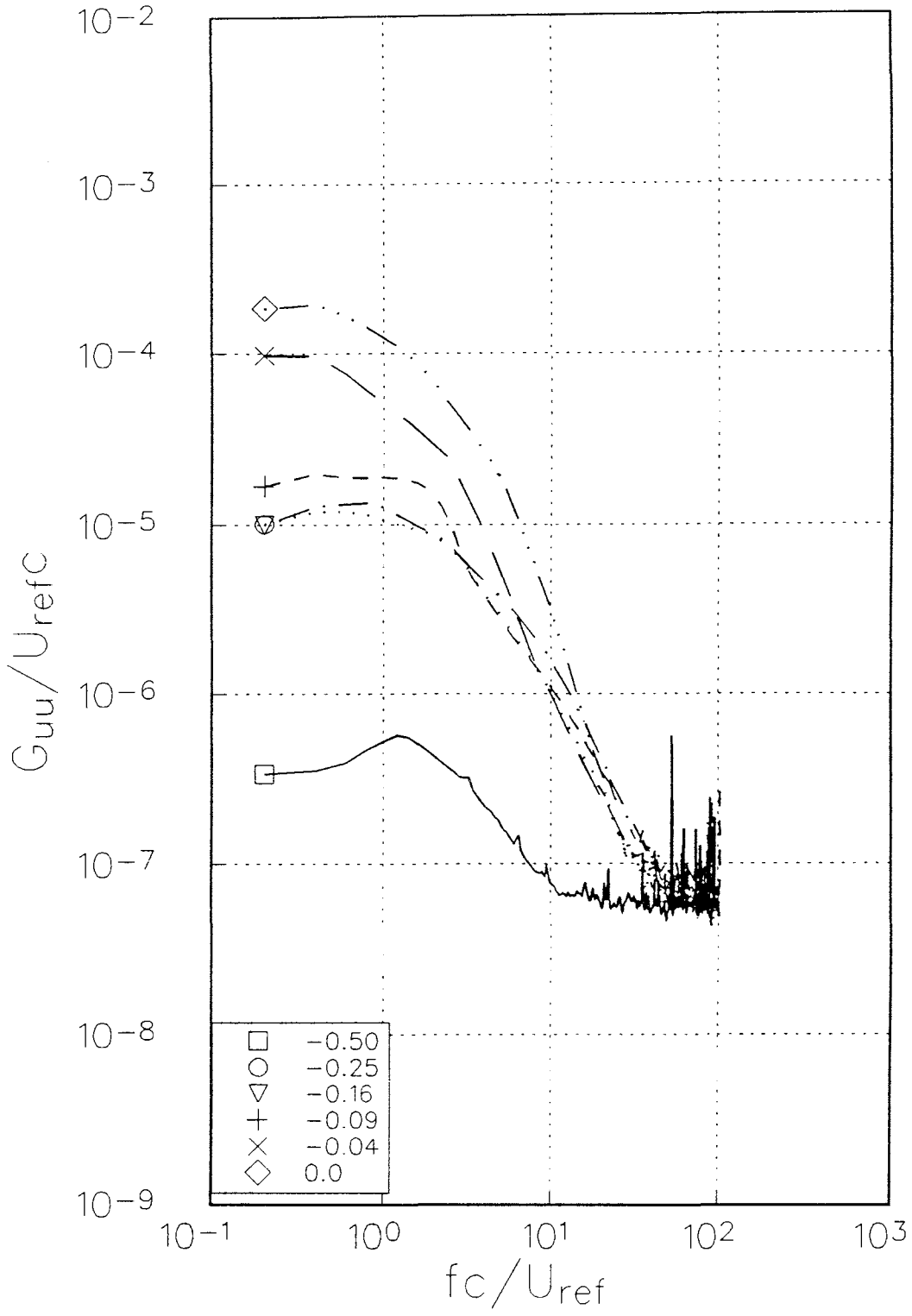

Figure 3.33(a) Autospectra of U component velocity fluctuations measured at various z/c locations for Re_c=400000, x/c=30, α=2.5°.

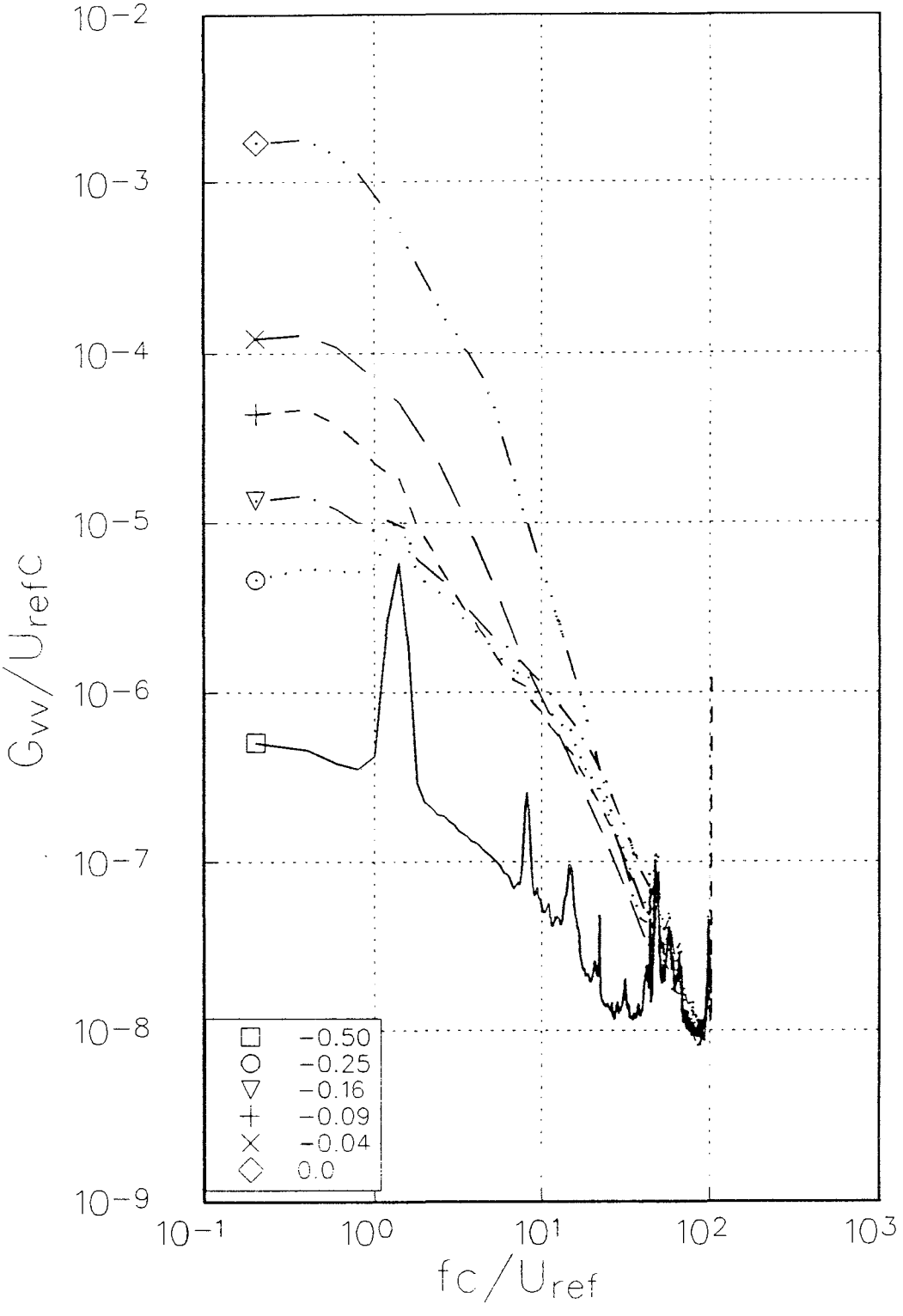

Figure 3.33(b) Autospectra of V component velocity fluctuations measured at various z/c locations for Re_c=400000, x/c=30, α=2.5°.

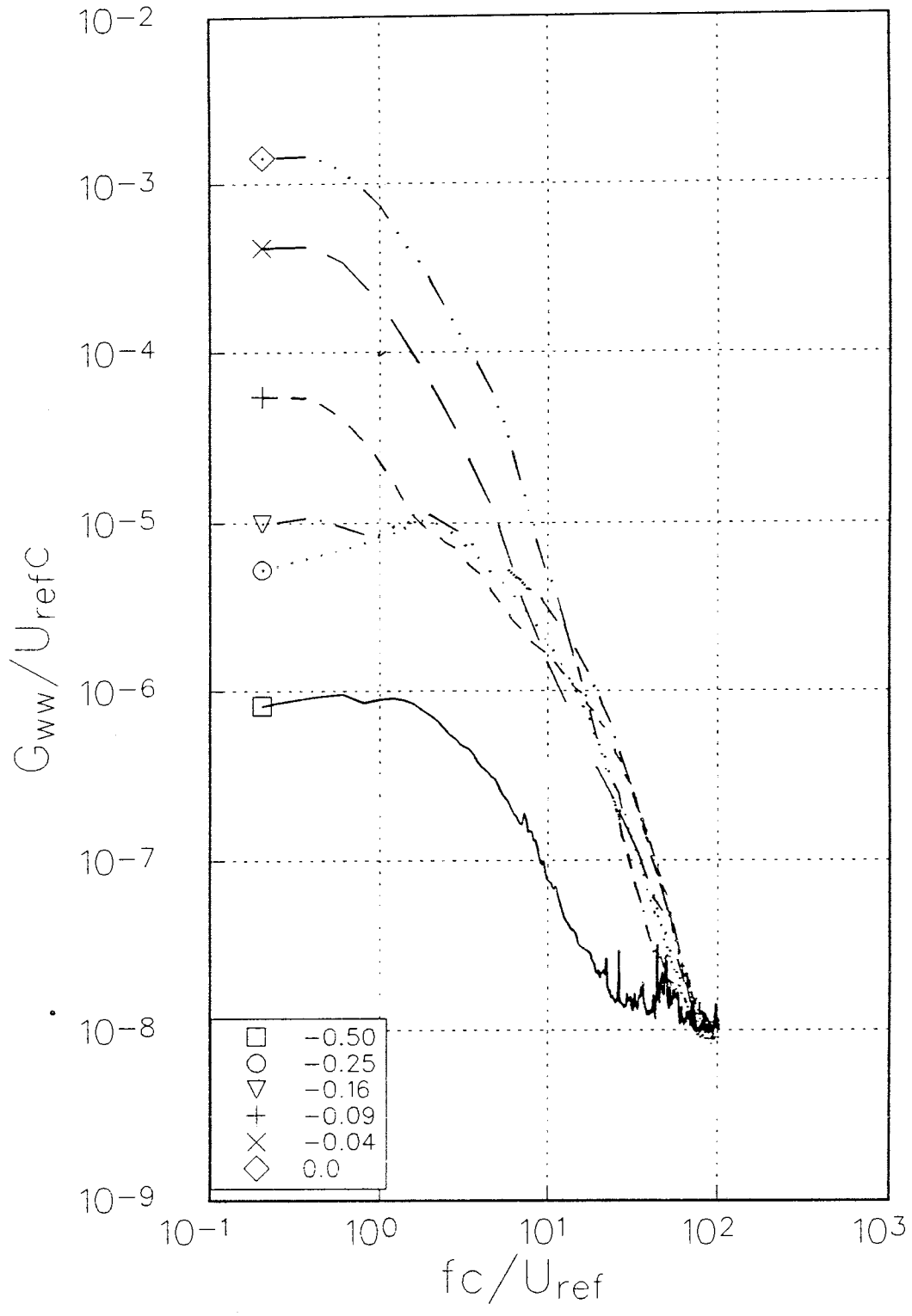

Figure 3.33(c) Autospectra of W component velocity fluctuations measured at various z/c locations for Re_c=400000, x/c=30, α=2.5°.

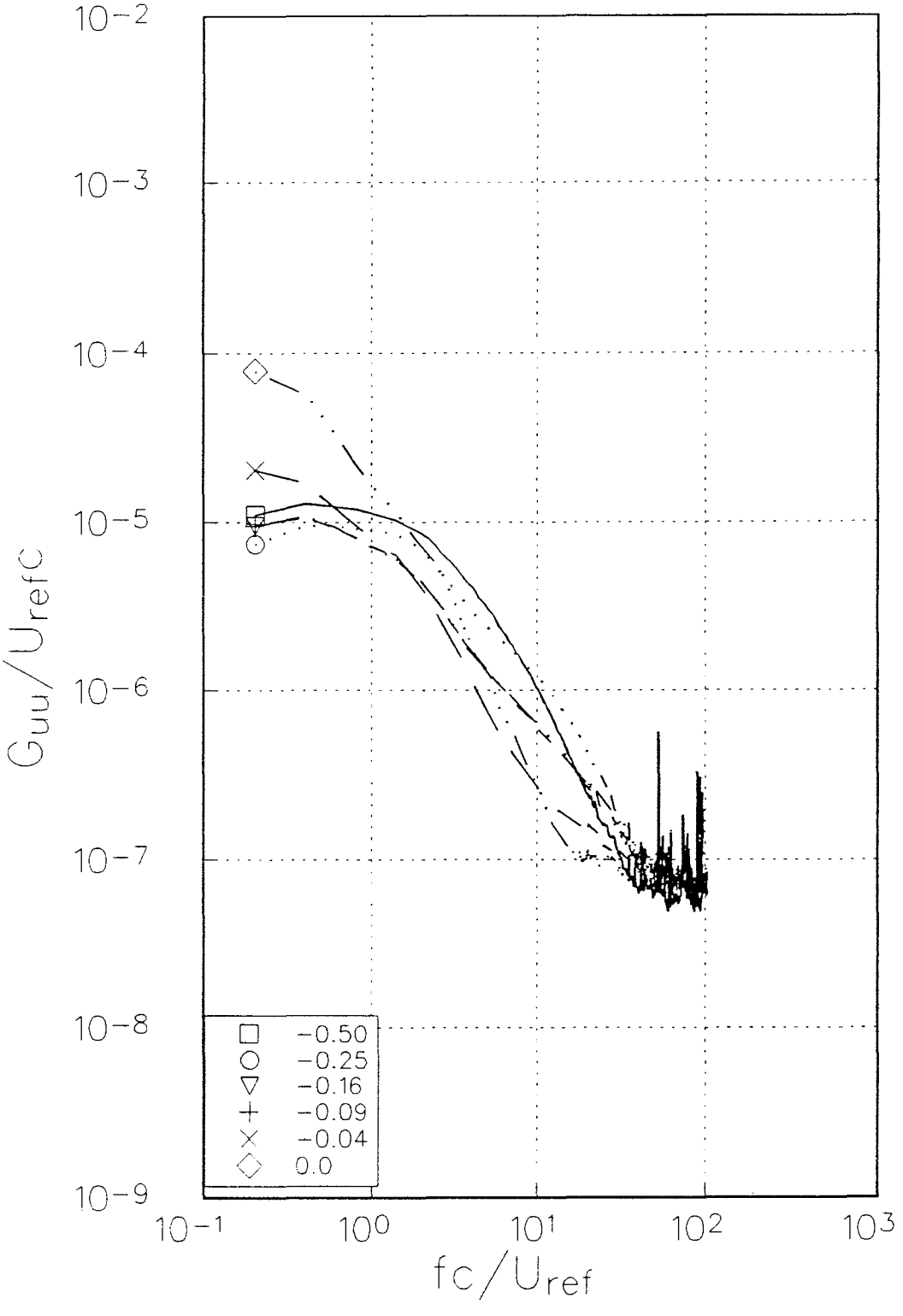

Figure 3.34(a) Autospectra of U component velocity fluctuations measured at various z/c locations for Re_c=400000, x/c=30, α=7.5°.

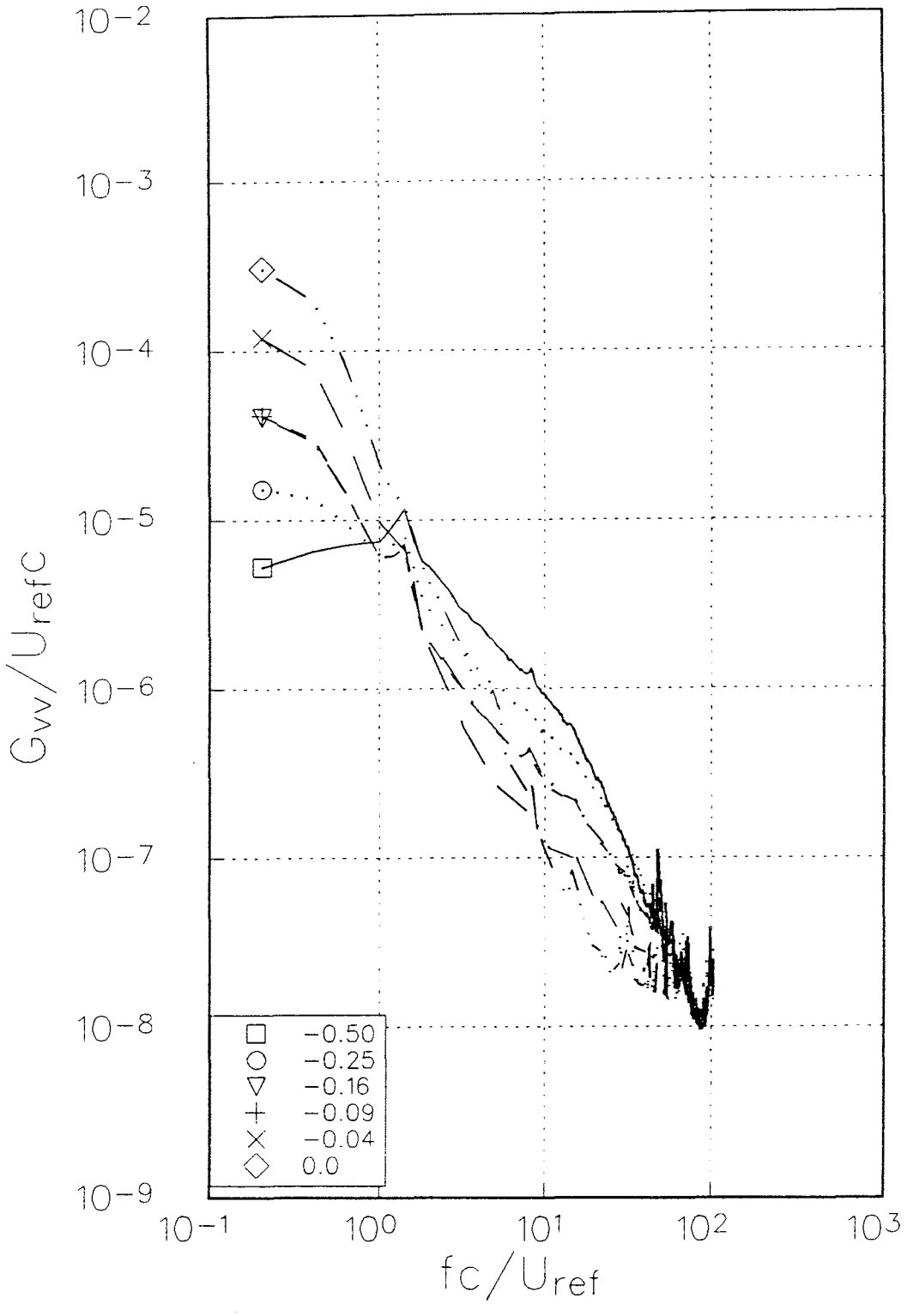

Figure 3.34(b) Autospectra of V component velocity fluctuations measured at various z/c locations for Re_c=400000, x/c=30, α=7.5°.

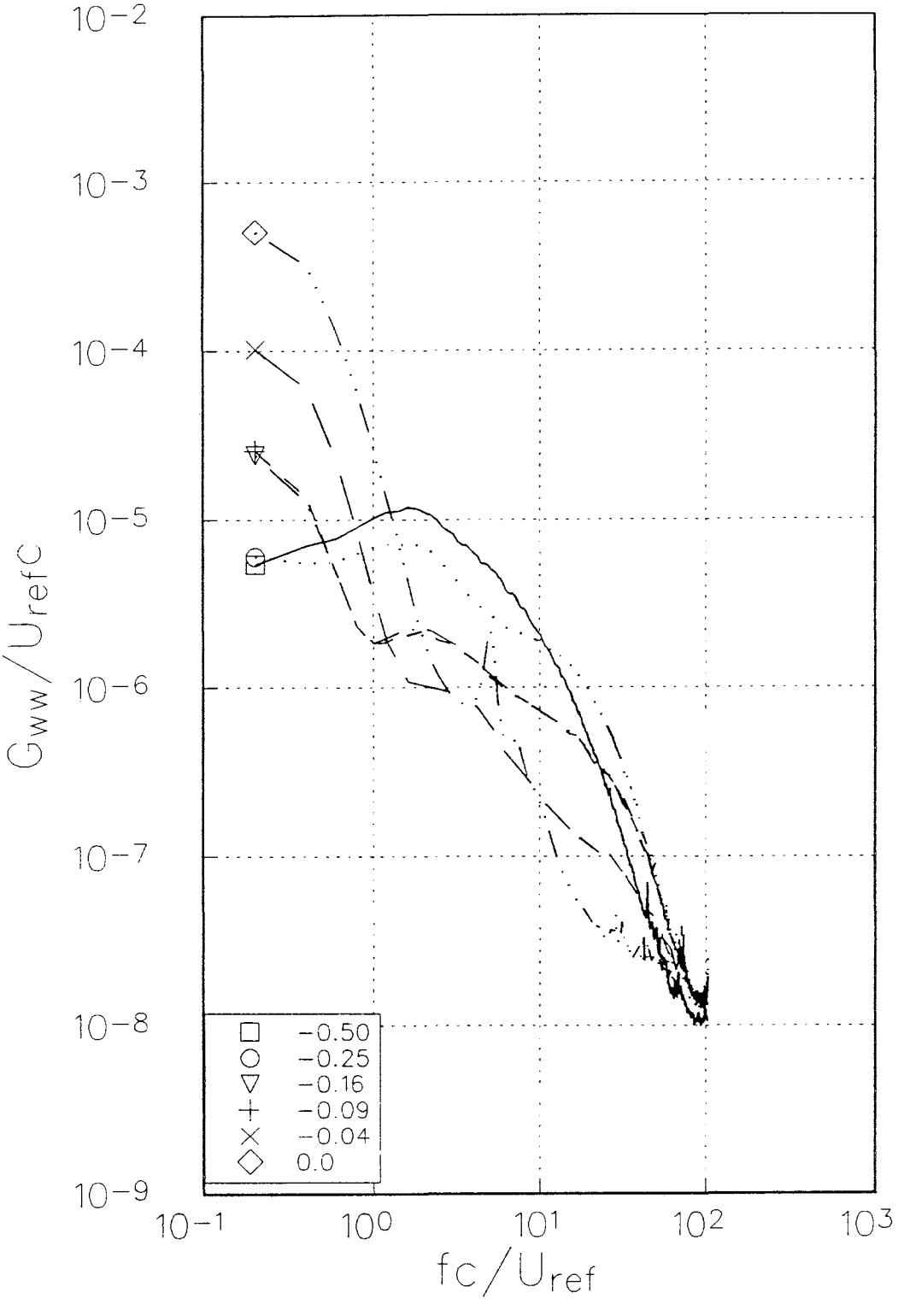

Figure 3.34(c) Autospectra of W component velocity fluctuations measured at various z/c locations for Re_c=400000, x/c=30, α=7.5°.

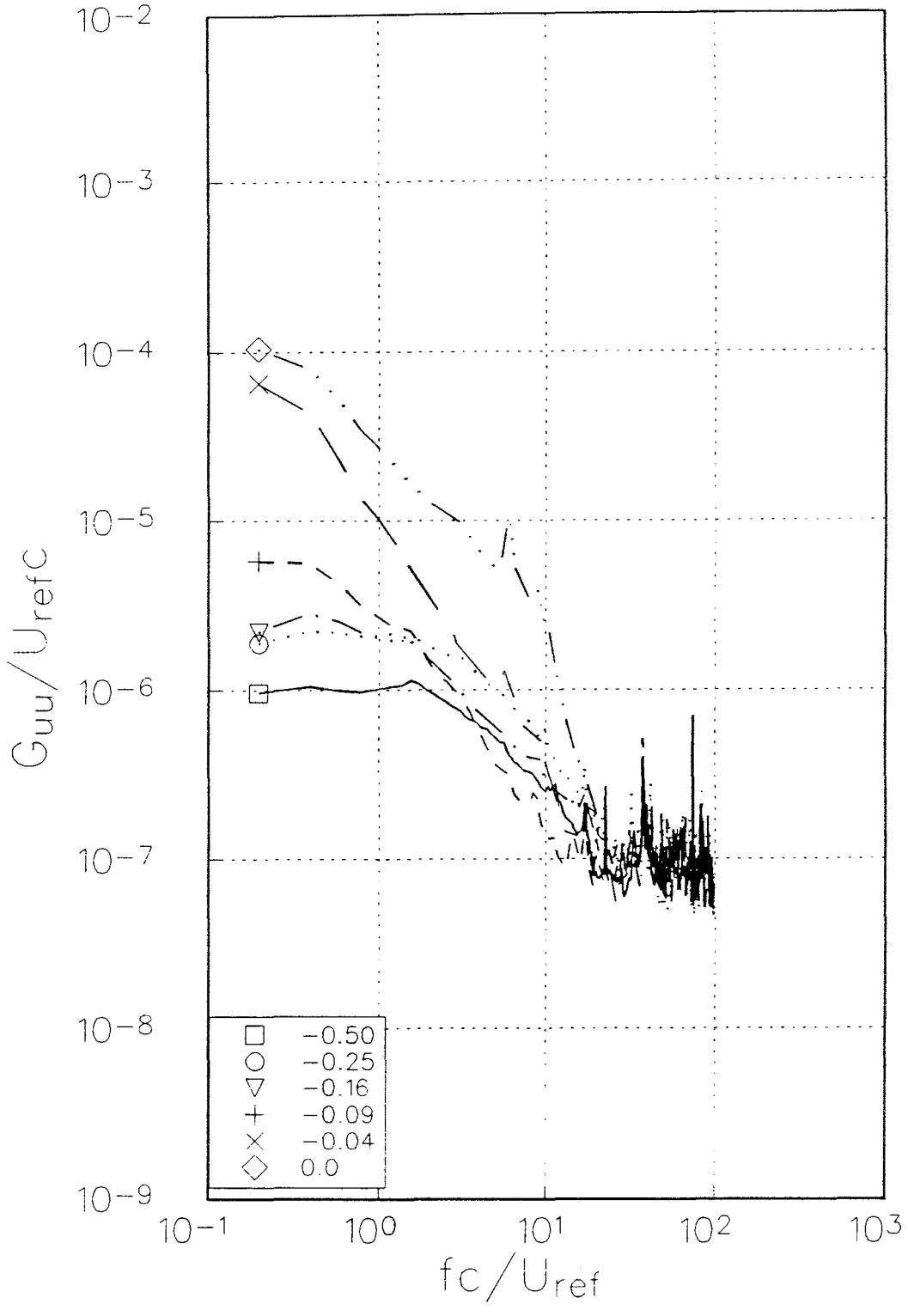

Figure 3.35(a) Autospectra of U component velocity fluctuations measured at various z/c locations for Re_c=530000, x/c=30, α=5.0°, no trip.

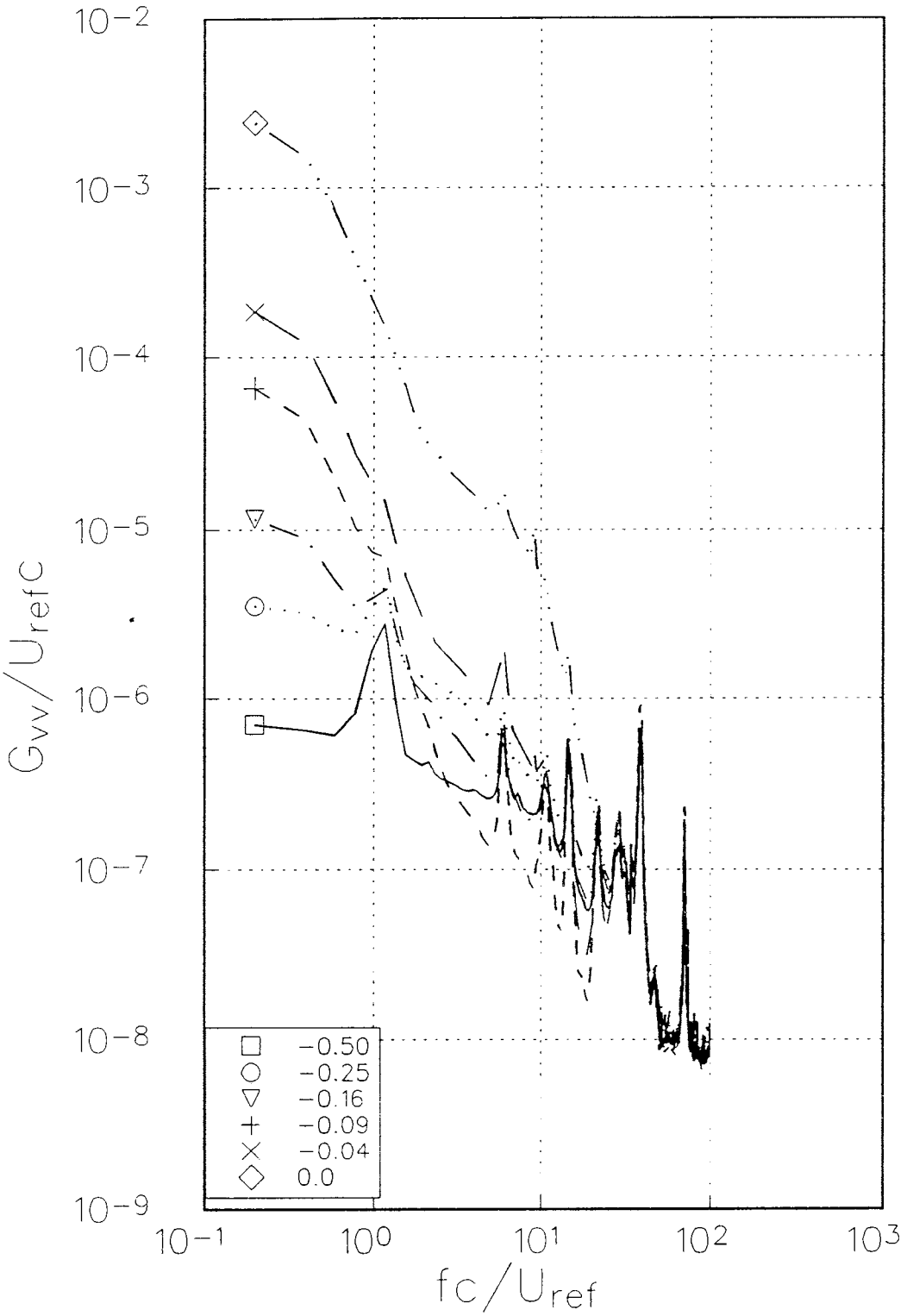

Figure 3.35(b) Autospectra of V component velocity fluctuations measured at various z/c locations for Re_c=530000, x/c=30, α=5.0°, no trip.

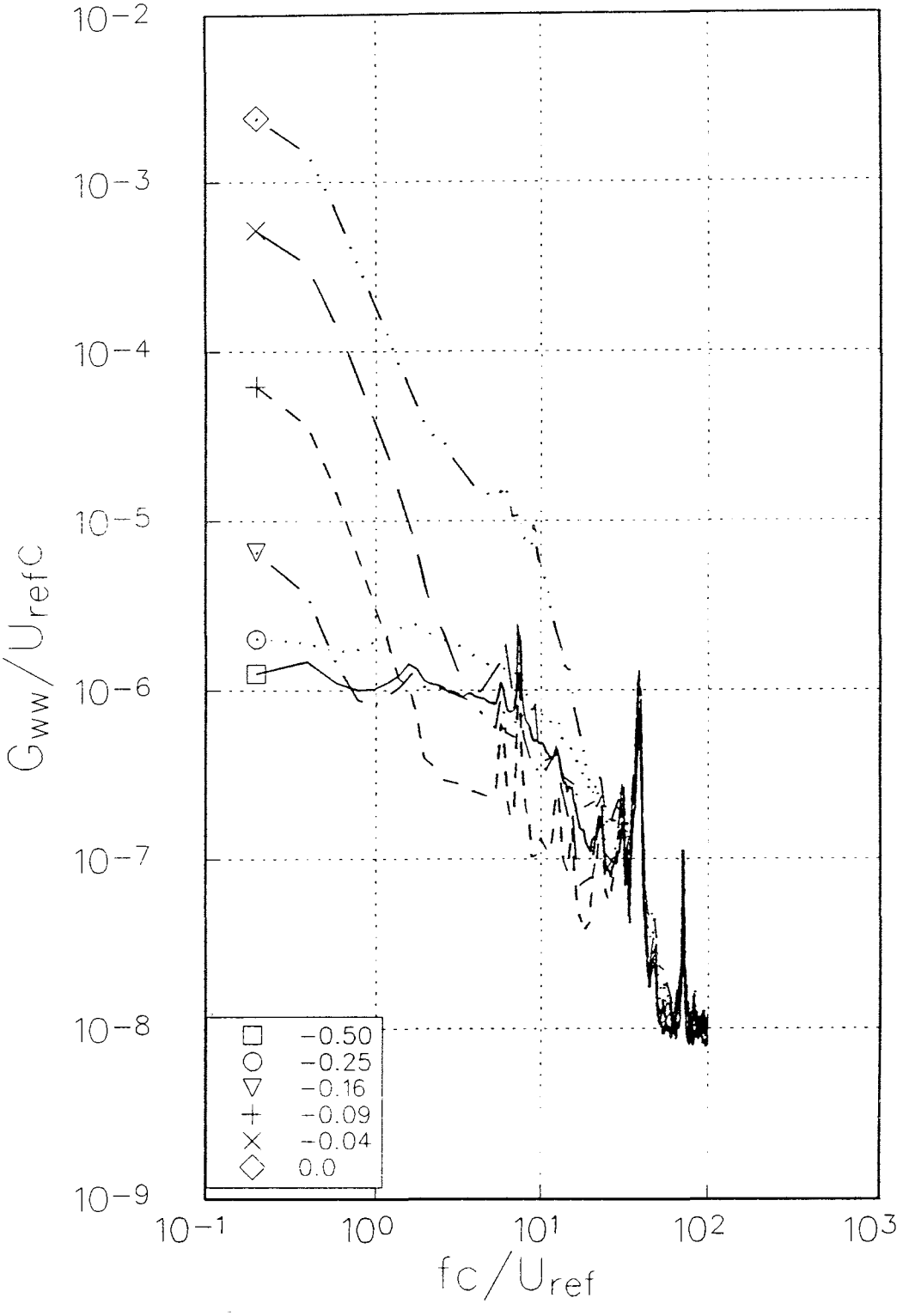

Figure 3.35(c) Autospectra of W component velocity fluctuations measured at various z/c locations for Re_c=530000, x/c=30, α=5.0°, no trip.

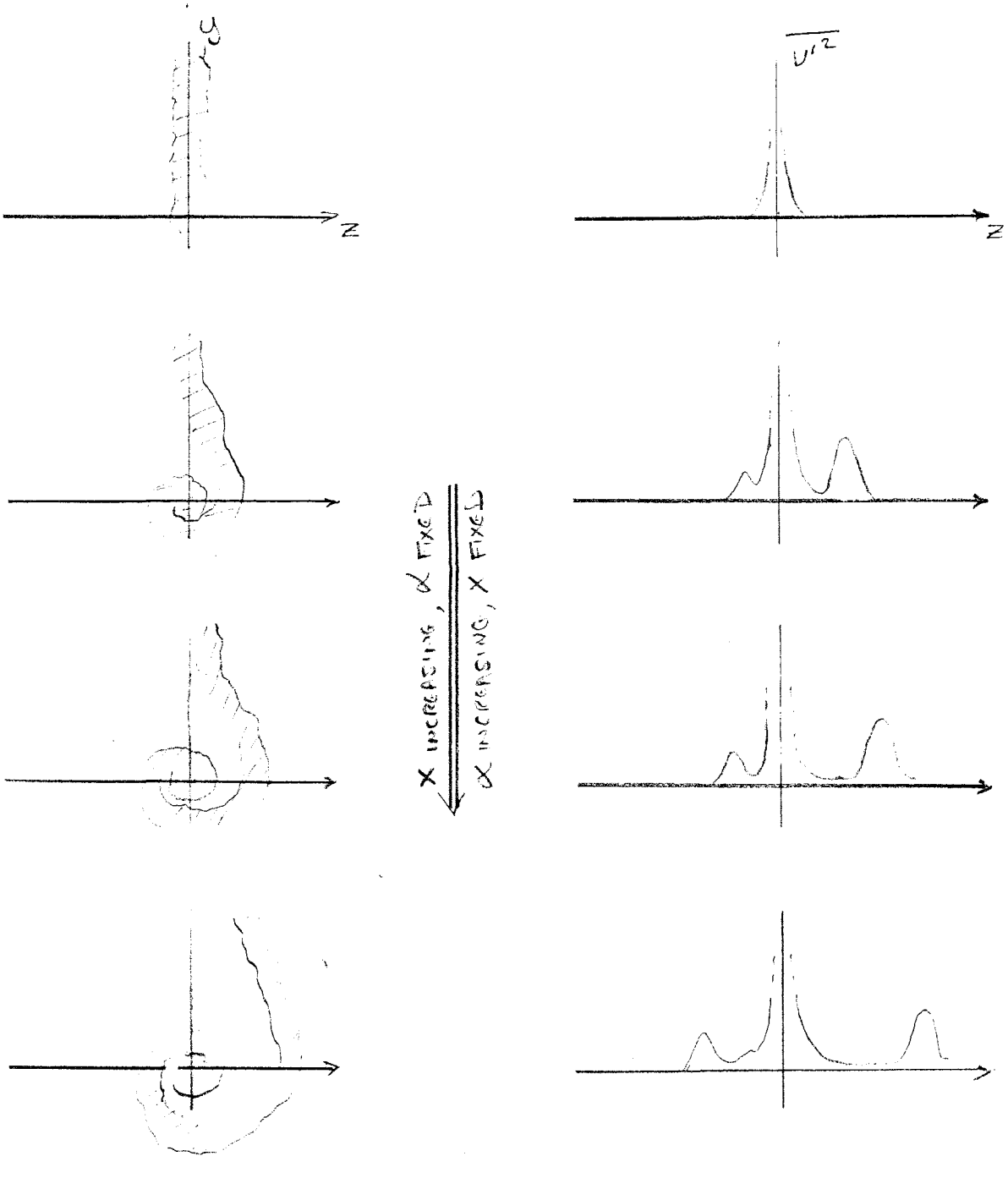

Figure 3.36 Schematic showing the roll up of the wing wake as observed in a z-wise profile.

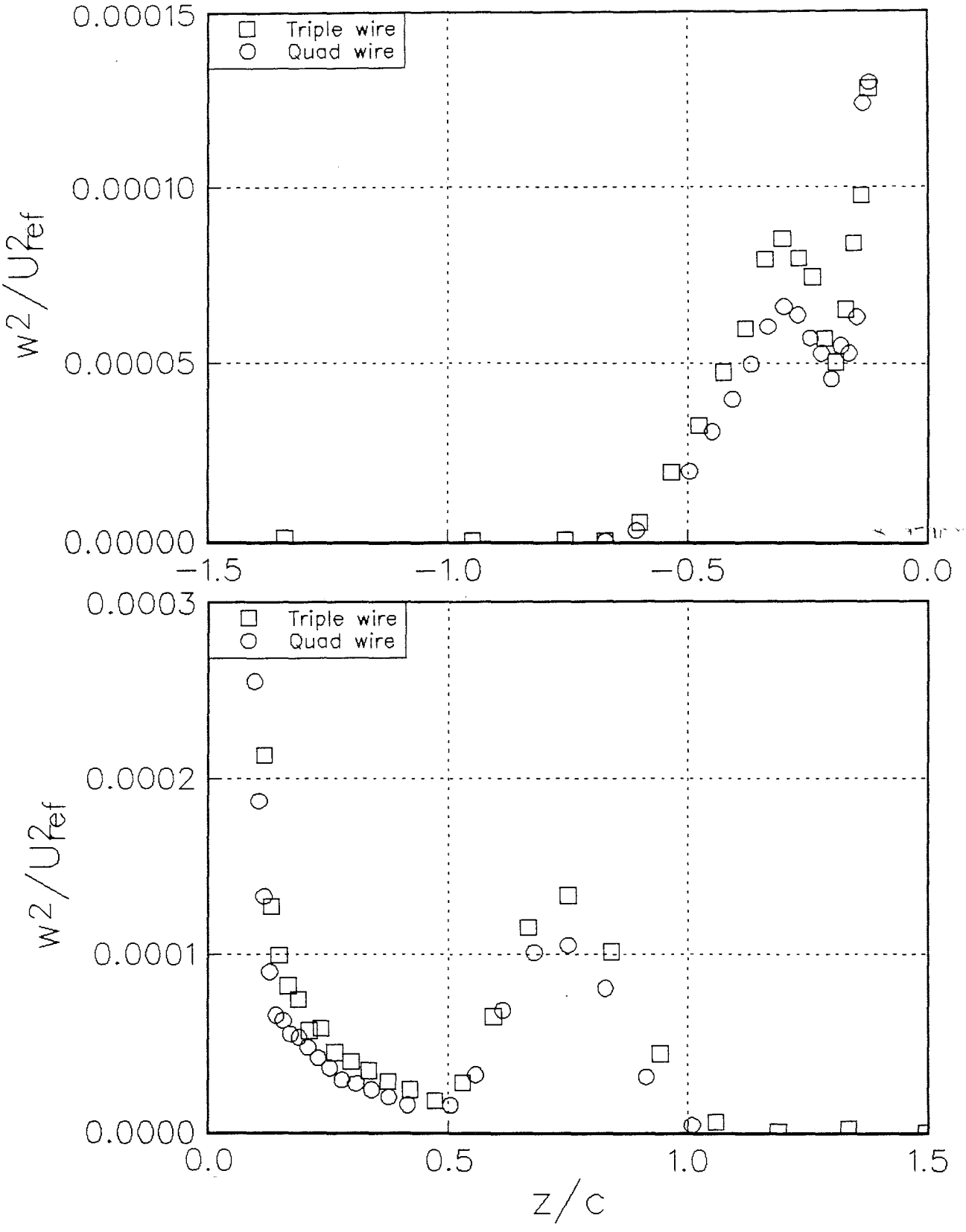

Figure 3.37 Comparison of $\overline{w^2}$ profiles measured in the wake region with the triple at quad hot-wire probes. Re_c=260000, α=5.0°, x/c=30.

4. FURTHER DISCUSSION

4.1 The core motions

4.1.1 Spectra

We begin this section by re-examining the core spectra measured with the triple wire and presented in figures 3.9 and 3.21-27, including in our discussion parts (d) and (e) of these figures which show, respectively, UQ coherence and phase. U is the axial velocity, Q is the instantaneous magnitude of the tangential velocity i.e. $\sqrt{(V^2+W^2)}$. The significance of UQ is that it distinguishes velocity fluctuations generated by coherent wandering of the core from those associated with motions that distort the local structure, such as turbulence. To see this, consider the idealized core velocity profiles shown in figure 4.1, intended to be representative of most of the present flows. The tangential velocity and axial velocity both increase in magnitude monotonically from the core center to its edge. Coherent wandering of such a vortex across a fixed probe located in the core would clearly produce correlated fluctuations in the measured instantaneous tangential and axial velocity magnitudes. UQ spectra should therefore show significant coherence and a zero phase at frequencies where coherent wandering is the dominant contributor to velocity fluctuations.

Interestingly in all cases, except the vortex generated with the wing at 7.5° angle of attack (figure 3.27) there is significant UQ coherence at zero phase at frequencies below $fc/U_{ref}=1$. The lack of UQ coherence in the 7.5° case may be attributed to the unusual axial velocity profile here (figure 3-17a) which contains a peak at its center and thus a non-monotonic variation in U with radius. This result suggests that velocity fluctuations in the core center can be split into three distinct frequency bands;

Band I, $fc/U_{ref}<.01$, significant VW coherence, significant UQ coherence at zero phase. Velocity fluctuations presumably generated by coherent but anisotropic wandering of the vortex. Typically this band contains about 65% of the total energy.

Band II, $.01<fc/U_{ref}<1.$, no VW coherence, significant UQ coherence at zero phase. Velocity fluctuations here are presumably generated by coherent isotropic motions. Typically

about 35% of the total energy.

Band III, $fc/U_{ref>}$ 1., little or no significant VW and UQ coherence. Weak velocity fluctuations generated possibly by turbulence, or core instabilities. Typically less than 2% of the total energy.

The three bands are illustrated graphically in figures 4.2 a-c where all the core autospectra have been plotted together in terms of

$$\frac{G_{uu}U_{ref}}{\overline{u^2}c} \quad vs \quad fc/U_{ref}$$

for example. These figures show a surprising degree of similarity in the shapes of the core spectra (ignoring, perhaps, those measured in the 2.5° case), and an approximate scaling of frequency in all three bands on U_{ref} and c. As will be discussed below the scaling on U_{ref} may be significant. The scaling on c is probably fortuitus since this distance was fixed throughout the experiments. Other distances, such as the core radius and streamwise distance also varied little. Note that despite some effort we have yet to find an exact frequency scaling for the spike that appears in the spectra in band III.

4.1.2 Magnitude, direction and effects of coherent motions

If we assume, as is suggested above, that all or nearly all of the velocity fluctuations in the core center are generated by coherent motions in bands I and II it is possible to make crude estimates of the magnitude and direction of those motions. Consider a fixed probe immersed in an axisymmetric vortex core that is wandering in a non-isotropic fashion. The probe will measure large turbulence stresses $\overline{v^2}$, $\overline{w^2}$, and $-\overline{vw}$ at the vortex center as a consequence of the wandering. The principle direction of this stress system should correspond to the preferred direction of the motions. Assuming solid-body rotation in the core the r.m.s. amplitude of the motions σ_r will be related to the magnitude of the principle stress p by the expression

$$\sigma_r = \sqrt{p} \Big/ \left.\frac{\partial V}{\partial z}\right|_{z=0} \qquad (1)$$

where $\partial V/\partial z|_{z=0}$ is the tangential velocity gradient in the core. These parameters have been plotted for the present cases in figure 4.3. In each case a series of lines has been drawn, the direction of which corresponds to the principle stress direction, the length of which corresponds to the r.m.s. amplitude calculated according to the above equation. Although these calculations are only really valid at the core center points to either side of the center are included in figure 4.2 to give some idea of the uncertainty involved. This figure shows that the anisotropic motions have a preferred direction that lies between 20° and 45° to the z axis. The apparent r.m.s. amplitude of the motions varies from .011c for case 2 (Re_c=260000, α=5.0°, x/c=30) to 0.02c for case 7 (Re_c=400000, α=2.5°, x/c=30), approximately consistent with the observations of Devenport and Sharma (1990). There does not appear to be much consistent variation of these quantities with Reynolds number or streamwise distance (cases 1 to 6). Changes in angle of attack from 5° (cases 7 and 8) and removal of the wing trip appear to increase the amplitude and angle of the motions.

An important issue is the extent to which these motions may have smoothed the measured mean velocity profiles. Such smoothing could lead to overestimates of the core size and underestimates of the peak tangential velocity, as has been demonstrated by Corsiglia et al. (1973). A simple qualitative way to evaluate the effects of the smoothing is to examine records of instantaneous tangential (V) velocity at the core edge. If smoothing were important then instantaneous peak tangential velocities would be much greater than those seen on time average. Figure 4.4 shows just such a record measured close to the core edge in the baseline case. Ignoring high-frequency fluctuations, this shows instantaneous peak V velocities to be about $.28U_{ref}$, compared to a long time average of $.24U_{ref}$. We therefore conclude that the effects of smoothing, while not insignificant, were relatively small.

4.1.3 Possible causes

Before discussing some possible causes of the wandering it is important to realize that coherent wandering motions can be transmitted by a vortex core as helical waves. These waves, first described by Lord Kelvin(1880), are transmitted at speeds close to the free stream velocity. There is a lower limit on their wavelength of 1 core diameter. In the present flows this would corresponding to a frequency seen by a fixed probe of about $fc/U_{ref} = 8$. Interestingly this is near the upper bound of band II, consistent with the idea that some of the coherent motions of the present vortices are associated with such waves.

There are several potential causes of the vortex wandering; wind tunnel unsteadiness, inviscid induction and buffeting of the core by turbulence in the spiral wake. At first sight wind-tunnel unsteadiness seems a very probable cause of the anisotropic motions. The slow wandering could be generated by gradual flow direction changes of less than $\pm .2^{o}$ acting over length of the vortex. On closer examination, however, this explanation appears less attractive. There are three possible sources of low-frequency flow direction changes in the wind tunnel. Wind gusts outside (the present tunnel being vented to the outside through an air-exchange tower), unsteady separation somewhere in the wind tunnel circuit or unsteadiness in the test section boundary layers. Wind gusts can be discounted since the motions appear to scale on free stream velocity (figure 4.2). Separation in the wind tunnel circuit also seems an improbable cause since the direction and magnitude of the motions appear to be a function of angle of attack. The only consistent explanation would be unsteadiness in the test section boundary layers set up by the adverse pressure gradients produced by the wing. The intensity and perhaps direction of this type of unsteadiness would be expected to be a function of angle of attack. It is an open question, however, as to whether motions at such low frequencies could be produced by the boundary layers in this way.

A more likely source of both isotropic and anisotropic motions is inviscid induction. This could take two forms.

(i) Interaction of the vortex with its images in the wind tunnel walls. Crow (1970) demonstrated theoretically that two line vortices of opposite sign will undergo an instability as a consequence of their mutual interaction. One interesting feature of the Crow instability is that it is anisotropic, its preferred direction being at 45^{o} to the plane of the vortices.

Applying Crow's theory to the present vortex and its nearest image (that produced by the lower test section wall) gives a most unstable frequency of about $fc/U_{ref}=.01$, the upper bound of the frequency band in which anisotropic motions were observed. It therefore seems possible that this instability, modified by the other vortex images could be responsible for a proportion of the anisotropic motions.

(ii) True self induction. As discussed by Leonard (1985) a curved line vortex induces velocities upon itself that make it unstable. The present vortices, like all single-wing vortices, are curved inboard over their first few chordlengths. This curvature could, conceivably, generate motions which are then transmitted downstream as helical waves. Another self induction mechanism that could account for anisotropic movement is interaction of the vortex core the spiral wake. The spiral wake is, of course, a non-axisymmetric vortex sheet. It is therefore reasonable to suppose that this combination is subject to the same types of instabilities and chaotic motions seen in pairs and groups of line vortices.

A large contributor to the isotropic motions may be buffeting of the core by turbulence in the spiral wake. In turbulent boundary layers, where the flow is constrained by a solid wall, this type of 'inactive' motion contributes as much as 30% to the normal stresses in the near-wall region (Bradshaw (1967)). Without a solid surface we might reasonably expect such motion to be much greater. If this were the case one might, at first suppose that the magnitude of the motions would decay with streamwise distance following the decay of turbulence in the spiral wake. However, this ignores the inviscid wave carrying nature of the vortex core and probable increase in size of wake structures with streamwise distance. Core motions due to turbulence might therefore remain constant or even increase with x.

4.2 Flow structure in the core region

In this section we shall refer to the properties of the vortex in terms of the cylindrical coordinate system shown in figure 4.5. Note that for the z-wise profiles presented in chapter 3, the tangential and axial mean-velocity components V_θ and V_x correspond to $|V|$ and U respectively, and the radial coordinate r is simply $|z|$.

In table 4.1 we have tabulated a number of parameters for each of the vortices and locations studied. Core radius r_1, core circulation Γ_1, peak tangential velocity $V_{\theta 1}$, velocity gradient at the core center $(\partial V_\theta/\partial r)_{r=0}$, centerline axial velocity deficit, root circulation Γ_0 and a number of non-dimensional parameters are included.

4.2.1 Circulation

In vortex flows circulation, calculated along circular paths centered on the vortex, is generally presented as a function of r, the radius of that path. For the present measurements circulation was calculated assuming axisymmetry, i.e. by writing

$$\Gamma = 2\pi r V_\theta = 2\pi \left| zV \right| \qquad (2)$$

Each z profile therefore yielded two estimates of the circulation distribution, one for positive and one for negative z. These two estimates are compared for the baseline case in figure 4.6 in which Γ has been normalized on the root circulation of the wing Γ_0 and r on the core radius r_1. This comparison shows the assumption of axisymmetry to be reasonable (though by no means perfect) for $r/r_1<4$. For $r/r_1>4$ the two circulation estimates diverge because of the non-symmetric influence of the spiral wake which, even 30 chordlengths downstream of the wing still contains a large portion of the bound circulation. This is also why the profiles show only 90% of the bound circulation at the outer edge of the measurements.

Circulation estimates for all the cases are plotted together in figure 4.7 in terms of Γ/Γ_0 and r/r_1. For clarity this figure, and all subsequent figures, includes only circulation calculated from measurements made on the negative z side of the vortex center. Obviously the circulation profiles do not collapse in this form. However, they do show some consistent similarities, in particular a region of solid-body rotation inside the core where Γ varies as r_2 and a region outside the core edge where Γ varies semi-logarithmically with r.

The collapse of the data in these regions can be substantially improved by normalizing Γ on the core circulation Γ_1 (figure 4.8). In this form the circulation profiles

inside the core region are identical to within their uncertainty, regardless of conditions[1]. Outside the core the collapse is better than before but there is still some dependence of the slope of the semi-logarithmic region on conditions. Breaking up the comparison to show separately the effects of Reynolds number Re_c, streamwise distance x/c, wing trip and angle of attack α (figures 4.10-4.13) shows the first 3 of these parameters to have little if any influence on the circulation distribution. The slope of the semi-logarithmic region appears only to be a function of angle of attack (figure 4.12). The effects of angle of attack appear particularly strong between 5.0 and 2.5° where the slope of the semi-logarithmic region increases sufficiently for it to form a tangent to the core profile at 2.5°.

This type of behavior was first noticed by Hoffman and Joubert (1963) (henceforward referred to as HJ) for split-wing vortices. They presented experimental data and theoretical arguments which show that the type of circulation profile seen 2.5° is indicative of a fully turbulent vortex i.e one in which viscous shear stresses are unimportant. In contrast, the type of profile seen in all other cases, where the semi-logarithmic region is not tangent to the core profile, indicates a vortex in which viscous stresses play a role, presumably in the region of highest shear just outside the core. This second result is particularly interesting since it implies some relaminarization of the turbulent fluid that rolls up to form the vortex core. Certainly we do see a rapid reduction in turbulence stress levels in the spiral wake as the core is approached. Another piece of evidence that tends to support the above interpretation of the circulation profiles is the V and W component auto spectra measured in the core center (figure 4.2). These spectra have the same form in all but the 2.5° case. At high frequencies likely to be associated with turbulence they all show relatively low spectral levels when compared to measurements made in the spiral wake. They also show a spike near fc/U_{ref} attributed to laminar core instability of the type seen by Singh and Uberoi (1976). In the 2.5° case spectral levels at mid and high frequencies are as much as an order of magnitude larger and the spike can no longer be seen. The implication is exactly what one would expect - that there are substantial differences between the turbulence as well as the

---

[1]This indicates that there must be a linear relationship between $(\partial V_\theta/\partial r)_{r=0}$ and $V_{\theta 1}/r_1$. As shown in figure 4.9, this is indeed the case, the line having a slope of 1.9.

mean-flow structure of viscous and fully turbulent vortices.

We have summarized below some of HJs theorems beginning with a dimensional analysis for the circulation distribution. Assuming axisymmetry HJ argue that the circulation profile of a vortex can only be function of Γ_0, x, U_{ref}, ν and r, i.e.

$$\Gamma = f_1(\Gamma_0, U_{ref}, r, x, \nu) \tag{3}$$

or

$$\frac{\Gamma}{\Gamma_0} = f_2\left(\frac{U_{ref}x}{\Gamma_o}, \frac{r}{x}, \frac{U_{ref}x}{\nu}\right) \tag{4}$$

The same argument, applied to the non-distributive dependent variables of core circulation and radius leads to,

$$\frac{\Gamma_1}{\Gamma_0} = f_3\left(\frac{U_{ref}x}{\Gamma_0}, \frac{U_{ref}x}{\nu}\right) \tag{5}$$

$$\frac{r_1}{x} = f_4\left(\frac{U_{ref}x}{\Gamma_0}, \frac{U_{ref}x}{\nu}\right) \tag{6}$$

Now, in a fully turbulent vortex the mean-velocity field should be independent of viscosity in which case

$$\frac{\Gamma}{\Gamma_0} = f_2\left(\frac{U_{ref}x}{\Gamma_o}, \frac{r}{x}\right) \tag{7}$$

$$\frac{\Gamma_1}{\Gamma_0} = f_3\left(\frac{U_{ref}x}{\Gamma_0}\right) \tag{8}$$

$$\frac{r_1}{x} = f_4\left(\frac{U_{ref}x}{\Gamma_0}\right) \tag{9}$$

Through a series of measurements HJ appeared to demonstrate that for values of the parameter $U_{ref}x/\Gamma_o > 150$ a fully turbulent vortex was produced with a circulation profile like that of the present 2.5° case. For $U_{ref}x/\Gamma_o < 150$, Γ/Γ_0 and r_1/x appeared to be functions of $U_{ref}x/\nu$ and circulation profiles like those seen in the rest of the present cases were observed.

HJ also developed a theory to explain the existence of the semi-logarithmic region. In the core region their measurements, like the present, showed circulation profiles which collapsed when plotted in terms of Γ/Γ_1 and r/r_1, indicating that here

$$\frac{\Gamma}{\Gamma_1} = f_5\left(\frac{r}{r_1}\right) \tag{10}$$

Outside this region they argue that $d\Gamma/dr$ should eventually become independent of r_1. Assuming the existence of an overlap region where both these conditions hold gives, in this region,

$$\frac{d\Gamma}{dr} = \Gamma_1 f_5'\left(\frac{r}{r_1}\right)\frac{1}{r_1} \neq \textit{function of } r_1 \tag{11}$$

This is only possible of f_5 has the form

$$\frac{\Gamma}{\Gamma_1} = A.\ln\left(\frac{r}{r_1}\right) + B \qquad (12)$$

In a fully turbulent vortex where the semi-log region appears to form a tangent to the core profile HJ suggest

$$\frac{\Gamma}{\Gamma_1} = 2.14\log_{10}\left(\frac{r}{r_1}\right) + 1 \qquad (13)$$

B must be unity if the logarithmic region passes through the core edge since here, by definition, $\Gamma/\Gamma_1 = 1$ and $r/r_1 = 1$.

We begin our discussion of HJs theorems and there relevance to the present measurements by clearing up a minor omission. Differentiating equation (12) with respect to r/r_1 gives

$$\frac{d(\Gamma/\Gamma_1)}{d(r/r_1)} = \frac{d(rV_\theta/r_1V_{\theta_1})}{d(r/r_1)} = \frac{V_\theta}{V_{\theta_1}} + \frac{r}{V_{\theta_1}}\frac{dV_\theta}{dr} = \frac{A}{r/r_1} \qquad (14)$$

At the core edge, by definition, $V_\theta/V_{\theta 1} = r/r_1 = 1$ and $dV_\theta/dr = 0$. Thus $A=1$. We have then

$$\frac{\Gamma}{\Gamma_1} = \ln\left(\frac{r}{r_1}\right) + 1 \qquad (15)$$

or

$$\frac{\Gamma}{\Gamma_1} = 2.3\log_{10}\left(\frac{r}{r_1}\right) + 1 \qquad (16)$$

So, HJs semi-logarithmic profile requires no empirical constants for fully turbulent vortices.

Figure 4.12 clearly shows the circulation profile for the present 2.5° case to be consistent with equation (16). Consistent with HJs observations, table 4.1 shows the 2.5° case to be the only one for which the parameter $U_{ref}x/\Gamma_0 > 150$, it being 240. In all other cases $U_{ref}x/\Gamma_0 <= 120$.

One of the curious features of HJs results is that their criterion for fully turbulent flow does not itself depend on viscosity. Another oddity seen in the present measurements is the way in which the circulation profiles depend on HJs non-dimensional parameters. Consider figure 4.12 which shows the effects on the circulation profile of varying $U_{ref}x/\Gamma_0$ from 80 to 120 (see table 4.1) while holding $U_{ref}x/\nu$ constant at $1.2x10^7$. These effects are substantial. Now consider figure 4.10 which shows the effects of varying $U_{ref}x/\nu$ from $4.0x10^6$ to $1.6x10^7$ while holding $U_{ref}x/\Gamma_0$ at 120. The effects are almost negligible despite the fact that the vortex is not fully turbulent and therefore should be dependent on viscosity. Finally consider the circulation profiles of figure 4.11 which show the effects of varying $U_{ref}x/\theta$ and $U_{ref}x/\Gamma_0$ simultaneously from $8.0x10^6$ and 80 to $1.2x10^7$ and 120 respectively. We would expect, given the previous results, some significant change because of the variation in $U_{ref}x/\Gamma_0$. However, none is seen.

There are two possible explanations of this anomaly. The first is that this is a coincidence and a consequence of the precise combination of parameters chosen. The second explanation, which seems more likely, requires the reworking of HJs dimensional analysis. In their analysis HJ ignored variables relating to the initial conditions of the vortex. However, our measurements have revealed the spiral structure of the wake surrounding the core, the geometry of which presumably scales on the wing size. We therefore argue that the circulation distribution may be a function of chordlength c as well as Γ_0, U_{ref}, r, x, and ν. Symbolically,

$$\Gamma = f_6(\Gamma_0, U_{ref}, r, x, \nu, c) \tag{17}$$

or

$$\frac{\Gamma}{\Gamma_0} = f_7\left(\frac{U_{ref}x}{\Gamma_0}, \frac{r}{x}, \frac{U_{ref}x}{\nu}, \frac{U_{ref}c}{\Gamma_0}\right) \tag{18}$$

alternatively

$$\frac{\Gamma}{\Gamma_0} = f_8\left(\frac{x}{c}, \frac{r}{c}, \frac{U_{ref}x}{\nu}, \frac{U_{ref}c}{\Gamma_0}\right) \tag{19}$$

Similarly we have

$$\frac{\Gamma_1}{\Gamma_0} = f_9\left(\frac{x}{c}, \frac{U_{ref}c}{\nu}, \frac{U_{ref}c}{\Gamma_0}\right) \tag{20}$$

$$\frac{r_1}{c} = f_{10}\left(\frac{x}{c}, \frac{U_{ref}c}{\nu}, \frac{U_{ref}c}{\Gamma_0}\right) \tag{21}$$

The inclusion of chordlength leads to the new parameter $U_{ref}c/\Gamma_0$ which is in fact 2/(root-section lift coefficient) and therefore depends only on angle of attack. The grouping of equation (19) seems much more consistent with the present measurements which show the circulation profile to be strongly dependent on angle of attack but only weakly dependent on x. Interestingly, it is also consistent with HJs results. Almost all of their measurements

were made at the same streamwise location. They varied $U_{ref}x/\Gamma_0$ almost exclusively by changing angle of attack. They were therefore unable to distinguish between $U_{ref}x/\Gamma_0$ and $U_{ref}c/\Gamma_0$.

If we accept $U_{ref}c/\Gamma_0$ as the controlling parameter then HJs results imply that it is this that determines whether or not the vortex is fully turbulent. This has important structural implications. With $U_{ref}x/\Gamma_0$ setting the criterion for fully turbulent flow one can envisage the development of the vortex with streamwise distance from a viscous to a fully turbulent state, perhaps through a sudden transition process. However, with $U_{ref}c/\Gamma_0$ as the controlling parameter then the state of the vortex is fixed by its initial conditions i.e. a wing at a given angle of attack will produce either a viscous or turbulent vortex which then will remain permanently in that state.

One final issue we would like to address HJs result that the criterion for fully turbulent flow is independent of viscosity. This could well be true for the range of Reynolds numbers they examined (and possibly all higher Reynolds numbers) but it cannot be universal. Picture, for example, creeping flow of a highly viscous fluid past a low angle of attack wing. Obviously this would not produce a turbulent vortex. Viscosity must therefore enter the problem.

Obviously there is much scope for future work here to investigate more closely those parameters that control the state of the vortex, including such effects as lift distribution which the recent results of Zsoldos (1992) suggest may be important. There is also a need examine in greater detail the structural differences between viscous and turbulent vortices. The state of the vortex is likely to be important to a number of applications and an important initial condition in the process of vortex bursting.

4.2.2 Vorticity and rate of strain directions

Figures 4.14 through 4.23 show profiles of vorticity vector direction and rate-of-strain vector direction in the core region. Using the coordinate system of figure 4.5 the mean vorticity vector is defined as

$$\vec{\omega} = \left(\frac{1}{r}\frac{\partial U}{\partial \theta} - \frac{\partial V_\theta}{\partial x}\right)\vec{e}_r + \left(\frac{\partial V_r}{\partial x} - \frac{\partial U}{\partial r}\right)\vec{e}_\theta + \left(\frac{\partial V_\theta}{\partial r} + \frac{V_\theta}{r} - \frac{1}{r}\frac{\partial V_r}{\partial \theta}\right)\vec{e}_x \qquad (22)$$

By analogy we define the rate of strain vector as

$$\vec{\epsilon} = \left(\frac{1}{r}\frac{\partial U}{\partial \theta} + \frac{\partial V_\theta}{\partial x}\right)\vec{e}_r + \left(\frac{\partial V_r}{\partial x} + \frac{\partial U}{\partial r}\right)\vec{e}_\theta + \left(\frac{\partial V_\theta}{\partial r} - \frac{V_\theta}{r} + \frac{1}{r}\frac{\partial V_r}{\partial \theta}\right)\vec{e}_x \qquad (23)$$

Neglecting gradients with respect to θ we obtain

$$\vec{\omega} = -\frac{\partial U}{\partial r}\vec{e}_\theta + \left(\frac{\partial V_\theta}{\partial r} + \frac{V_\theta}{r}\right)\vec{e}_x \qquad (24)$$

By analogy we define the rate of strain vector as

$$\vec{\epsilon} = \frac{\partial U}{\partial r}\vec{e}_\theta + \left(\frac{\partial V_\theta}{\partial r} - \frac{V_\theta}{r}\right)\vec{e}_x \qquad (25)$$

The directions of these vectors relative to the X axis are therefore given by

$$\Phi_\omega = \arctan\left(\frac{-\partial U/\partial r}{\partial V_\theta/\partial r + \dfrac{V_\theta}{r}}\right) \qquad (26)$$

$$\Phi_{\epsilon} = \arctan\left(\frac{\partial U/\partial r}{\partial V_{\theta}/\partial r - \frac{V_{\theta}}{r}}\right) \tag{27}$$

These are plotted as functions of r/r1. The intention of these plots is to reveal the effects of the various conditions studied on the vorticity and rate of strain fields and to determine the probable alignment of any coherent turbulent structures surrounding the core.

The profiles of vorticity direction, plotted together in figure 4.14 and as functions of Re_c, x/c, α and wing trip in figure 4.15-18 are surprisingly similar in all cases within two core radii of the vortex center. As in the circulation distributions the only significant variation in Φ_{ω} in this region occurs with angle of attack, but even these effects are small. At the core center $\Phi_{\omega}=0$ and the vorticity vector is aligned with the core axis, as one would expect. However, moving radially outward it begins to deviate from that direction. Near $r/r_1=2$ a maximum is reached, the vorticity vector in most cases being skewed by more than 35° here.

In two-dimensional flows one intuitively expects the large turbulent structures to be aligned approximately with the mean vorticity vector. However, this does not happen in a rotational flow such as a vortex. Consider, for example, a large core of solid body rotation with an axial velocity deficit. Physically one would expect such a flow to produce mostly large structures aligned with the circumferential direction. However, the vorticity vector has a large axial component. Perhaps a better indicator of probable turbulent structure, which works in this example, is the rate of strain direction defined above. (This is logical since it is the rate of strain that gives rise to the structures in the first place). In contrast to those of Φ_{ω}, the profiles of Φ_{ϵ} (figure 4.19) appear most similar outside the core region. Inside the core there are large variations because $\partial U/\partial r$ and $\partial V_{\theta}/\partial r - V_{\theta}/r$ both fall towards zero here. Φ_{ϵ} varies strongly with Reynolds number and angle of attack (figures 4.20 and 4.22) in the core region. There are also some effects of the trip (figure 4.23). Changes in x/c (figure 4.19) appear, however, to have a negligible effect on the profile. Overall these figures suggest that, if they exist, large turbulent structures near the edge of the core would be

aligned at about 15° to the core axis. Skewing would then decrease with radial distance outward from this point.

4.3 The turbulence spectrum in the spiral wake

As explained in chapter 3 fully developed two-dimensional wakes can be described entirely using two scaling parameters; u_o the maximum velocity deficit and L_o, the distance between the wake center and the point where the deficit is half its maximum value. The spiral wake surrounding a vortex core is considerably more complex. First, it is inherently three-dimensional in that it contains a non-uniform vortex sheet shed from the wing. Second it is strained by the circumferential velocity field of the vortex. Third it is strongly curved in the transverse direction.

With these additional effects it is surprising to find a strong similarity in the velocity autospectra measured in the spiral wake, regardless of conditions. This similarity is illustrated in figures 4.24a-c where all the spiral wake spectra (z/c=-.5 and -.025) of figures 3.28-3.35 are compared. To make this comparison the spectra were normalized to unit area and plotted against frequency in terms of fc/U_{ref}. (Note that the discrete spikes in these spectra, which are due to electrical noise, should be ignored.) Most of the differences between the spectra plotted in figure 4.24 are a consequence of Reynolds number effects which change the slope of the spectrum at higher frequencies where dissipation is important. This can be seen in figures 4.25a-c where only those autospectra measured at Re_c=400000 are presented.

Despite the fairly reasonable collapse of the spectra in these figures it is unlikely that wing chordlength is the correct scaling parameter for frequency. A much more appropriate parameter is the length scale L_o used in two-dimensional wakes. Unfortunately there was too much uncertainty in the present axial velocity measurements (see for example figure 3.14(a)) for L_o to be determined reliably. Instead it was computed empirically using the relationship

$$\frac{L_o}{\theta} = 0.32\sqrt{\frac{x}{\theta}+320} \qquad (28)$$

due to Wygnanski et. al (1986). Here θ was taken as the initial wake mometum deficit deduced from the single hot-wire measurements (see table 3.3). While this relationship is intended for two-dimensional wakes, scaling frequency on the values of L_o it produces does slightly improve in the collapse (figures 3.26a-c).

(1)	(2)	(3)	(4)	(5)	(6)	(7)	(8)	(9)	(10)	(11)	(12)
5.0	130000	30	.250	.0837	.0652	.204	5.63	.136	120	3.94×10^6	4.0
5.0	260000	30	.250	.0689	.0488	.225	8.43	.170	120	7.88×10^6	4.0
5.0	400000	30	.250	.0697	.0467	.237	9.77	.140	120	1.19×10^7	4.0
5.0	530000	30	.250	.0672	.0433	.247	10.6	.151	120	1.58×10^7	4.0
5.0	400000	20	.250	.0690	.0413	.265	11.8	.155	80	7.99×10^6	4.0
5.0	400000	25	.250	.0696	.0433	.256	10.9	.128	100	1.04×10^7	4.0
2.5	400000	30	.125	.0249	.0444	.089	3.72	.146	240	1.20×10^7	8.0
7.5	400000	30	.375	.1196	.0517	.367	13.9	.178	80	1.18×10^7	2.7
5.0	530000	30	.250	.0731	.0434	.268	11.2	.096	120	1.55×10^7	4.0

(1) Angle of attack α
(2) Reynolds number based on chord Re_c
(3) Streamwise distance x/c
(4) Non-dimensional root circulation $\Gamma_0/U_{ref}c$
(5) Non-dimensional core circulation $\Gamma_1/U_{ref}c$
(6) Core radius r_1/c
(7) Peak tangential velocity at core edge $V_{\theta 1}/U_{ref}$
(8) Peak tangential velocity gradient at core center $\partial V_\theta/\partial r|_{r=0} * c/U_{ref}$
(9) Centerline axial velocity deficit notmalized on U_{ref}
(10) $U_{ref}x/\Gamma_0$
(11) $U_{ref}x/\nu$
(12) $U_{ref}c/\Gamma_0$, (reciprocal of column 3)

Table 4.1 Vortex parameters

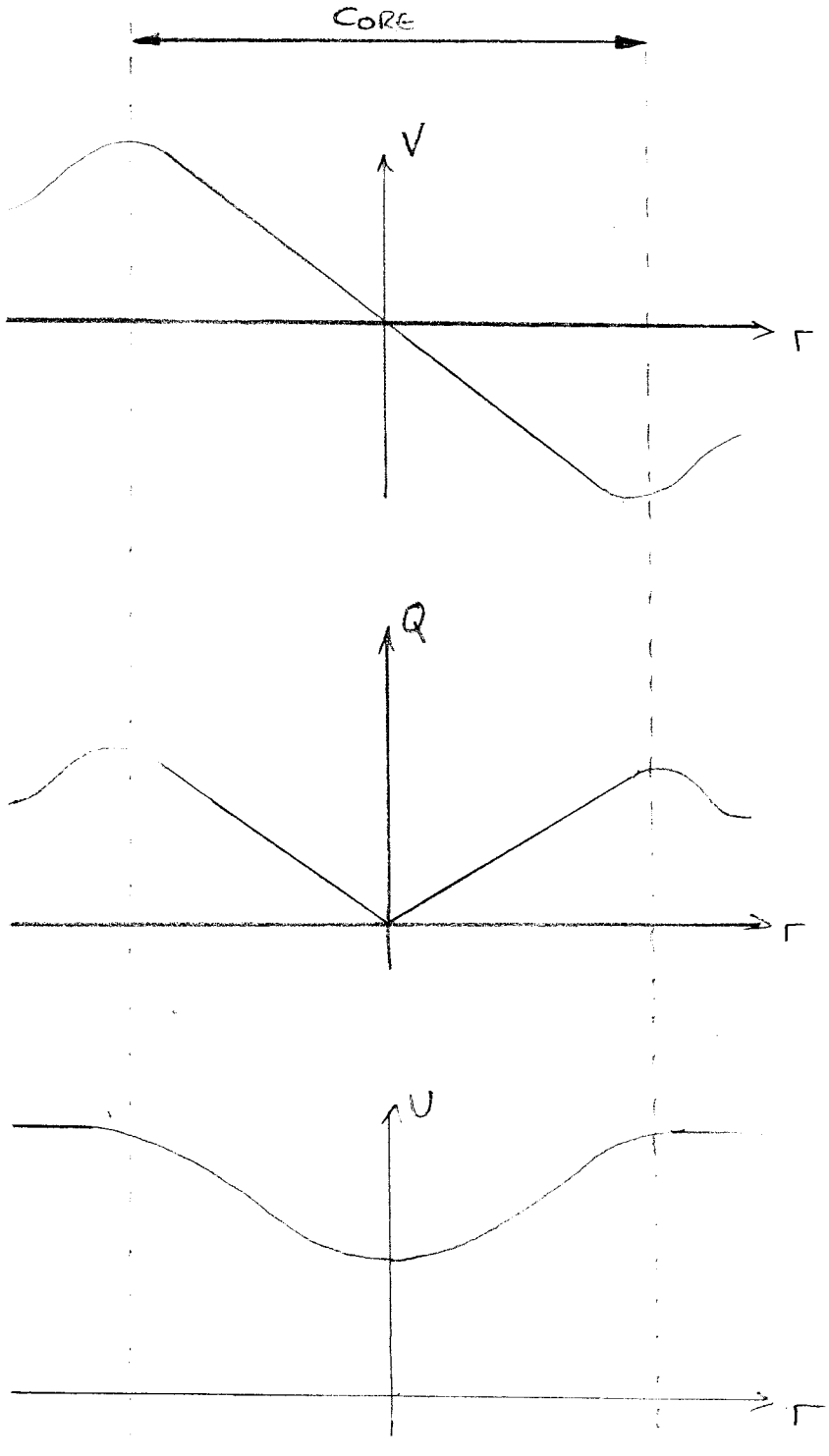

Figure 4.1 Idealized core velocity profiles.

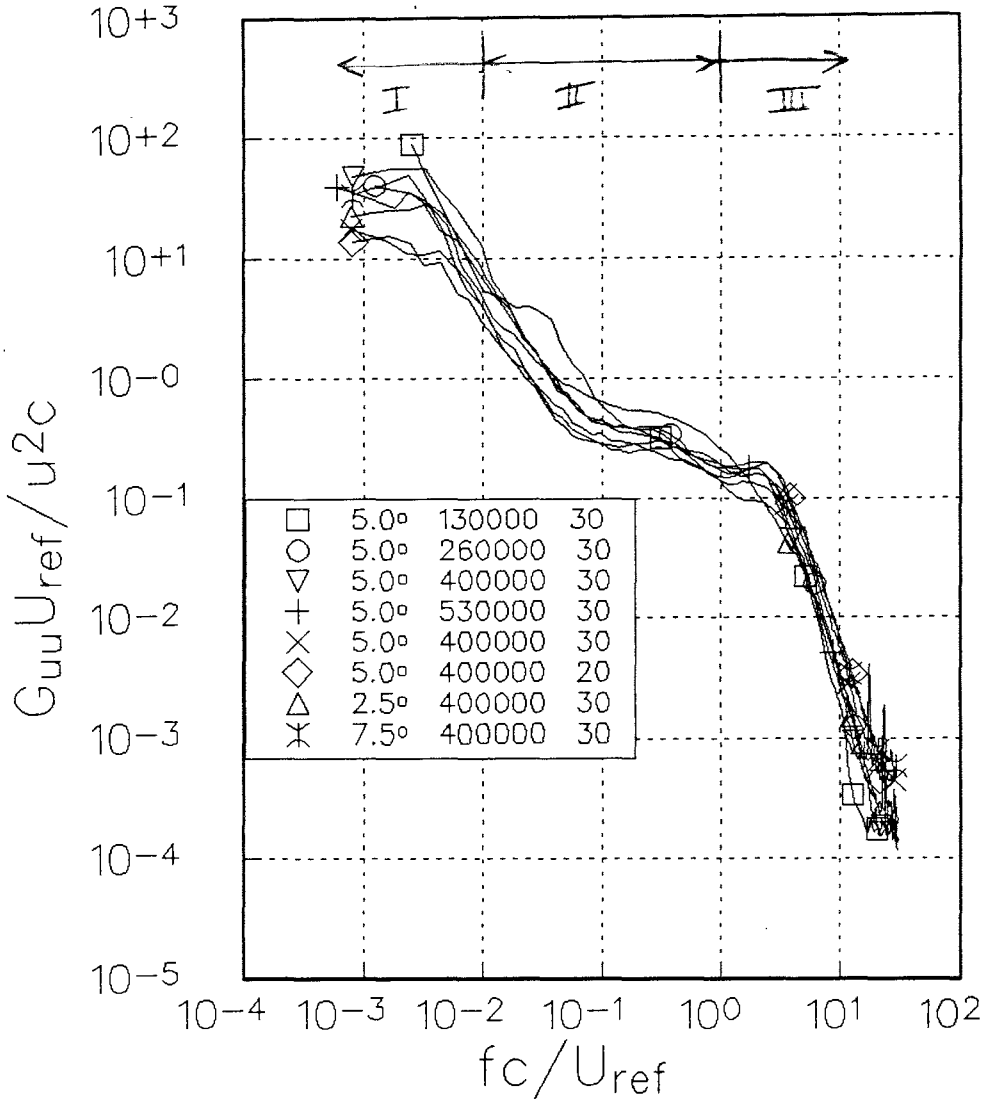

Figure 4.2(a) Comparison of core auto spectra $G_{uu}c/\overline{u^2}U_{ref}$ showing the three frequency bands.

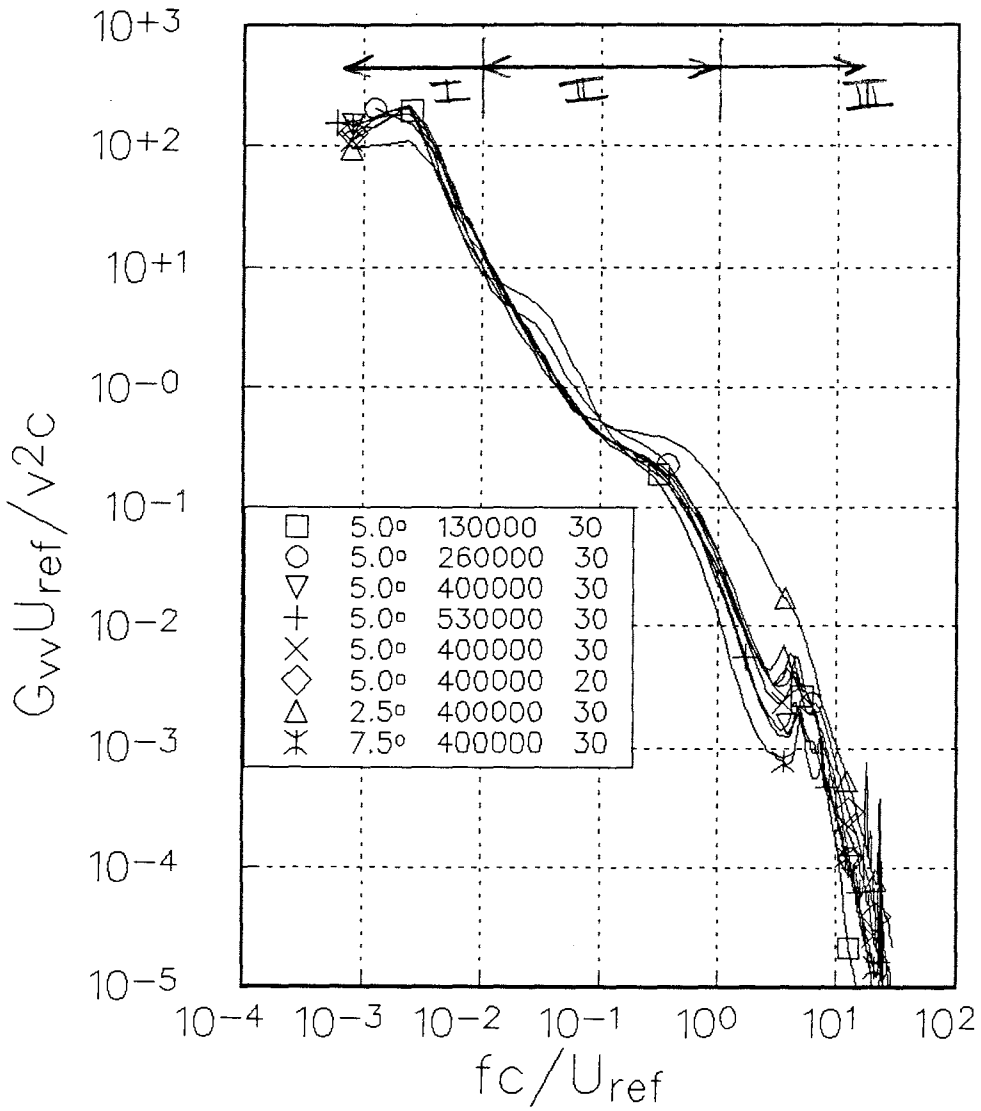

Figure 4.2(b) Comparison of core auto spectra $G_{vv}c/\overline{u^2}U_{ref}$ showing the three frequency bands.

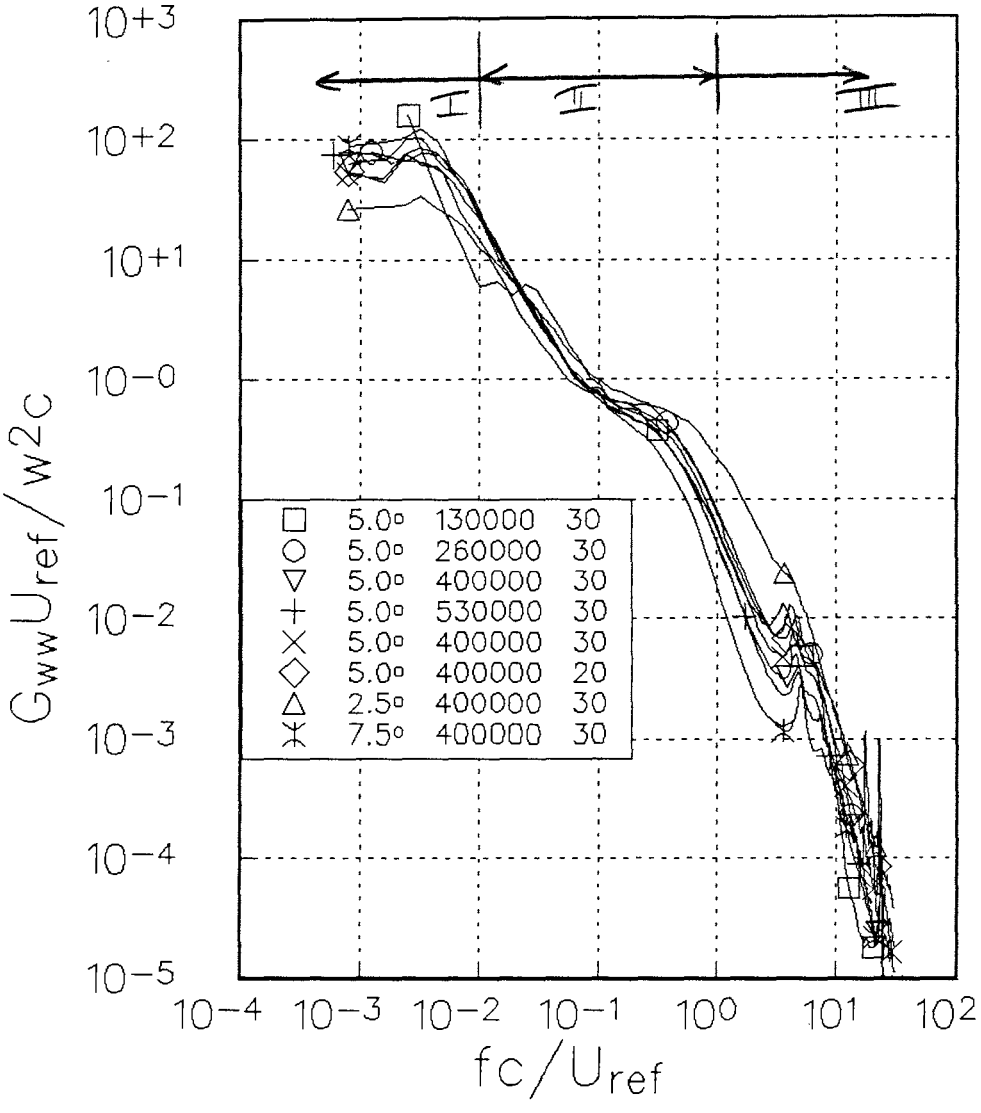

Figure 4.2(c) Comparison of core auto spectra $G_{ww}c/\overline{u^2}U_{ref}$ showing the three frequency bands.

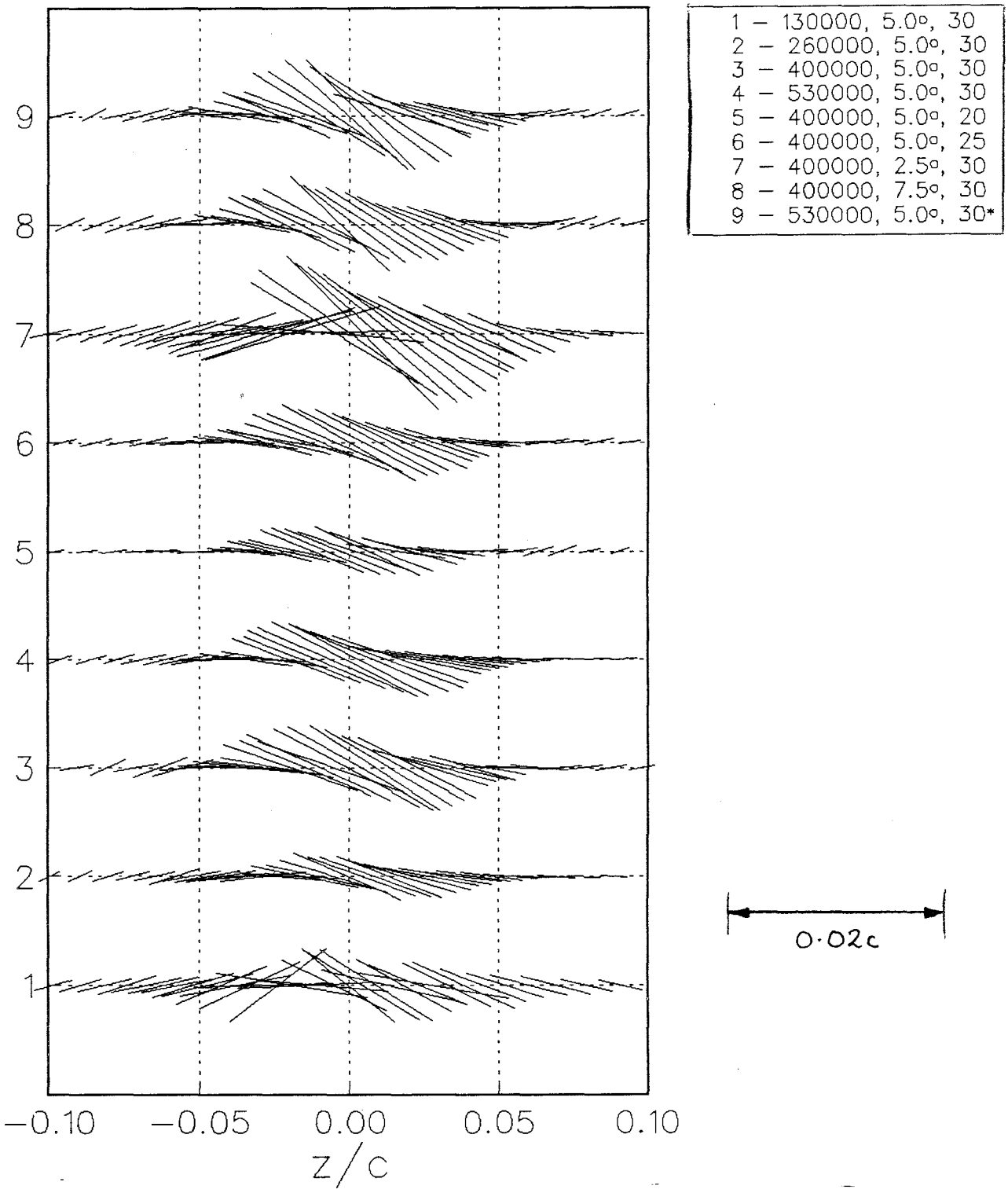

Figure 4.3 Lines showing the probable extent and direction of the coherent wandering motions of the vortex.

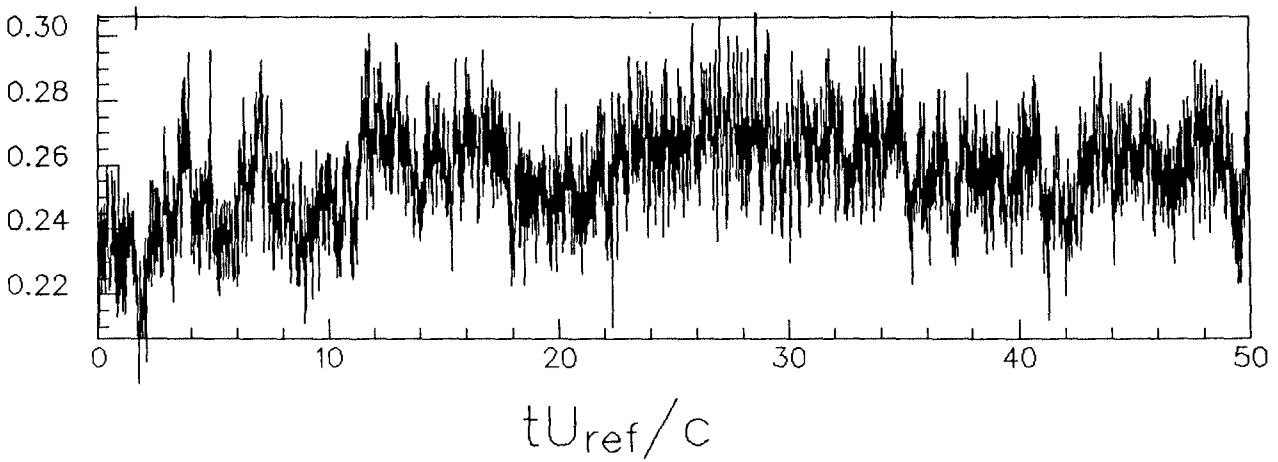

Figure 4.4 V-component velocity fluctuations at the edge of the core in the baseline case.

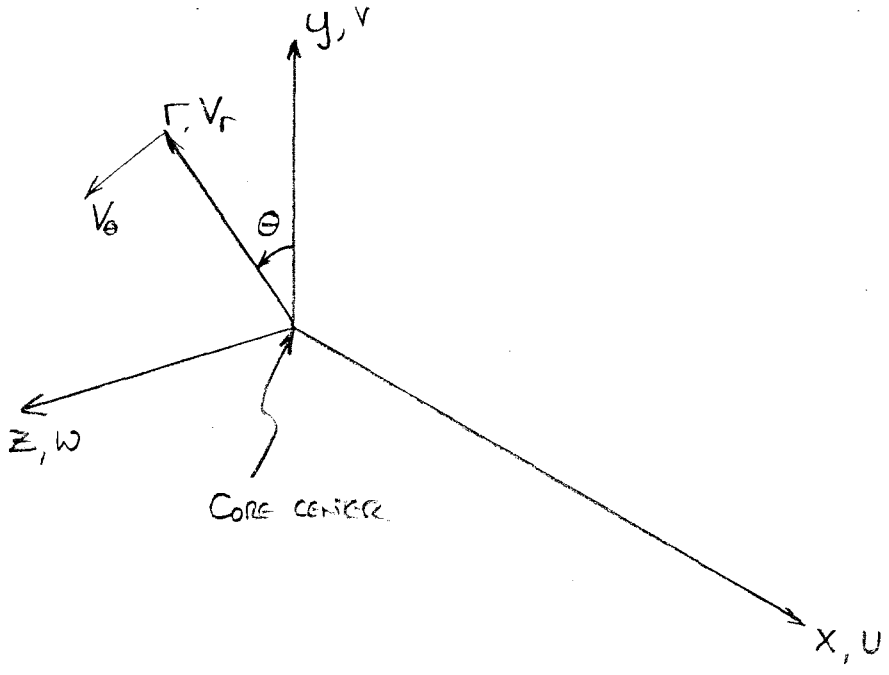

Figure 4.5 Cylindrical coordinate system.

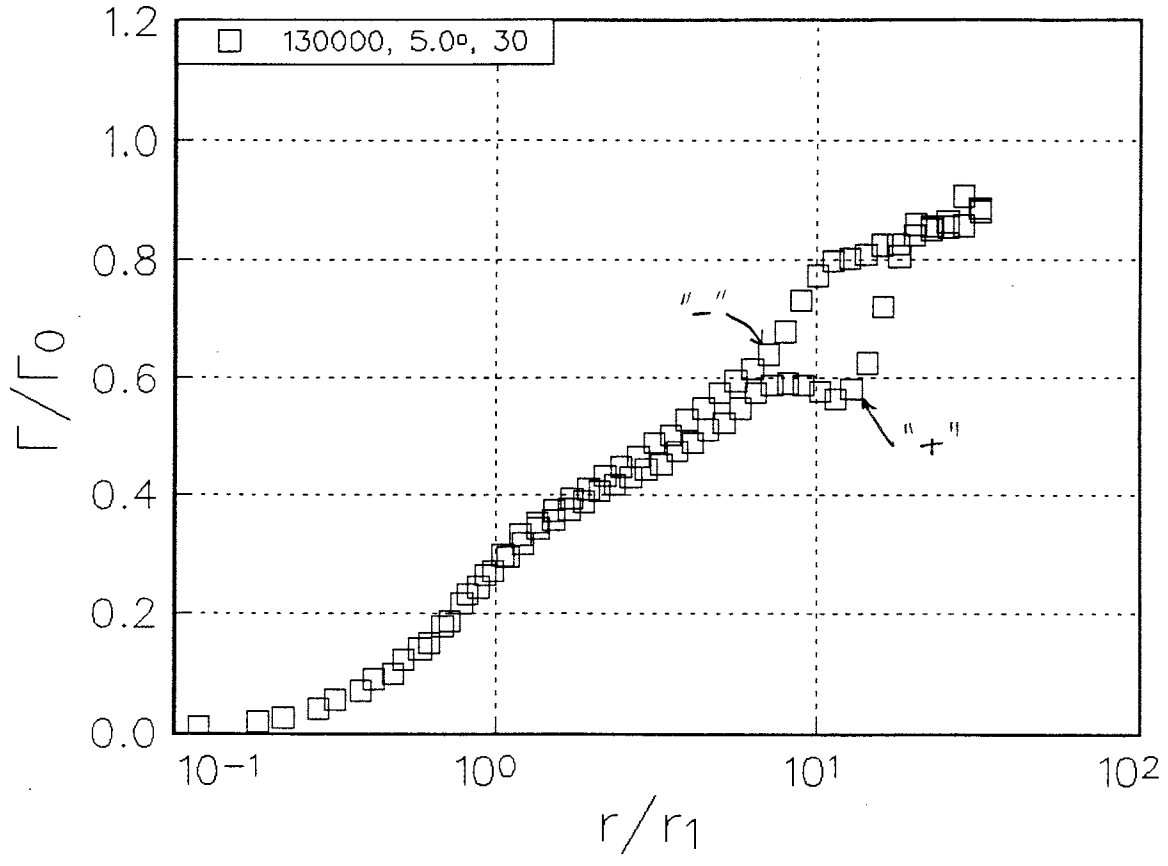

Figure 4.6 Circulation profiles for the baseline case calculated from measurements made on the positive (+) and negative (-) z sides of the vortex center.

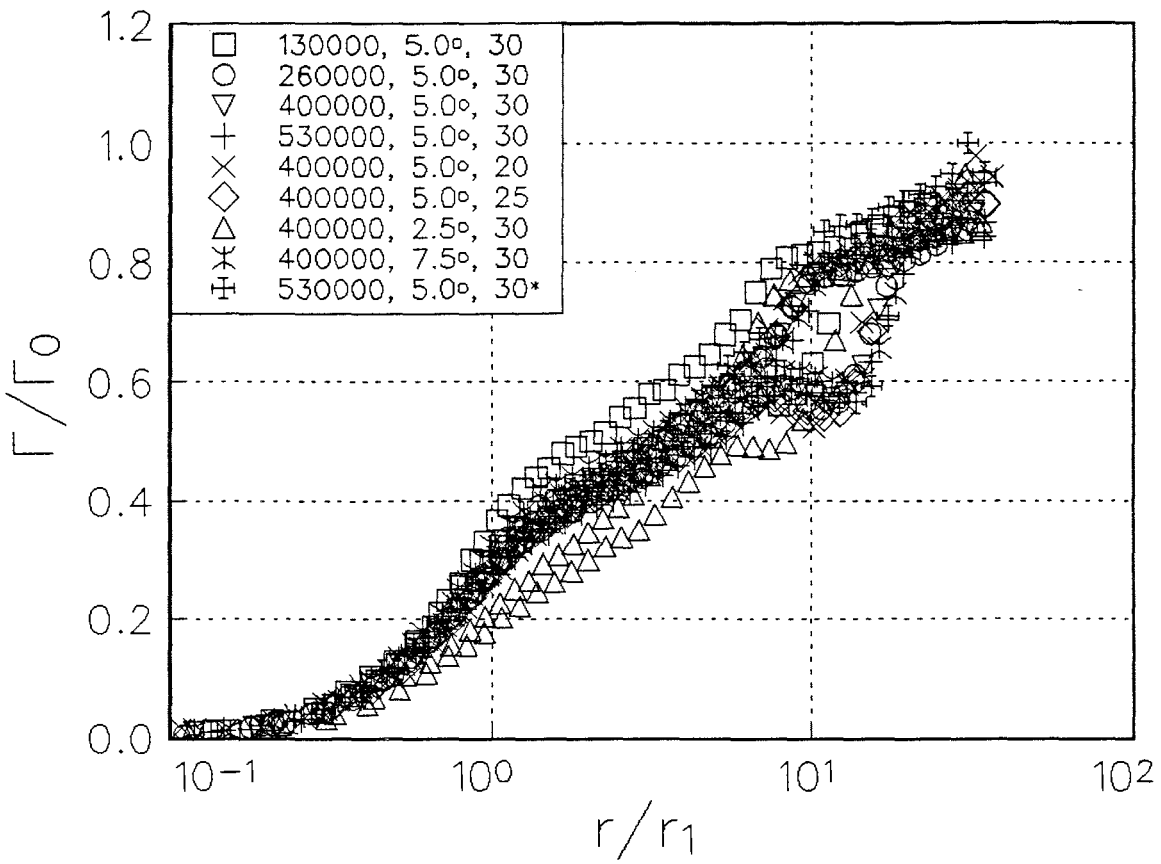

Figure 4.7 Circulation profiles for all cases normalized on total bound circulation Γ_0. Items in legend are, respectively, Re_c, α and x/c. Asterisk indicates case with wing trip removed.

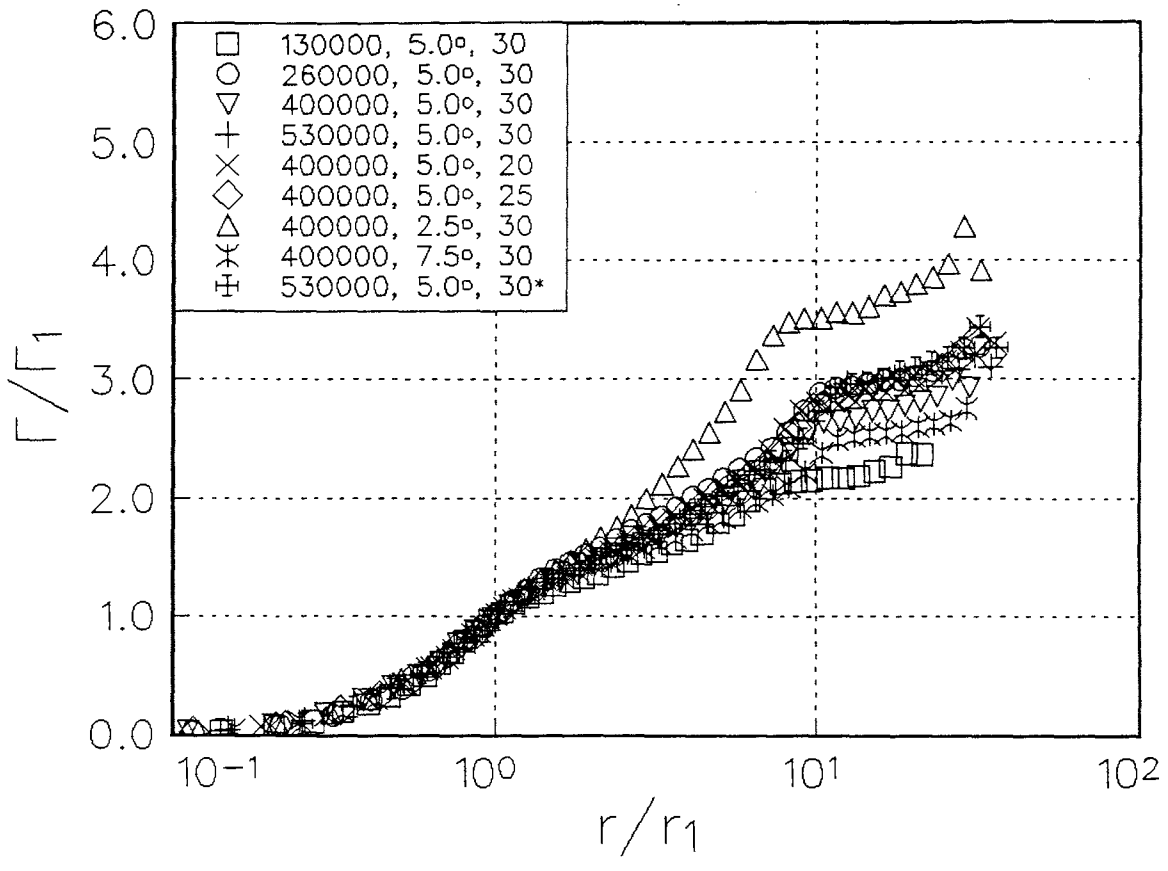

Figure 4.8 Circulation profiles for all cases normalized on core circulation Γ_1. Items in legend are, respectively, Re_c, α and x/c. Asterisk indicates case with wing trip removed.

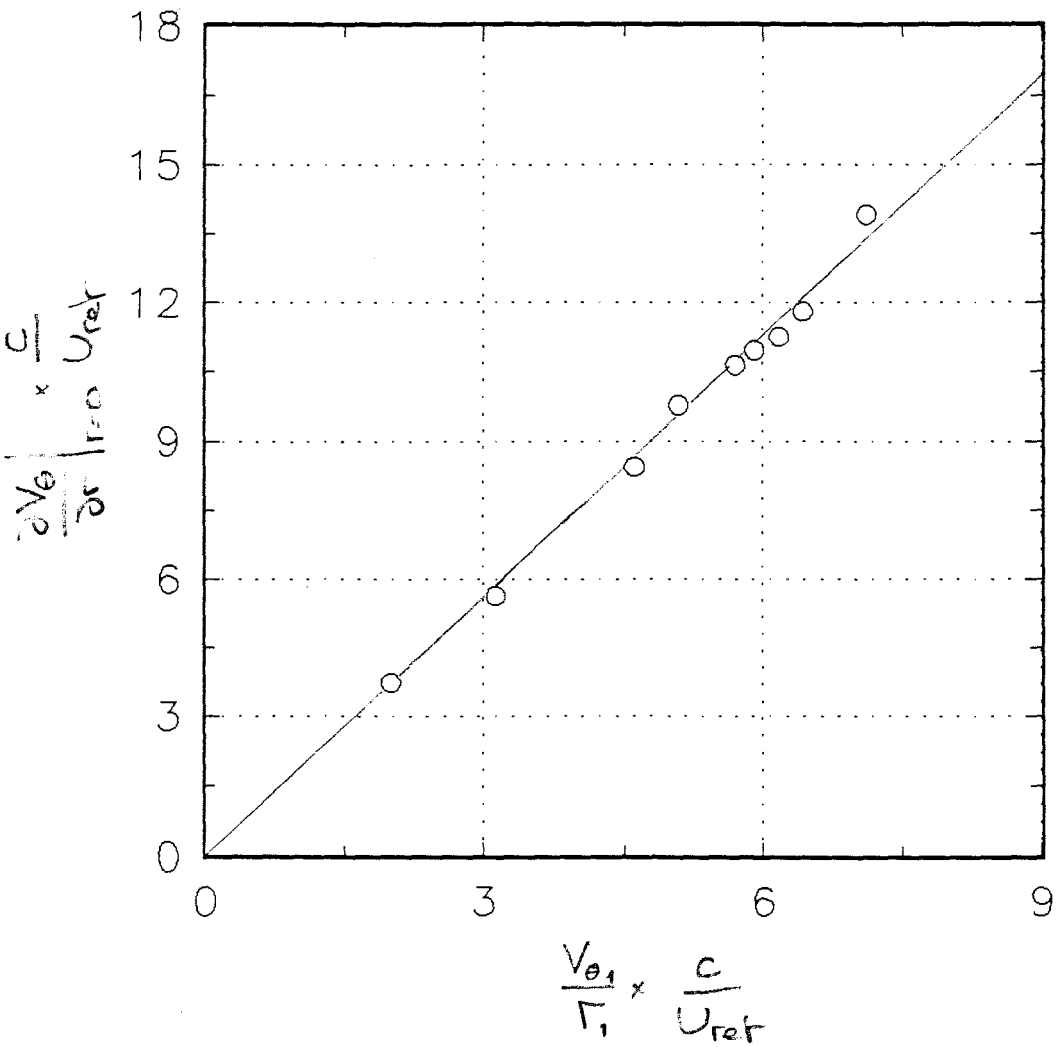

Figure 4.9 $V_{\theta 1}/r_1$ vs $\partial V_\theta/\partial r\,|_{r=0}$ for all cases.

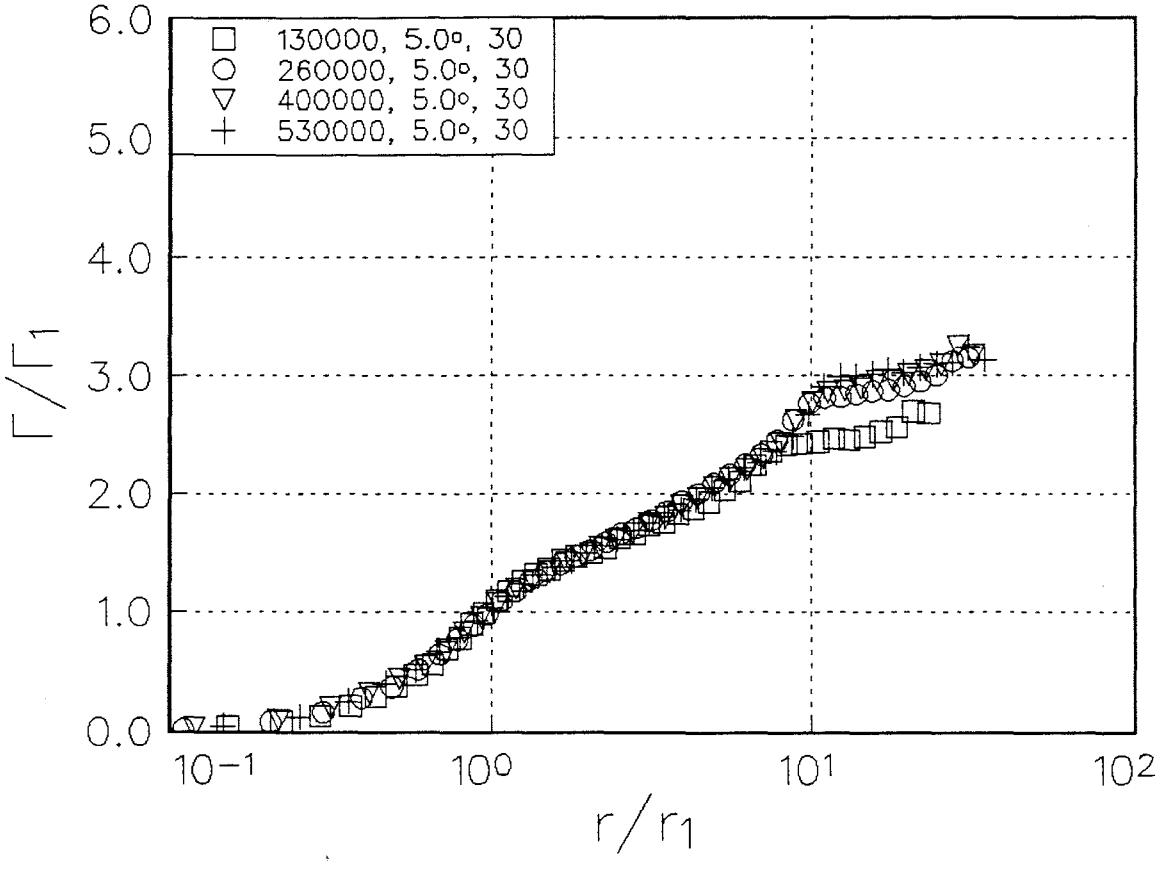

Figure 4.10 Circulation profile normalized on core circulation Γ_1 as a function of Re_c for $x/c=30$, $\alpha=5.0°$.

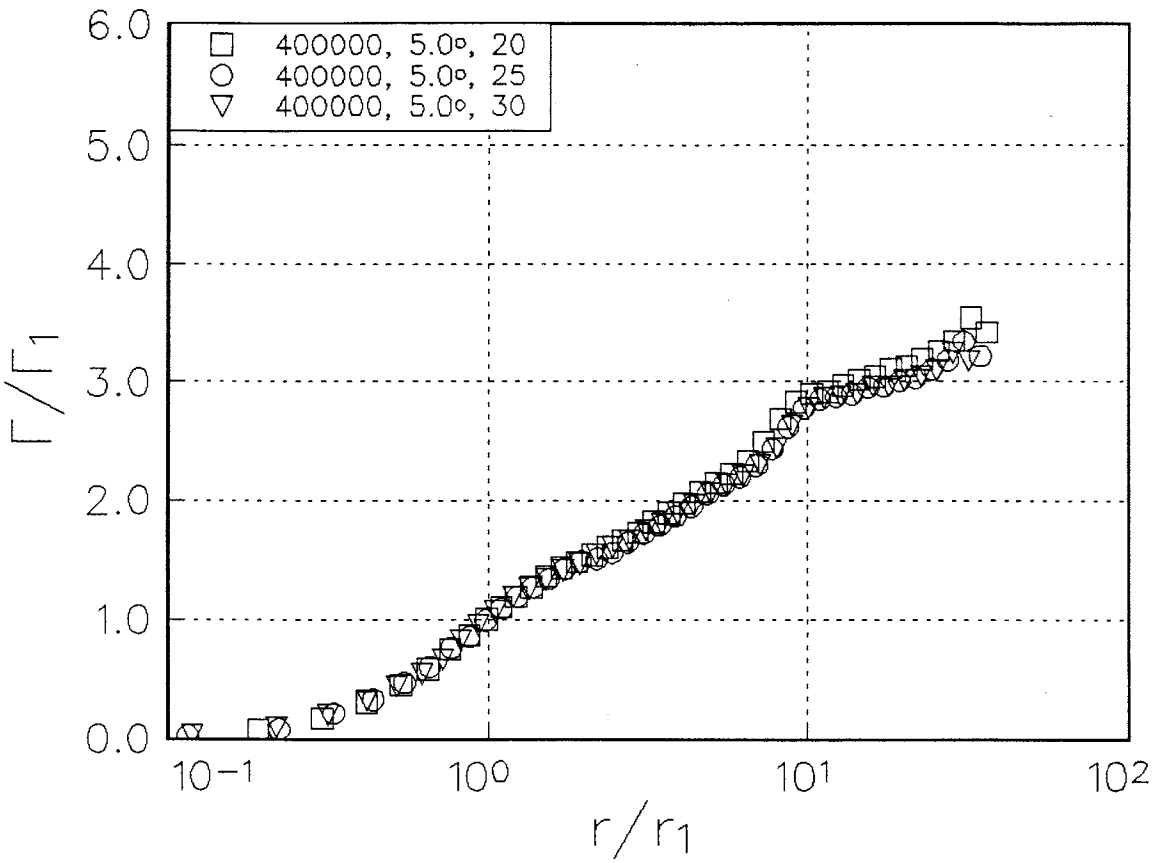

Figure 4.11 Circulation profile normalized on core circulation Γ_1 as a function of x/c for Re_c=400000, α=5.0°.

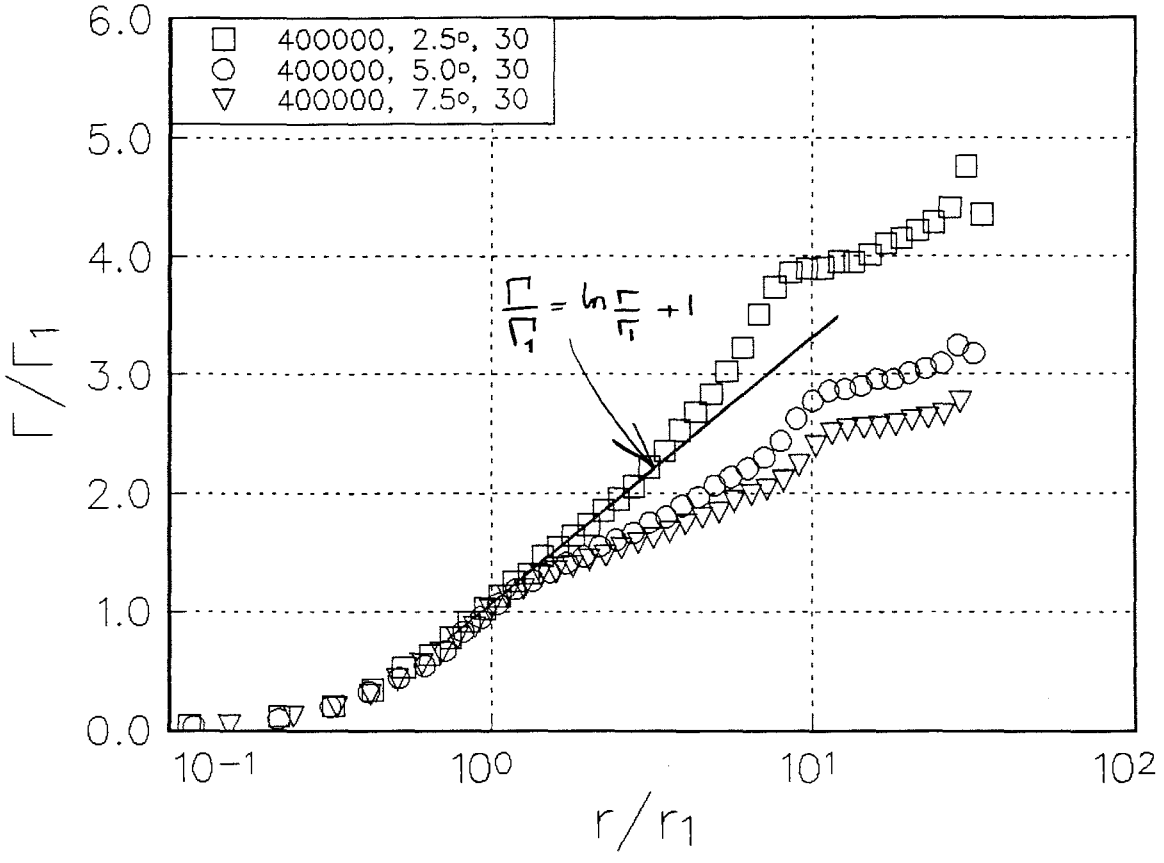

Figure 4.12 Circulation profile normalized on core circulation Γ_1 as a function of α for Re_c=400000, x/c=30.

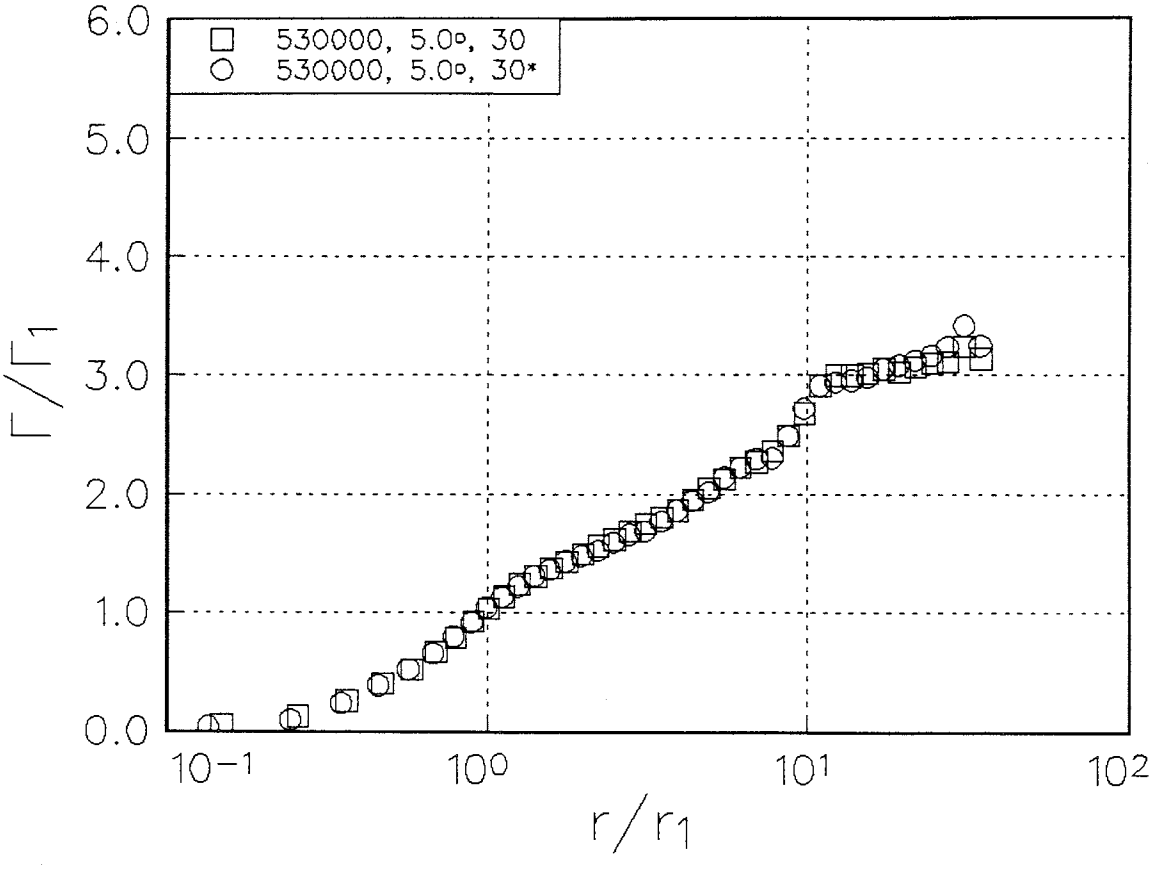

Figure 4.13 Circulation profile normalized on core circulation Γ_1 as a function of wing trip at x/c=30, Re_c=530000, α=5.0°. Case without trip identified by asterisk in legend.

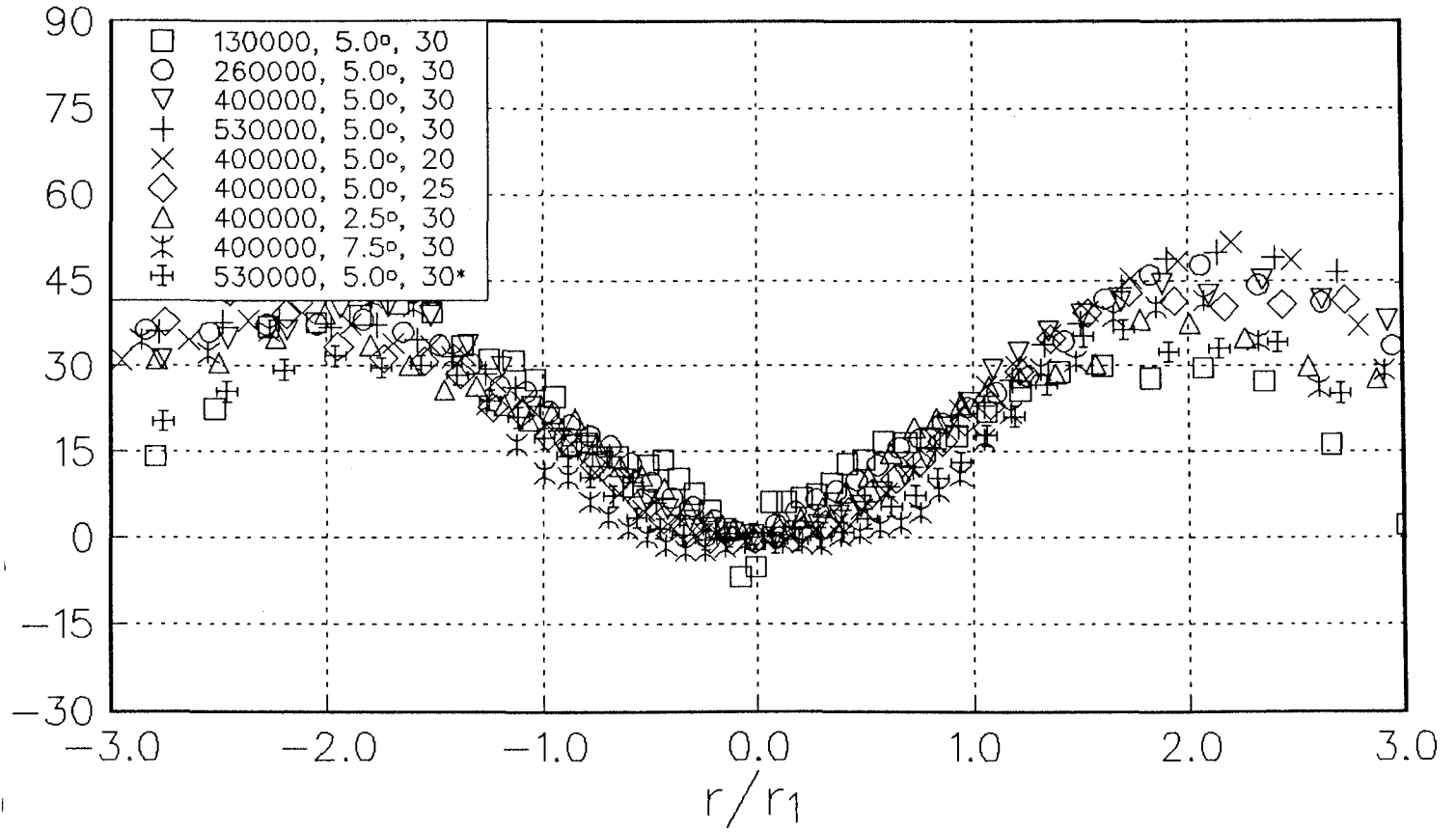

Figure 4.14 Profiles of vorticity direction Φ_ω, all cases. Items in legend are, respectively, Re_c, α and x/c. Asterisk indicates case with wing trip removed.

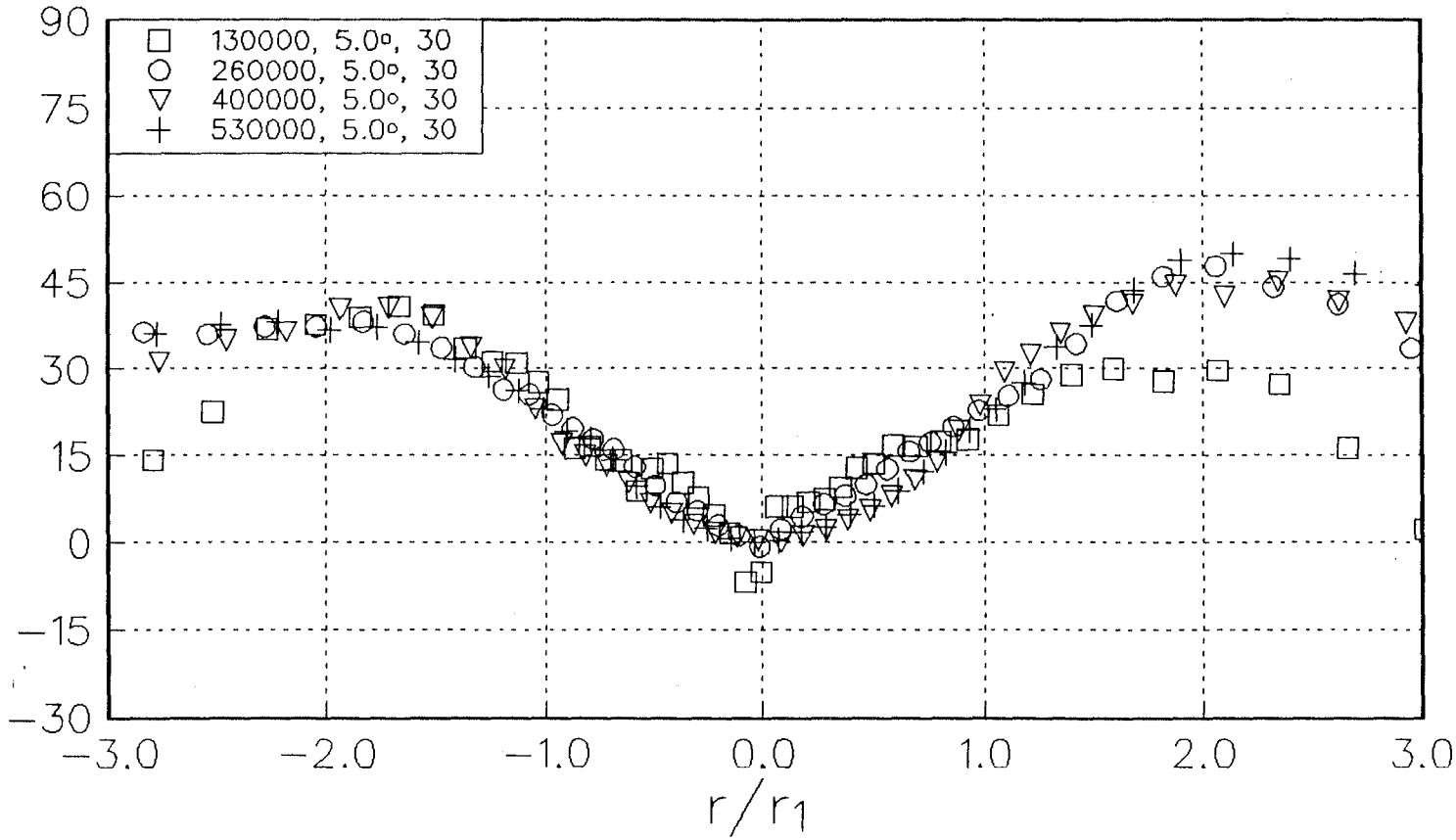

Figure 4.15 Profile of vorticity direction Φ_ω as a function of Re_c for x/c=30, α=5.0°.

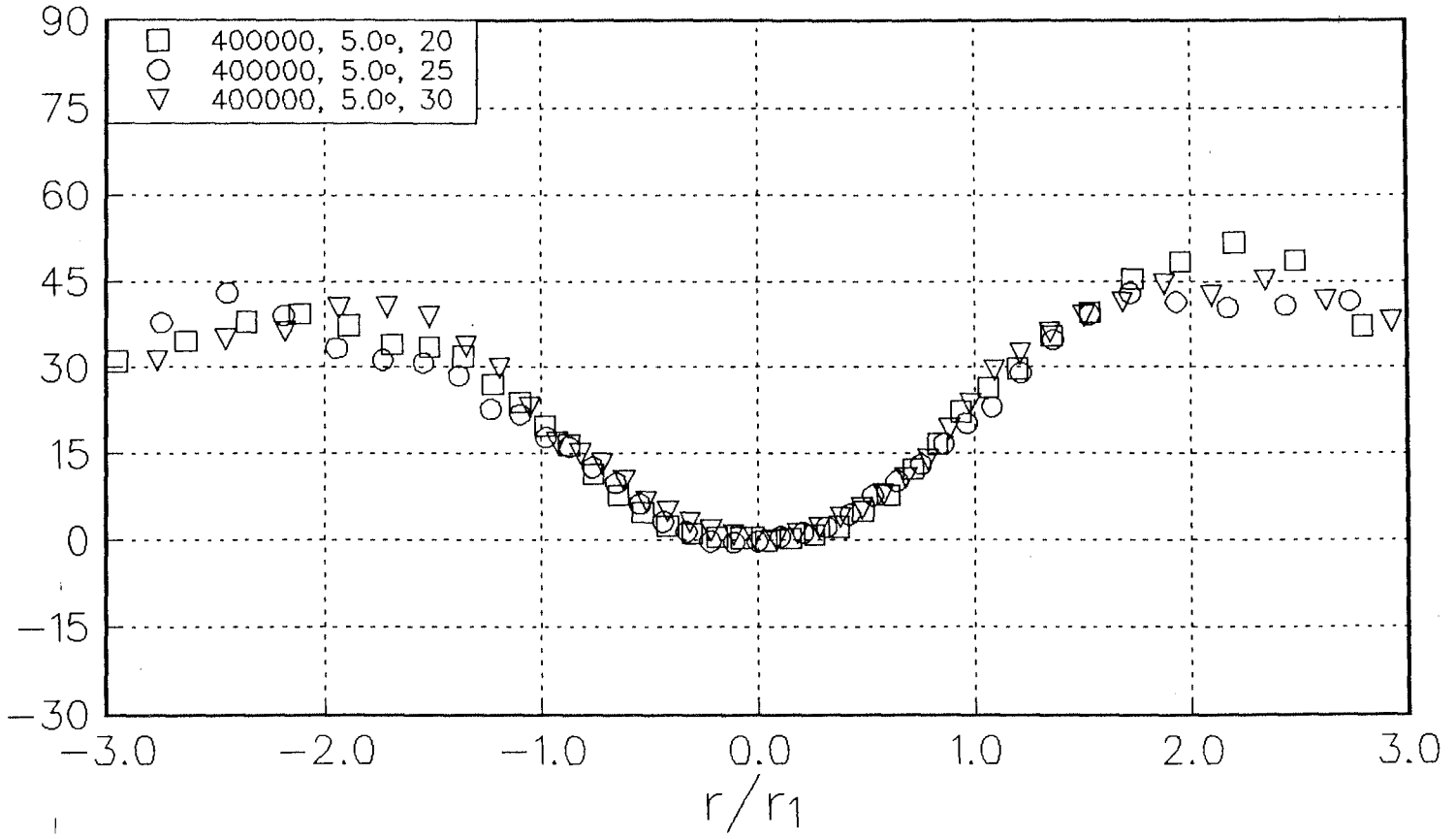

Figure 4.16 Profile of vorticity direction Φ_ω as a function of x/c for Re_c=400000, α=5.0°.

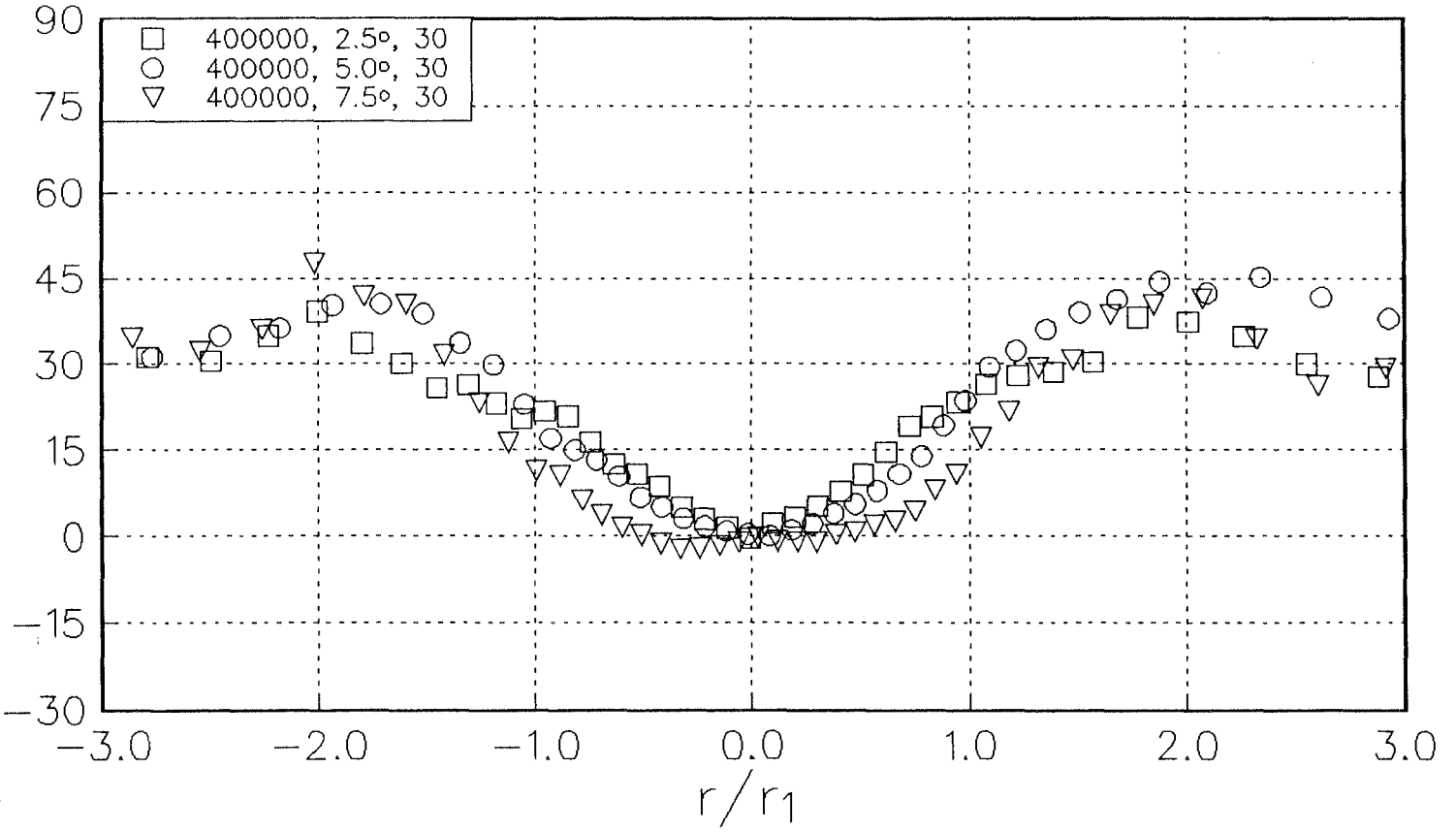

Figure 4.17 Profile of vorticity direction Φ_ω as a function of α for Re_c=400000, x/c=30.

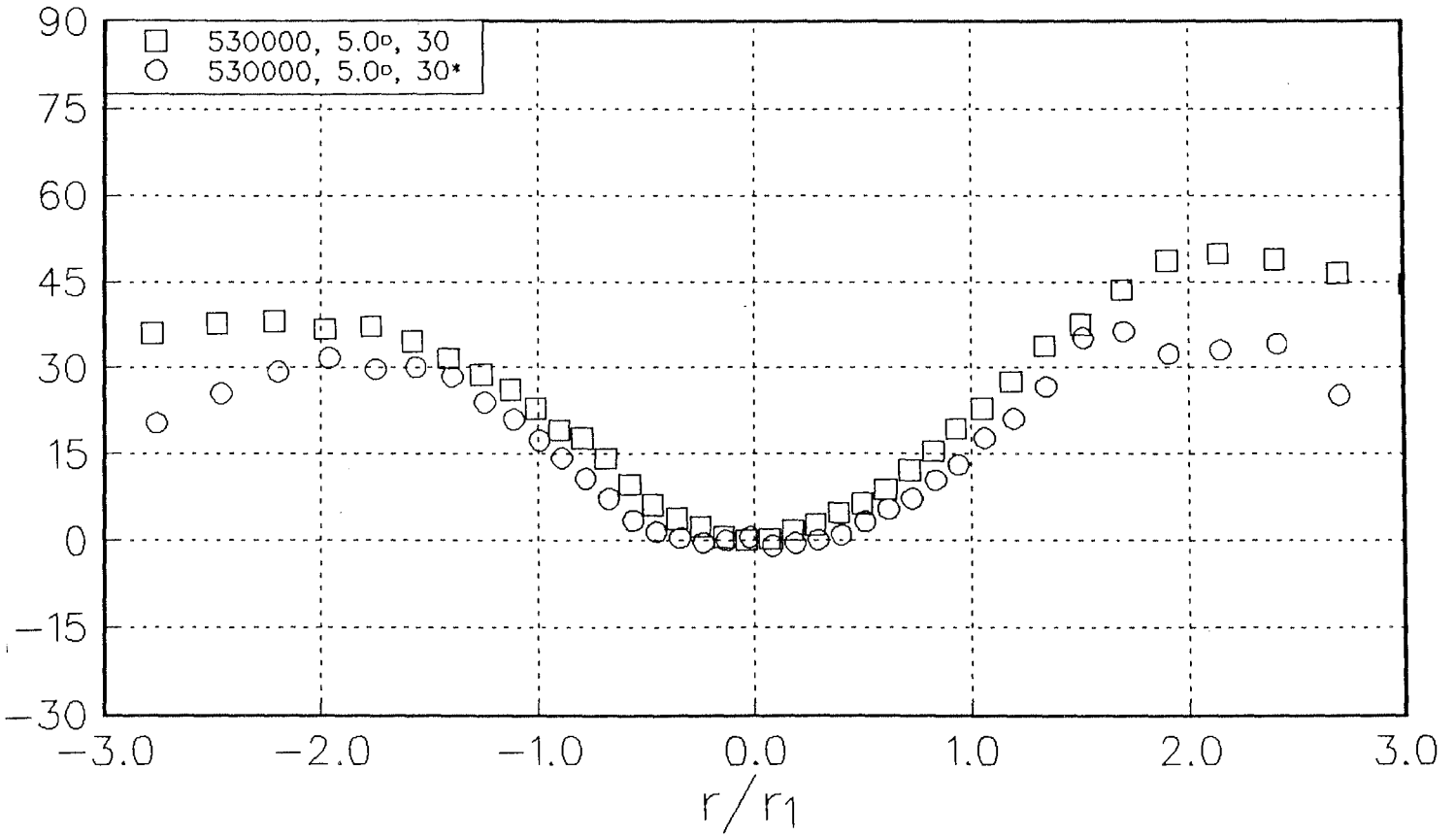

Figure 4.18 Profile of vorticity direction Φ_ω as a function of wing trip at x/c=30, Re_c=530000, α=5.0°. Case without trip identified by asterisk in legend.

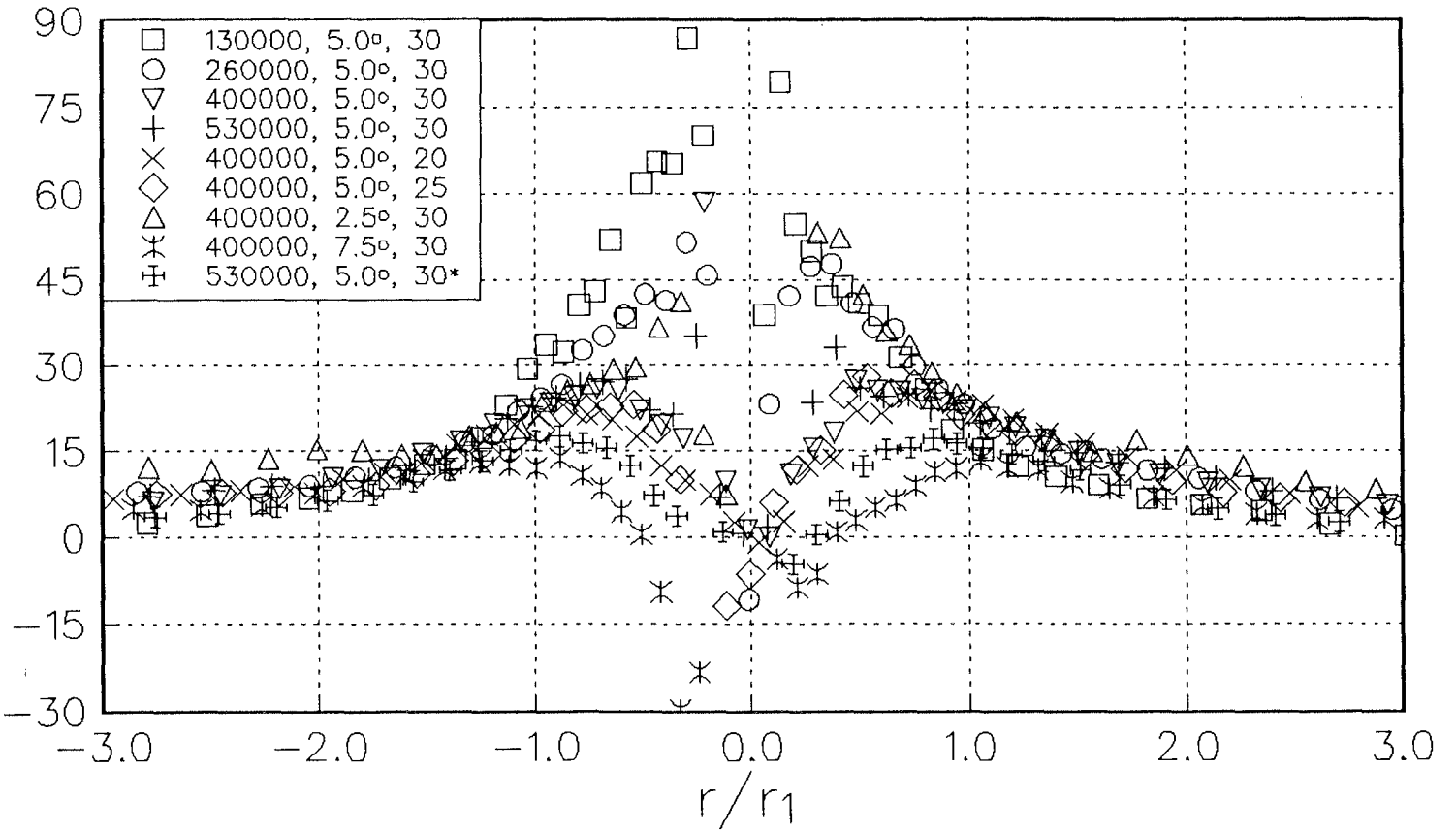

Figure 4.19 Profiles of rate-of-strain direction Φ_ε, all cases. Items in legend are, respectively, Re_c, α and x/c. Asterisk indicates case with wing trip removed.

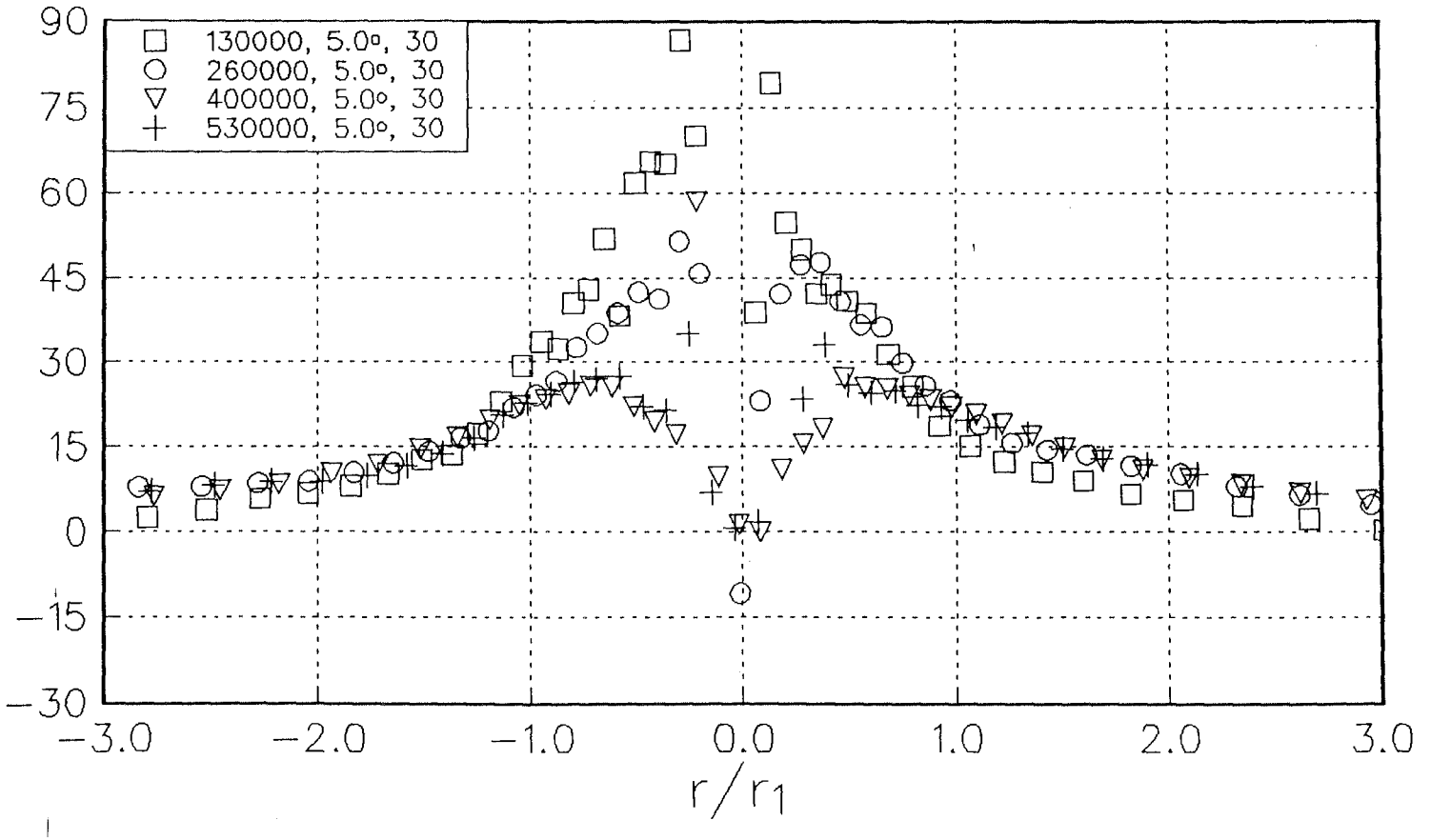

Figure 4.20 Profile of rate-of-strain direction Φ_ϵ as a function of Re_c for x/c=30, α=5.0°.

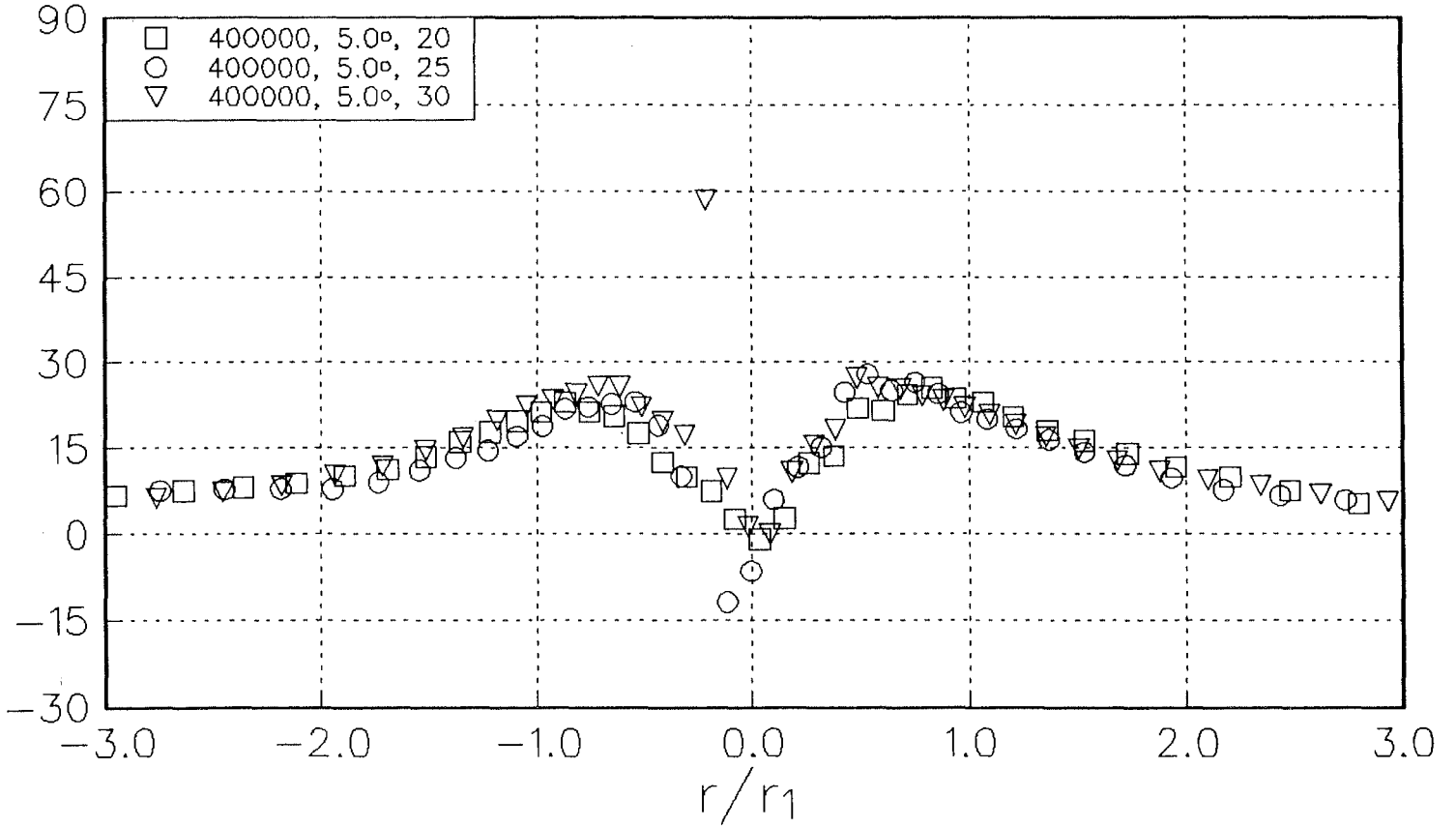

Figure 4.21 Profile of rate-of-strain direction Φ_ϵ as a function of x/c for Re_c=400000, α=5.0°.

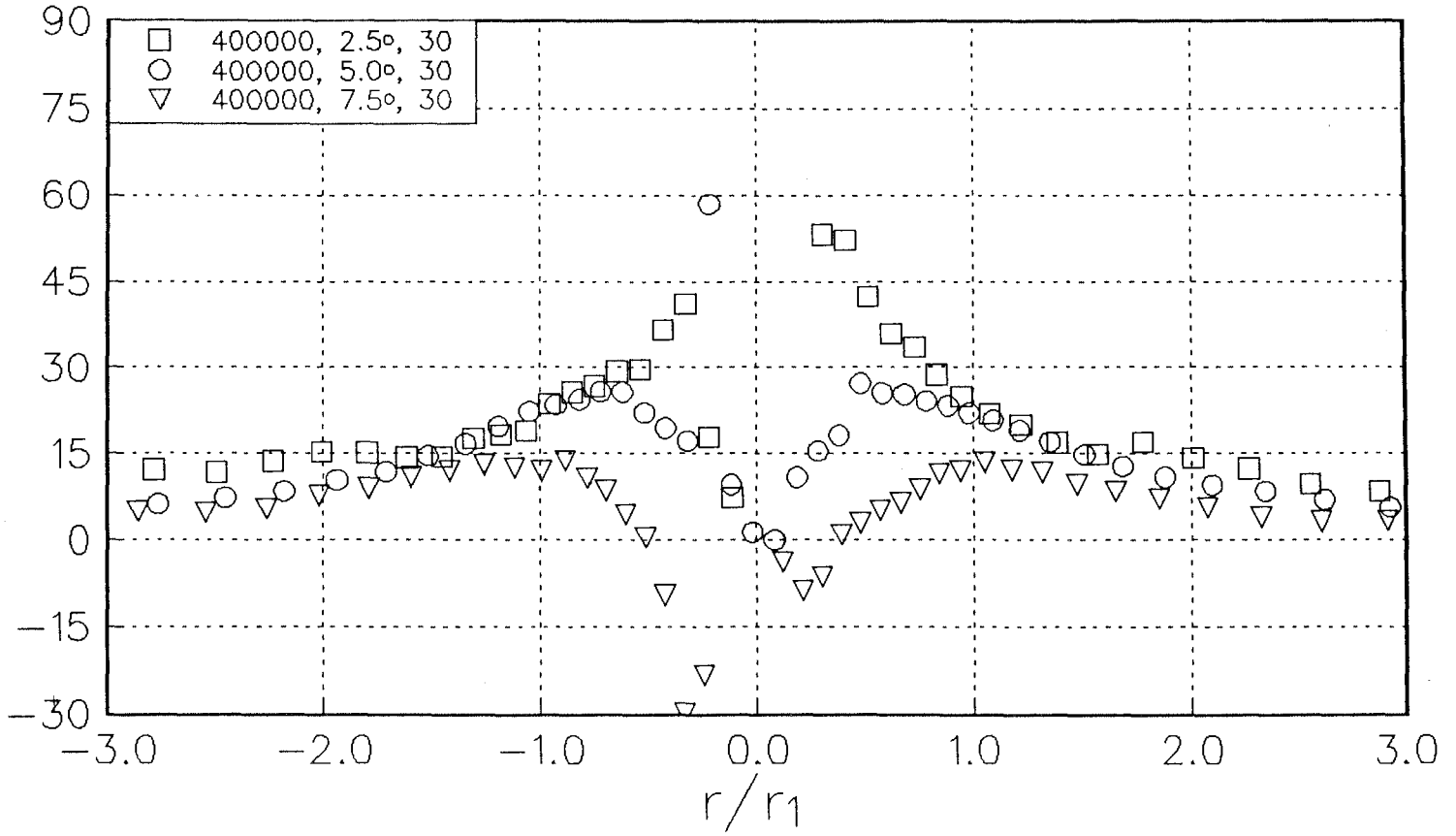

Figure 4.22 Profile of rate-of-strain direction Φ_ϵ as a function of α for Re_c=400000, x/c=30.

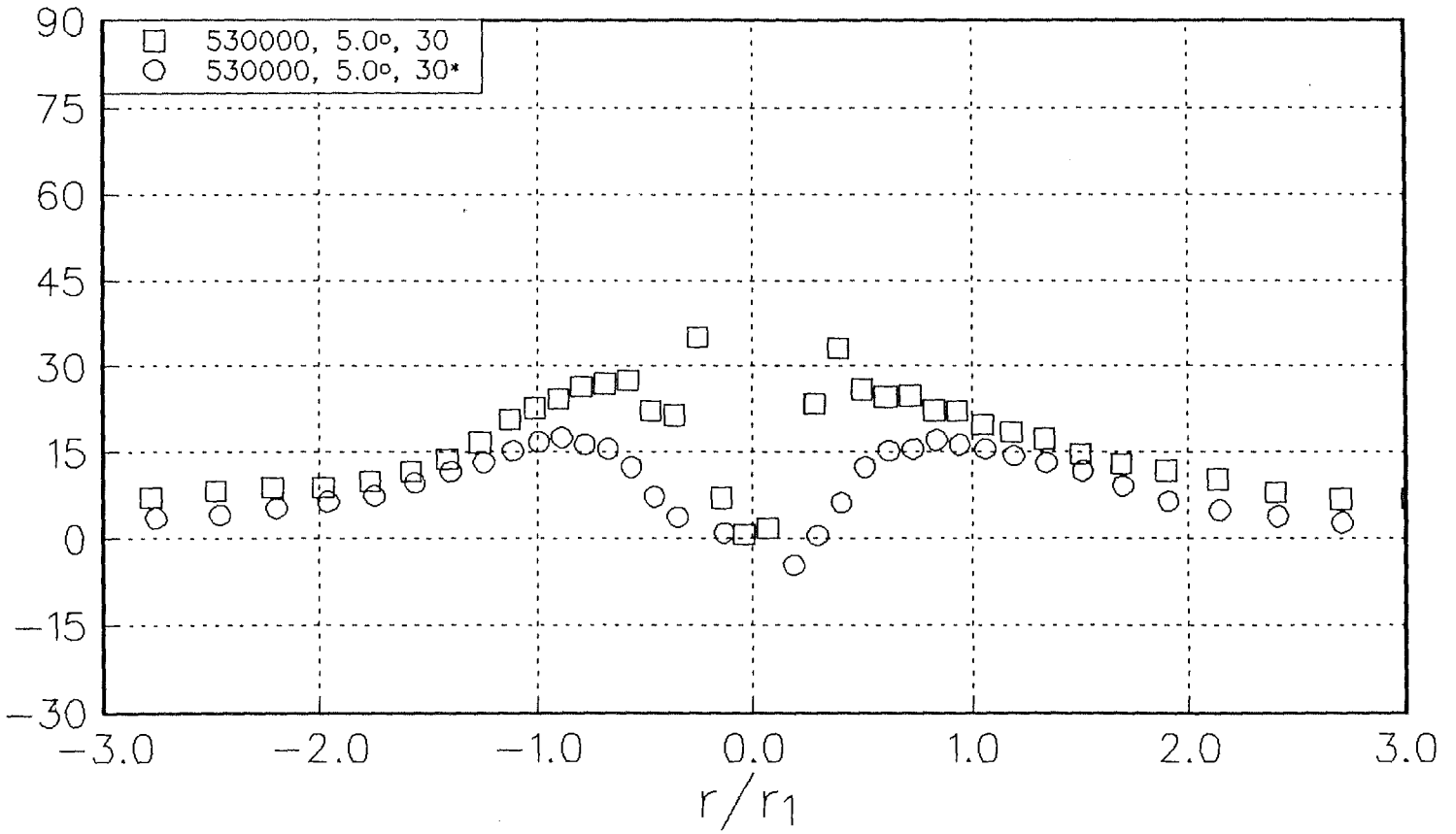

Figure 4.23 Profile of rate-of-strain direction Φ_ϵ as a function of wing trip at x/c=30, Re_c=530000, α=5.0°. Case without trip identified by asterisk in legend.

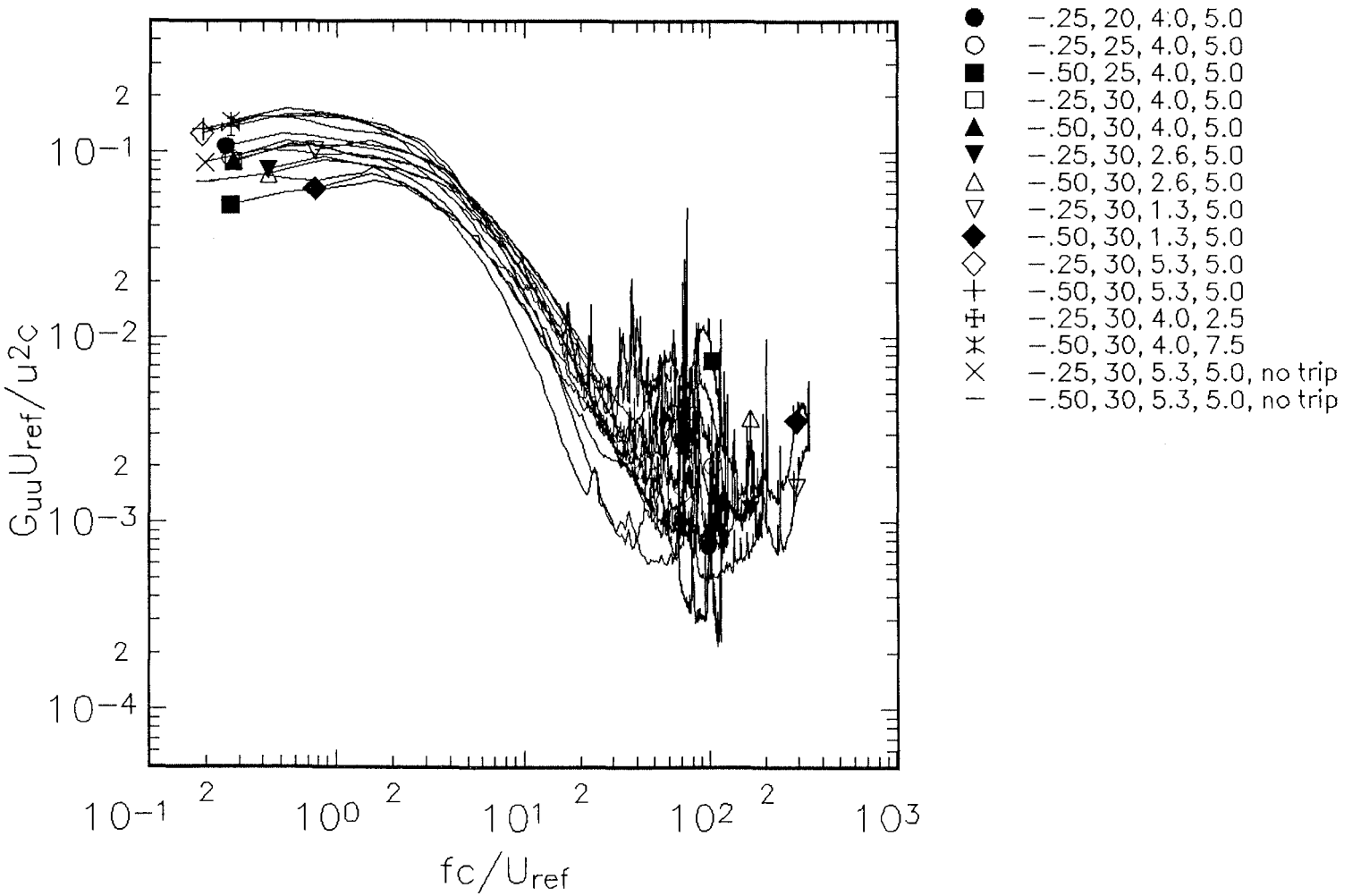

Figure 4.24(a) U component autospectra measured at all conditions in the spiral wake normalized to unit area and plotted against fc/U_{ref}.

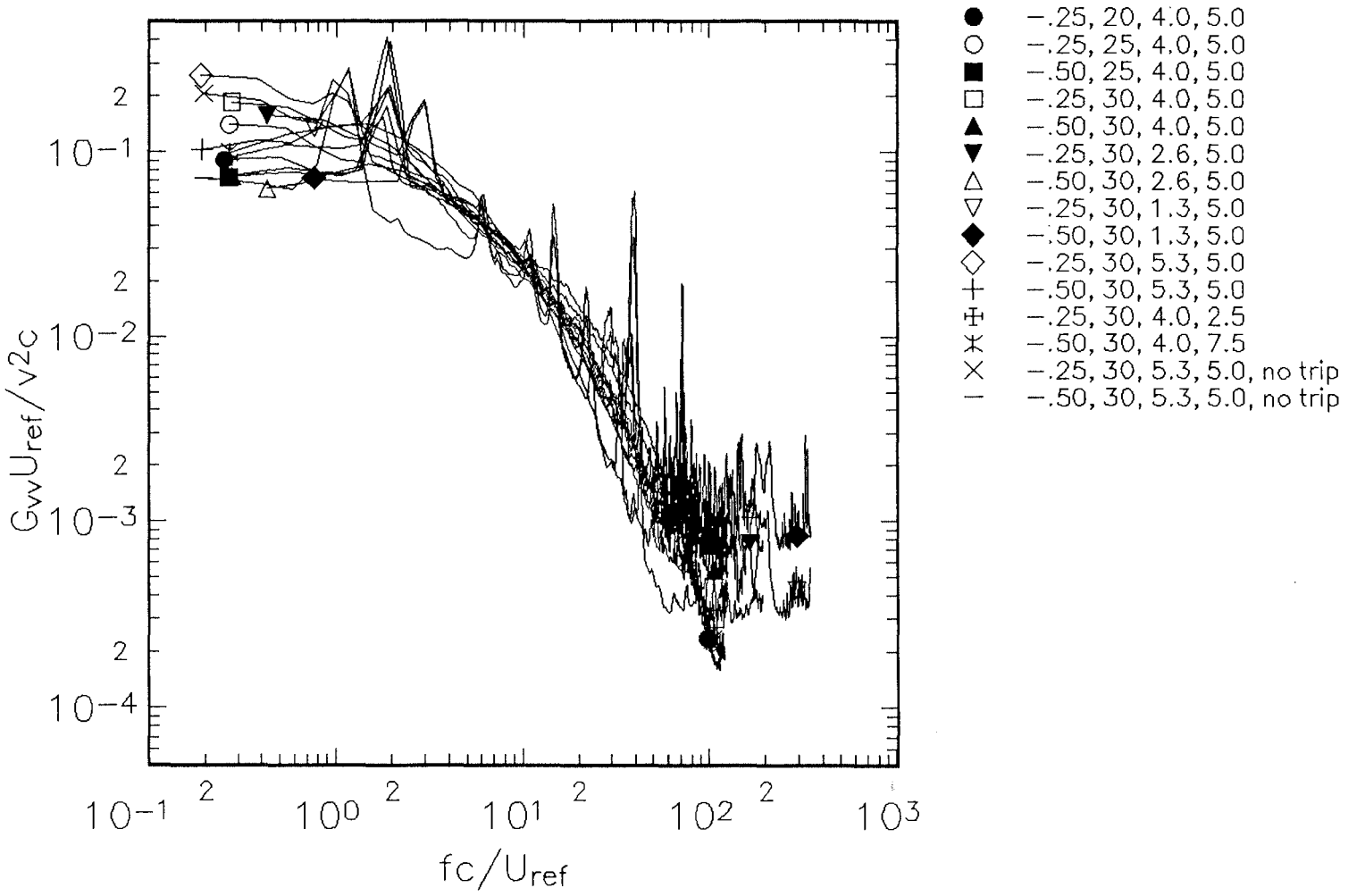

Figure 4.24(b) V component autospectra measured at all conditions in the spiral wake normalized to unit area and plotted against fc/U_{ref}.

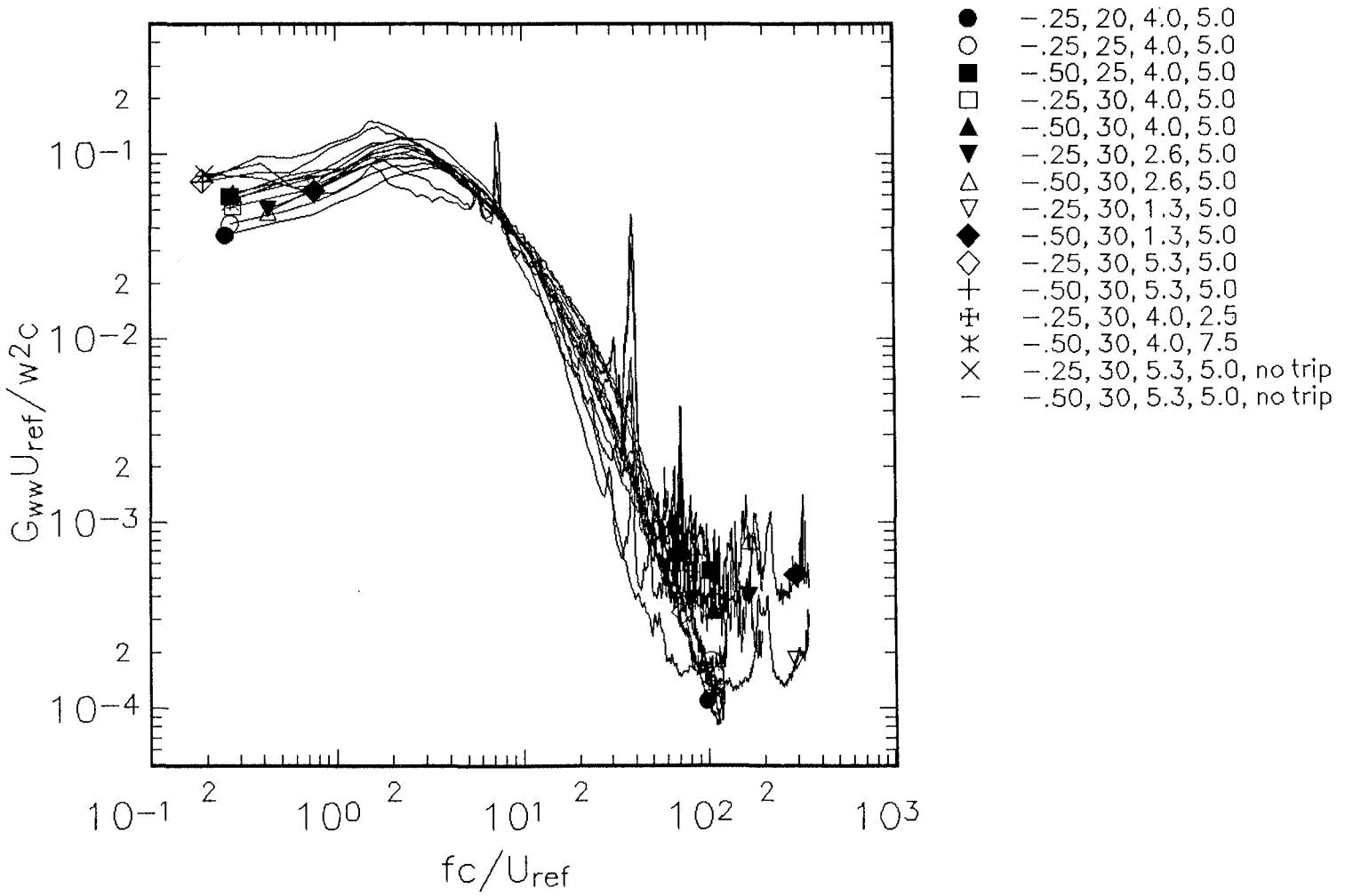

Figure 4.24(c) W component autospectra measured at all conditions in the spiral wake normalized to unit area and plotted against fc/U_{ref}.

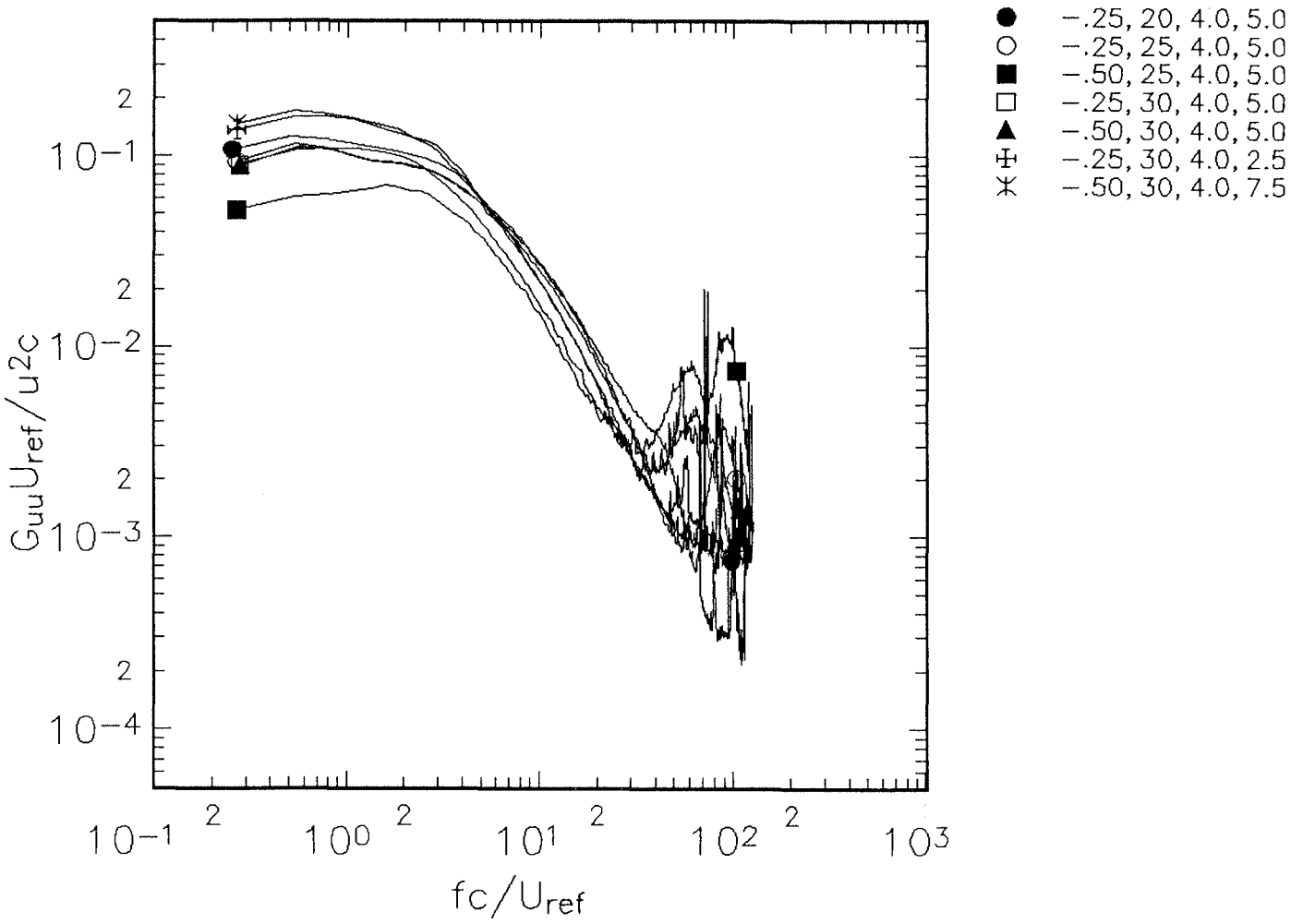

Figure 4.25(a) U component autospectra measured at Re_c=400000 in the spiral wake normalized to unit area and plotted against fc/U_{ref}.

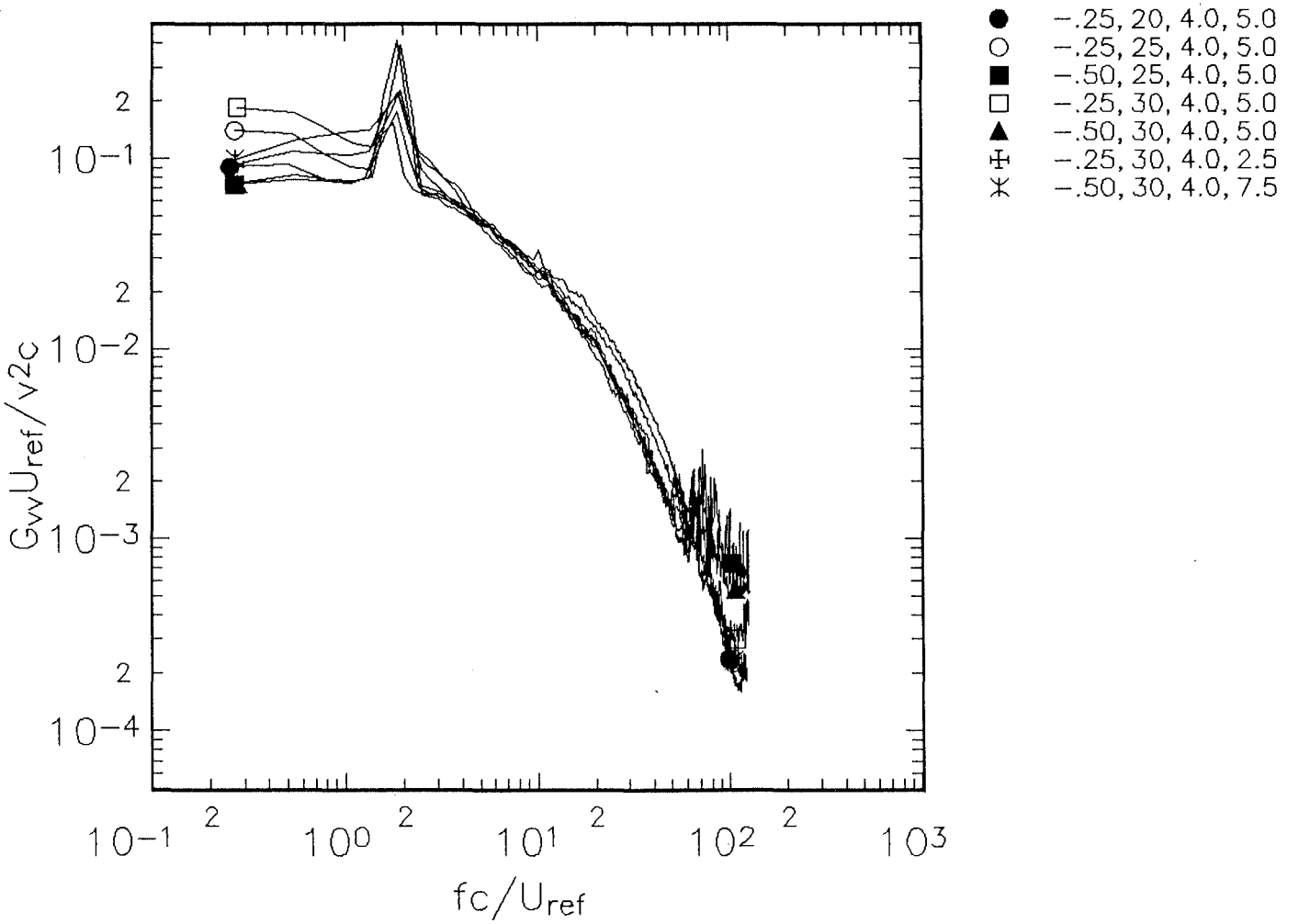

Figure 4.25(b) V component autospectra measured at Re_c=400000 in the spiral wake normalized to unit area and plotted against fc/U_{ref}.

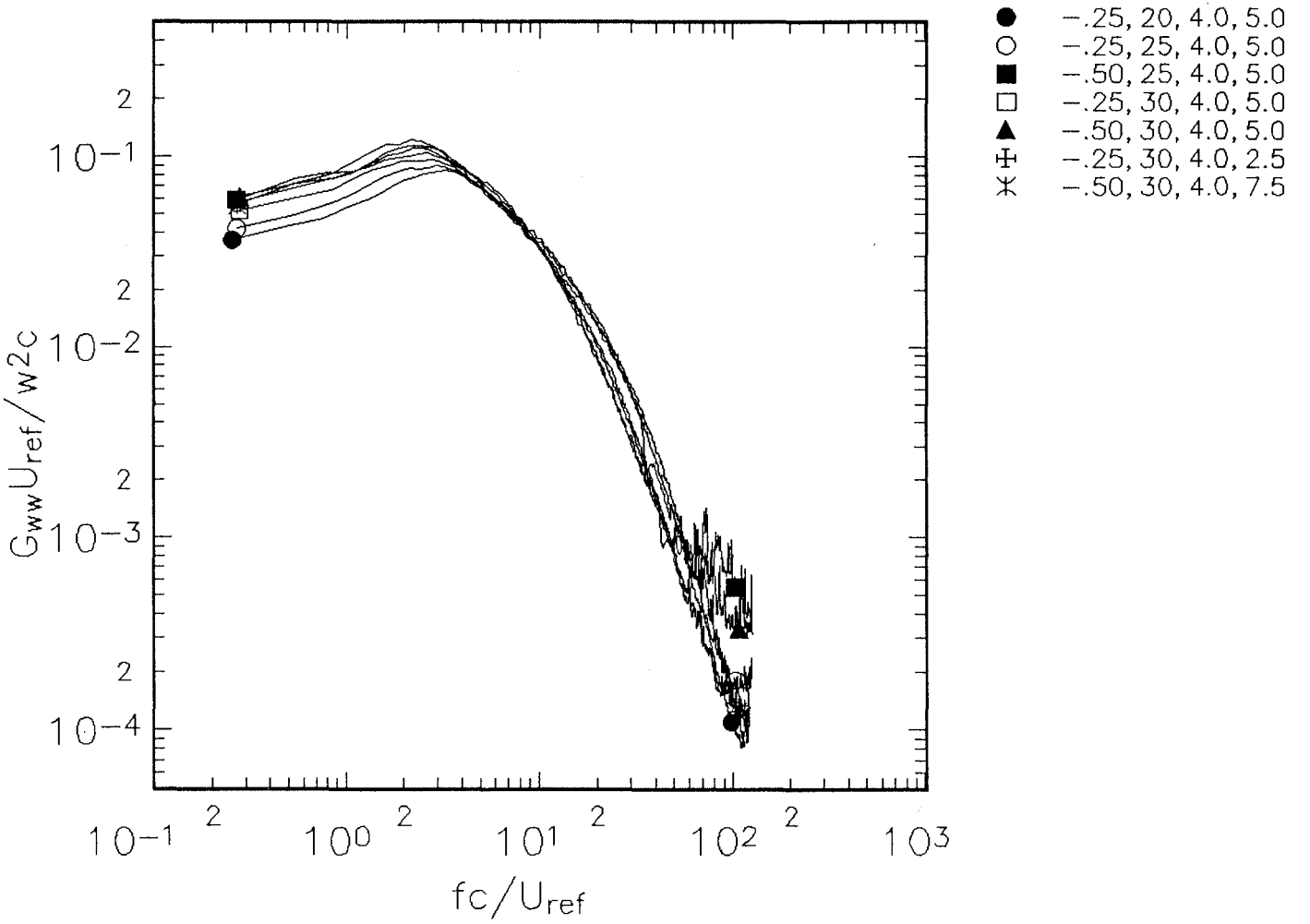

Figure 4.25(c) W component autospectra measured at Re_c=400000 in the spiral wake normalized to unit area and plotted against fc/U_{ref}.

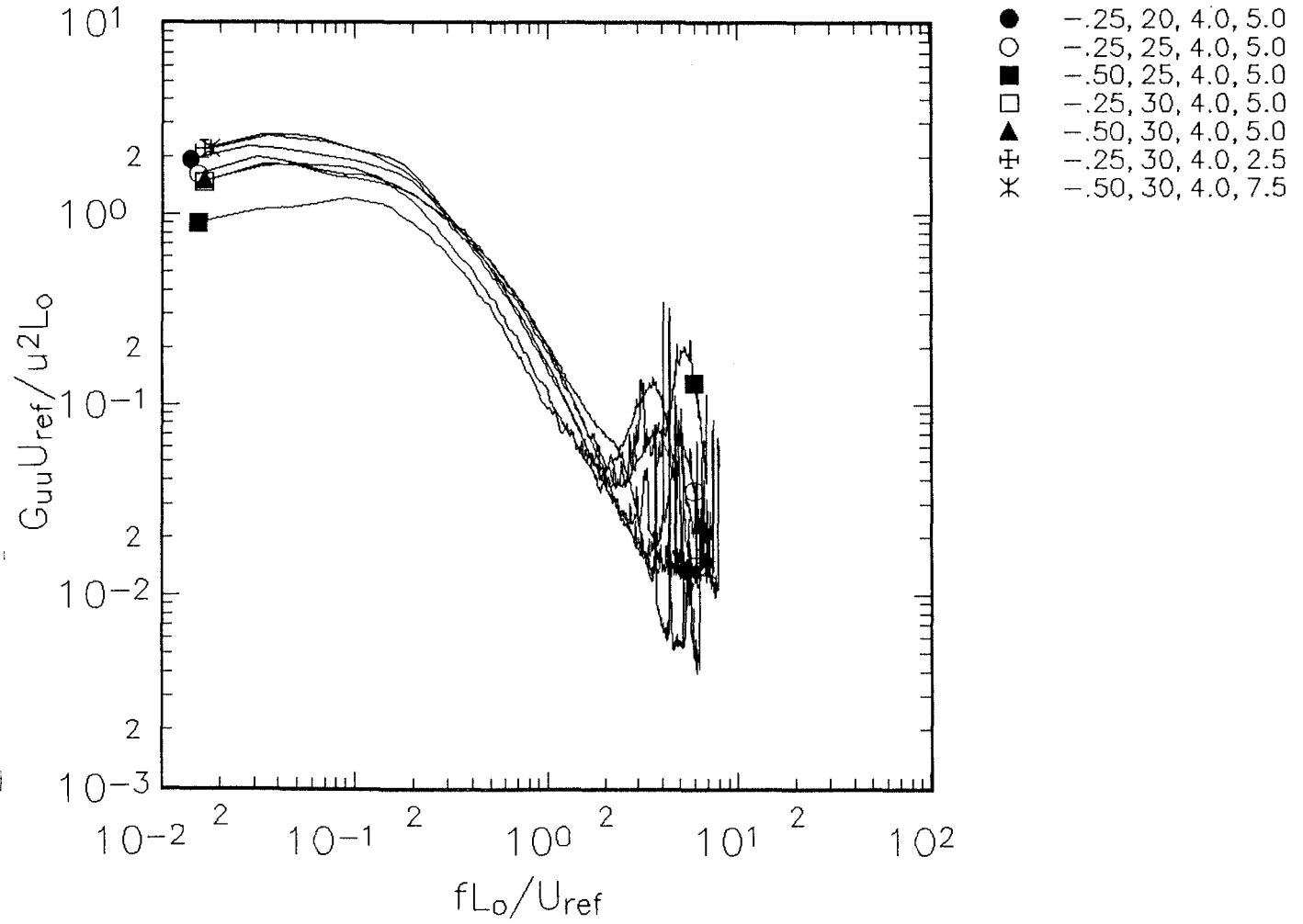

Figure 4.26(a) U component autospectra measured at Re_c=400000 in the spiral wake normalized to unit area and plotted against fL_o/U_{ref}.

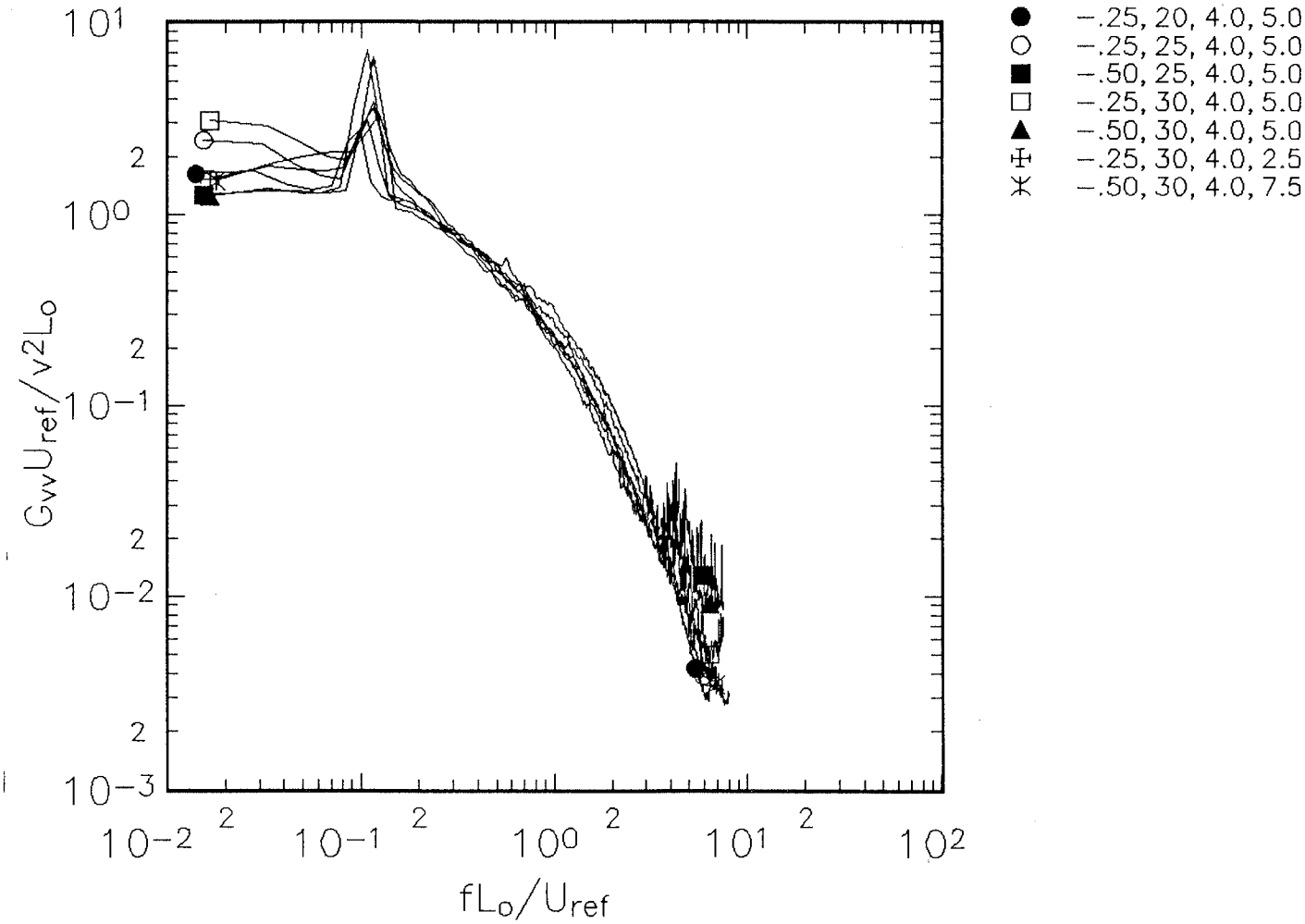

Figure 4.26(b) V component autospectra measured at Re_c=400000 in the spiral wake normalized to unit area and plotted against fL_o/U_{ref}.

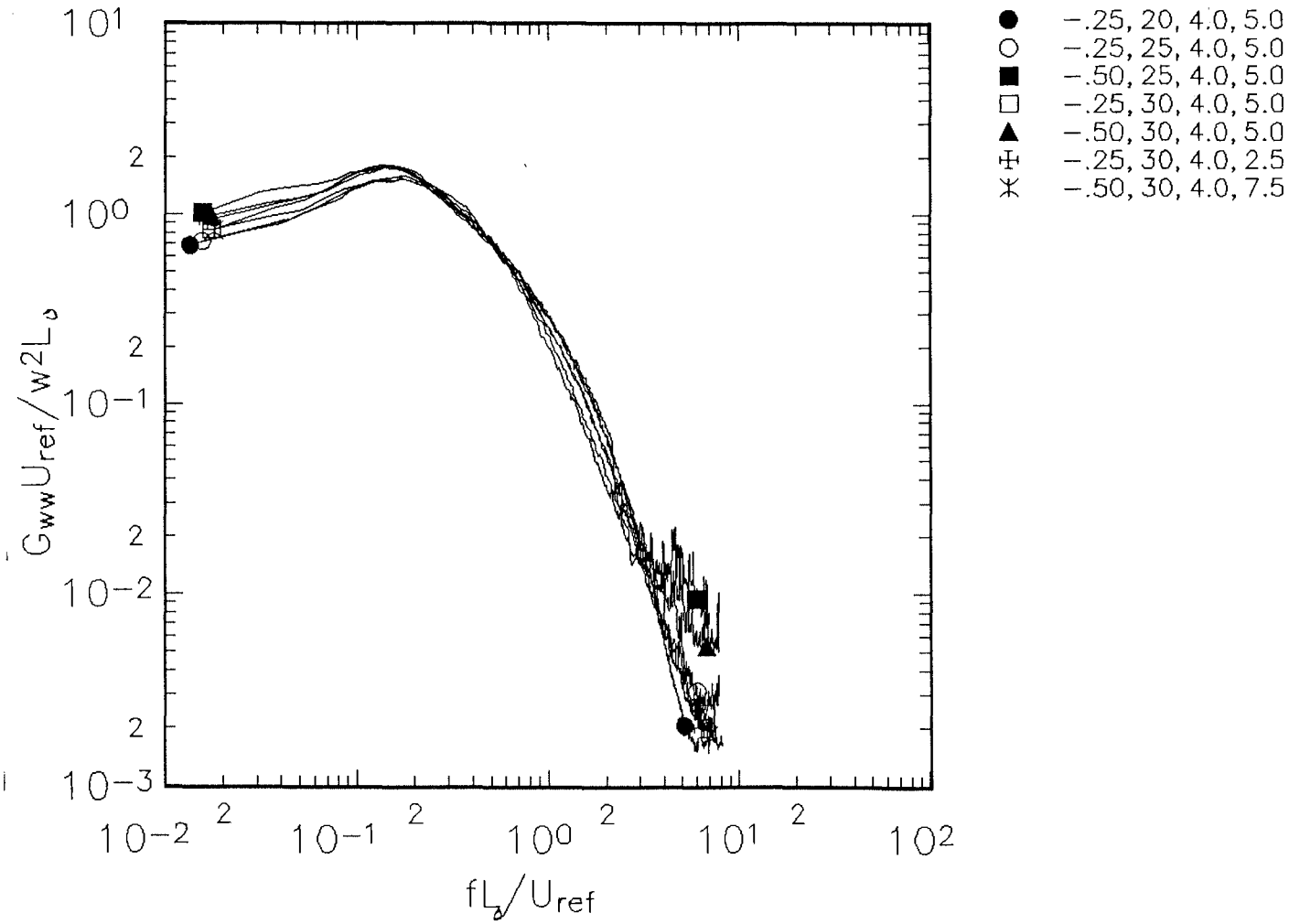

Figure 4.26(c) W component autospectra measured at Re_c=400000 conditions in the spiral wake normalized to unit area and plotted against fL_o/U_{ref}.

5. CONCLUSIONS

Measurements have been performed on the tip vortex shed by a single rectangular NACA 0012 half wing placed in a wind tunnel test section. The properties of the vortex were studied for a range of angles of attack (2.5° to 7.5°) and chord Reynolds numbers (130000 to 530000). Detailed three-component velocity, turbulence and spectral measurements were made using multiple hot wires between 20 and 30 chordlengths downstream of the wing. An in depth analysis of errors present in the X-array and triple hot-wire techniques was performed, leading to the formulation and application of correction procedures for electrical noise, velocity gradient and probe misalignment effects.

The resulting velocity measurements show the flow to consist of a small axisymmetric core surrounded by a large non-axisymmetric region in which the wing wake forms a spiral around the core. In contrast to the results of previous workers, most of whom studied vortices generated by split wing configurations, there is little if any axisymmetric region of merged turbulent flow. Turbulence levels in the spiral wake decay with downstream distance. They also fall as the core is approached, presumably because of the of the transverse straining and curvature experienced by the turbulent structures here. Turbulence spectra measured in the wake are very similar in form, regardless of conditions and exact location. At most conditions true turbulence levels in and immediately adjacent to the core are very low. Velocity fluctuations, however, are intense as a consequence of coherent lateral motions of the core and possible wave motions and instabilities travelling along it. The coherent motions were found to have an r.m.s. amplitude of between .01 and .02 chordlengths, depending on conditions and location. Velocity autospectra in the core show the lateral motions to be anisotropic at very low frequencies an isotropic and mid frequencies. A large part of these motions may well be self induced.

Circulation profiles show Hoffman and Joubert's (1963) semi-logarithmic region, and in one case reveal the core to be fully turbulent. Hoffman and Joubert's theoretical arguments concerning the semi-logarithmic region and the dimensional analysis of the circulation distribution have been reexamined. Their analysis, which suggests that the

normalized circulation distribution should only be a function of the parameters $U_{ref}x/\Gamma_o$ and $U_{ref}x/\nu$, does not appear fully consistent with the present results. These suggest that the parameter $U_{ref}c/\Gamma_o$ (closely related to the angle of attack of the wing) is the primary factor affecting the mean-flow structure of the vortex, including whether or not the flow is fully turbulent. This result, which is also consistent with Hoffman and Joubert's experimental data, has profound implications for the vortex structure. It suggests that, at least over the range of conditions studied in the present experiments, the flow structure is fixed by initial conditions and does not develop significantly with streamwise distance.

REFERENCES

Baker G R, Barker S J, Bofah K K and Saffman P G, 1974, "Laser anemometer measurements of trailing vortices in water", Journal of Fluid Mechanics, vol 65, p 325-336.

Bandyopadhyay P, Stead D and Ash R, 1991, "Organized nature of a turbulent trailing vortex", AIAA Journal, vol. 29, no. 10, pp. 1627-1633.

Bearman P W, 1971, "Corrections for the effect of ambient temperature drift on hot-wire measurements in incompressible flow", DISA Information, vol. 11, pp 25-30.

Bradshaw P, 1967, "Inactive motion and pressure fluctuations in turbulent boundary layers", Journal of Fluid Mechanics", vol. 30, pt. 2, pp 241-258.

Chigier N A and Corsiglia V R, 1972, "Wind tunnel studies of wing wake turbulence", Journal of Aircraft, vol 9, p820-825.

Choi K and Simpson R L, 1987, "Some mean-velocity, turbulence, and unsteadiness characteristics of the VPI&SU Stability Wind Tunnel", Report VPI-AOE-161, VPI&SU, Blacksburg, VA.

Corsiglia V R, Schwind R G, and Chigier N A, 1973, "Rapid scanning, three-dimensional hot-wire anemometer surveys of wing-tip vortices", Journal of Aircraft, vol 10, p752.-757

Crow S C 1970, "Stability theory for a pair of trailing vortices", AIAA Journal, vol 8, p 2172-2179.

Devenport W J and Sharma G, 1991, "Far-field turbulence structure of the tip vortex shed by a single rectangular wing", Eighth Symposium on Turbulent Shear Flows.

Gasparek E, 1960, "Viscous decay of a vortex", Masters thesis, Syracuse University, NY.

Green S I and Acosta A J, 1991, "Unsteady flow in trailing vortices", Journal of Fluid Mechanics, vol 227, pp 107-134.

Hoffman E R and Joubert P N, 1963, "Turbulent line vortices", Journal of Fluid Mechanics, vol 16, pp 395.

Jorgensen F E, 1971, "Directional sensitivity of wire and fiber-film probes", Disa Information, No. 11, pp. 31-37.

Lord Kelvin, 1880, "Vibrations of a columnar vortex", Mathematical and Physical Papers, vol. 4, Cambridge University Press.

Kline S J and McClintock F A, 1953, "Describing uncertainties in single-sample experiments", Mechanical Engineering, vol. 75, pp. 3-8.

Lee H, 1980, "Mean a turbulent flow measurement in the near wake of a self-propelled submarine- and/or airship-like model at pitch or yaw", MS thesis, VPI&SU, Blacksburg, VA.

Leonard A, 1985, "Computing three-dimensional compressible flows with vortex elements", Annual Reviews of Fluid Mechanics, vol. 17, pp. 523-559.

Lundren T S and Ashurst W T, 1989, "Area-varying waves on curved vortex tubes with application to vortex breakdown", Journal of Fluid Mechanics, vol. 200, pp 283-307.

Leuchter O and Solignac J L, 1983, "Experimental investigation of the turbulence structure of vortex wakes", Proceedings of the 5th Symposium on Turbulent Shear Flows, Ithaca, NY, pp. 5.31-5.36.

Marshall J S, 1991, "A general theory of curved vortices with circular cross section and variable core area", Journal of Fluid Mechanics, vol. 229, pp 311.

Mason W H and Marchman J F, 1972, "Far-field structure of an aircraft trailing vortex, including effects of mass injection", NASA CR 62078.

Maxworthy T, Hopfinger E J and Redekopp L G, 1985, "Wave motions on vortex cores", Journal of Fluid Mechanics, vol. 151, pp 141-165.

Orloff K L, 1971, "Experimental investigation of upstream influence in a rotating flowfield", PhD thesis, University of California, Santa Barbara.

Phillips W R C and Graham J A H, 1984, "Reynolds stress measurements in a turbulent trailing vortex", Journal of Fluid Mechanics, vol 147, pp 353-371.

Reynolds G A, 1979, "Experiments on the stability of the Blasius boundary layer", MS thesis, VPI&SU, Blacksburg, VA.

Sarpkaya T, 1992, "Three dimensional interactions of vortices with a free surface", AIAA 30th Aerospace Sciences Meeting, Jan 6-9, Reno, NV. Paper AIAA-92-0059.

Singh P I and Uberoi M S, 1976, "Experiments on vortex stability", Physics of Fluids, vol 19, p 1858-1863.

Stifle K E and Panton R L, "Experiments concerning the theories of vortex_breakdown", AIAA 29th Aerospace Sciences Meeting, Reno, NV, Jan 6-9. Paper AIAA-91-0736.

Wygnanski I, Champagne F and Marasli B, "On the large scale structures in two-dimensional small-deficit turbulent wakes", Journal of Fluid Mechanics, vol 168, pp 31-71, 1986.

Zsoldos J S, 1992, "An experimental investigation of the interaction of wing-tip vortex pairs", MS thesis, VPI&SU.

Zsoldos J S and Devenport W J, 1991, "Flow visualization of interacting wing-tip vortex pairs", Report VPI-AOE-177, AOE Dept., VPI&SU, Blacksburg, VA.

APPENDIX: ERRORS AND CORRECTIONS IN HOT-WIRE MEASUREMENTS

Measurements made with cross and triple hot-wire probes are subject to a number of bias errors and uncertainties. The purpose of this appendix is to describe these and some related correction procedures. For a discussion of quad hot-wire errors see Zsoldos (1992).

As an example of the effects of some of the errors, figure A.1 compares mean velocity and turbulence stress profiles measured through the vortex with the cross and triple-wire probes in the baseline case (Re_c=400000, α=5°, x/c=30). These data have been corrected only for the effects of electrical noise (described below). This comparison is typical of other conditions. While agreement between the two sets of results is good at most points, there are some significant differences. Most of these are in the core region. Here, U/U_{ref} is about 7.5% smaller for the triple-wire than the cross-wire (figure A.1a). The V/U_{ref} profile measured with the triple wire is asymmetric showing higher tangential velocities on the negative than on the positive z side. The triple wire $\overline{w^2}/U_{ref}^2$ profile appears slightly off center, shifted about 0.01c in the positive z direction (figure A.1b). Those of $-\overline{uv}/U_{ref}^2$ and $-\overline{uw}/U_{ref}^2$ have quite different shapes than for the cross hot wire (figure A.1c). In the spiral wake there are also some differences in the shapes of the minor shear stress ($-\overline{vw}/U_{ref}^2$ and $-uv/U_{ref}^2$) profiles measured with the two techniques (e.g. near z/c=0.7).

A.1 Bias Errors

A.1.1 Electrical noise

During a measurement electrical noise in the anemometer bridges and amplifiers appears like a velocity fluctuation. It has little effect on mean velocities but alters the measured turbulence stresses and produces spurious features in velocity spectra. Noise is only important if it produces apparent velocity fluctuations comparable to or larger than the real fluctuations. Thus in the single hot-wire measurements made in the near-wake of the wing (section 3.2), where turbulence levels were relatively large, it had a negligible effect. However, it was significant in the cross and triple hot-wire measurements made in the wing

wake surrounding the vortex between x/c=20 and 30.

There is little that can be done about spectral features generated by the noise (other than pointing them out). Turbulence stresses, however, may be corrected simply by subtracting out contributions produced by the noise, these contributions being determined from measurements made in the free stream where, in the present work, the true velocity fluctuations were almost negligible. Strictly speaking, this correction should be performed on the mean squares and correlations of the effective cooling velocities, rather than the velocity components themselves since it is the effective velocities that are determined directly from the electrical signals. Note also that this correction assumes that the mean flow velocity does not vary greatly from its free-stream value over the range of measurements so that the slope of the velocity calibration curve can be considered constant. All velocity measurements made with the cross- triple- and quad-wire probes were corrected in this way. Before correction electrical noise produced artificial turbulence intensities in the free stream of about 0.6%.

A.1.2 Velocity gradient errors in cross-wire measurements

These errors are significant but may be analyzed and at least partly corrected. Consider the cross-wire probe shown in figure A.2. At a given roll angle ψ the mean effective velocities sensed by the two wires, their mean squares and the correlation between them are recorded. Measurements made at three or more roll angles are combined to yield all components of mean velocity and of the Reynolds stress tensor (see section 2.4.2). The equations for the mean and mean-square effective velocities are

$$\overline{U_{eff}} = \sqrt{A}\,\overline{U} + \frac{D}{2\sqrt{A}}\overline{V} + \frac{E}{2\sqrt{A}}\overline{W} \qquad (1)$$

$$\overline{u_{eff}^2} = A\overline{u^2} + \frac{D^2}{4A}\overline{v^2} + \frac{E^2}{4A}\overline{w^2} + D\overline{uv} + E\overline{uw} + \frac{DE}{2A}\overline{vw} \qquad (2)$$

The equation for the correlation is

$$\overline{u_{eff_a}u_{eff_b}} = \sqrt{A_aA_b}\,\overline{u^2} + \frac{D_aD_b}{4\sqrt{A_aA_b}}\overline{v^2} + \frac{E_aE_b}{4\sqrt{A_aA_b}}\overline{w^2} + \left(\frac{D_a}{2}\sqrt{\frac{A_a}{A_b}} + \frac{D_b}{2}\sqrt{\frac{A_b}{A_a}}\right)\overline{uv} + \left(\frac{E_b}{2}\sqrt{\frac{A_a}{A_b}} + \frac{E_a}{2}\sqrt{\frac{A_b}{A_a}}\right)\overline{uw} + \left(\frac{D_aE_b}{4\sqrt{A_aA_b}} + \frac{D_bE_a}{4\sqrt{A_aA_b}}\right)\overline{vw} \quad (3)$$

where the subscripts a and b distinguish the two sensors of the probe.

These equations and the procedure employed to solve them implicitly assume that the velocity components U, V and W have the same values at the wire locations as they do at the center of rotation 'o' , (figure A.2). This will not be the case if velocity gradients are significant. In such a situation the measured mean and mean square effective velocities and effective velocity correlation may be related to their values at 'o' through first order Taylor series expansions,

$$\overline{U_{eff_o}} = \overline{U_{eff}} + \nabla\overline{U_{eff}}\,\vec{\delta} \quad (4)$$

$$\overline{u_{eff_o}^2} = \overline{u_{eff}^2} + \nabla\overline{u_{eff}^2}\,\vec{\delta} \quad (5)$$

$$\overline{u_{eff_a}u_{eff_b}}\Big|_o = \overline{(u_{eff_a} + \nabla u_{eff_a}.\vec{\delta}_a)(u_{eff_b} + \nabla u_{eff_b}.\vec{\delta}_b)} \quad (6)$$

here $\vec{\delta}$ is a vector representing the magnitude (0.5mm) and direction of the normal distance from the wire to 'o' (see figure A.2). Note that $\vec{\delta}_a = -\vec{\delta}_b$.

Equation 6 is not useful for the purposes of correction. Expansion of its right hand side and substitution of the velocity components into the resulting correction terms produces only unknown velocity derivative correlations. The mean and mean-square velocities, however, may be corrected since the required gradients can be estimated by substituting equations 1 and 2. For example, equation 4 becomes

$$\nabla\overline{U_{eff}} = \sqrt{A}\left(\frac{\partial\overline{U}}{\partial y}\vec{j}+\frac{\partial\overline{U}}{\partial z}\vec{k}\right) + \frac{D}{2\sqrt{A}}\left(\frac{\partial\overline{V}}{\partial y}\vec{j}+\frac{\partial\overline{V}}{\partial z}\vec{k}\right) + \frac{E}{2\sqrt{A}}\left(\frac{\partial\overline{W}}{\partial y}\vec{j}+\frac{\partial\overline{W}}{\partial z}\vec{k}\right) \tag{7}$$

the x derivatives having been ignored.

To correct measurements made with the cross hot-wire probe the following procedure was followed;

(a) Calculation of mean velocity and Reynolds stress profiles from the cross-hot wire effective-velocity measurements ignoring velocity-gradient effects.

(b) z derivatives of mean velocities and stresses obtained by numerical differentiation of these profiles.

(c) y derivatives obtained by assuming flow axisymmetry.

(d) Adjustment of the measured mean and mean square effective velocities using equations 4 and 5.

(e) Re-calculation of the mean-velocity and Reynolds stress profiles.

Corrected measurements for the baseline case are shown in figure A.3. The corrections had their greatest effect on mean axial velocity measurements in the core (figure A.3a), their values being reduced by typically $2\%U_{ref}$ here. The corrections also have a noticeable effect upon the shear-stress profiles here (figure A.3c).

A.1.3 Velocity gradient errors in triple-wire measurements

These may also be corrected to a degree. Consider the triple-wire probe shown in figure A.4. Viewed end on the three orthogonal sensors of this probe form an equilateral triangle. As described in chapter 2, the effective velocities experienced by the three sensors may be related to the velocity components in a coordinate system aligned with the sensors by inverting the equations

$$\begin{pmatrix} U_{eff_1}^2 \\ U_{eff_2}^2 \\ U_{eff_3}^2 \end{pmatrix} = \begin{pmatrix} k^2 & 1 & h^2 \\ h^2 & k^2 & 1 \\ 1 & h^2 & k^2 \end{pmatrix} \cdot \begin{pmatrix} U_s^2 \\ V_s^2 \\ W_s^2 \end{pmatrix} \tag{8}$$

which gives

$$\begin{pmatrix} U_s^2 \\ V_s^2 \\ W_s^2 \end{pmatrix} = \frac{1}{D} \begin{pmatrix} k^4-h^2 & h^4-k^2 & 1-h^2k^2 \\ 1-k^2h^2 & k^4-h^2 & h^4-k^2 \\ h^4-k^2 & 1-k^2h^2 & k^4-h^2 \end{pmatrix} \cdot \begin{pmatrix} U_{eff_1}^2 \\ U_{eff_2}^2 \\ U_{eff_3}^2 \end{pmatrix} \tag{9}$$

where $D = 1-3k^2h^2+h^6+k^6$. These relations implicitly assume that the three velocity components have the same values at the wire locations as at the centroid of the measurement volume 'o' (figure A.4). If they do not then the velocity components at 'o' may be expressed as

$$\begin{pmatrix} U_s^2 \\ V_s^2 \\ W_s^2 \end{pmatrix} = \frac{1}{D}\begin{pmatrix} k^4-h^2 & h^4-k^2 & 1-h^2k^2 \\ 1-k^2h^2 & k^4-h^2 & h^4-k^2 \\ h^4-k^2 & 1-k^2h^2 & k^4-h^2 \end{pmatrix}.\begin{pmatrix} U_{eff_1}^2+\nabla U_{eff_1}^2.\vec{\delta}_1 \\ U_{eff_2}^2+\nabla U_{eff_2}^2.\vec{\delta}_2 \\ U_{eff_3}^2+\nabla U_{eff_3}^2.\vec{\delta}_3 \end{pmatrix} \quad (10)$$

or

$$\begin{pmatrix} U_s^2 \\ V_s^2 \\ W_s^2 \end{pmatrix} = \begin{pmatrix} U_s^2 \\ V_s^2 \\ W_s^2 \end{pmatrix}_m + \frac{1}{D}\begin{pmatrix} k^4-h^2 & h^4-k^2 & 1-h^2k^2 \\ 1-k^2h^2 & k^4-h^2 & h^4-k^2 \\ h^4-k^2 & 1-k^2h^2 & k^4-h^2 \end{pmatrix}.\begin{pmatrix} \nabla U_{eff_1}^2.\vec{\delta}_1 \\ \nabla U_{eff_2}^2.\vec{\delta}_2 \\ \nabla U_{eff_3}^2.\vec{\delta}_3 \end{pmatrix} \quad (11)$$

Where subscript 'm' refers to the measured values ignoring gradient effects and $\vec{\delta}$ is a vector representing the magnitude (0.71mm) and direction of the normal distance from each of the wires to 'o' (see figure A.4). We may obtain expressions for the gradients of effective velocity squared by substituting equation 8. This gives, for example,

$$\nabla U_{eff_1}^2 = 2V_s\nabla V_s + 2k^2U_s\nabla U_s + 2h^2W_s\nabla W_s \quad (12)$$

Since $k^2 << h^2$ and $k^2 << 1$ terms multiplied by k^2 may be neglected. Substituting the resulting expressions back into equation 11, we obtain, for example,

$$U_s^2 = U_{s_m}^2 + \left(2V_s\nabla V_s + 2h^2 W_s \nabla W_s\right).\vec{\delta}_1(k^4 - h^2)/D + \left(2W_s\nabla W_s + 2h^2 U_s \nabla U_s\right).\vec{\delta}_2(h^4 - k^2)/D + \left(2U_s\nabla U_s + 2h^2 V_s \nabla V_s\right).\vec{\delta}_3(1 - h^2k^2)/D \quad (13)$$

Splitting the velocity components into their mean and fluctuating parts, taking the square root, neglecting second order terms and finally recombining the means and fluctuations leads to

$$U_s = U_{s_m} + \frac{1}{D\overline{U}_s}\left[\overline{U}_s\nabla U_{s'}.(\vec{\delta}_3 + h^6\vec{\delta}_2) + h^2\overline{V}_s\nabla V_{s'}.(\vec{\delta}_3 - \vec{\delta}_1) + h^4\overline{W}_s\nabla W_{s'}.(\vec{\delta}_2 - \vec{\delta}_1)\right] \quad (14)$$

$$V_s = V_{s_m} + \frac{1}{D\overline{V}_s}\left[h^4\overline{U}_s\nabla U_{s'}.(\vec{\delta}_3 - \vec{\delta}_2) + \overline{V}_s\nabla V_{s'}.(\vec{\delta}_1 + h^6\vec{\delta}_3) + h^2\overline{W}_s\nabla W_{s'}.(\vec{\delta}_1 - \vec{\delta}_2)\right] \quad (15)$$

$$W_s = W_{s_m} + \frac{1}{D\overline{W}_s}\left[h^2\overline{U}_s\nabla U_{s'}.(\vec{\delta}_2 - \vec{\delta}_3) + h^4\overline{V}_s\nabla V_{s'}.(\vec{\delta}_1 - \vec{\delta}_3) + \overline{W}_s\nabla W_{s'}.(\vec{\delta}_2 + h^6\vec{\delta}_1)\right] \quad (16)$$

To obtain corrections for the mean velocity components we simply average these equations, which does not change their form. Corrections for the normal and shear turbulence stresses in the wire coordinate system may be obtained by squaring or multiplying and then averaging these equations. This gives some terms which may be estimated but some, involving correlations of velocity derivatives, which may not. Ignoring the latter leaves,

$$\overline{u_s^2} = \overline{u_{s\,m}^2} + \nabla\overline{u_s^2}.(\vec{\delta}_3 + h^6\vec{\delta}_2)/D \quad (17)$$

$$\overline{v_s^2} = \overline{v_{s_m}^2} + \nabla\overline{v_s^2}.(\vec{\delta}_1 + h^6\vec{\delta}_3)/D \tag{18}$$

$$\overline{w_s^2} = \overline{w_{s_m}^2} + \nabla\overline{w_s^2}.(\vec{\delta}_2 + h^6\vec{\delta}_1)/D \tag{19}$$

$$\overline{u_s v_s} = \overline{u_s v_{s_m}} + \frac{h^4\overline{U_s}}{2D\overline{V_s}}\nabla\overline{u_s^2}.(\vec{\delta}_3 - \vec{\delta}_2) + \frac{h^2\overline{V_s}}{2D\overline{U_s}}\nabla\overline{v_s^2}.(\vec{\delta}_3 - \vec{\delta}_1) \tag{20}$$

$$\overline{v_s w_s} = \overline{v_s w_{s_m}} + \frac{h^4\overline{V_s}}{2D\overline{W_s}}\nabla\overline{v_s^2}.(\vec{\delta}_1 - \vec{\delta}_3) + \frac{h^2\overline{W_s}}{2D\overline{V_s}}\nabla\overline{w_s^2}.(\vec{\delta}_1 - \vec{\delta}_2) \tag{21}$$

$$\overline{u_s w_s} = \overline{u_s w_{s_m}} + \frac{h^4\overline{W_s}}{2D\overline{U_s}}\nabla\overline{w_s^2}.(\vec{\delta}_2 - \vec{\delta}_1) + \frac{h^2\overline{U_s}}{2D\overline{W_s}}\nabla\overline{u_s^2}.(\vec{\delta}_2 - \vec{\delta}_3) \tag{22}$$

To use these equations the z and y derivatives of the mean velocity and stress components were estimated from uncorrected data in the manner as for the cross wire (see above).

Corrected triple wire mean-velocity measurements for the baseline case are presented alongside corrected cross-wire data in figure A.3. The axial velocity correction is substantial, amounting to about $+3\%U_{ref}$ at the core center and greatly improving the agreement between the two techniques. An slight increase is also seen in the magnitude of V component, though this does not remove the asymmetry across the core. The corrections have at most small effects on the normal stresses. In the shear stresses, gradient correction appears to have improved somewhat the agreement between the $-\overline{u\,v}$ profiles.

The large effect of the corrections on the axial mean velocity measured with the triple wire may be understood physically with reference to figure A.4. Suppose the probe shown here were placed with its centroid at the middle of an axial vortex core in which the fluid is rotating in a clockwise direction. Although at the centroid there is no tangential velocity, a tangential velocity is felt at the wire locations. This has the effect of reducing equally the effective velocity sensed by each of the wires thereby lowering the measured value of the axial velocity. Applying equations 14 through 16 to this situation, and taking h as unity we obtain,

$$U = U_m - \frac{\delta}{D}\left(\frac{\partial V}{\partial z} - \frac{\partial W}{\partial y}\right) \tag{23}$$

i.e. the measured axial velocity is increased by an amount proportional to the axial vorticity, which in this example is negative.

A.1.4 Probe misalignment during calibration

Calibration misalignment refers to a difference between the presumed flow direction and the actual direction during velocity calibration of the hot-wire probe. The sensors of the cross and triple wire probes were calibrated simultaneously for velocity by placing them in the free stream, aligning the probe stem approximately with the flow direction, and varying the flow velocity. For such a calibration to be accurate one must know accurately the ratio between the effective velocity experienced by each sensor and the flow velocity, in effect the orientation of each sensor relative to the flow. With the cross wire this orientation could be determined at the time of calibration by rolling the sensors of this probe through 180°. Calibration misalignment was therefore not a problem with this probe. With the triple wire, however, ratios of the effective to flow velocities were measured at the start of the experiments after first calibrating the triple-wire sensors separately with their axes normal to the flow. Anemometer drift during this initial measurement or subsequent settling of the traverse gear could therefore have caused calibration misalignment errors in measurements made with this probe. Another factor may have been variations in the free-stream flow

direction since triple-wire calibrations were not always made at the same absolute y and z locations.

These errors may be corrected using the following procedure, which is somewhat similar to that used to correct gradient errors. We begin with the equations for the velocity components in wire coordinates in terms of the effective velocities.

$$\begin{pmatrix} U_s^2 \\ V_s^2 \\ W_s^2 \end{pmatrix} = \mathbf{A}.\begin{pmatrix} U_{eff_1}^2 \\ U_{eff_2}^2 \\ U_{eff_3}^2 \end{pmatrix} \tag{24}$$

Where **A** represents the coefficient matrix in equation 9. If, during velocity calibration, the effective velocity experienced by each sensor differs slightly from its assumed value then we shall have,

$$\begin{pmatrix} U_s^2 \\ V_s^2 \\ W_s^2 \end{pmatrix} = \mathbf{A}.\begin{pmatrix} U_{eff_1}^2(1+\epsilon_1) \\ U_{eff_2}^2(1+\epsilon_2) \\ U_{eff_3}^2(1+\epsilon_3) \end{pmatrix} \tag{25}$$

where $\epsilon \ll 1$. Alternatively we may write

$$\begin{pmatrix} U_s^2 \\ V_s^2 \\ W_s^2 \end{pmatrix} = \begin{pmatrix} U_s^2 \\ V_s^2 \\ W_s^2 \end{pmatrix}_m + \mathbf{A}. \begin{pmatrix} U_{eff_1}^2 \epsilon_1 \\ U_{eff_2}^2 \epsilon_2 \\ U_{eff_3}^2 \epsilon_3 \end{pmatrix} \tag{26}$$

where subscript 'm' identifies the erroneous values measured as a result of the misalignment. Manipulating these equations in the same manner as was done for the velocity gradient corrections gives the following expressions, which ignore second order terms.

$$\overline{U_s} - \overline{U_{s_m}} = \frac{p_{11}}{2}\overline{U_{s_m}} + \frac{p_{12}}{2}\frac{\overline{V_{s\,m}^2}}{\overline{U_{s_m}}} + \frac{p_{13}}{2}\frac{\overline{W_{s\,m}^2}}{\overline{U_{s_m}}} \tag{27}$$

$$\overline{V_s} - \overline{V_{s_m}} = \frac{p_{21}}{2}\frac{\overline{U_{s\,m}^2}}{\overline{V_{s_m}}} + \frac{p_{22}}{2}\overline{V_{s_m}} + \frac{p_{23}}{2}\frac{\overline{W_{s\,m}^2}}{\overline{V_{s_m}}} \tag{28}$$

$$\overline{W_s} - \overline{W_{s_m}} = \frac{p_{31}}{2}\frac{\overline{U_{s\,m}^2}}{\overline{W_{s_m}}} + \frac{p_{32}}{2}\frac{\overline{V_{s\,m}^2}}{\overline{W_{s_m}}} + \frac{p_{33}}{2}\overline{W_{s_m}} \tag{29}$$

$$\overline{u_s^2} - \overline{u_{s_m}^2} = 2p_{11}\overline{u_{s_m}^2} + 2p_{12}\frac{\overline{V_{s_m}}}{\overline{U_{s_m}}}\overline{u_{s_m}v_{s_m}} + 2p_{13}\frac{\overline{W_{s_m}}}{\overline{U_{s_m}}}\overline{u_{s_m}w_{s_m}} \tag{30}$$

$$\overline{v_s^2} - \overline{v_{s_m}^2} = 2p_{21}\frac{\overline{U_{s_m}}}{\overline{V_{s_m}}}\overline{u_{s_m}v_{s_m}} + 2p_{22}\overline{v_{s_m}^2} + 2p_{23}\frac{\overline{W_{s_m}}}{\overline{V_{s_m}}}\overline{v_{s_m}w_{s_m}} \tag{31}$$

$$\overline{w_s^2} - \overline{w_{s_m}^2} = 2p_{31}\frac{\overline{U_{s_m}}}{\overline{W_{s_m}}}\overline{u_{s_m}w_{s_m}} + 2p_{32}\frac{\overline{V_{s_m}}}{\overline{W_{s_m}}}\overline{v_{s_m}w_{s_m}} + 2p_{33}\overline{w_{s_m}^2} \tag{32}$$

$$\begin{aligned}\overline{u_s v_s} - \overline{u_{s_m} v_{s_m}} = {} & p_{21}\frac{\overline{U_{s_m}}}{\overline{V_{s_m}}}\overline{u_{s_m}^2} + p_{12}\frac{\overline{V_{s_m}}}{\overline{U_{s_m}}}\overline{v_{s_m}^2} + (p_{11}+p_{22})\overline{u_{s_m}v_{s_m}} + \\ & p_{13}\frac{\overline{W_{s_m}}}{\overline{U_{s_m}}}\overline{v_{s_m}w_{s_m}} + p_{23}\frac{\overline{W_{s_m}}}{\overline{V_{s_m}}}\overline{u_{s_m}w_{s_m}}\end{aligned} \tag{33}$$

$$\overline{v_s w_s} - \overline{v_{s_m} w_{s_m}} = p_{32} \frac{\overline{V_{s_m}}}{\overline{W_{s_m}}} \overline{v_s^2}_m + p_{23} \frac{\overline{W_{s_m}}}{\overline{V_{s_m}}} \overline{w_s^2}_m + (p_{33} + p_{22}) \overline{v_{s_m} w_{s_m}} + p_{21} \frac{\overline{U_{s_m}}}{\overline{V_{s_m}}} \overline{u_{s_m} w_{s_m}} + p_{31} \frac{\overline{U_{s_m}}}{\overline{W_{s_m}}} \overline{u_{s_m} v_{s_m}} \tag{34}$$

$$\overline{u_s w_s} - \overline{u_{s_m} w_{s_m}} = p_{31} \frac{\overline{U_{s_m}}}{\overline{W_{s_m}}} \overline{u_s^2}_m + p_{13} \frac{\overline{W_{s_m}}}{\overline{U_{s_m}}} \overline{w_s^2}_m + (p_{11} + p_{33}) \overline{u_{s_m} w_{s_m}} + p_{12} \frac{\overline{V_{s_m}}}{\overline{U_{s_m}}} \overline{v_{s_m} w_{s_m}} + p_{32} \frac{\overline{V_{s_m}}}{\overline{W_{s_m}}} \overline{u_{s_m} v_{s_m}} \tag{35}$$

where

$$p_{ij} = \sum_{k=1}^{3} a_{ik} b_{kj} \epsilon_k \tag{36}$$

and 'a' and 'b' refer to the elements of **A** and **B**.

Comparisons between the cross and triple-wire measurements made after the experiments and examinations of the triple-wire measurements made in the free stream strongly suggested that the triple wire was misaligned consistently during calibrations, by about 1° in pitch and 0.4° in yaw. Corrections, deduced from equations 27 through 36, were therefore applied to these data.

Figure A.5 compares the final corrected measurements. This correction has benefitted

primarily the triple-wire V-component profiles which are much less asymmetric than before. It has also improved the agreement between the $-\overline{uw}$ and $-\overline{uv}$ shear stress profiles in the core region and the spiral wake (figure A.5c).

A.1.5 Remaining differences

Despite the above corrections some consistent differences remained between the cross and triple-wire data sets. These are listed below.

(a) Differences in the mean axial velocity distribution in the core center. Typically the corrected cross-wire measurements lie 2% above the triple wire results.

(b) Differences in the $\overline{v^2}$ magnitudes in the positive z arm of the spiral wake. As in figure A.5(b), at z/c=0.75, the triple-wire measurements appear consistently low here, by about 15%.

(c) Differences in the position of the peak in the $\overline{v^2}$, $\overline{w^2}$ and $\overline{vw}$ profiles in the core center. Generally, measured with the triple wire these peaks appear off center, shifted slightly in the positive z direction.

(d) Differences in the $\overline{u^2}$ profiles near the edge of the core region. These, illustrated for the baseline case in figure A.5, appear both more and less serious at other conditions. Generally, measurements of $\overline{u^2}$ near the edge of the core appear a little larger with the triple than the cross hot-wire.

(e) Different shapes in the profiles of $\overline{uv}$ and $\overline{vw}$ (the minor stresses) in the spiral shear layer. The differences in figure A.5c are fairly typical of all other cases.

(f) Different shapes in the profiles of $\overline{uw}$ in the core region.

All these remaining differences, except perhaps (b), appear consistent with residual errors in the corrected triple wire measurements due to velocity gradients across this probe. Velocity gradient errors would have been greatest with the triple wire because of its larger measurement volume size (.012c compared to .05c for the cross wire). Furthermore velocity gradient corrections for the mean velocities were exact for the cross wire but ignored second order terms for the triple wire. Thus the mean axial velocities measured with the cross-wire probe are more reliable. The ignored second order terms may well have been significant in

the highly unsteady flow near the center of the core. Presumably the neglected second order and gradient correlation terms in the triple wire corrections are responsible for the remaining differences in the turbulence stresses

A.2 Uncertainties

Tables A.1 and A.2 list uncertainty estimates for the cross and triple-wire measurements calculated for 95% confidence limits using the method of Kline and McClintock (1953). The following sources of uncertainty are included in these estimates.

(a) Limited numbers of samples taken to form averages.

(b) Calibration drift.

(c) Sensor angles.

(c) Probe angle (pitch, yaw, roll).

(d) Pitch and yaw sensitivities.

The following are not included.

(a) Limited sampling period.

(b) Neglected terms or uncertainties in correction procedures described above.

(c) Any non-repeatability or probe sensitivity in the flow (thought to be negligible).

(d) Any eccentricity in the cross-wire roll mechanism (also thought to be negligible).

It is worth noting that uncertainties due to limited sampling period may have been significant if not dominant in some cross-wire turbulence-stress measurements made in the core region. The turbulence stresses were calculated from measurements made at a number of roll angles, the assumption being that the measurements were made for long enough at each roll angle for them to be statistically stationary. Bearing in mind the very low frequency lateral vortex motions it is possible that this assumption was not always justified.

	Wake region		Core edge		Core center	
Quantity	Value	Uncert.	Value	Uncert.	Value	Uncert.
U/U_e	9.8×10^{-1}	8.6×10^{-3}	9.3×10^{-1}	1.2×10^{-2}	8.7×10^{-1}	7.9×10^{-3}
V/U_e	-3.5×10^{-2}	1.7×10^{-2}	-2.2×10^{-1}	1.7×10^{-2}	-6.4×10^{-2}	1.5×10^{-2}
W/U_e	2.2×10^{-2}	1.3×10^{-3}	-1.1×10^{-2}	7.9×10^{-3}	-1.2×10^{-2}	2.3×10^{-3}
$\overline{u^2}/U_e^2$	8.9×10^{-5}	1.6×10^{-6}	2.5×10^{-4}	4.4×10^{-6}	9.7×10^{-4}	1.7×10^{-5}
$\overline{v^2}/U_e^2$	6.0×10^{-5}	3.4×10^{-6}	5.4×10^{-4}	5.7×10^{-5}	1.2×10^{-2}	7.9×10^{-4}
$\overline{w^2}/U_e^2$	1.3×10^{-4}	7.0×10^{-6}	3.7×10^{-3}	2.1×10^{-4}	1.9×10^{-2}	1.1×10^{-3}
$\overline{uv}/U_e^2$	-3.3×10^{-6}	1.5×10^{-6}	2.1×10^{-4}	3.3×10^{-5}	-5.8×10^{-4}	1.8×10^{-4}
$\overline{vw}/U_e^2$	-5.3×10^{-6}	2.5×10^{-6}	-1.5×10^{-4}	1.1×10^{-4}	-5.9×10^{-3}	4.1×10^{-4}
$\overline{uw}/U_e^2$	3.7×10^{-5}	7.5×10^{-7}	3.8×10^{-4}	1.8×10^{-5}	5.3×10^{-4}	1.2×10^{-4}

Table A.1 Typical uncertainties in measurements made with the X-array hot-wire probe.

	Wake region		Core edge		Core center	
Quantity	Value	Uncert.	Value	Uncert.	Value	Uncert.
U/U_e	9.8×10^{-1}	1.3×10^{-2}	9.2×10^{-1}	1.3×10^{-2}	8.5×10^{-1}	1.2×10^{-2}
V/U_e	-3.5×10^{-2}	2.0×10^{-2}	-2.2×10^{-1}	1.7×10^{-2}	1.1×10^{-2}	1.9×10^{-2}
W/U_e	4.8×10^{-3}	2.1×10^{-2}	1.4×10^{-2}	2.8×10^{-2}	-2.3×10^{-2}	1.8×10^{-2}
$\overline{u^2}/U_e^2$	8.0×10^{-5}	3.4×10^{-6}	4.9×10^{-4}	2.0×10^{-5}	1.2×10^{-3}	4.5×10^{-5}
$\overline{v^2}/U_e^2$	4.6×10^{-5}	2.2×10^{-6}	1.2×10^{-4}	2.9×10^{-5}	1.0×10^{-2}	5.9×10^{-4}
$\overline{w^2}/U_e^2$	1.4×10^{-4}	7.5×10^{-6}	5.9×10^{-3}	2.6×10^{-4}	1.8×10^{-2}	8.6×10^{-4}
$\overline{uv}/U_e^2$	-5.4×10^{-6}	3.5×10^{-6}	1.8×10^{-4}	2.0×10^{-5}	-3.3×10^{-4}	1.4×10^{-4}
$\overline{vw}/U_e^2$	-1.2×10^{-5}	4.3×10^{-6}	-4.7×10^{-4}	2.1×10^{-4}	-5.2×10^{-3}	5.0×10^{-4}
$\overline{uw}/U_e^2$	3.8×10^{-5}	4.7×10^{-6}	-9.7×10^{-5}	5.1×10^{-5}	-6.9×10^{-4}	2.1×10^{-4}

Table A.2 Typical uncertainties in measurements made with the triple hot-wire probe.

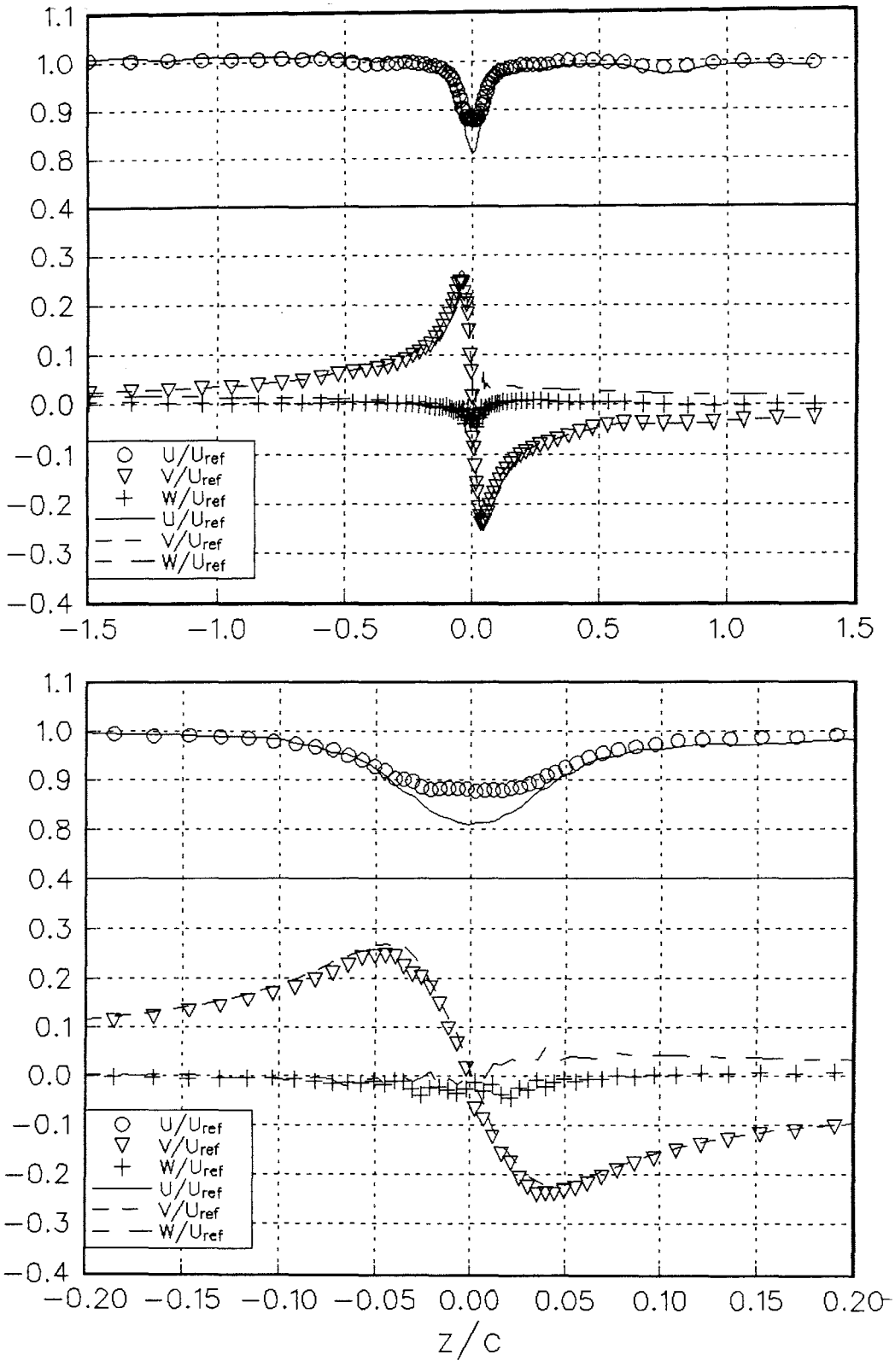

(a) Mean velocities

Figure A-1 Comparison of cross- and triple hot-wire measurements in the baseline case after correction for electrical noise only. Symbols - cross hot-wire, lines - triple hot-wire.

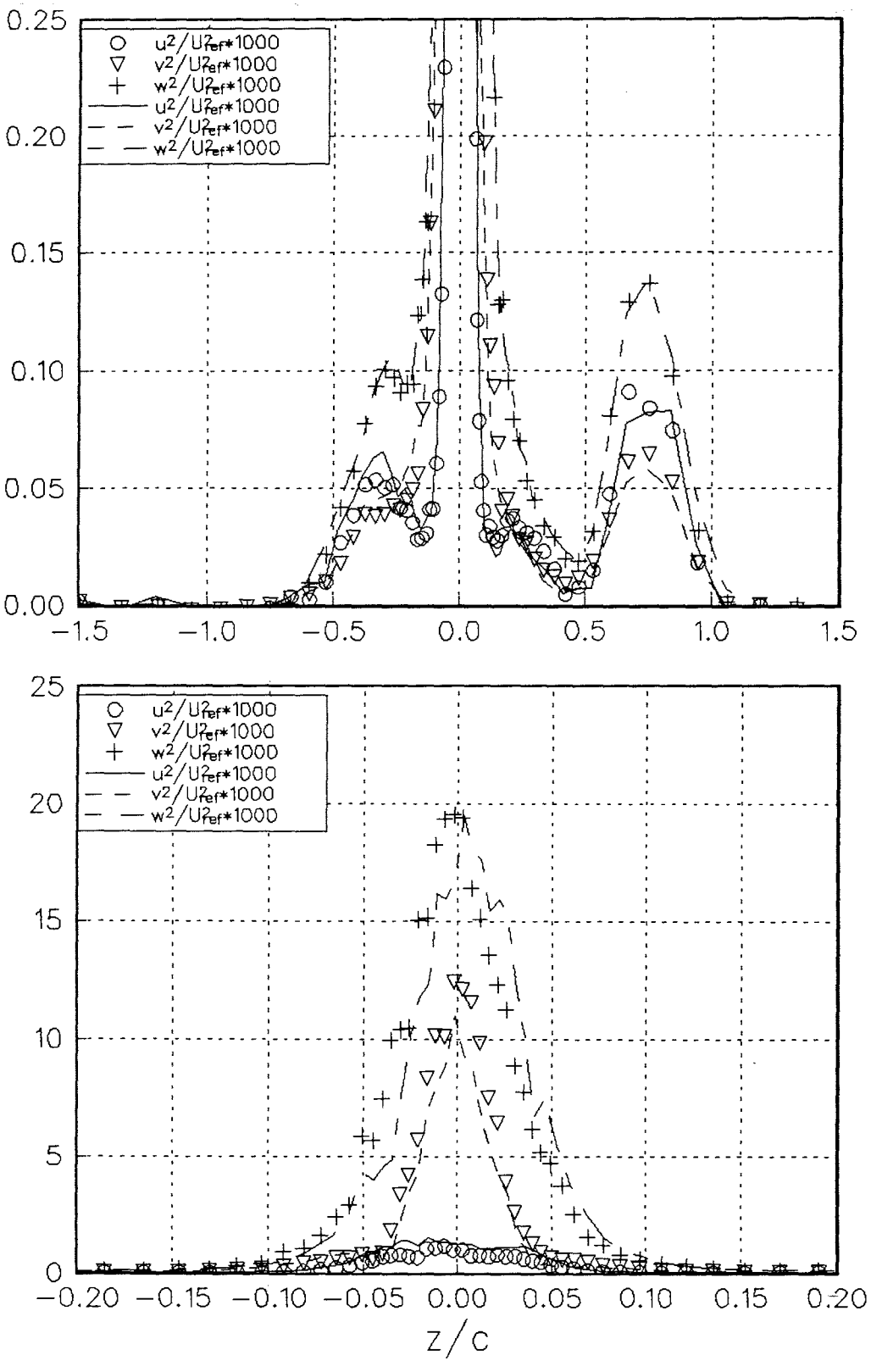

(b) Normal stresses

Figure A-1 Comparison of cross- and triple hot-wire measurements in the baseline case after correction for electrical noise only. Symbols - cross hot-wire, lines - triple hot-wire.

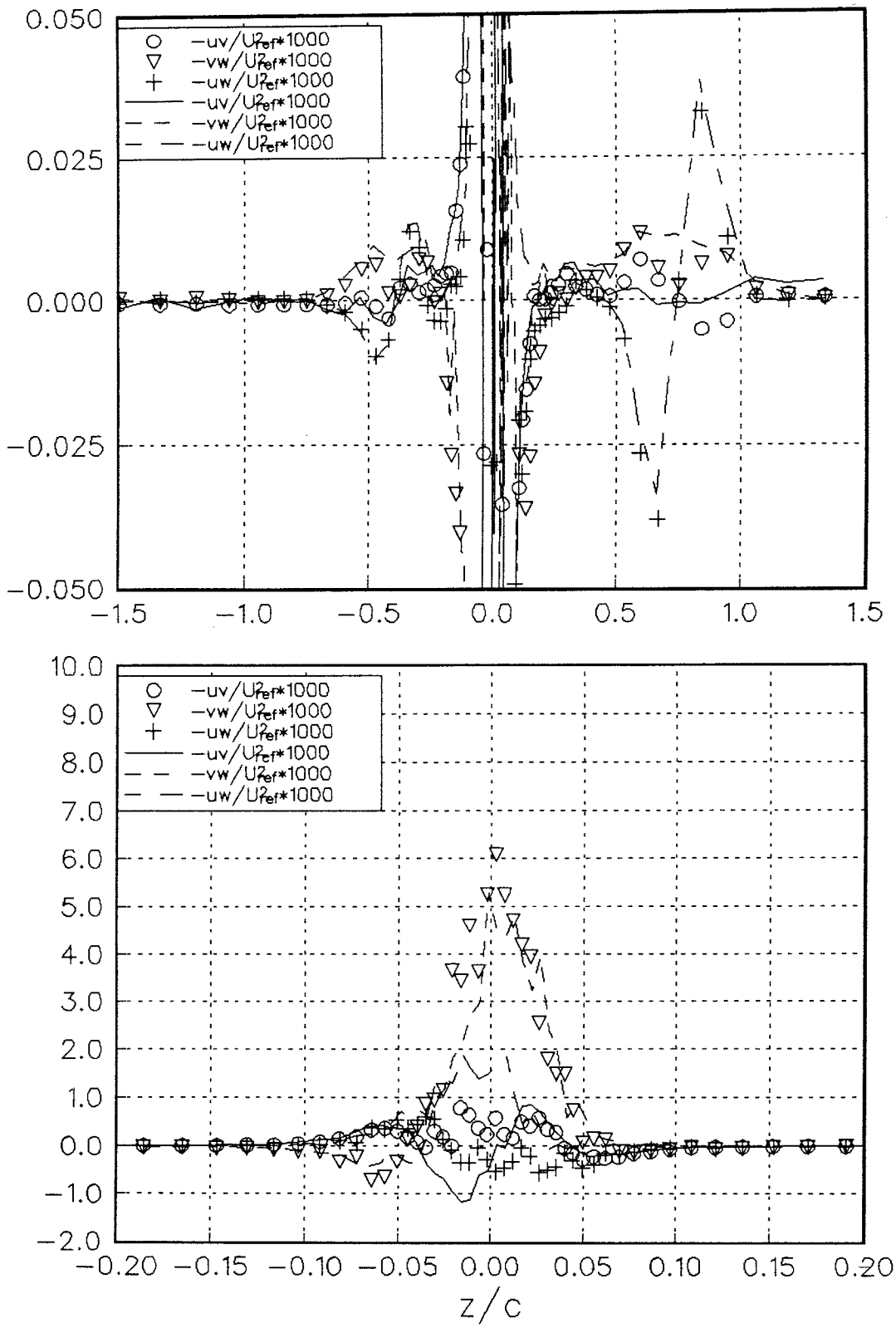

(c) Shear stresses

Figure A-1 Comparison of cross- and triple hot-wire measurements in the baseline case after correction for electrical noise only. Symbols - cross hot-wire, lines - triple hot-wire.

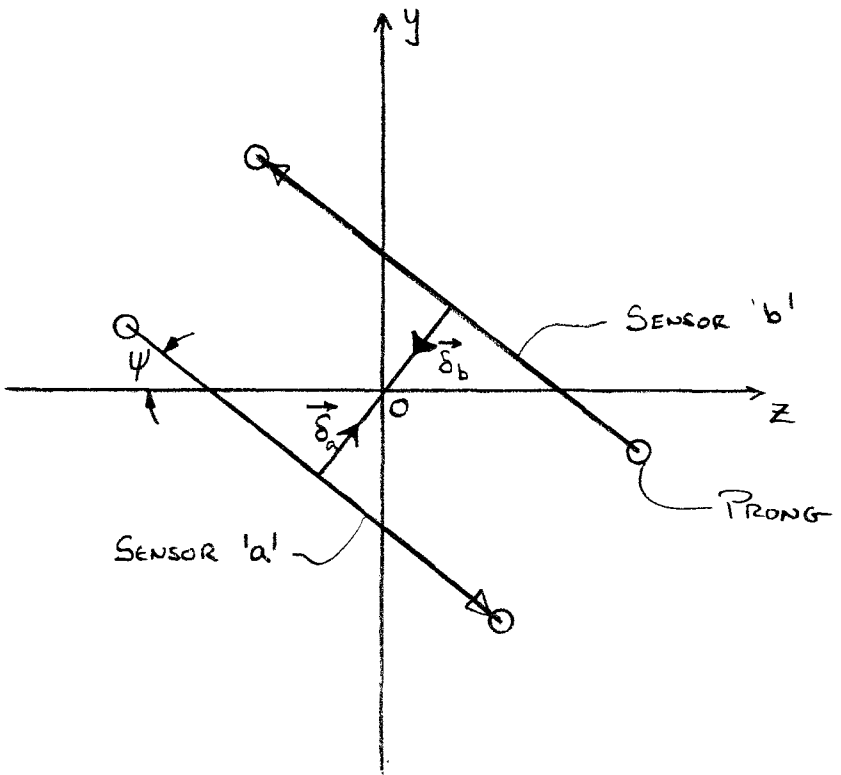

Figure A-2 Schematic of the cross hot-wire probe viewed from upstream. Sensors tilted at 45° to the plane of the paper, ends with arrow heads being furthest downstream.

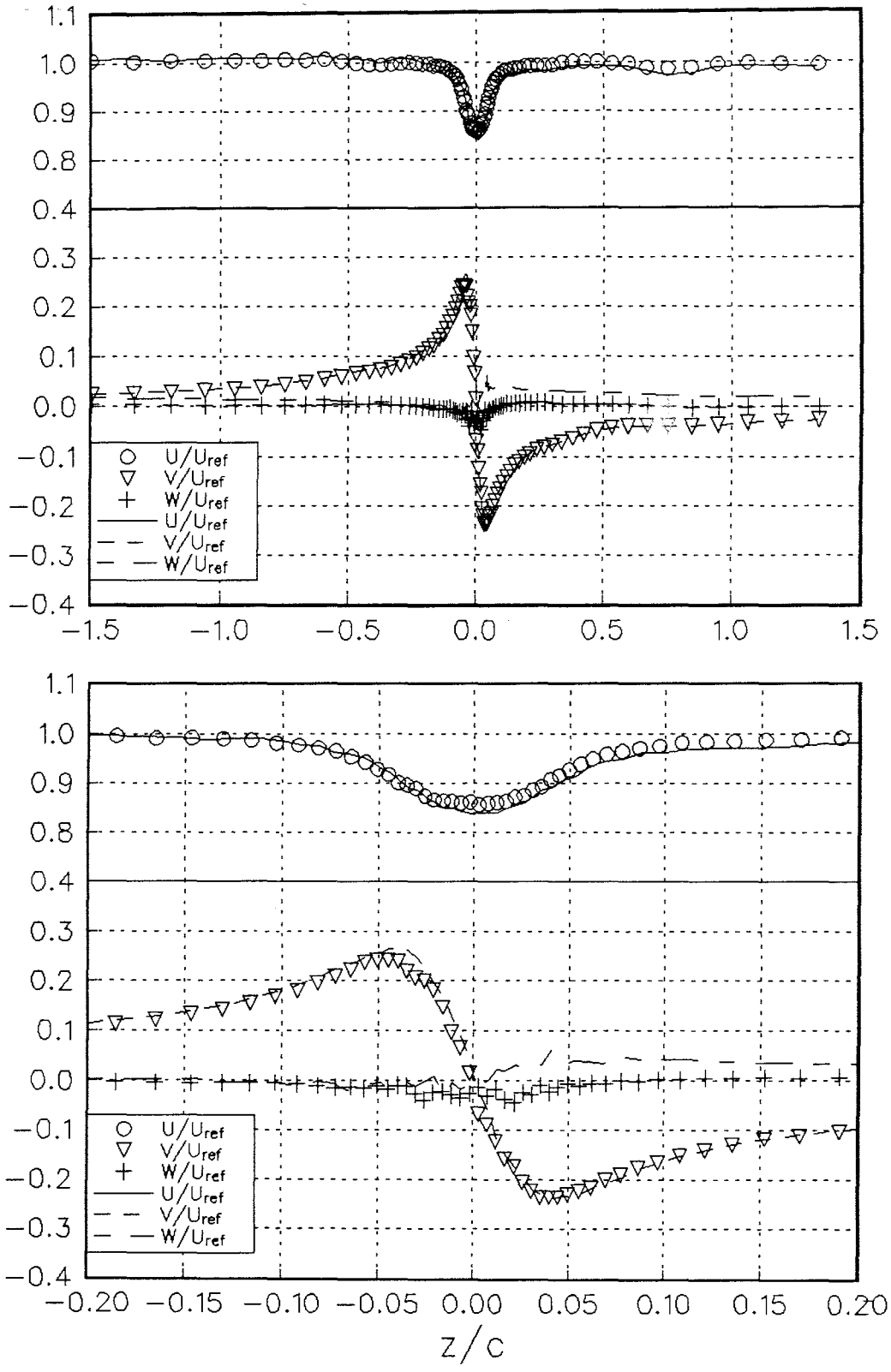

(a) Mean velocities

Figure A-3 Comparison of cross- and triple hot-wire measurements in the baseline case after correction for electrical noise and velocity gradient. Symbols - cross hot-wire, lines - triple hot-wire.

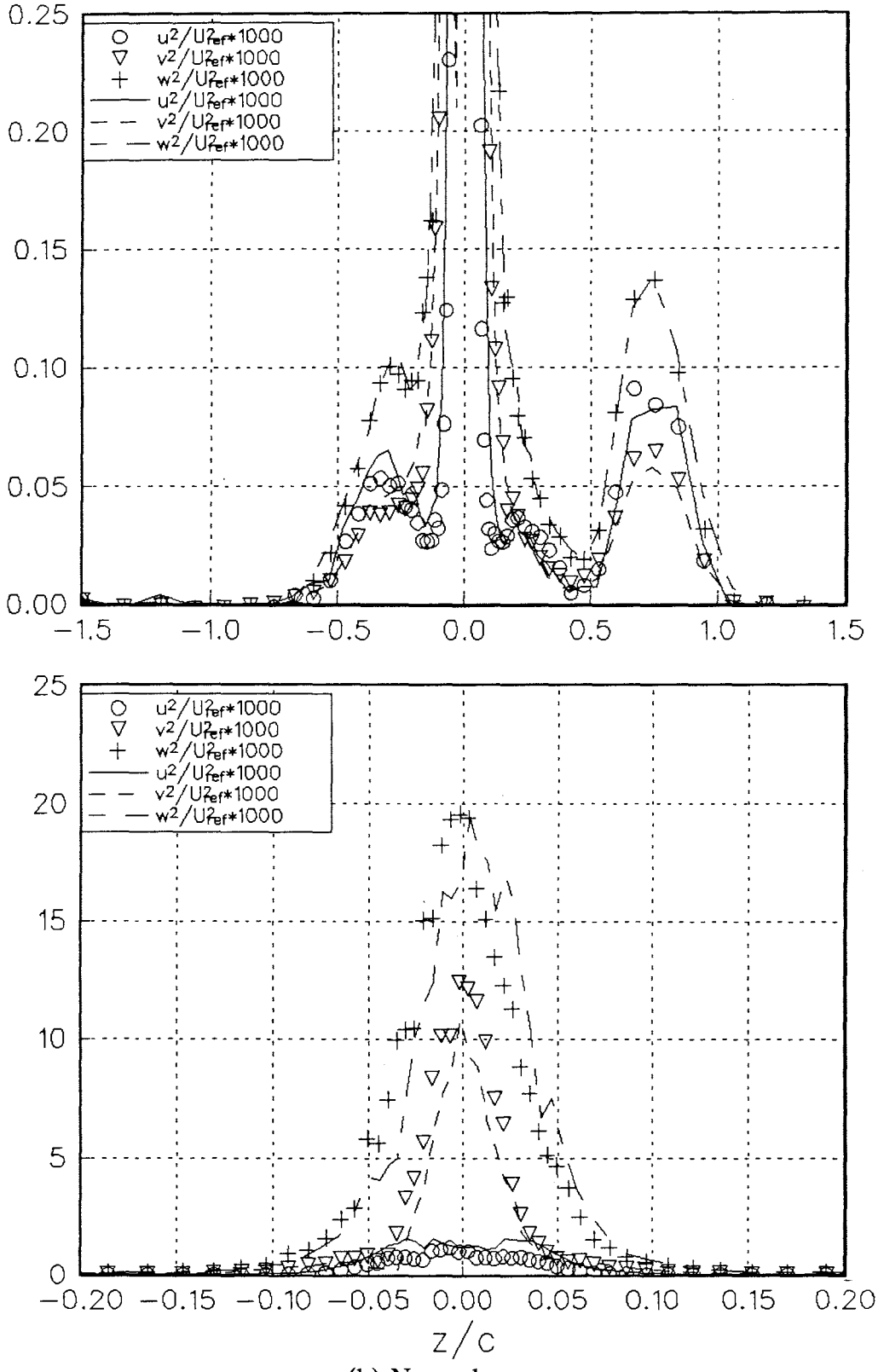

(b) Normal stresses

Figure A-3 Comparison of cross- and triple hot-wire measurements in the baseline case after correction for electrical noise and velocity gradient. Symbols - cross hot-wire, lines - triple hot-wire.

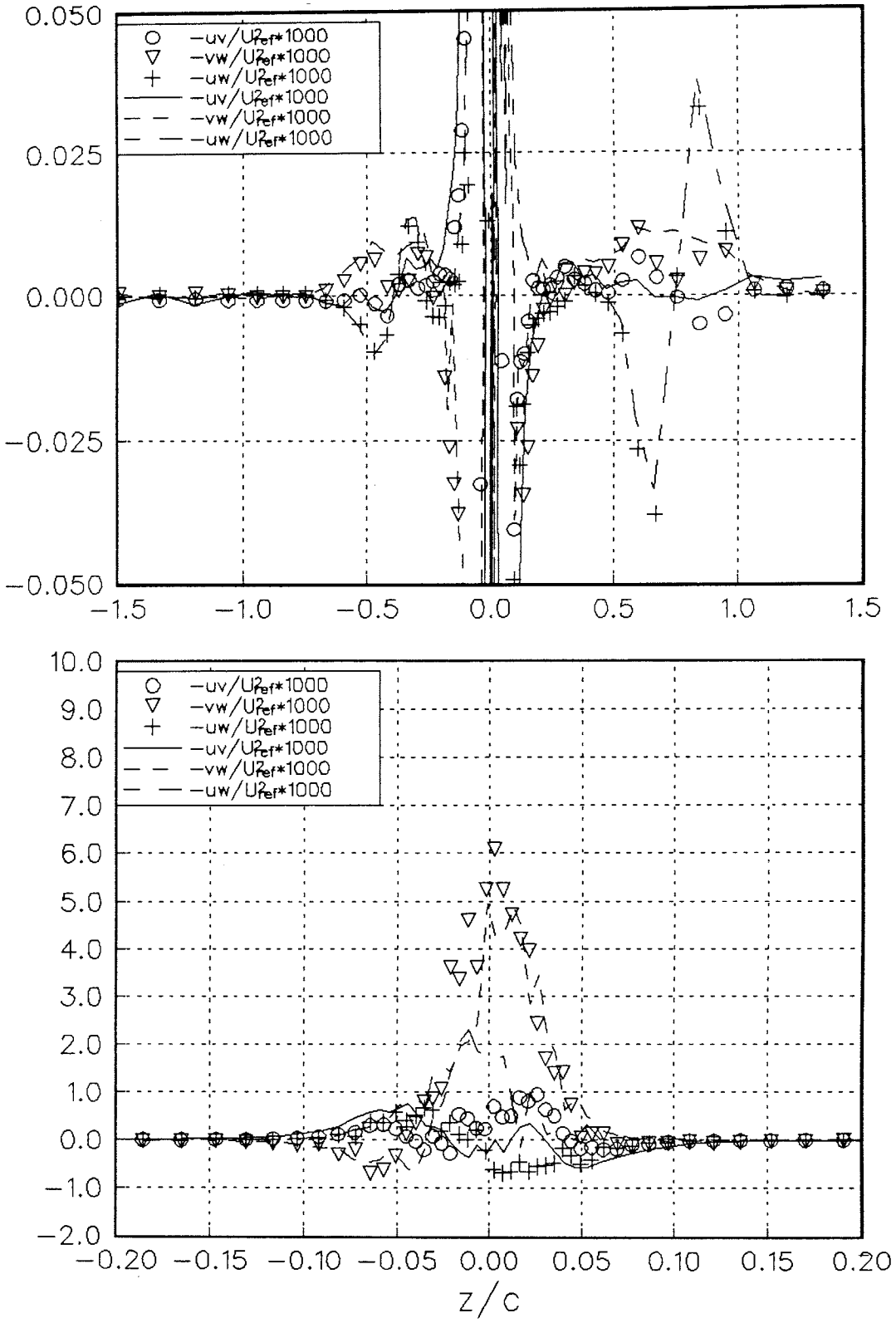

(c) Shear stresses

Figure A-3 Comparison of cross- and triple hot-wire measurements in the baseline case after correction for electrical noise and velocity gradient. Symbols - cross hot-wire, lines - triple hot-wire.

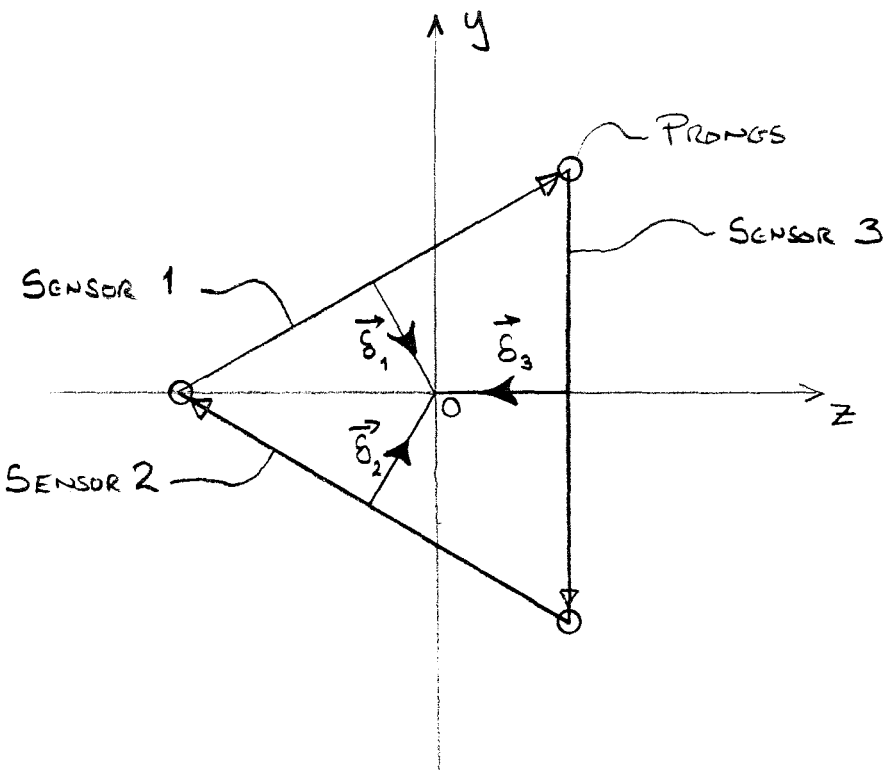

Figure A-4 Schematic of the triple hot-wire probe viewed from upstream. Sensors tilted at 35.3° to the plane of the paper, ends with arrow heads being furthest downstream.

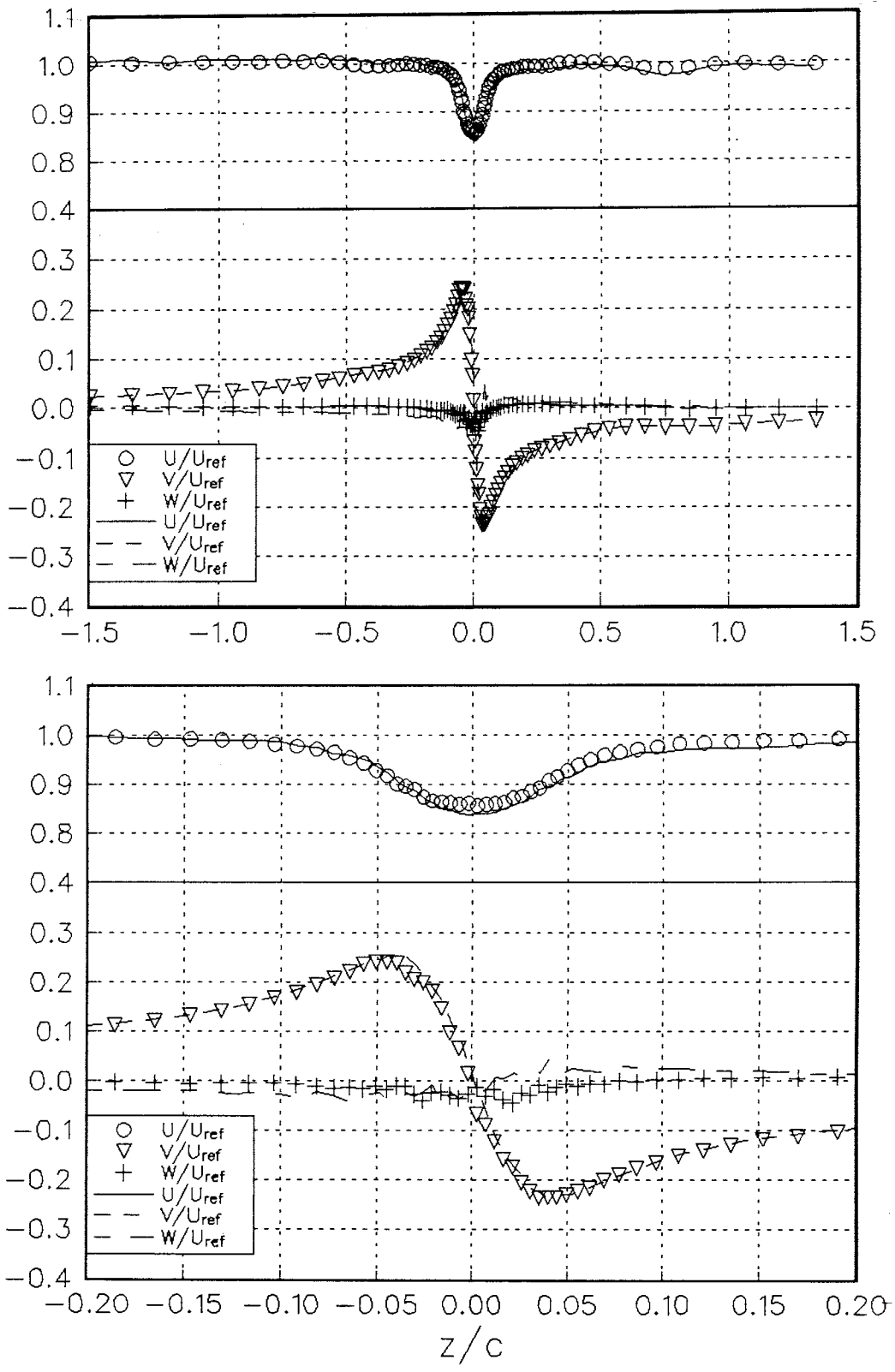

(a) Mean velocities

Figure A-5 Comparison of final cross- and triple hot-wire measurements in the baseline case after correction for electrical noise, velocity gradient and calibration misalignment. Symbols - cross hot-wire, lines - triple hot-wire.

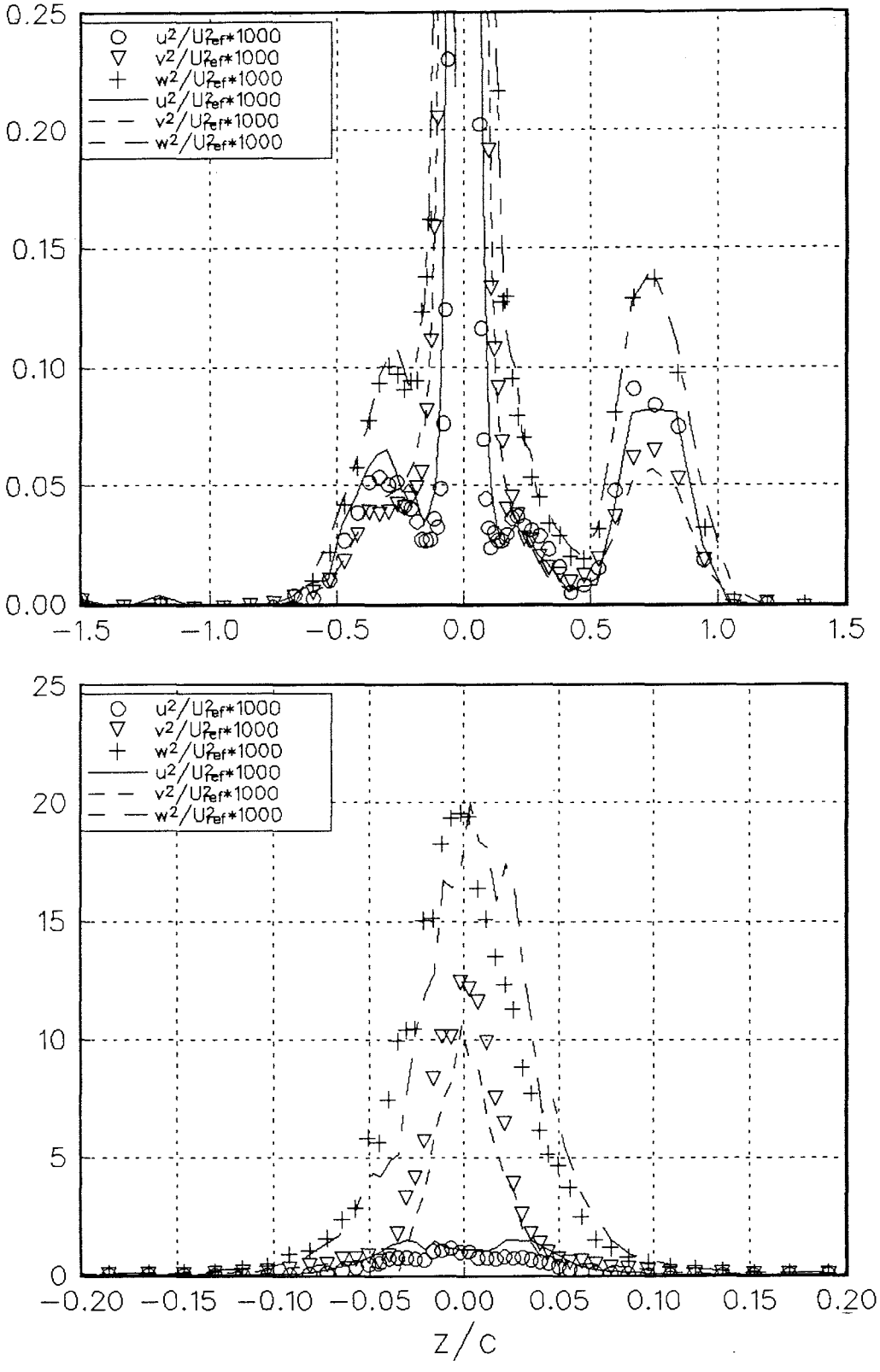

(b) Normal stresses

Figure A-5 Comparison of final cross- and triple hot-wire measurements in the baseline case after correction for electrical noise, velocity gradient and calibration misalignment. Symbols - cross hot-wire, lines - triple hot-wire.

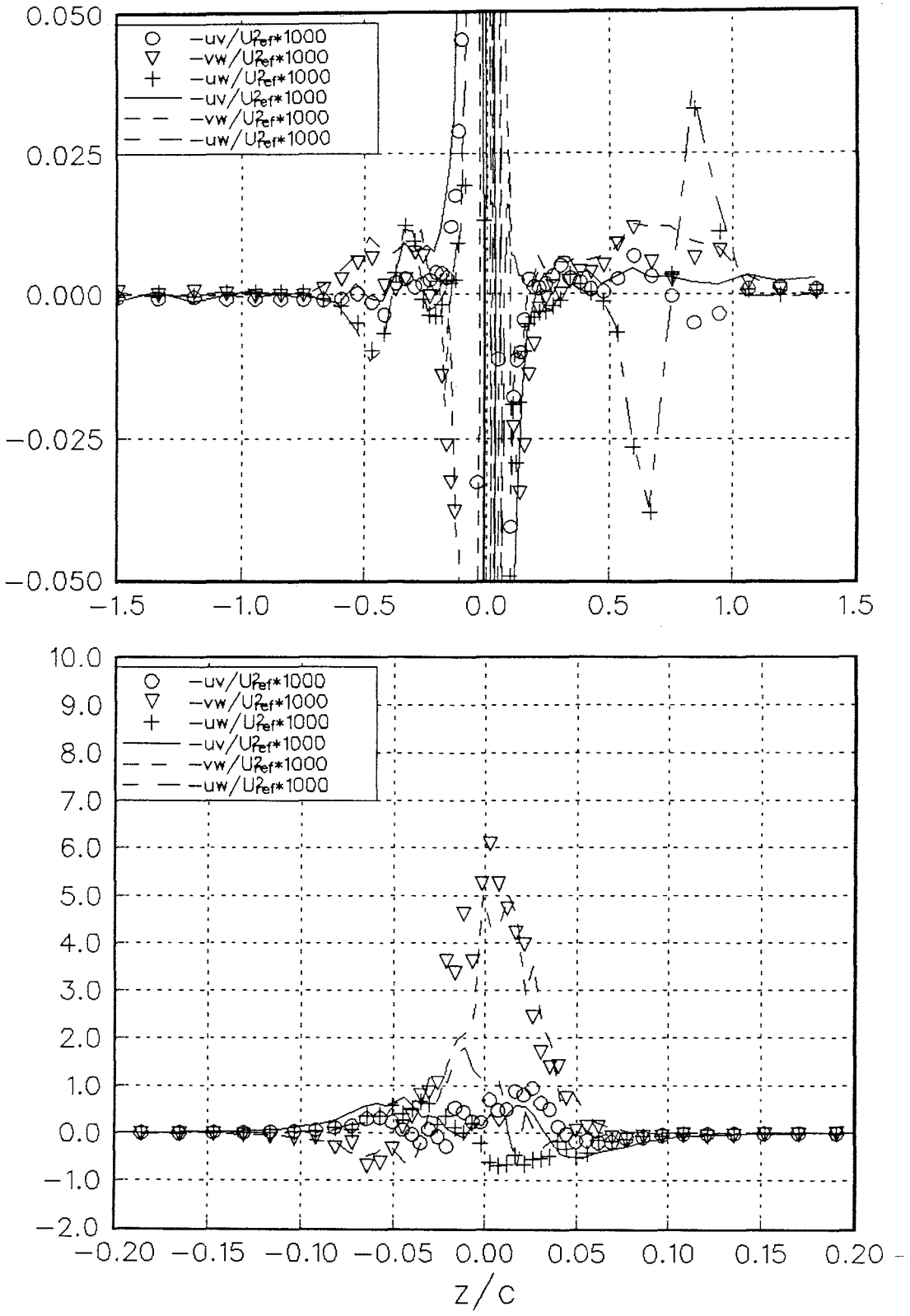

(c) Shear stresses

Figure A-5 Comparison of final cross- and triple hot-wire measurements in the baseline case after correction for electrical noise, velocity gradient and calibration misalignment. Symbols - cross hot-wire, lines - triple hot-wire.

PART II: THEORY AND NOISE PREDICTIONS

1. INTRODUCTION

Experimental measurements, Brooks et al(1987), have identified the mid-frequency broadband noise from helicopter rotors to be generated by the interaction of the rotor with its own wake. A typical noise spectrum for a rotor in forward flight is shown in figure 1.1, and this demonstrates that, for constant rotor thrust, the broadband noise level is a strong function of the tip path plane angle. As the tip path plane angle is increased the spectral level drops significantly, and this has been shown (Glegg(1991)) to correlate with the ingestion of the wake into the forward sector of the rotor disc plane. At small values of the tip path plane angle the rotor wake is close to the blades, but as the tip path plane angle is increased the wake moves away from the rotor and there is a corresponding reduction in noise level. This noise mechanism was defined by Brooks et al(1987) as Blade Wake Interaction (BWI) noise, and has been shown to be the dominant contributor to the subjectively important part of the noise spectrum for the approach stage of a helicopter flyover. A method for predicting BWI noise was developed by Glegg(1991) using the calculated trailing vortex trajectories from the rotor blades, and estimates of the vortex turbulence based on measurements by Phillips and Graham(1984). It was found that good predictions of the spectral level could be obtained, and the correct scaling with tip path plane angle was achieved, but the spectral shape was not well predicted. The measurements by Phillips and Graham(1984) were made on a trailing vortex from a split wing arrangement and did not give the spectrum of the turbulent velocity fluctuations which define the spectral shape of the radiated noise. Consequently the prediction method estimated the noise spectrum by assuming a Von Karman approximation for the turbulence energy spectrum and estimating the integral lengthscales from similar flows.

However to obtain a better understanding of BWI noise more details are required on the features of the turbulent flow in a vortex. This report describes an experiment which has been specifically designed to measure this flow using a single wing in a wind tunnel, and this part of the report will show how the measurements can be incorporated into the BWI noise prediction scheme. Comparisons of the results with rotor noise measurements will also be given.

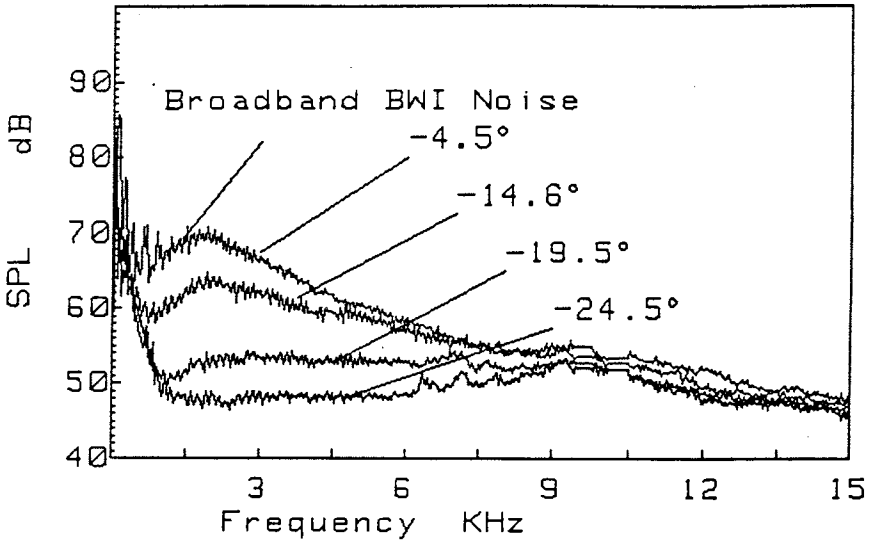

Figure 1-1. Measured helicopter noise spectra from a model scale rotor in a wind tunnel showing the broadband BWI noise as a function of the tip path plane angle of the rotor to the flow direction.

2. MODELING OF THE TURBULENCE

The turbulent flow measurements in the vortex have identified two different mechanisms for generating the unsteady velocity fluctuations at a fixed point. Close to the vortex center the flow is dominated by the small lateral motions of the vortex core, and at the edge of the vortex the turbulence in the spiral wake is the most important feature. In this section we will consider both of these flows and develop analytical models to describe their features. First we will consider an analytical model of the mean flow profile, and then this will be used to predict the unsteady flow due to the lateral motions of the vortex core. Then in section 2.3 a model will be presented for the turbulence spectrum in the spiral wake on the outside of the vortex.

2.1 The Mean Velocity Profile of the Vortex

Schlinker and Amiet (1983) and Howe (1988) define a model of the azimuthal and axial velocity in a vortex as a function of the radial distance from it's center. This model couples a solid body rotation in the viscous core with a $1/r$ decay in the outer region. The azimuthal velocity is given by:

$$V_\theta(r) = C\frac{v_0 r_0}{r}\left[1 - e^{-\alpha(r/r_0)^2}\right] \qquad (1)$$

where $\alpha=1.25643$ and $C=(1+0.5/\alpha)=1.398$. The maximum azimuthal velocity is v_O and occurs at a radius of r_O. The circulation at large r is given by $\Gamma_\infty=2\pi C v_O r_O$.

The axial velocity deficit model is

$$U(r) = U_{ref} - U_D e^{-\alpha(r/r_0)^2} \qquad (2)$$

where U_D is the axial velocity deficit on the centerline.

The experimental results suggest that $v_O=0.25U_{ref}$, $r_O=0.0.046c$ and $U_D=0.15U_{ref}$. Using these parameters the predicted and measured mean velocity profiles are given in Figures 2.1 and 2.2. In general this model gives a good fit to the azimuthal velocity in the viscous core but under predicts the velocity in the outer region, suggesting that the field is not decaying as rapidly as expected from the simple model given here. The width of the axial velocity deficit is also under predicted. However, in the analysis which follows we are concerned with the velocity induced by lateral motions of the vortex core which will not be affected by errors in the outer region or in the axial velocity deficit.

2.2 The Small Lateral Motions of the Vortex

The flow visualizations showed small lateral perturbations of the vortex by the tunnel flow. Since there are large velocity gradients in the velocity field of the vortex, the perturbations will induce additional unsteady velocity fluctuations at a fixed measurement point. The purpose of this section is to evaluate this effect using a simplified model of the mean velocity profile in the vortex. It will be assumed that the motions of the vortex core are isotropic, which is the case for the velocity fluctuations in the frequency range $0.3<fc/U_{ref}<10$ where the wind tunnel induced disturbances of the vortex core are not significant. In this frequency range there is little or no coherence between the V and W velocity fluctuations. We suspect that velocity fluctuations here may be the result of random lateral motions of the core generated as it is buffeted by the surrounding wake turbulence. In turbulent boundary layers 'inactive' motion of this type contributes as much as 30% to the normal stresses in the near wall region (see

Bradshaw(1967)). Without the restraint of a solid interface we might expect such motion to have a greater effect.

The unsteady velocity components can be evaluated by considering the vortex center as displaced from the center of the co-ordinate system by **z** which is a random function of observer time at a fixed streamwise location (see figure 2.3). A turbulent eddy located at **x** relative to the origin of the co-ordinate system, is displaced from the center of the vortex by **y** , such that $\mathbf{x}=\mathbf{y}+\mathbf{z}(t)$. The mean velocity field of the vortex is defined as $\mathbf{V}(\mathbf{y})$ and the unsteady turbulence component as $\mathbf{v}(\mathbf{y},t)$, and both are a function of the displacement from the vortex center. The velocity measured by a fixed probe will have a mean component $\mathbf{U}(\mathbf{x})$ and an unsteady component $\mathbf{u}(\mathbf{x},t)$, given by

$$\mathbf{U}(\mathbf{x})+\mathbf{u}(\mathbf{x},t)=\mathbf{V}(\mathbf{x}-\mathbf{z}(t))+\mathbf{v}(\mathbf{x}-\mathbf{z}(t),t) \qquad (3)$$

If the displacements of the vortex are small in comparison with the the core radius then we can expand the right hand side of this equation in a Taylor series, to first order,

$$\mathbf{U}(\mathbf{x})+\mathbf{u}(\mathbf{x},t)=\mathbf{V}(\mathbf{x})+\mathbf{v}(\mathbf{x},t)-(\mathbf{z}(t).\nabla)(\mathbf{V}+\mathbf{v}) \qquad (4)$$

This shows that the measured mean component $\mathbf{U}(\mathbf{x})$ is, to first order, the same as the mean flow about the vortex. The unsteady component is a combination of the turbulence associated with the vortex and velocity fluctuations induced by the time varying lateral displacements.

We assume that **v** and $\mathbf{z}=(0,\alpha,\beta)$ are uncorrelated so that the mean square velocity components are

$$\left\langle \mathbf{u}^2 \right\rangle = \left\langle \mathbf{v}^2 \right\rangle + \left\langle \left(\alpha \frac{\partial \mathbf{V}}{\partial y} + \beta \frac{\partial \mathbf{V}}{\partial z} \right)^2 \right\rangle \qquad (5)$$

If the vortex displacements can be assumed to be isotropic with an rms displacement ε, then

$$<\alpha^2>=<\beta^2>=\varepsilon^2 \quad \text{and} \quad <\alpha\beta>=0 \qquad (6)$$

the three components of the normal turbulent stresses due to the lateral vortex motion can be defined as

$$\left\langle u'^2 \right\rangle = \varepsilon^2 \left\{ \left(\frac{\partial U}{\partial y} \right)^2 + \left(\frac{\partial U}{\partial z} \right)^2 \right\} \qquad (7)$$

$$\left\langle v'^2 \right\rangle = \varepsilon^2 \left\{ \left(\frac{\partial V}{\partial y} \right)^2 + \left(\frac{\partial V}{\partial z} \right)^2 \right\} \qquad (8)$$

$$\left\langle w'^2 \right\rangle = \varepsilon^2 \left\{ \left(\frac{\partial W}{\partial y} \right)^2 + \left(\frac{\partial W}{\partial z} \right)^2 \right\} \qquad (9)$$

where $\mathbf{V}=(U,V,W)$. By using the mean velocity profiles described in the previous section we obtain

$$V = -\frac{z}{r} V_\theta(r) \qquad W = \frac{y}{r} V_\theta(r) \qquad (10)$$

so that

$$\frac{\partial U}{\partial y} = \frac{y}{r}\frac{\partial U}{\partial r} \qquad \frac{\partial U}{\partial z} = \frac{z}{r}\frac{\partial U}{\partial r} \qquad (11)$$

$$\frac{\partial V}{\partial y} = -\frac{zy}{r^2}\left\{ r\frac{\partial}{\partial r}\left(\frac{V_\theta}{r} \right) \right\} \qquad \frac{\partial V}{\partial z} = -\frac{V_\theta}{r} - \frac{z^2}{r^2}\left\{ r\frac{\partial}{\partial r}\left(\frac{V_\theta}{r} \right) \right\} \qquad (12)$$

$$\frac{\partial W}{\partial y} = \frac{V_\theta}{r} + \frac{y^2}{r^2}\left\{ r\frac{\partial}{\partial r}\left(\frac{V_\theta}{r}\right)\right\} \qquad \frac{\partial W}{\partial z} = \frac{zy}{r^2}\left\{ r\frac{\partial}{\partial r}\left(\frac{V_\theta}{r}\right)\right\} \tag{13}$$

The measurements were taken on y=0 and so these equations can be simplified to give the three components of the normal turbulent stresses as

$$\left\langle u'^2 \right\rangle = \varepsilon^2 \left(\frac{\partial U}{\partial r}\right)^2 \tag{14}$$

$$\left\langle v'^2 \right\rangle = \varepsilon^2 \left(\frac{V_\theta}{r} + r\frac{\partial}{\partial r}\left(\frac{V_\theta}{r}\right)\right)^2 = \varepsilon^2 \left(\frac{\partial V_\theta}{\partial r}\right)^2 \tag{15}$$

$$\left\langle w'^2 \right\rangle = \varepsilon^2 \left(\frac{V_\theta}{r}\right)^2 \tag{16}$$

By using equations (1) and (2) we obtain

$$\left\langle u'^2 \right\rangle = \varepsilon^2 \left(U_D \frac{2\alpha r}{{r_0}^2} e^{-\alpha(r/r_0)^2} \right)^2 \tag{17}$$

$$\left\langle v'^2 \right\rangle = \varepsilon^2 \left(C\frac{v_0 r_0}{r^2}\left[1 - \left(1 + 2\alpha(r/r_0)^2\right)e^{-\alpha(r/r_0)^2}\right]\right)^2 \tag{18}$$

$$\left\langle w'^2 \right\rangle = \varepsilon^2 \left(C\frac{v_0 r_0}{r^2}\left[1 - e^{-\alpha(r/r_0)^2}\right]\right)^2 \tag{19}$$

Notice here that as r becomes small we can approximate

$$1-exp(-\alpha(r/r_O)^2)\approx\alpha(r/r_O)^2 \tag{20}$$

so that

$$\left\langle w'^2\right\rangle=\left\langle v'^2\right\rangle=\varepsilon^2\left(C\frac{\alpha v_0}{r_0}\right)^2=3.08\left(\frac{\varepsilon v_0}{r_0}\right)^2 \tag{21}$$

In figure 2.4 the normal turbulent stresses are shown for the baseline case where the measurements were taken 30 chords downstream of the airfoil. These show that $<v'^2>=<w'^2>=0.0064U_{ref}^2$ and since $v_O=0.25U_{ref}$ and $r_O=0.046c$, we can compute ε as $0.00838c$ (1.73mm). Figure 2.4 also shows the predicted normal turbulent stresses obtained using this model and the agreement with the measurements is excellent. The only noticeable error is in the predicted value of $<u'^2>$ close to $z=0$. However the effects of finite probe size and low turbulence levels at this point may cause he predicted dip to be filled in. Also it should be noted that the velocity deficit model is not as accurate as the tangential velocity profile model (see figure 2.2), and this may also be the cause of the error.

The turbulent shear stresses can also be predicted using this approach, since

$$\begin{aligned}
\langle u'\,v'\rangle &= \varepsilon^2\left\{\left(\frac{\partial U}{\partial y}\right)\left(\frac{\partial V}{\partial y}\right)+\left(\frac{\partial U}{\partial z}\right)\left(\frac{\partial V}{\partial z}\right)\right\}\\
\langle u'\,w'\rangle &= \varepsilon^2\left\{\left(\frac{\partial U}{\partial y}\right)\left(\frac{\partial W}{\partial y}\right)+\left(\frac{\partial U}{\partial z}\right)\left(\frac{\partial W}{\partial z}\right)\right\}\\
\langle v'\,w'\rangle &= \varepsilon^2\left\{\left(\frac{\partial V}{\partial y}\right)\left(\frac{\partial W}{\partial y}\right)+\left(\frac{\partial V}{\partial z}\right)\left(\frac{\partial W}{\partial z}\right)\right\}
\end{aligned} \tag{22}$$

Inspection of equations (11)-(13) shows that the only non-zero turbulent shear stress on $y=0$ is the $\langle u'v' \rangle$ component which is given by

$$\langle u'\, v' \rangle = \varepsilon^2 \left\{ \left(\frac{\partial U}{\partial z} \right) \left(\frac{\partial V}{\partial z} \right) \right\} = \varepsilon^2 \left\{ \left(\frac{\partial U}{\partial r} \right) \left(\frac{\partial V_\theta}{\partial r} \right) \right\} \tag{23}$$

In terms of the simplified model this can be defined as

$$\langle u'\, v' \rangle = \varepsilon^2 \left(U_D \frac{2\alpha r}{r_0^{\,2}} e^{-\alpha (r/r_0)^2} \right) \left(C \frac{v_0 r_0}{r^2} \left[1 - \left(1 + 2\alpha (r/r_0)^2 \right) e^{-\alpha (r/r_0)^2} \right] \right) \tag{24}$$

and is plotted in figure 2.5. This feature of the flow is not well predicted by the flow model. This may be due to the fact that the axial component of the mean flow is not predicted accurately enough to fit the data. Also figure 2.5 shows that the $\langle vw \rangle$ component of the shear stresses is larger than the $\langle uv \rangle$ component whereas the theory would suggest thta this should be zero. Currently we have no explanation for this result, and these features of the flow do not appear to be explained by this simplified model.

The turbulence spectrum of the velocity fluctuations can also be obtained from this model. For example if we consider the spectrum of the velocity components in the transverse direction, then equations (15) and (16) implies that

$$G_{vv}(f) = G_{\varepsilon\varepsilon}(f) \left(\frac{\partial V_\theta}{\partial r} \right)^2$$

$$G_{ww}(f) = G_{\varepsilon\varepsilon}(f) \left(\frac{V_\theta}{r} \right)^2 \tag{25}$$

Since at the center of the vortex $\partial V\theta/\partial r = V\theta/r = \alpha C v_o/r_o$ it follows that for isotropic motions of the vortex core

$$G_{vv}(f) = G_{ww}(f) = G_{\varepsilon\varepsilon}(f)\left(\frac{\alpha C v_o}{r_o}\right)^2 \tag{26}$$

Figure 2.6 shows the spectra of the turbulent velocity fluctuations at the center of the vortex core plotted on an absolute scale. It is seen that for frequencies $fc/U_{ref} > 6x10^{-3}$ the spectra are identical as suggested by the isotropic model. To evaluate $G_{\varepsilon\varepsilon}(f)$ we can use the Von Karman interpolation formula, with a correction for viscous dissipation based on Pao's postulate. (The Von Karman interpolation formula for transverse velocity fluctuations is multiplied by a viscous dissipation correction factor given by equation 3-146a in Hinze(1975). See also the appendix of Amiet (1975)). This gives

$$G_{\varepsilon\varepsilon}(f) = \Lambda\varepsilon^2 \frac{4L}{3U_{ref}} \frac{(3+8\hat{k}_1^2)e^{-\frac{3}{2}\left(\frac{\hat{k}_1}{k_d L}\right)^{4/3}}}{(1+\hat{k}_1^2)^{11/6}} \tag{27}$$

where

$$\hat{k}_1 = \frac{4\omega L}{3U_{ref}} \tag{28}$$

Λ is a scaling constant which ensures integral closure (equal to 0.5 when $k_d L \sim \infty$), L is the integral lengthscale of the turbulence, and $k_d L$ specifies the scale of the viscous dissipation. For the mid frequency range corresponding to fc/U_{ref} greater than 0.1 the lateral motions are assumed isotropic and the spectra can be estimated using $k_d L = 8$, $L/c = 0.45$, $\Lambda = 0.9022$ and $\varepsilon = 0.0045c$. The value of ε calculated from these measurements

is approximately half the value estimated from the measurements of the normal stresses. However since the normal stresses will be affected by incomplete filtering of the non isotropic motions of the vortex core at low frequencies, and also the high frequency energy not accounted for by this model, this difference is to be expected. The important point about this result is that BWI noise is primarily generated in the frequency range corresponding to $0.5<fc/U_{ref}<4$ in which the prediction given by equation (27) appears to work well. Therefore it would appear that a noise prediction based on this result would correctly account for the effects of the isotropic motions of the core and their potential for BWI noise generation.

One of the problems with ascertaining the accuracy of this turbulence spectra is that the low frequency energy is masked by the non-isotropic motions of the vortex which are attributed to the wind tunnel flow. A alternative fit to the measured spectra which had less low frequency energy was also considered in the form

$$G_{\varepsilon\varepsilon}(f) = 12.57\varepsilon^2 \frac{c}{U_{ref}} \frac{\hat{k}_1^2 e^{-\frac{3}{2}\left(\frac{\hat{k}_1}{k_d L}\right)^{4/3}}}{(1+\hat{k}_1^2)^{11/6}} \qquad (29)$$

where $k_dL=15$, $L/c=0.45$, and $\varepsilon=0.00275c$. This result is also shown in figure 2.6 and only varies slightly from the fit given by equation (27) in the range of interest $0.5<fc/U_{ref}<4$. This difference is caused entirely by the different values chosen for k_dL , and would not occur if the same value was used. The empirical model of the spectra given by equation (29) therefore gives an upper bound for the for the turbulence levels due to the core motions at high frequencies and has significantly reduced energy at low frequencies.

2.3 The Turbulence in the Wake Spiral

If it is assumed that the turbulence in the wake spiral is generated by the blade boundary layers, it may be considered as a distorted form of two dimensional wake turbulence. Wygnanski et al (1986) have shown that the turbulence in the wakes of many different types of body can be scaled on the wake width L_O which can be defined in terms of the momentum thickness Θ of the wake as $L_O=0.32\Theta\sqrt{(x/\Theta+380)}$. One of the unexpected results of this study was the remarkably good scaling which this type of normalization gave to the turbulent spectrum of the velocity fluctuations in the wake spiral. Figure 2.7 shows the collapse of the $G_{ww}(f)$ spectra when they are normalized as $G_{ww}(f)U_{ref}/w^2L_O$ and plotted against fL_O/U_{ref}. An empirical fit to these spectra can be obtained based on the Von Karman interpolation formula with the turbulence lengthscale proportional to L_O and a correction for viscous dissipation, based on Saffmans hypothesis (Hinze(1975), equation 3.147).

$$G_{ww}(f) = \Lambda w^2 \frac{4\gamma L_o}{3U_{ref}} \frac{(3+8\hat{k}_1^2)e^{-S\hat{k}_1^2}}{(1+\hat{k}_1^2)^{11/6}} \qquad (30)$$

$$\hat{k}_1 = \frac{4\omega\gamma L_o}{3U_{ref}} \qquad S = \frac{c}{\gamma\kappa R_{ec}\Theta}$$

where γ is defined as the ratio of the integral lengthscale of the turbulence to the wake width and is determined from the measurements to be $\gamma=0.2$. The parameter κ is proportional to the turbulence intensity and is found to be 0.216 , and the constant Λ ensures integral closure. The derivation of the parameter S is given in appendix II.1. This normalized spectrum is shown in figure 2.7, and gives remarkably good agreement with the measurements in this part of the wake.

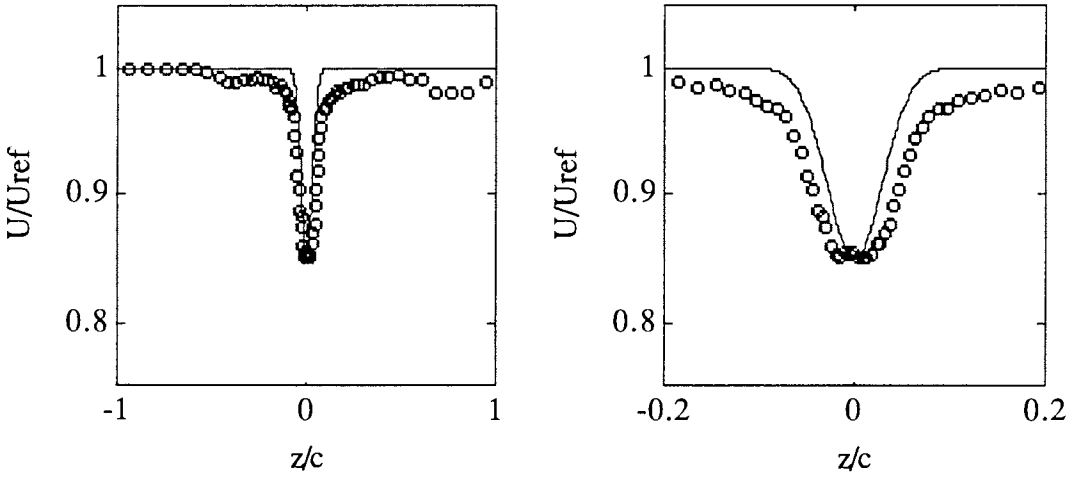

Figure 2.1 The mean axial velocity profiles at 30 chords downstream normalsed on U_{ref} for the baseline case.

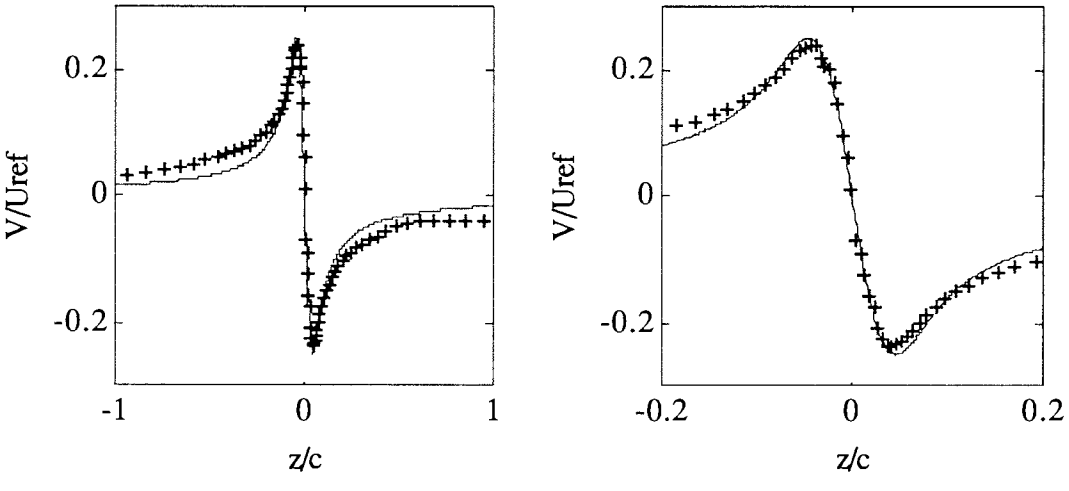

Figure 2.2 The tangential velocity profiles at 30 chords downstream normalsed on U_{ref} for the baseline case.

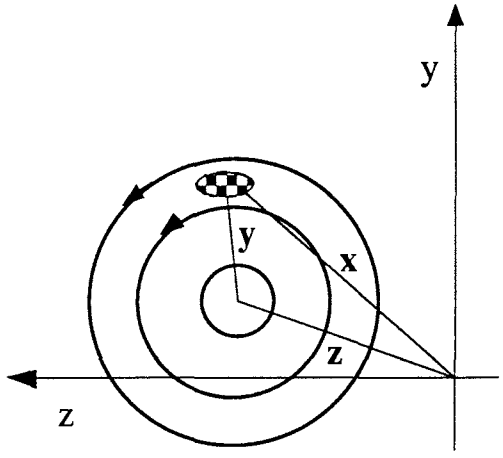

Figure 2.3 The co-ordinate system relative to the center of the vortex for the calculation of vortex motion induced velocity fluctuations

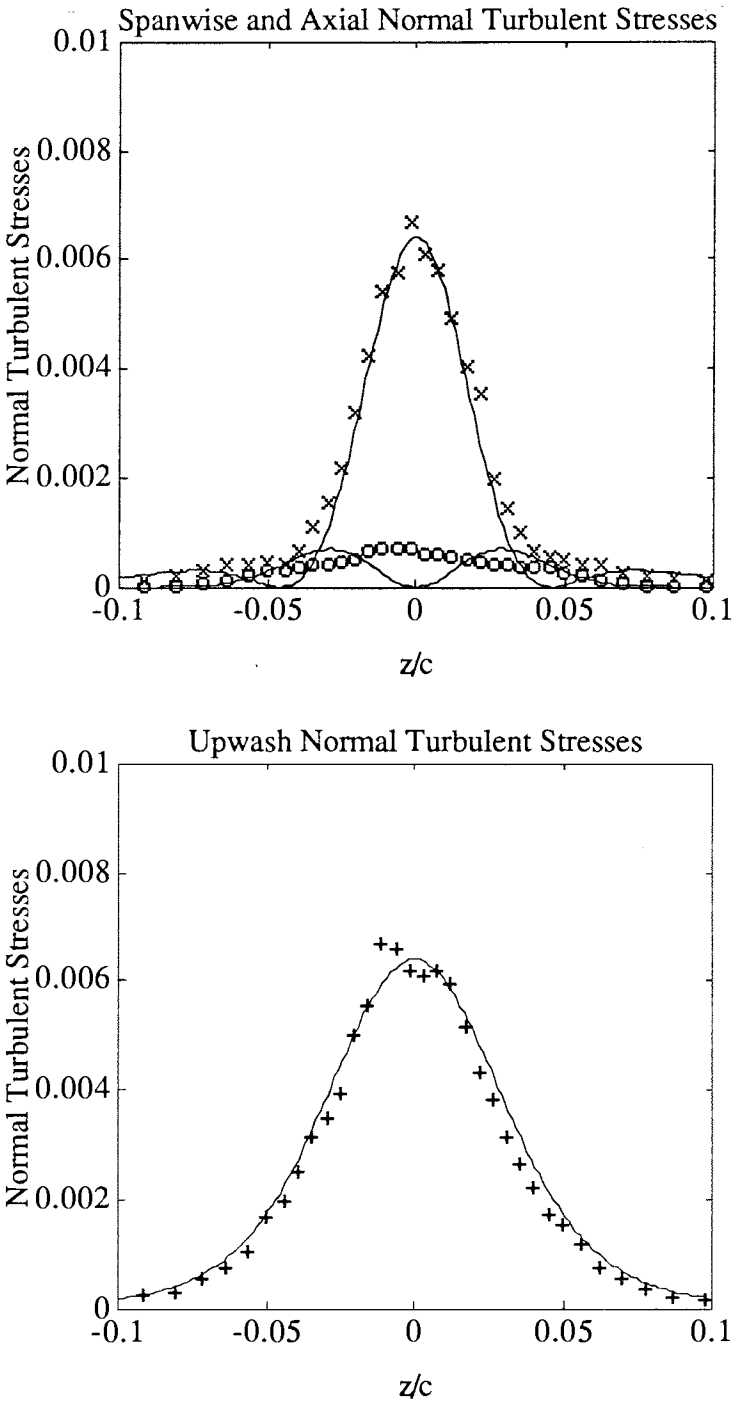

Figure 2.4 The normal turbulent stresses measured and predicted 30 chords downstream of the blade for the baseline case (o-<u>,x-<v>, +-<w>)

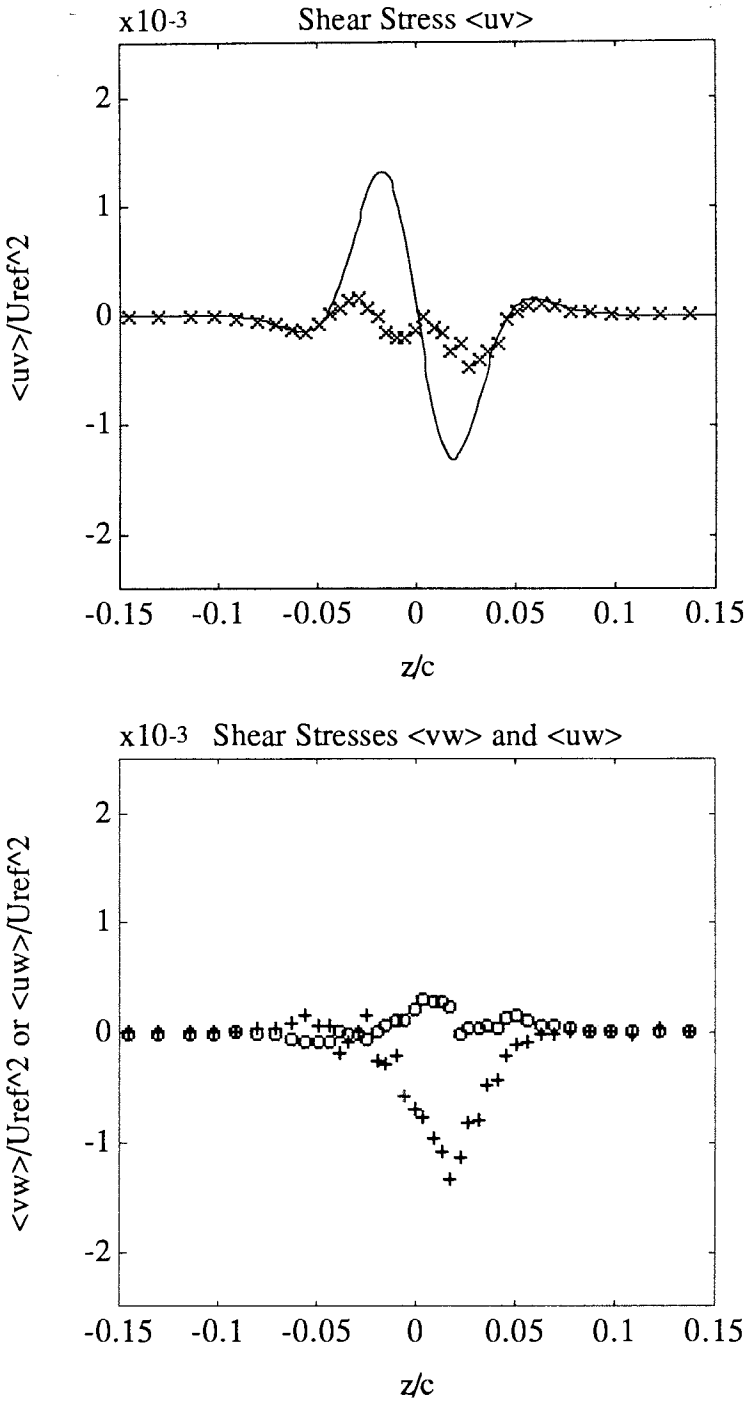

Figure 2.5 Predicted and measured shear stresses in the vortex core. Lines represent predictions and symbols the measurements (x-<uv>,o-<uw>, +-<vw>)

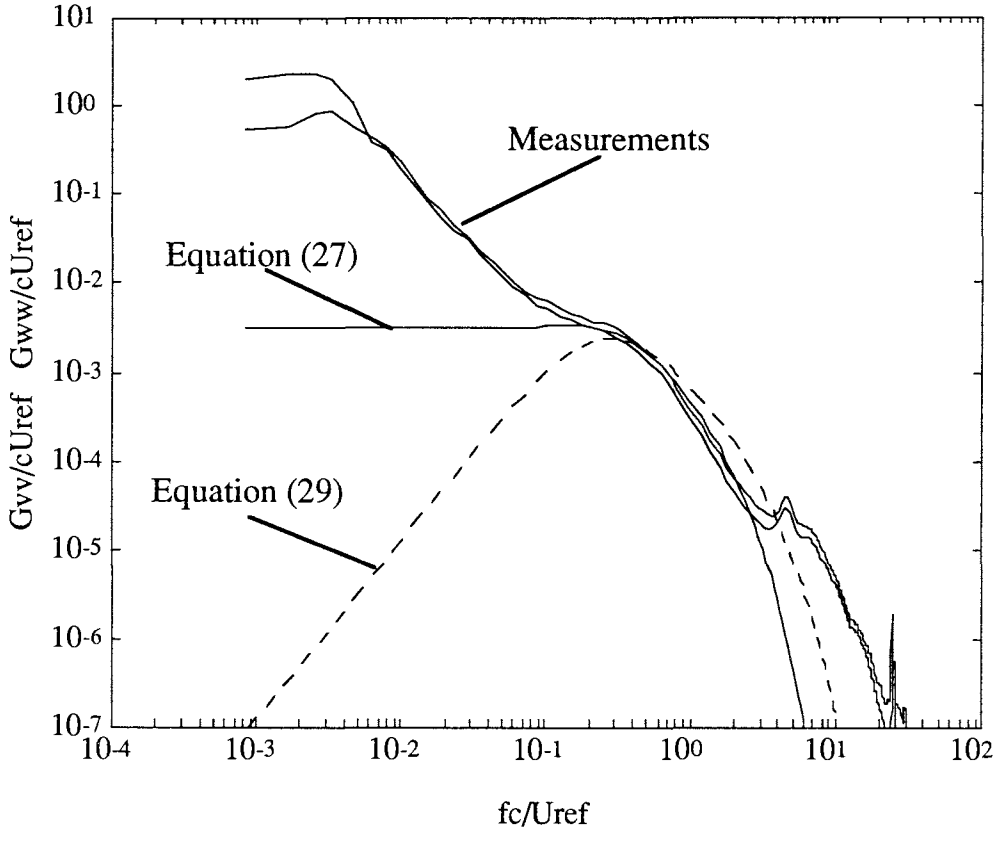

Figure 2.6 Measured and predicted spectra of the velocity fluctuations in the vortex core for the baseline case 30 chords downstream.

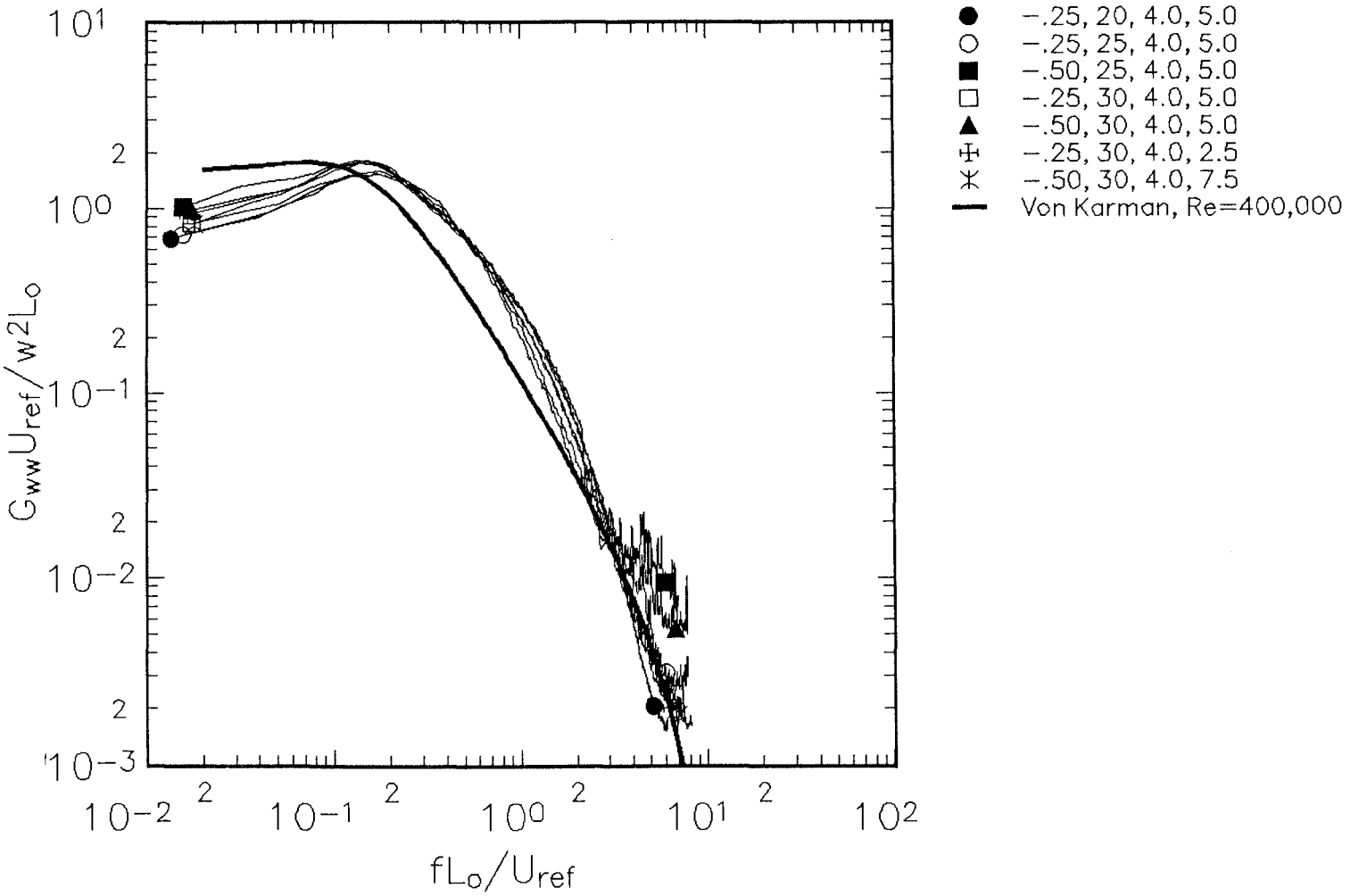

Figure 2.7 Comparison of turbulence spectra in spiral wake with theoretical spectrum based on equation (30).

3. NOISE PREDICTIONS

Blade wake interaction noise is generated by the unsteady blade loads which result from the passage of the blades through their own wake. To calculate BWI noise we use the aeroacoustic model developed by Amiet(1975) and Glegg(1991). This gives the power spectrum of the acoustic pressure fluctuations in the far field of the rotor, caused by upwash turbulent velocity fluctuations, in terms of the contributions from spanwise segments of the blade of length b_e . For the case of BWI noise, the spanwise segment b_e corresponds to the width of the vortex wake on the blade and the contribution from each blade/vortex interaction is summed to give the total field. Each interaction gives a contribution to the acoustic far field spectrum which is given by

$$S_{pp}^{L}(\mathbf{x},\omega)=\left[\frac{\omega\rho_o c x_3}{4\pi c_o r_o^2}\right]^2 \frac{2\pi^3 U b_e}{(1-M_r)}|\chi_3|^2\Psi_{33}(k_1,k_2) \qquad (31)$$

where r_O=|**x**| is the distance between source and receiver and $x3$ is the distance of the observer below the blade. U is the blade speed at the vortex interaction, M_r is the Mach number of the blade in the direction of the observer, c_O is the speed of sound and $\chi 3$ is the blade response function. The wavenumber spectrum of the upwash components is given by $\Psi 33(k1,k2)$ where $k1$=-ω (1-M_r)/U and $k2$=-ω $x2/c_O r_O$,with $x2$ the distance from the blade vortex interaction to the observer in the spanwise direction. All the parameters required to calculate the noise are defined by the rotor design apart from the wake width b_e and the wavenumber spectrum of the turbulence.

The turbulence in the wake is assumed to be dominated by the flow near the trailing tip vortices, and so it is first necessary to define the loci of the blade/vortex interactions, Glegg(1991), and then to use a model of the turbulence associated with the vortex to calculate the unsteady flow encountered by the blades. The experimental results

suggest that there are two dominant features of the unsteady flow which must be considered. The first is the turbulence in the spiral wake, and the second is the unsteady upwash caused by the small lateral displacements of the vortex. In this section we will consider the noise levels generated by each of these mechanisms.

3.1 Noise Generated by the Spiral Wake

The turbulence in the spiral wake was found to collapse using a Von Karman energy spectrum, with a correction for viscous dissipation, which gives a simple formulation for the wavenumber spectrum of the turbulence. This is very similar to the turbulence model used in the original BWI noise prediction method, Glegg(1991). However, the measurements presented in this report show that the turbulence intensities and integral lengthscales are smaller than used in the original model. The modification of the prediction method to incorporate the measured spectra is however relatively straightforward, the major difficulty being to estimate the geometry of immersion of the blade in the spiral wake. This will affect both the local turbulence intensity distribution and the spanwise length of the blade which is exposed to turbulent velocity fluctuations, and will be a function of the displacement of the vortex center from the blade. The vortex displacement can be calculated from the wake code, but the functional dependence of the turbulence intensity distribution on this displacement is complex. However it will only affect the intensity of the radiated noise and will have a minor affect on the spectral shape. Consequently a relatively simple model of the blade immersion in the wake is sufficient to give first estimates of the BWI noise spectrum. Consequently the functional form for the spanwise extent of the wake was taken to be of the form

$$b_e = WL_o e^{-|z/2L_o|} \qquad (31)$$

where $W = 10$ is a constant which gives the best fit to the data and z is the distance of the vortex core below the blade.

Figure 3.1 shows the calculations of the radiated noise spectrum using the wake spiral model described here in comparison with experimental noise measurements given by Brooks et al(1987). It is seen that the levels are of the correct order of magnitude at the high frequencies, but do not predict the low frequencies well. The peak of the broadband noise in the measured spectra occurs at 1500 Hz, while the peak in the predicted spectra occurs at 4500 Hz. This indicates that the turbulence lengthscales in the spiral wake are significantly shorter than required to predict BWI noise. Also we note that the width of the blade immersion being taken as ten times the wake width in equation (31) suggests an unrealistically large immersion width. This will have the effect of increasing the predicted levels, and it is unlikely that this mechanism generates more noise than predicted here. Since the measured levels are higher than predicted and the spectral shape is incorrect it would appear that the turbulence in the wake spiral is not the dominant contributor to the acoustic source levels.

3.2 Unsteady Motions of the Vortex

The blade vortex interactions which cause BWI noise occur when the vortex core is aligned with the direction of blade motion, and so if the vortex is fixed in space there are no changes in upwash velocity as the blade passes through the vortex with a constant displacement from the vortex center. However if the vortex has a random lateral displacement from its mean position then there will be unsteady velocity fluctuations on the blade, since the velocity distribution will move relative to the blade surface. The upwash will be anti-symmetric about the instantaneous spanwise location of the vortex core, and the spatial location of the distribution will be time varying in blade based co-ordinates. The anti-symmetric feature of the upwash gives an anti-symmetric unsteady

load distribution on the blade which is acoustically inefficient, since it is equivalent to a quadrupole source mechanism. Also the lateral motions of the vortex are predominantly of low frequency, and so it would appear that this mechanism of generating unsteady loads on the blades is not acoustically important. However, since the spiral wake turbulence does not account for the measured BWI noise spectrum, calculations have also been carried out to evaluate the noise generated by the lateral motions of the vortex.

The acoustic field from a blade moving through a vortex with lateral motions can be evaluated using equation (30) as described above. However the wavenumber spectrum of the upwash velocity fluctuations on the blade and the effective blade span must be defined. These will depend on the time varying upwash encountered by the blade and so we must develop a suitable model for this based on the description of the flow given in section 2.1. We will assume that the vortex passes either above or below the vortex core, and does not split the core, so that the blade is passing through a free vortex flow. If the blade is displaced by a distance $z+\beta(t)$ from the vortex core (see figure 3.2) then the upwash encountered by the blade is given by

$$W(y,t)=\frac{\Gamma_\infty(y+\alpha(t))}{2\pi r^2(t)} \tag{32}$$

where $r(t)$ is the distance from vortex core center to the spanwise location y on the blade. A linear model of the unsteady component of the upwash can be defined as before by using a Taylor series expansion of equation (32) for small displacements α,β of the vortex from its mean position. This gives the unsteady component of the upwash as

$$w(y,t)=\left(\alpha(t)\frac{\partial}{\partial y}+\beta(t)\frac{\partial}{\partial z}\right)\frac{\Gamma_\infty y}{2\pi r^2} \tag{33}$$

To obtain the wavenumber spectrum of the upwash velocity fluctuations we need to evaluate the Fourier integral (see Glegg(1991))

$$\hat{w}(k_1,k_2)=\frac{U}{(2\pi)^2}\int_{-T}^{T}\int_{-R}^{R} w(t,y)e^{ik_1Ut-k_2y}dtdy \qquad (34)$$

which on evaluation gives

$$\hat{w}(k_1,k_2)=\left(ik_2\hat{\alpha}(k_1U)+\hat{\beta}(k_1U)\frac{\partial}{\partial z}\right)\frac{\Gamma_\infty U e^{-|k_2 z|}}{4\pi} \qquad (35)$$

The wavenumber spectrum required for equation (30) is defined as

$$\Psi_{33}(k_1,k_2)=\frac{2\pi^2}{UTb_e}E\left[|\hat{w}(k_1,k_2)|^2\right] \qquad (36)$$

Also the power spectrum of the lateral displacements can be defined as

$$S_{\varepsilon\varepsilon}(k_1U)=\frac{\pi}{T}E\left[|\hat{\alpha}(k_1U)|^2\right]=\frac{\pi}{T}E\left[|\hat{\beta}(k_1U)|^2\right] \qquad (37)$$

If the lateral motions of the vortex core are isotropic we can combine equations (35), (36) and (37) to give

$$b_e\Psi_{33}(k_1,k_2)=\frac{k_2^2U\Gamma_\infty^2}{8\pi}S_{\varepsilon\varepsilon}(k_1U)e^{-2|k_2 z|} \qquad (38)$$

This result can be combined with equation (30) to give the acoustic field from this type of vortex interaction on the basis of the measurements presented in section 2.1. The

circulation of the vortex is easily defined and the spectrum of the lateral displacements is obtained from equation (27) or (29) since $S_{\varepsilon\varepsilon}(\omega)=G_{\varepsilon\varepsilon\lambda}(f)/4\pi$. The final result is

$$S_{pp}^{L}(\mathbf{x},\omega)=\left[\frac{\omega^2\rho_o c x_2 x_3}{4\pi c_o^2 r_o^3}\right]^2 \frac{\pi^2 U^2 \Gamma_\infty^2 e^{-2|k_2 z|}}{4(1-M_r)}|\chi_3|^2 S_{\varepsilon\varepsilon}(k_1 U) \qquad (39)$$

The analysis shows that the acoustic efficiency will have a quadrupole type directionality, given by $x2x3/r_O^2$, and will scale with frequency as $\omega^4 exp(-/\omega x2z/c_O r_O/)$ where z is the vertical displacement of the vortex from the blade. This demonstrates that as z increases, there will be a change in the spectral shape of the radiated noise and when z becomes comparable with the acoustic wavelength the exponential term will reduce the noise levels at high frequencies, ($z>>\lambda$), while not affecting the levels at low frequencies ($z<<\lambda$). The minimum distance between the vortex core and the blade is therefore an important parameter and it is assumed that this must be at least one core radius. One of the difficulties with this model is that it predicts that there will be a null in the directivity pattern directly beneath the rotor where $x2$ is zero. The measured directivity of BWI noise shows that there is a maximum in this direction and so we expect some inherent difficulties when comparing this prediction method with measured data.

BWI noise predictions made using equations (39) and (29) to modify the noise prediction code described in section 3.1 are shown in figure 3.1. This prediction depends on estimates of the circulation in the vortex core and the radius of the core, which are difficult parameters to estimate for a helicopter rotor which has a continuously varying angle of attack. Using reasonable estimates enables a best fit to the measured noise spectrum to be obtained. Note that the predicted spectral shape does not have the spectral peak which is identified in the measured spectrum. In order to enhance this peak the turbulence model used for these calculations was the one with the lowest low frequency energy content (equation (29)), and in spite of this the correct spectral shape was not

achieved. Furthermore it was found that the scaling of the predictions with changes in the tip path plane angle (which controls the vortex/blade displacement) was not compatible with the measurements. However this is not surprising considering the differences between the measured and predicted directionality.

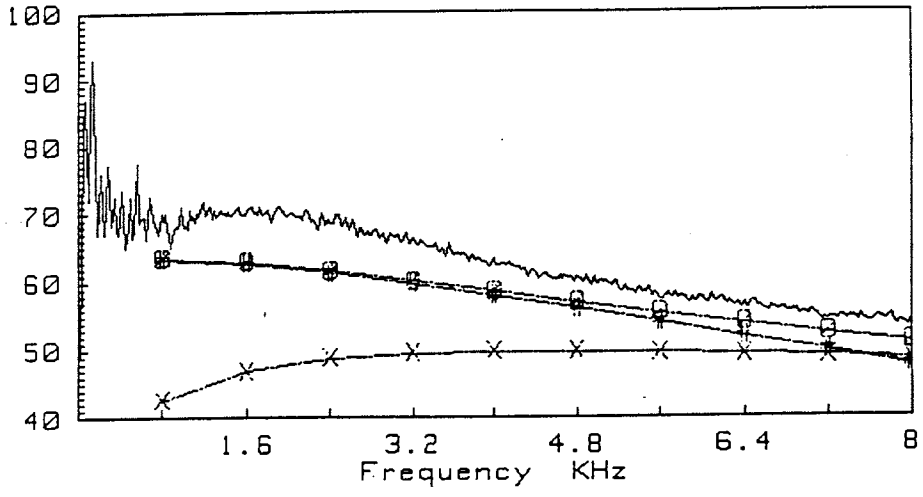

Figure 3.1 Comparison between measured and predicted BWI noise levels using the wake model and the lateral vortex motion model. (-x- the turbulent wake model, -#- lateral vortex motion model, -o- total predicted measurements)

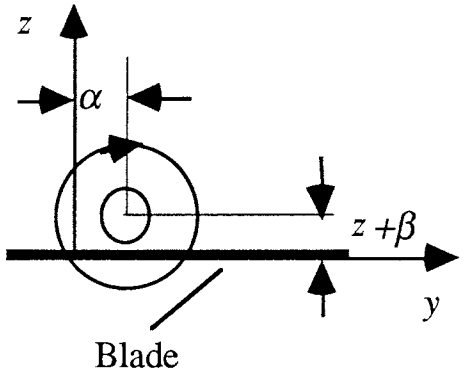

Figure 3.2 The vortex displacement from the blade used in the lateral vortex motions model.

4.CONCLUSION

This section of the report has described how wind tunnel measurements of the unsteady flow about a trailing tip vortex can be applied to the prediction of helicopter BWI noise. The flow measurements have identified three different features of the flow. At low frequencies the mean flow in the wind tunnel causes anisotropic lateral motions of the vortex which induce large unsteady velocities at a point. At mid frequencies the vortex is displaced isotropically from its mean position causing large velocity fluctuations in the vortex core. In addition to this there is a turbulent region in the spiral wake which is wrapped around the vortex core. Estimates of the noise produced by these different frequency regimes of the unsteady flow show that it is the mid frequency region of isotropic vortex motions which is the most important mechanism for noise production, but the spectral shape and the predicted directionality for this mechanism are not in agreement with the measurements of BWI noise. The original noise prediction scheme based on the concept of a turbulent vortex, has been shown to be the wrong basis for the correct description of the flow, but in spite of this the results presented by Glegg (1991) are significantly better than those presented here. This suggests that the flow measured in the wind tunnel cannot be used as an input for the turbulence upwash spectrum encountered on a helicopter rotor. One of the features of a real helicopter rotor which was not considered is the effect of a downstream blade on the trailing tip vortex. This may cause the vortex to burst and/or induce a different turbulent flow structure in the rotor disc plane. Measurements to evaluate this concept are planned for the future.

REFERENCES

Amiet R., 1975, "Acoustic radiation from an airfoil in a turbulent stream", Journal of Sound and Vibration, Vol 41, pp 407-420

Bradshaw P., 1967, "Inactive motion and pressure fluctuations in turbulent boundary layers", J. Fluid Mechanics, Vol 30, Pt 2, pp 241-258

Brooks, T.F., Marcolini, M.A., and Pope D.S., 1987, "Main Rotor Broadband Noise Study in the DNW", Presented at the AHS Specialist meeting on Aerodynamics and Aeroacoustics, Arlington, Texas.

Glegg S.A.L., 1991, "Prediction of blade-wake interaction noise based on a turbulent vortex model", AIAA Jnl. Vol 29(10), pp1545-1551.

Howe M.S., 1988, "Research on Lifting Surface Noise", BBN Report 6890, Bolt Beranek and Newman, Cambridge, Mass.

Hinze J.O.,1975, "Turbulence", 2nd edition, McGraw Hill Inc., New York.

Phillips W R C and Graham J A H, 1984, "Reynolds stress measurements in a turbulent trailing vortex", Journal of Fluid Mechanics, vol 147, p 353.

Schlinker R.H. and Amiet R. K.,(1983), "Rotor-Vortex Interaction Noise", AIAA 83-0720, Presented at the 8th AIAA Aeroacoustics Conference, Atlanta, Georgia

Wygnanski I., Champagne F.,and Marasli B., 1986, "On the large-scale structures in two-dimensional, small-deficit, turbulent wakes", Journal of Fluid Mechanics vol 168, pp31-71

APPENDIX II.1

Equation (30) gives the Von Karman turbulence spectrum corrected for viscous dissipation based on Saffmans approximation given by Hinze(1975) equation 3.147. The high frequency asymptote of the turbulent energy spectrum is specified as $k_1^{-5/3}exp(-\sigma k_1^2/sk_d^2)$, where $\sigma/s=4$. The wavenumber k_d is the inverse of the Kolmogoroff lengthscale and can be defined using Hinze equation 3.106a as $k_d=(\varepsilon/\nu^3)^{1/4}$ where ν is the kinematic viscosity and ε is defined by equation 3.99 as $\varepsilon=30\nu u^2/\lambda^2$. Finally u is the rms turbulent velocity fluctuations which can be specified as proportional to the free stream velocity $u=\kappa U_{ref}$, and λ is the dissipation scale of the turbulence given by equation 3.76 et seq. as $2L/\pi^{1/2}$. We have therefore

$$k_d = \left(\frac{30\pi u^2}{4\nu^2 L^2}\right)^{1/4} = \frac{1}{L}\left(\frac{30\pi}{4}\right)^{1/4}\left(\frac{\gamma\kappa L_o \mathrm{Re}_c}{c}\right)^{1/2}$$

where Re_C is the Reynolds number based on chord and $L=\gamma L_O$ where L_O is the wake width. Since

$$\hat{k}_1 = k_1 / k_e = 4k_1 L / 3$$

we can write

$$\frac{\sigma k_1^2}{sk_d^2} = S\hat{k}_1^2$$

where $S=4(k_e/k_d)^2 = 9/4(k_dL)^2$. Substituting from above gives

$$S = \frac{9}{2(30\pi)^{1/2}} \left(\frac{\gamma \kappa L_o \, \mathrm{Re}_c}{c} \right)^{-1}$$

Since the wake width L_O can be specified as proportional to the momentum thickness of the wake Θ and κ is an arbitrary constant we obtain

$$S = \frac{c}{\gamma \kappa L_o \, \mathrm{Re}_c}$$